Finite frequency dynamics in correlated quantum conductors

Jonas Müller

université
PARIS-SACLAY

Finite frequency dynamics in correlated quantum conductors

Thèse de doctorat de l'université Paris-Saclay

École doctorale n° 564, Physique en Île-de-France (PIF)
Spécialité de doctorat: Physique
Unité de recherche: Université Paris-Saclay, CEA, CNRS, SPEC, 91191, Gif-sur-Yvette, France.
Référent: Faculté des sciences d'Orsay

Thèse présentée et soutenue en visioconférence totale, le 14 décembre 2020, par

Jonas MÜLLER

Composition du Jury:

Hélène BOUCHIAT Directrice de recherche, LPS Orsay (MESO)	Présidente
Franck BALESTRO Maître de conférences (HDR), Institut Néel (LPEM)	Rapporteur & Examinateur
Pascal DEGIOVANNI Directeur de recherche (HDR), ENS de Lyon (PHYS)	Rapporteur & Examinateur
Sophie DJORDJEVIC Ingénieur de recherche, LNE	Examinatrice
Max HOFHEINZ Maître de conférences, Université Sherbrooke	Examinateur

Patrice ROCHE Directeur de recherche, CEA (SPEC)	Directeur de thèse
Carles ALTIMIRAS Chercheur, CEA (SPEC)	Co-encadrant

Thèse de doctorat

NNT: 2020UPASP061

Finite frequency dynamics in correlated quantum conductors

Jonas Müller

Doctoral School "Physique en Île-de-France"

University Paris-Saclay

A thesis submitted for the degree of

Doctor of Physics

December 2020

Abstract

Finite frequency dynamics in correlated quantum conductors

Jonas Müller[1]

[1]Nanoelectronics group (GNE), SPEC, CEA-Saclay, Orme des Merisiers, 91191 Gif-sur-Yvette Cedex, France.

Due to the recent progresses on the fabrication of high mobility semiconducting materials, it has become possible to fabricate smaller and smaller electrical devices. With the decrease in size, the governing laws for the electrical circuits change and need thus to be experimentally explored and understood in order to be able to deliberately engineer those sub-micron scale conductors. In this work, we present the new experimental methods that we have developed in order to investigate the fundamental physics of electronic transport across mesoscopic conductors based on the measurement of electrical fluctuations.

In the first part of the thesis we present a novel design of a back-action free quantum detector to separately measure the power spectral density of current fluctuations for positive (absorption noise) and negative (emission noise) frequencies. State-of-the-art on-chip detectors suffer from back-action effects that modify the transport properties of the measured conductor. Our approach, following the proposal of Lesovik & Loosen, allows to directly extract the absorption and emission noise from a measurement of the power exchanged between a quantum conductor and a finite frequency linear resonator, which we have tested for a SIS junction coupled to an RF-cavity filter. Our results stress the physical meaning of the Kubo formula which, coupled to a quantum description of the measurement setup, provides a quantum version of Joule's theorem.

In the second part of the thesis, we present the design and construction of an experimental platform for time dependent RF-measurements in high magnetic fields. The goal is to investigate the detection back-action, known as Dynamical Coulomb Blockade (DCB), of a single conduction channel interacting with a single electromagnetic mode. The main challenge is the engineering of high impedance RF resonators, used as impedance transformer, to efficiently couple the high impedance channel of $25.8\,\mathrm{k}\Omega$ to the mismatched $50\,\Omega$ RF-detection equipment. State-of-the-art impedance transformers are not able to operate under the applied magnetic fields that are required to obtain a single electronic channel. We have firstly designed and tested a magnetic field tolerant resonator, a planar metallic coil on a AlGaAs-GaAs hetero-structure, that provides a high characteristic impedance of $1\,\mathrm{k}\Omega$ at a resonance frequency of $5.4\,\mathrm{GHz}$. Using two resonators in series, an effective detection impedance of $27\,\mathrm{k}\Omega$ is achievable that provides sufficient coupling to a single channel. With all the methodologies developed in this thesis, it is now possible to perform a series of experiments in the near future.

Acknowledgements

Firstly I would like to thank my supervisors P. Roche and co-supervisor C. Altimiras. I am sincerely grateful to Carles for giving me the opportunity to be part of his project and for his continuous patience, many discussions, and vast knowledge with which he has helped and guided me throughout the entirety of my PhD thesis. I also thank Patrice for his advise and many discussions, peppered with his humorous interjections, and foremost his valuable feedback on my presentations. They both gave me valuable information and ideas through their critical reflections and have always motivated me to carry on further. Thank you very much.

Furthermore I thank all of the members of the nano-electronics group (GNE), the Quantronics group (QNO), the nano-fabrication atelier (AdN) and the workshop of the "Solid-State physics department" (SPEC) at CEA who have taught, supported and motivated me during the preparation and completion of this PhD thesis. Thanks to F. Portier for his valuable feedback on my manuscript, to H. Le Sueur with whom I had many discussions trying to solve my numerous sample fabrication issues and to D. Vion for his helpful instructions regarding e-beam lithography and also sharing his laboratory for many of my test measurements. I also greatly appreciate the continuous assistance of P. Orfila and S. Delprat with all the technical challenges of the clean-room fabrication. Thanks also to U. Gennser of C2N, who provided us with the crucial AlGaAs substrates for our project.

My special thanks goes to my friends and colleagues Z. Ifthikar, M. Jo and F. Da Silva-Barbosa. Zubair not only supervised me for certain parts of the projects but has also managed to familiarize me with new aspects of physics that I could not grasp by myself. Myunglae has assisted me with practical challenges of sample fabrication but I value him the most for our off-topic conversations which helped me to keep my stress levels in check. Fernanda has been a long-time companion in the clean room and suffered similar challenges and throw-backs but has remained a beacon of positive thinking throughout. I thank you all and sincerely hope that I may manage to stay in touch with you.

Lastly but not at the least, I want to thank my family for supporting me during the writing of my thesis. The stressful and quite depressing months, also during the COVID-19 confinement, would not have been sufferable without you. I especially thank my wife who has also assisted me in translating parts of my thesis into French.

Dedication

I dedicate this thesis to my family and especially to my parents and grandparents who had dreamed for me to achieve a PhD as the educational keystone in the pursuit of a happy life. However in retrospect, I would not describe my PhD as such but rather a struggle and disillusionment. Due to many setbacks I ended up without any break-through achievements that I had learned to expect in a PhD thesis, so that I questioned myself: is all what I have done and I myself even worth anything? My realization now is that failing to achieve one's initial goal is not a failure by itself as long as it contributes to the scientific progress:

"I have not failed. I have just found 10,000 ways that won't work." - T. A. Edison[1]

More than three years of hard work are worth showing and I can find pride in knowing to have built a foundation on which somebody else may find success. I believe this to be my direction for the future: I want to continue to contribute to the progress of science and humanity as a whole wherever I can. Thus it appears to be what my parents had envisioned and having achieved this goal is a relief and a joyful event. Thank you.

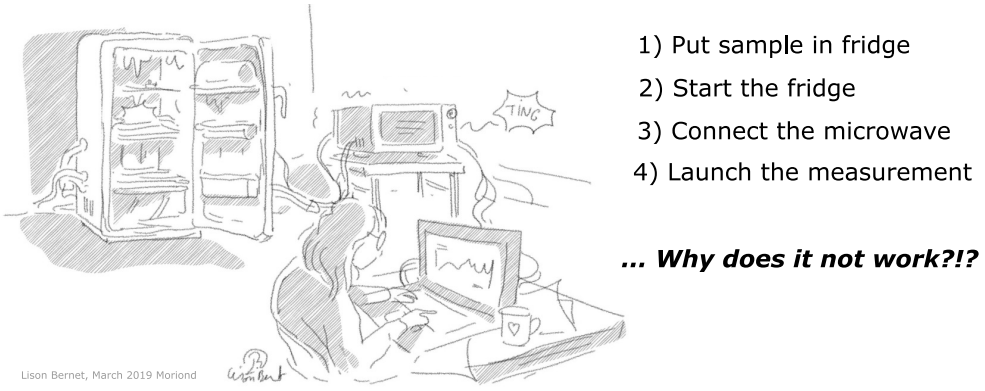

[1] J. L. Elkhorne. Edison — The Fabulous Drone, in Vol. 73, No. 3 (March 1967), p. 52

Abbreviations

2DEG	Two-Dimensional Electron Gas
ACF	Auto-Correlation Function
BCB	Bisbenzo Cyclo Butene
DCB	Dynamical Coulomb Blockade
EBR	Edge Bead Removal
FDR	Fluctuation Dissipation Relation
FDT	Fluctuation Dissipation Theorem
MBE	Molecular Beam Epitaxy
NIN	Normal-conducting/Insulating/Normal-conducting
PAT	Photon Assisted Transport
PCB	Printed Circuit Board
QC	Quantum Conductor
(D)QD	(Double) Quantum Dot
QED	Quantum Electro Dynamics
(F)QHE	(Fractional) Quantum Hall Effect
QPC	Quantum Point Contact
QSA	Quantum Spectrum Analyzer
RF	Radio Frequency
RRR	Residual Resistivity Ratio
SCB	Static Coulomb Blockade
SIS	Super-conducting/Insulating/Super-conducting
SNR	Signal to Noise Ratio
SQUID	Superconducting quantum interference device
SWR	Standing Wave Ratio
VNA	Vectorial Network Analyzer
ZPF	Zero Point Fluctuations

Physical constants

Constant:	**Symbol**	**Value**	**Unit**
Boltzmann constant	k_B	$1.380649 \cdot 10^{-23}$	J/K
Elementary charge	e	$1.602176 \cdot 10^{-19}$	C
Planck constant	h	$6.626070 \cdot 10^{-34}$	Js
Electron mass	m_e	$9.109383 \cdot 10^{-31}$	kg
Electric permittivity	ϵ_0	$8.854187 \cdot 10^{-12}$	C^2/Nm^2
Magnetic permeability	μ_0	$1.256637 \cdot 10^{-6}$	Tm/A
Conductance quantum	$G_0 = e^2/h$	$3.874045 \cdot 10^{-5}$	S
Resistance quantum	$R_0 = h/e^2$	$2.581281 \cdot 10^4$	Ω

Contents

Chapter i

Résumé de la thèse - Version française

Contents

Les dernières décennies ont vu progresser le développement des matériaux semiconducteur de haute mobilité, ainsi que la fabrication de circuits électriques dans des échelles micro puis nanométriques, permettant la miniaturisation de dispositifs électriques de plus en plus rapides. Ce progrès ouvre néanmoins des nouvelles questions et des nouveaux défis pour les ingénieurs et physiciens. Car quand les conducteurs électriques deviennent suffisamment petits, et qu'ils sont refroidis à suffisamment basse température, les lois usuelles gouvernant l'électricité ne tiennent plus donnant notamment lieu à des nouvelles lois de composition d'impédances [1–8]. La physique mésoscopique étudie et décrit ces phénomènes situés à la frontière des mondes macroscopique et microscopique, dans lesquels des phénomènes quantiques se manifestent à grande échelle. En effet, lorsque les dimensions du conducteur deviennent comparables à la longueur de cohérence de phase L_Φ, les électrons ne peuvent plus être simplement décrits comme des particules, mais doivent aussi être considérés comme des ondes. La cohérence de phase parmi les ondes électroniques, comme dans toute

autre phénomène ondulatoire, donne lieu à des effets d'interférence d'origine quantique. Cette cohérence de phase est fragile et diminue avec le taux d'interaction avec l'environnement acoustique (phonons) et électronique. Ainsi ces effets quantiques sont observables seulement à des températures cryogéniques qui "gèlent" ces collisions.

Par la granularité de la charge, et par l'aspect probabiliste de la dynamique quantique, les courants microscopiques traversant les conducteurs quantiques fluctuent et se couplent naturellement aux modes électromagnétiques présents dans le circuit. Pour des fréquences telles que $hf \gg k_B T$, la dynamique de ces modes est dominée aussi par les fluctuations quantiques et ont donc aussi un comportement quantique. Une conséquence de ce couplage électrodynamique est que les propriétés de transport d'un conducteur quantique ne sont plus intrinsèques, mais dépendent des propriétés du circuit dans lequel ils s'insèrent [3, 9–13]. Il est donc nécessaire de développer une compréhension de ces effets pour comprendre les lois quantiques de l'électricité qui permettront l'ingénierie de circuits contenant des conducteurs quantiques ($L < L_\Phi$) couplés à des champs EM quantiques ($hf > k_B T$). En pratique, il s'agît de conduire des expériences sur des échantillons micro et nano-structurés fabriqués en salle blanche, dans des environnements cryogéniques équipés d'un système de mesure électriques de bas bruit. Dans le domaine on utilise des réfrigérateurs à dilution, atteignant des températures de 20 mK typiquement, de sorte à ce que le régime électrodynamique $hf \gg k_B T$ est obtenu dans les quelques GHz, fréquences pour lesquelles il existe de l'excellente électronique commerciale ultra bas bruit.

i.1 Emission, absorption et dissipation dans un conducteur quantique

Un élément clé de la dynamique quantique est que les observables physiques ont des fluctuations [14]. Ainsi, au-delà de la réponse déterministe d'un conducteur quantique, caractérisée par son impédance ou sa caractéristique I(V), le courant s'écoulant dans le circuit présente des fluctuations même à l'équilibre et à température nulle [15]. Une conséquence de ce seuil de bruit de point zéro est que la densité spectrale de bruit (DSB) caractérisant les fluctuations d'un signal quantique est génériquement différente pour les fréquences positives et négatives [15]. Ainsi, les théorèmes classiques reliant la DSB au contenu énergétique d'un signal physique à son contenu énergétique (théorème de Wiener-Khinchin [16–18]) doivent être révisé afin de comprendre cette différence. La théorie de la réponse linéaire [19] donna un premier pas dans cette direction en reliant l'asymétrie de la DSB à la réponse linéaire réelle (dissipative) du conducteur à une sollicitation externe. Cette relation formelle a été étayée par Caldeira et Leggett [20] qui montrèrent que la friction mécanique visqueuse, ou les pertes électriques par effet Joule, peuvent être modélisées quantiquement par un couplage linéaire à un bain d'oscillateurs harmoniques caractérisés par leur impédance mécanique ou électrique. Finalement, les outils développés dans les années 80 pour décrire des systèmes quantiques ouverts [21, 22] ont permis de décrire non seulement la dynamique quantique du système, mais aussi son intéraction

(quantique) avec son appareil de mesure. Il en résulte que pour un système couplé linéairement à son appareil de mesure, à l'ordre le plus bas dans ce couplage; la puissance délivrée par le système est proportionnelle à la DSB prise à des fréquences négatives, tandis que la puissance qu'il absorbe l'est à fréquences positives [23]. Ce résultat donne donc un sens physique à la DSB des signaux quantiques que l'on nomme bruit d'émission et d'absorption, et combiné à la relation de Kubo [19] décrit quantiquement l'effet Joule. Dans la première partie de cette thèse, nous présentons une expérience dans laquelle nous mesurons le bruit d'émission et d'absorption d'une jonction tunnel supraconducteur-isolant-supraconducteur (SIS) à partir de la puissance qu'elle échange avec une résonateur électromagnétique linéaire, dont le contenu énergétique peut être ajusté indépendamment. Complétées par une mesure vectorielle de la réponse linéaire de la jonction, nos expériences ferment expérimentalement la formule de Kubo car elles nous permettent de comparer les trois quantités reliées par celle-ci. Ces expériences, réalisées sur un conducteur fortement non-linéaire et mis dans un état hors équilibre, montrent à quel point la formule de Kubo est un résultat général.

i.2 Bruit à fréquence finie, un banc de test expérimental pour des fluides fortement corrélés

La mesure des fluctuations quantiques est aussi intéressante car elles portent des informations précises sur les détails microscopiques du système mesuré. Par exemple, dans le cas des conducteurs quantiques la granularité de la charge donne lieu à du bruit de grenaille quantique [24, 25]. Cela permet de mesurer la charge dans un fluide dilué, quand la Dans des conducteurs où les électrons ont une faible probabilité d'être transmis, le bruit de grenaille permet de mesurer précisément la charge transportée, et quand la probabilité de transmission devient comparable à l'unité le bruit de grenaille témoigne de la statistique des porteurs de charge. Ce genre d'information est d'autant plus importante dans les circuits quantiques mésoscopiques, car en diminuant la taille du circuit les effets d'interaction Coulombienne deviennent de plus en plus importants, et peuvent donner lieu notamment à une dynamique de fluides quantiques fortement corrélés. Qu'ils proviennent des contraintes imposées par un champs magnétique intense, comme dans les effets Hall quantiques [26–29], ou par le confinement électrostatique créant de petites gouttelettes électroniques ayant une grande énergie de charge [30, 31], une propriété générique de ces liquides quantiques est que leurs excitations de basse énergie ont des propriétés très différentes de celles des liquides Fermi plus usuels. Ces excitations peuvent porter notamment des charges fractionnaires [32, 33], et même avoir une statistique d'échange fractionnaire différente de celles portées par des fermions ou des bosons. Grâce au résultats (exacts) de la théorie quantique des champs en basse dimensionnalité [42], les propriétés d'équilibre de ces liquides quantiques sont bien établies. Par contre, leur dynamique hors équilibre est largement moins comprise car d'un côté elles sont notoirement difficiles de prédire théoriquement, mais d'un autre côté elles sont aussi plus difficiles à mesurer, car

en plaçant ces fluides hors-équilibre il devient plus probable que l'énergie parte vers des degrés de liberté inattendus ou mal contrôlés ce qui complique considérablement l'interprétation des données.
Comme il filtre les canaux temporels, la mesure du bruit à fréquence finie dans ces fluides fortement corrélés donne des informations statistiques pertinentes, même dans l'absence d'une théorie complète. L'image physique est la suivante: l'énergie maximale que le fluide peut échanger avec son circuit de mesure lorsqu'une excitation de charge q le traverse est donné par le travail qV, où V est la tension continue fournie par le générateur qui met le fluide hors équilibre. Ainsi un signal de fréquence f ne peut être émis que si ce travail permet de créer un photon à cette fréquence: $qV > hf$. Contrairement au bruit de basse fréquence qui moyenne dans le temps tous les canaux de conduction, le bruit à fréquence finie contient donc une information spectroscopique permettant d'identifier séparément la charge de différents canaux de transmission.
Il est néanmoins difficile d'accéder expérimentalement à cette information: en ayant une dimensionnalité réduite (un faible nombre de canaux électroniques transmis), l'impédance des circuits logeant ces fluides corrélés est élevée de l'ordre du quantum de resistance $R_{\mathrm{K}} = 25,8\,\mathrm{k}\Omega$. Mais pour que ces effets spectroscopiques soient pertinents, il faut être dans le régime quantique $hf > k_B T$ce qui revient à mesurer la DSB dans les quelques GHz. Comme la communauté technologique a favorisé un standard de mesure GHz de basse impédance ($50\,\Omega$), il en résulte un faible transfert d'énergie entre le conducteur quantique et un système de détection standard, donnant lieu à une faible efficacité de détection. Il est donc nécessaire de transformer l'impédance de détection pour l'adapter à des impédances de l'ordre de R_{K}. Finalement, une conséquence de l'usage de fortes impédances de détection est que le conducteur interagi fortement avec son circuit de mesure. En effet, lorsqu' un pulse de charge est transmis vers le circuit de mesure de haute impédance, il en résulte une forte chute de tension modifiant donc la polarisation de l'échantillon. Quand l'impédance de détection est de l'ordre de R_{K}, cette rétroaction du système de mesure modifie fortement les propriétés de transport du conducteur cohérent, en donnant lieu à des processus de diffusion inélastiques. Cette physique est bien comprise pour des jonctions tunnel [44,45], mais on ne dispose que de quelques résultats précis pour des conducteurs ayant une transmission finie essentiellement à l'équilibre [3, 12, 13, 46].

Dans la deuxième partie de cette thèse, nous présentons un système expérimental afin de sonder cette physique. Nous avons mis en place et testé un système de mesure RF dans un réfrigérateur à dilution équipé d'une bobine de 14 T. Nous avons notamment développé des techniques d'adaptation d'impédance compatibles avec l'usage des forts champs magnétiques donnant lieu une impédance de détection d'environ $15\,\mathrm{k}\Omega$ à $5\,\mathrm{GHz}$ avec une bande passante de mesure d'environ $400\,\mathrm{MHz}$. Bienque nous n'ayions pas trouvé le temps de l'exploiter ce système, l'ensemble d'outils et de méthodologie que nous avons développés permettront bientôt de réaliser des expériences de pointe.

Les objectifs principaux de cette thèse sont de mesurer le bruit d'émission et d'absorption d'un conducteur par la mesure des échanges d'énergie avec un environnement électromagnétique controlé; ainsique de développer un banc de test expérimental pour mesurer de la dynamique hors équilibre à fréquence fine de conducteur cohérents soumis à des champs magnétiques intense. Les outils développés ouvrent la possibilité de sonder la dynamique fortement corrélée de conducteurs cohérents à faible nombre de canaux de transmission dans des régimes de forte intéraction.

i.3 Détection du bruit d'absorption

Dans la première partie de la thèse, nous décrivons une expérience qui donne l'accès à ce qu'on appelle le bruit de courant d'absorption et d'émission d'un conducteur quantique à partir de mesures de puissance électromagnétique.
Des expériences précédentes, qui tentaient de mesurer séparément le bruit d'absorption et d'émission d'un conducteur quantique non linéaire hors d'équilibre, ont créé des techniques de détection sur puce spécifiques, qui permettent de mesurer les signaux de bruit à haute fréquence en exploitant l'effet de transport assisté par photons (PAT) [47, 48]. Les spectres de fluctuation de courant sont imprimés sur la courbe I(V) d'un conducteur non linéaire couplé, par example une jonction tunnel supraconductrice-isolante-supraconductrice (SIS) et sont ainsi lisibles avec des techniques de mesure basse fréquence standard. Cela a été démontré avec succès pour différents conducteurs, tels que Jonctions Josepshon et points quantiques [49–52]. Bien qu'il soit beaucoup plus facile de sonder les fluctuations en mesurant leur empreinte sur le courant à travers le conducteur de détection, cette approche présente des inconvénients: lorsque l'échantillon et le détecteur sont à proximité, comme c'est le cas pour les détecteurs sur puce utilisés dans [49–52], on risque de mesurer les excitations de phonons [53] provoquées par le chauffage Joule en plus des fluctuations électromagnétiques. En consequence, il est nécessaire de calibrer le système pour ce couplage, ce qui n'a jusqu'à présent été démontré que pour les jonctions Josephson [51, 52]. D'un autre côté, un avantage de détecteur SIS est qu'il a été prouvé de pouvoir mesurer à la fois le bruit d'émission et le bruit d'absorption. Les résultats de [51] et [54] montrent l'asymétrie du bruit bien que leurs résultats ne soient pas quantitatifs. Pour qu'un détecteur SIS puisse mesurer le bruit d'absorption, il doit être polarisé en tension. Cela signifie que le système peut émettre de l'énergie vers le conducteur mesuré qui peut ensuite modifier les propriétés de transport du conducteur via un effet de transport photo-assisté (inversé) . Cette action de retour de détection, dans le cas de [51], [55] et [54], était du même ordre que celui du bruit d'absorption de sorte que le signal ne pouvait pas être extrait car l'échantillon et le détecteur avaient une symétrie couplage.
Nous avons implémenté et validé une configuration de détection radicalement différente, qui a été proposée par Lesovik et Loosen [23]: Nous mesurons simplement la puissance échangée entre un conducteur quantique et un résonateur linéaire à fréquence

finie dont le nombre d'occupation de photons n_B peut être réglé extérieurement. L'idée est qu'un résonateur vide ne peut absorber que de la puissance et donc va se coupler au bruit d'émission S^e, tandis qu'une population finie se couple inégalement au bruit d'émission et d'absorption S^a. Un étalonnage soigneux de la population du résonateur permet ainsi d'extraire les deux quantités des mesures d'échange de puissance à différentes populations. La densité spectrale de puissance échangée s'écrit:

$$P_{exch.} = Re[Z_{Detection}]((n_B + 1)S^e - n_B S^a)), \tag{i.1}$$

qui est valable dans la limite de la source actuelle [56] où $Z_{Source} \gg Z_{Detection}$. Pour respecter cette limite, nous avons réalisé plusieurs expériences avec Z_{Source} dans la plage de quelques kΩ et un schéma de détection d'environ 50 Ω. La faible impédance de détection rend négligeables les effets de blocage dynamique de Coulomb (DCB) (effets de contre-action dans le vide) ainsi que les effets de transport assisté par photons (PAT) lorsque le résonateur est excité (PAT incohérent). Il s'agit donc d'un schéma avec contre-action disparaissant.
La configuration expérimentale est illustrée dans la figure i.1: Dans le réfrigérateur de dilution sur l'étage à basse température, nous utilisons une jonction SIS comme conducteur de test. Une jonction SIS est choisie non seulement parce qu'elle est considerablement simple à fabriquer, mais aussi qu'elle est éminemment non linéaire et donne ainsi une nette différence entre son bruit d'émission et d'absorption. Il est couplé capacitivement via un té de polarisation au résonateur RF et au schéma de détection RF. Le résonateur est un filtre à cavité passe-bande avec une fréquence de résonance de $f_0 = 6,8\,\mathrm{GHz}$ et une bande passante de 600 MHz. L'occupation photonique de ce résonateur peut être réglée par l'émission de puissance de bruit d'une jonction NIN polarisée en courant continu. Selon la population du résonateur, il sera possible d'observer l'interaction entre la jonction SIS et le résonateur, qui sera lui-même imprimée dans la puissance échangée lorsque la jonction SIS est polarisée en courant continu. Pour mesurer ce signal RF de la puissance échangée, nous utilisons une ligne de mesure RF composée d'un préamplificateur cryogénique à l'étage 4 K et de deux amplificateurs à faible bruit à température ambiante pour amplifier davantage le signal. Un filtre à cavité, qui a les mêmes propriétés que celui vu par la jonction SIS, supprime les contributions de bruit d'amplification ajoutées avant que le signal est redressé par une diode et le signal résultant de tension continue est enregistré. Afin d'obtenir les valeurs correctes de la puissance échangée, il est nécessaire de convertir cette tension, qui est proportionnelle à la puissance, en déterminant le facteur de proportionnalité. Le facteur comprend le gain de l'amplificateur et toute amplification ou atténuation supplémentaire de la ligne de détection que nous obtenons en calibrant notre configuration.
La jonction SIS est puis balayée en polarisation continue pour différentes conditions de polarisation de la jonction NIN, qui correspond à différents nombres d'occupation photonique du résonateur, et la puissance totale émise $P(V_{SIS}, V_{NIN})$ du système est détectée dans la diode RT. Pour récupérer les signaux de bruit pur, plusieurs corrections doivent être appliquées. Premièrement, nous corrigeons la dérive temporelle du gain de la ligne de mesure en soustrayant une mesure de biais zéro $P(V_{SIS} = 0, V_{NIN} =$

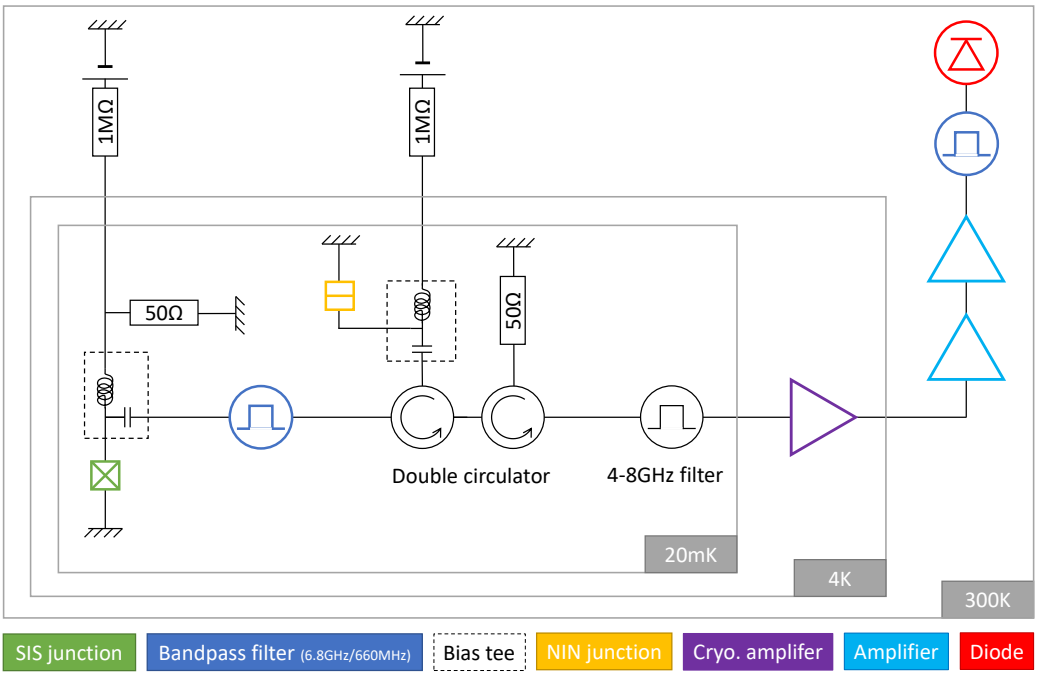

Figure i.1: Schéma de principe du dispositif de polarisation en courant continu et de détection RF pour la mesure de la puissance d'échange entre une jonction SIS et un résonateur linéaire dans notre réfrigérateur à dilution. L'occupation photonique du résonateur est ajustée avec la puissance de bruit qui est générée par une jonction NIN polarisée en courant continu. Les signaux de polarisation DC sont séparés du signal de mesure AC par des tés de polarisation qui guident le signal RF le long de notre ligne de détection comprenant plusieurs amplificateurs et une diode de redressement. Les circulateurs sont des éléments chiraux qui transmettent le signal RF initial à la ligne de détection mais qui acheminent le bruit provenant de l'amplificateur vers le sol via des terminaisons de 50 Ω. En plus des circulateurs, un filtre 4-8 GHz est ajouté avant la ligne de détection qui réduit le transfert de puissance vers l'amplificateur afin d'éviter sa saturation.

$0) = P_{noise}$ pour chaque point de données enregistré. P_{noise} est le bruit de fond émis par le préamplificateur 4 K, qui est également utilisé pour normaliser nos mesures. Deuxièmement, étant donnée que nous nous intéressons uniquement à la puissance échangée entre la jonction SIS et l'oscillateur à énergie finie, nous devons soustraire la puissance utilisée pour régler l'occupation de l'oscillateur : $\delta P_{exch.}(V_{SIS}, V_{NIN}) = P(V_{SIS}, V_{NIN}) - P(0, V_{NIN})$. La puissance échangée ainsi obtenue $\delta P_{exch.}$ est indiquée dans la figure i.2. Pour $V_{NIN} = 0$, on observe le comportement caractéristique du SIS avec une émission nulle de bruit en dessous de la bande d'énergie supraconductrice et son apparence à $2\Delta + hf_0 \approx 428\,\mu$eV où la jonction commence à émettre un signal RF. Il s'agit du bruit d'émission pur du système puisque le résonateur est inoccupé et que la jonction SIS ne peut pas absorber de puissance du résonateur. Par conséquent, pour toutes les autres mesures avec un biais fini appliqué sur la jonction NIN $V_{NIN} > 0$, l'occupation des modes du résonateur devient finie et une partie

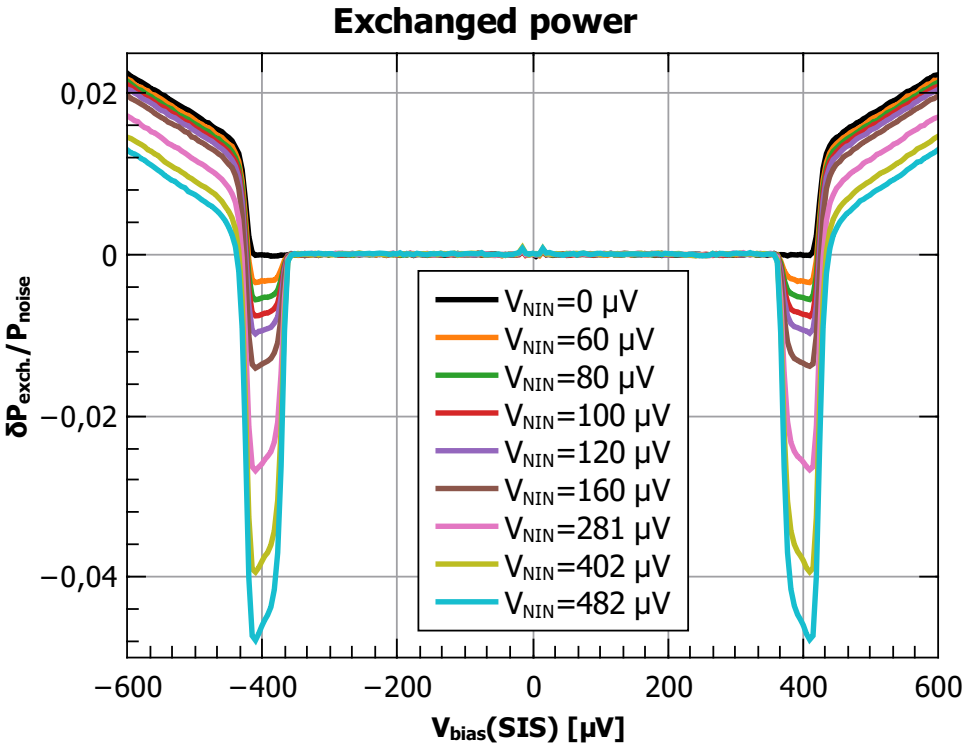

Figure i.2: Tracé de la puissance échangée entre la jonction SIS et son circuit environnant en fonction de la polarisation de la jonction SIS. Différentes courbes correspondent à un biais de jonction NIN différent et ainsi à un nombre d'occupation de photons différent du résonateur RF.

de son énergie peut être absorbée par la jonction SIS. Etant donné que le début du bruit d'absorption $eV - hf_0$ se produit plus tôt que celui de l'émission, la puissance échangée est négative dans l'intervalle $eV + hf_0 > eV > eV - hf_0$ où la jonction SIS ne peut absorber que l'énergie du résonateur. Ensuite, pour les biais supérieurs à $eV + hf_0$, la puissance échangée détectée est une combinaison de la puissance du bruit d'émission et du bruit d'absorption.
Nous pouvons séparer ces deux contributions de bruit, sur la base de la description de la puissance échangée par Lesovik et Loosen, avec l'équation i.1 [23] pour obtenir une expression du bruit d'absorption pour les mesures d'occupation de résonateur fini. Le bruit d'émission S^e peut être exprimé par la mesure de puissance échangée P_0 à V_{NIN}=0, pour laquelle le numéro d'occupation n_B et l'absorption le bruit est nul, pour obtenir

$$S^a = \frac{(n_B + 1)P_0 - P_{exch.}}{2Re(Z)n_B} = \frac{\Delta P}{2Re(Z)n_B} \tag{i.2}$$

Connaissant le numéro d'occupation précis n_B du résonateur, grâce à l'étalonnage, nous avons calculé le bruit d'absorption pour toutes les mesures avec différents biais NIN. Les résultats sont tracés sur la figure i.3 avec la mesure du bruit d'émission. Nous constatons que la courbe de bruit d'absorption n'est qu'autre que la courbe de bruit

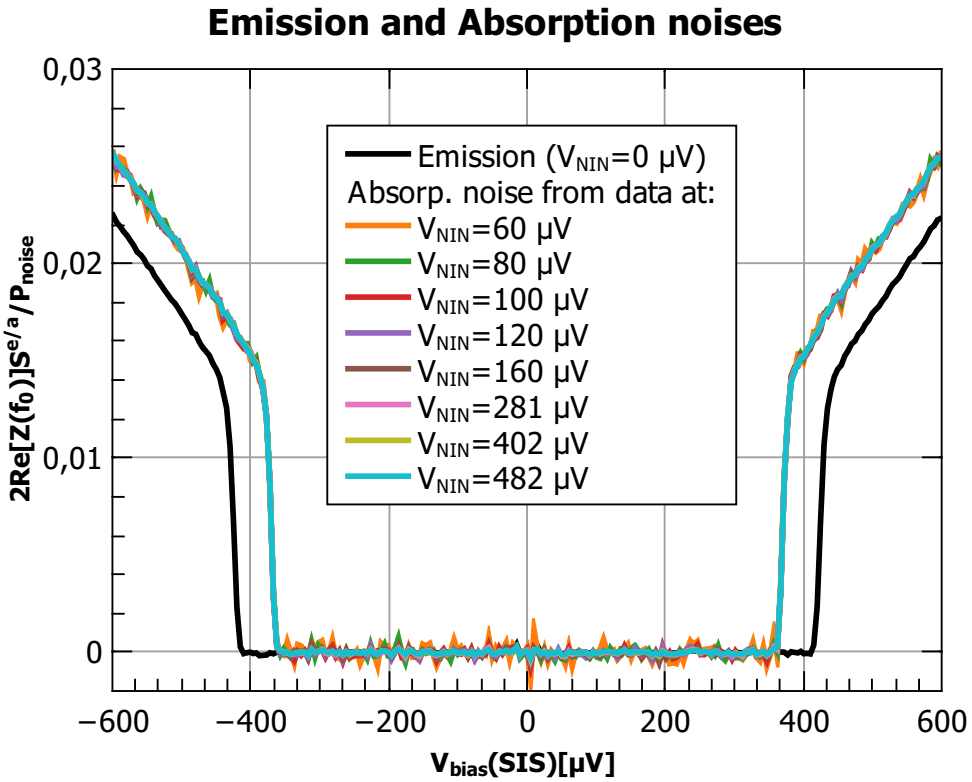

Figure i.3: Comparaison du bruit d'émission mesuré d'une jonction SIS tel qu'enregistré pour une occupation nulle du résonateur (noir) et du bruit d'absorption calculé à partir de mesures avec une occupation finie du résonateur fixée par la tension V_{NIN}.

d'émission avec un décalage du biais DC de 2 hf_0. Nous avons ainsi montré qu'il est possible de mesurer séparément le bruit d'émission et d'absorption d'un conducteur quantique à partir de la mesure de ses échanges d'énergie avec un résonateur linéaire proche de son état de vide. Ce schéma de détection, comme nous l'avons démontré en utilisant une jonction SIS comme conducteur d'essai, peut être appliqué à tout autre conducteur mésoscopique.
De plus, ce dispositif nous permet non seulement de mesurer le bruit d'absorption des différents systèmes, mais aussi de souligner la signification physique de la formule de Kubo [19]:

$$S^a - S^e = 2hf \cdot Re[Y_{emitter}], \tag{i.3}$$

qui, couplée à cette description quantique du dispositif de mesure, fournit une version quantique du théorème de Joule: La formule de Kubo indique simplement que la différence des densités spectrales de bruit est liée à la partie réelle de l'admission. Couplée à i.1, nous pouvons constater que la vitesse à laquelle l'énergie est prélevée dans l'environnement et dissipée dans le conducteur de la source est proportionnelle à l'admission de la source $Re[Y]$ en accord avec l'intuition classique de l'effet Joule.
Nous avons testé la formule de Kubo en calculant l'admittance du système à partir du

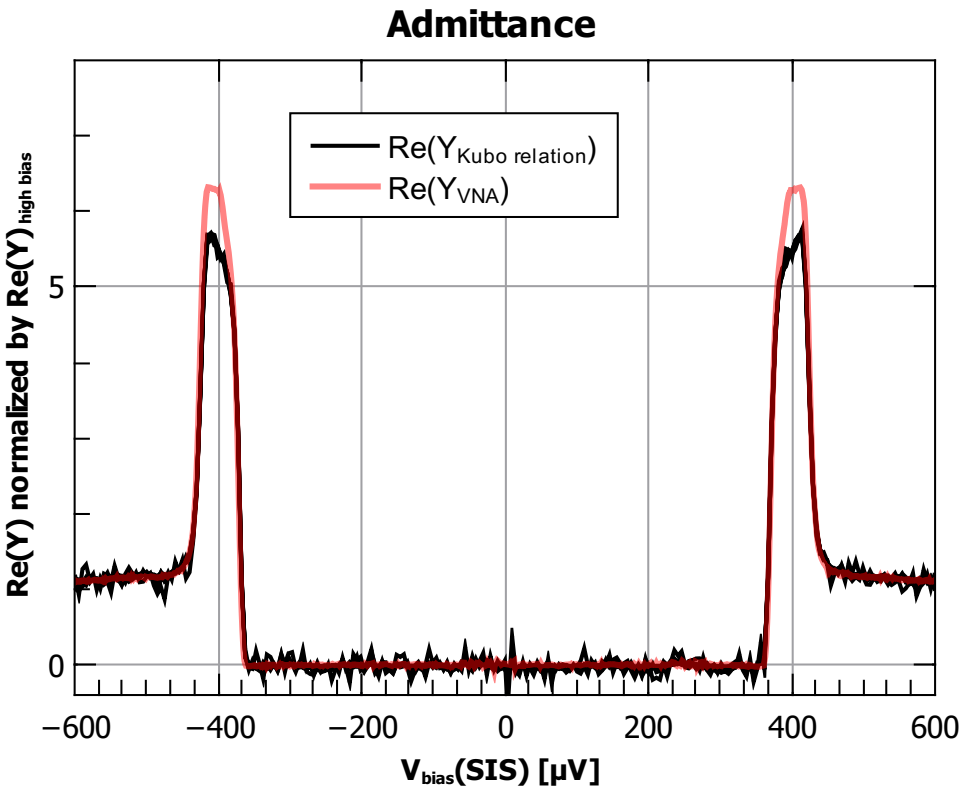

Figure i.4: Admittance calculée de la jonction SIS, en utilisant la formule de Kubo, basée sur les bruits d'émission et d'absorption mesurés (noir), comparée à l'admittance obtenue à partir d'une mesure de réponse linéaire utilisant un analyseur de réseau vectoriel (rouge). Nous trouvons un bon accord de l'admittance détectée sur la polarisation de la tension : un écart de 10% au voisinage de la tension d'écart à 400 μV. C'est un résultat plutôt satisfaisant compte tenu de la complexité de la procédure d'étalonnage de la chaîne RF.

bruit d'émission et d'absorption mesuré et en le comparant à l'admittance obtenue à partir d'une mesure de réponse linéaire sensible à la phase directe. Pour comparaison, nous montrons dans la figure i.4 nos résultats et l'admittance mesurés avec un analyseur de réseau vectoriel (VNA). Le résultat de notre mesure de détecteur s'aligne bien avec la référence VNA et fournit la première fermeture expérimentale de la relation de Kubo pour un conducteur quantique non linéaire [1]. Le faire pour un conducteur véritablement non linéaire éloigné de l'équilibre souligne la généralité d'une telle relation.

[1] La preuve pour un environnement ohmique linéaire a déjà été présentée dans [54]

i.4 Construire une plate-forme expérimentale pour effectuer des mesures RF sur des conducteurs de haute impédance aux champs magnétiques élevés

Dans la deuxième partie de la thèse, nous développons et réalisons une plate-forme expérimentale pour la mesure du bruit à haute fréquence des conducteurs mésoscopiques à basse température et à haut champ magnétique. Le cœur de notre système de test mésoscopique, le canal électronique unique (et éventuellement d'autres conducteurs mésoscopiques), sera défini dans un gaz électronique bidimensionnel (2DEG) dans une hétérostructure AlGaAs/GaAs. Ce matériau est idéal pour la création de notre plate-forme de test mésoscopique car il peut être utilisé dans plusieurs régimes physiques différents, rendus possibles grâce aux champs magnétiques et aux portes électrostatiques.
Le conducteur planaire peut être physiquement formé pour la création d'un confinement pour le 2DEG, qui est connecté par des contacts ohmiques. Dans l'ensemble, la géométrie de l'échantillon, telle qu'elle est illustrée dans la figure i.5, peut être définie par des techniques de fabrication communes de lithographie optique et par faisceau électronique pour servir de base à différentes expériences. En appliquant un champ magnétique perpendiculaire suffisamment élevé, les électrons entrent dans le régime dit de Hall quantique, où le courant traversant l'échantillon est transporté par des canaux de bord chiraux situés à proximité des bords de l'échantillon tandis que les électrons de masse sont localisés.
De plus, il est possible de manipuler électrostatiquement le 2DEG afin de définir différents conducteurs mésocopiques ou configurations, qui sont nécessaires pour différentes expériences. C'est pourquoi des portes métalliques sont définies par lithographie à faisceau d'électrons et déposées sur l'hétérostructure. En polarisant négativement ces portes, la densité électronique dans le 2DEG est localement appauvrie en raison de l'interaction répulsive de Coulomb. En utilisant deux portes fendues qui se rétrécissent en pointes fines avec un espace de quelques centaines de nanomètres entre elles, il est possible de définir un point de contact quantique [57, 58]. Sa transmission peut être réglée avec précision même pour un seul canal électronique [59–61] qui peut être utilisé pour contrôler l'interaction du canal dans notre expérience (voir figure i.5b). De même, nous pouvons adopter la même approche pour définir d'autres structures comme un "dot" quantique (voir figure i.5 c) ou utiliser de simples portes comme interrupteurs (voir figure i.5 a) afin de connecter et déconnecter des parties de la mésa comme des contacts ohmiques supplémentaires qui peuvent être utilisés pour mettre à la terre ou polariser le courant continu. Par conséquent, le 2DEG doit non seulement être connecté aux deux lignes de mesure RF requises (contacts ohmiques gauche et droit), mais aussi aux quatre autres contacts ohmiques. Douze connexions DC disponibles peuvent ainsi être utilisées pour contacter ou créer différents arrangements expérimentaux en façonnant la mesa avec des portes.

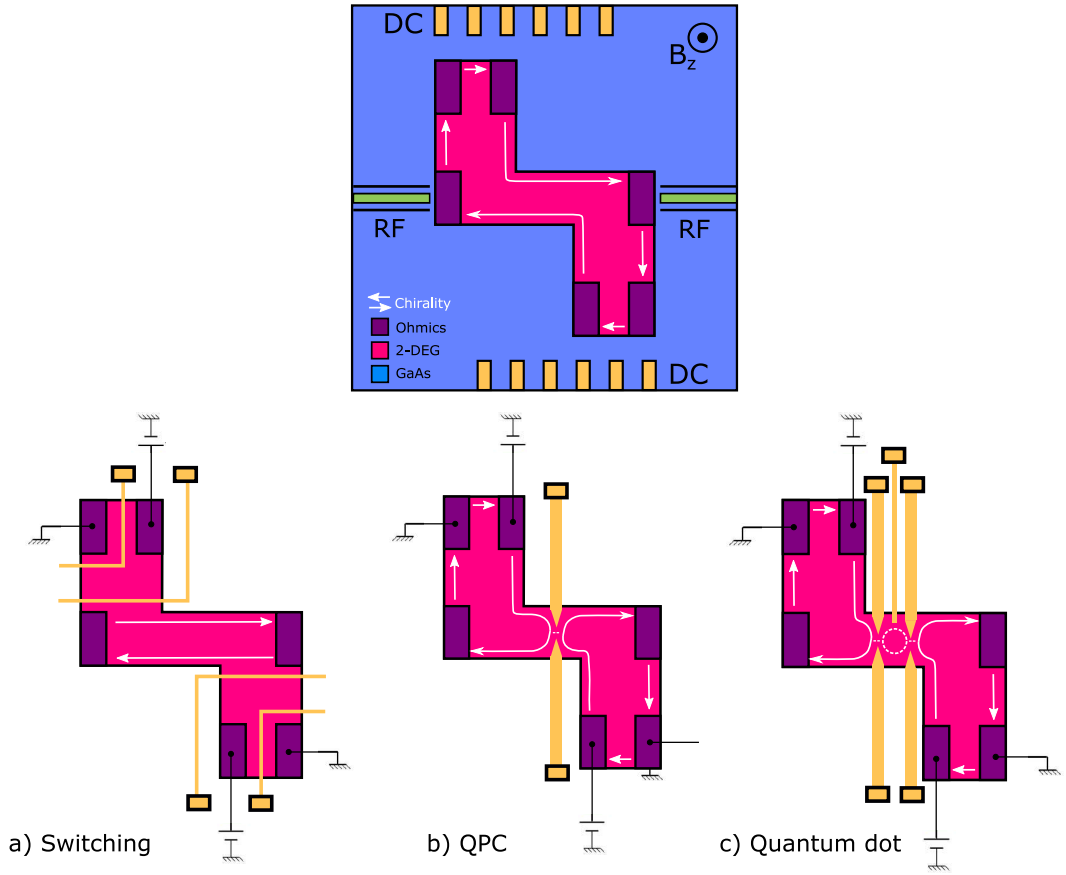

Figure i.5: Illustration schématique de la disposition de base mesa. La chiralité des courants de bord électroniques pour l'orientation du champ magnétique donné est indiquée en blanc. La mesa (rose) est contactée via des contacts ohmiques (violet) dont deux sont dédiés aux connexions RF (avec des guides d'ondes coplanaires sur la puce qui sont nécessaires pour les signaux RF) et un total de 4 contacts multi-usage accessibles via lignes DC. Le mesa de base peut être façonné de manière électrostatique pour différentes expériences en définissant différentes portes métalliques qui peuvent être polarisées à partir des ports DC comme indiqué ci-dessous: a) les portes sont utilisées pour déconnecter le 2DEG autour des contacts ohmiques supplémentaires qui fonctionnent comme un interrupteur marche/arrêt. Avec tous les contacts éteints, l'échantillon est dans une géométrie à 2 points dans laquelle les fluctuations de tension du circuit de détection à haute impédance polarisent l'échantillon, provoquant ainsi des effets de contre-action de détection [44]. En ajoutant des contacts ohmiques au système, une géométrie de barre Hall est réalisée qui peut être utilisée pour caractériser les propriétés 2DEG. Avec tous les contacts utilisés, une géométrie de masse intercalée permet de polariser en courant continu une mesure RF avec des effets DCB disparaissants. b) des portes divisées peuvent être créées qui se rétrécissent en points fins avec un espace étroit de quelques centaines de nanomètres pour réaliser des points de contact quantique lorsqu'elles sont polarisées; c) création d'un point quantique entre les QPC créés par des portes divisées. Une cinquième porte est capable d'ajuster le niveau d'énergie du point.

i.4.1 Mesure RF

Sortant des deux contacts désignés RF, des guides d'ondes coplanaires connectent le système mésoscopique à la configuration de détection de bruit haute fréquence. Avec les températures atteintes dans le réfrigérateur de dilution où l'expérience sera effectuée (T_{base} environ 15 mK), l'exigence $hf \gg k_B T$ est remplie pour les fréquences commençant par les quelques GHz [2]. Les instruments de détection disponibles dans le commerce dans la gamme des GHz sont conçus pour correspondre aux circuits de 50 Ω et présenteront un décalage considérable résultant en un transfert de puissance inefficace lorsqu'ils sont connectés à un canal électronique avec une impédance intrinsèque de l'ordre de $R_K = 25,8\,k\Omega$. Le principal défi pour la mesure du bruit est donc d'établir un couplage suffisant entre l'échantillon et la configuration de détection.

Une solution consiste à augmenter la durée pendant laquelle le signal est intégré. Néanmoins, cela conduit à un mauvais rapport signal/bruit comme il a été démontré pour les mesures de bruit dans le régime Hall quantique fractionnaire [62] même en utilisant des techniques avancées d'analyse de signal. Afin d'obtenir une meilleure résolution, qui nous fournit des fonctionnalités plus fines et un temps de mesure plus court, il est nécessaire d'utiliser un transformateur d'impédance qui permet de convertir l'impédance de détection standard 50 Ω en une impédance de détection plus élevée qui peut bien coupler au canal électronique haute impédance. Le transformateur le plus simple est le circuit LC-tank (figure i.6) qui est un circuit parallèle d'un condensateur C et d'une inductance L. L'impédance de sortie ou l'impédance de détection $Z(f)$ est mise à l'échelle comme $ReZ(f) \sim Z_c^2/R$, où $Z_C = \sqrt{L/C}$ est son impédance caractéristique qu'elle est proportionnelle à l'inductance et inversement proportionnelle à la capacité de shunt.

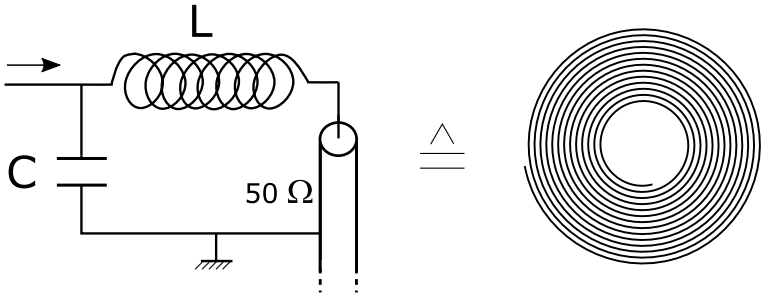

Figure i.6: Illustration schématique d'un résonateur à éléments groupés avec inductance parallèle L et capacité C. Les pertes internes sont représentées par une résistance R en série avec l'inductance. Un tel résonateur LC peut être réalisé sous la forme d'une bobine plane.

Dans le but d'obtenir une impédance de détection comparable à celle de R_K, une impédance caractéristique de 1 kΩ est nécessaire. Les transformateurs peuvent être fabriqués non seulement à partir d'éléments regroupés, par exemple des bobines planaires denses (voir [63, 64]), mais aussi à partir de guides d'ondes comme les résonateurs $\lambda/4$ [65–67], également appelés transformateurs quart d'onde. Bien que

[2] Pour une température $T_{mc} = 15$ mK le seuil de fréquence correspondant est d'environ 300 MHz

les éléments groupés doivent être conçus spécifiquement car la fréquence $f = 1/2\pi\sqrt{LC}$ dépend de l'inductance et de la capacité, la fréquence du transformateur quart d'onde peut être réglée librement en ajustant sa longueur. Cette dernière approche a été démontrée par E. Zakka-Bajjani et al. [66] pour la mesure du bruit de tir à un QPC avec une impédance caractéristique de 200 Ω. Ces impédances modérées permettent déjà une mesure quantitative du bruit d'émission. Des impédances plus élevées ont été obtenues par [68–72] en utilisant une chaîne de SQUIDs supraconducteurs comme transformateur quart d'onde, qui génèrent plusieurs kΩ d'impédance caractéristique. Le fort couplage a été démontré entre un mode EM et une jonction tunnel [72] ainsi qu'un point quantique [73]. Des impédances caractéristiques encore plus élevées ont été obtenues pour les résonateurs à guide d'onde coplanaire avec une inductance cinétique élevée de plus de 3 kΩ pour les systèmes hybrides Niobium-Tungstène [74] et atteignent jusqu'à 5 kΩ pour les films d'aluminium supraconducteurs désordonnés [75]. Bien que ces méthodes fournissent l'impédance caractéristique requise, elles ne sont pas adaptées à nos expériences car nous souhaitons travailler avec un canal électronique unique qui nécessite de forts champs magnétiques perpendiculaires où tout supraconducteur commun devient normalement conducteur [3]. Au lieu de cela, nous avons constaté qu'il est possible d'obtenir des impédances caractéristiques suffisamment élevées avec des résonateurs en bloc où l'inductance provient uniquement de l'influence magnétique et ne dépend pas de l'inductance cinétique. Un avantage de ce choix est que la plate-forme peut ainsi être utilisée pour des champs perpendiculaires bien au-delà de 2 T, de sorte que des expériences dans le régime de Hall fractionnaire sont possibles. Les pertes intrinsèques supplémentaires du matériau conducteur normal, par rapport aux résonateurs supraconducteurs, sont négligeables, puisque les pertes radiatives dans le circuit de détection 50 Ω sont dominantes.

i.4.2 Adaptation d'impédance élevée aux champs magnétiques élevés

Nous avons ensuite conçu un résonateur à éléments fragmentés, à savoir une bobine plane et très dense à l'échelle du micron, qui peut être fabriquée sur puce avec l'échantillon au moyen de la lithographie optique. La bobine résonante a été conçue en simulant ses propriétés avec le logiciel Sonnet® EM-Solver, en suivant de près les conceptions précédentes de C. Rolland pour des inducteurs spiralés gravés en Niobium sur des substrats de quartz qui ont atteint une impédance caractéristique de 1,97 kΩ à la fréquence de résonance de 4,4 GHz [77]. Nous avons également optimisé la conception de la bobine à fabriquer sur des hétérostructures GaAs/AlGaAs. La plus grande permittivité du substrat GaAs conduit à un shunt capacitif plus fort qui diminue Z_C et f, imposant ainsi plus de contraintes sur la capacité autorisée de la conception. Une deuxième contrainte est apportie par nos composants de circuit de détection pour la fréquence. Les éléments clés, l'amplificateur cryogénique, les circulateurs, les coupleurs et les filtres fonctionnent entre 4-8 GHz, en conséquence la

[3] Certains choix de matériaux existent qui restent supraconducteurs pour un champ dans le plan de $B > 2$ T [76]

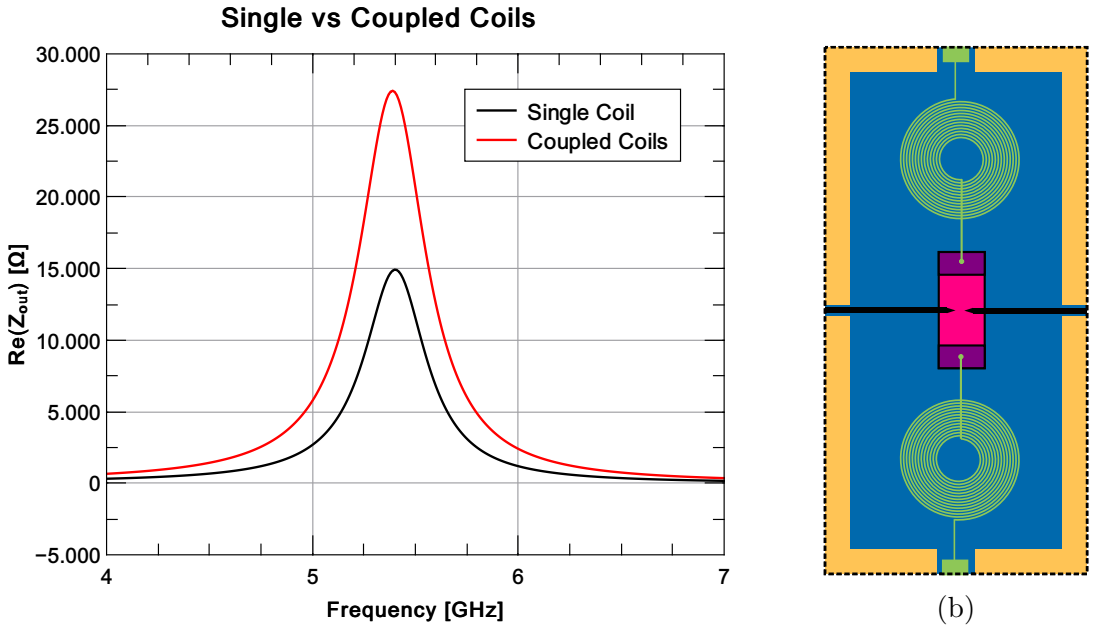

(a) (b)

Figure i.7: (a) Comparaison de l'impédance de sortie Z $_{out}$ telle que tracée pour la simulation de 2 bobines planes en série connectées à la mesa. Une illustration schématique de la disposition d'échantillon pour la simulation est montrée en (b). En couplant les bobines en série dans un arrangement symétrique autour du QPC, l'impédance caractéristique est grossièrement doublée de 1 à 2 kΩ, ce qui augmente l'impédance de détection de 18 à 27 kΩ, avec un décalage tolérable de la fréquence de résonance en raison de shunts capacitifs ajoutés.

fréquence de résonance du résonateur doit être dans cette limite avec une impédance caractéristique Z_c de quelques kΩ. Pour faciliter l'analyse, nous souhaitons que la largeur de bande du résonateur soit inférieure à k_BT/h. Cependant, plus la largeur de bande couplée est grande, plus l'expérience est rapide. Cela étant il faut trouver un compromis entre le quotient signal/bruit et la résolution énergétique, de sorte que nous visons un facteur de qualité (facteur Q), le quotient de la fréquence à la largeur de bande du résonateur, d'environ 10. L'objectif pour la fréquence de résonance a été fixé à 5 GHz, ce qui laisse un tampon au coupe-bande afin de pouvoir tolérer des shunts capacitifs supplémentaires inattendus.
La dernière contrainte, liée aux dimensions minimales du conducteur, est dû au choix de la méthode de fabrication. Afin de pouvoir fabriquer rapidement des résonateurs de grande surface, nous avons optimisé la conception à fabriquer par lithographie optique UV afin que la largeur et l'espacement des lignes de conducteurs ne puissent pas descendre en dessous du micron. La conception finale de la bobine est un conducteur enroulé 19,5 fois de 2 μm de largeur avec un espacement de 1 μm et atteint une impédance caractéristique de 1k Ω à 5,4 GHz avec Q=15. Nous utilisons une configuration en série du QPC entre deux bobines (voir figure i.7) qui donne une impédance de détection de 27 kΩ et se couple suffisamment bien à un seul canal électronique.

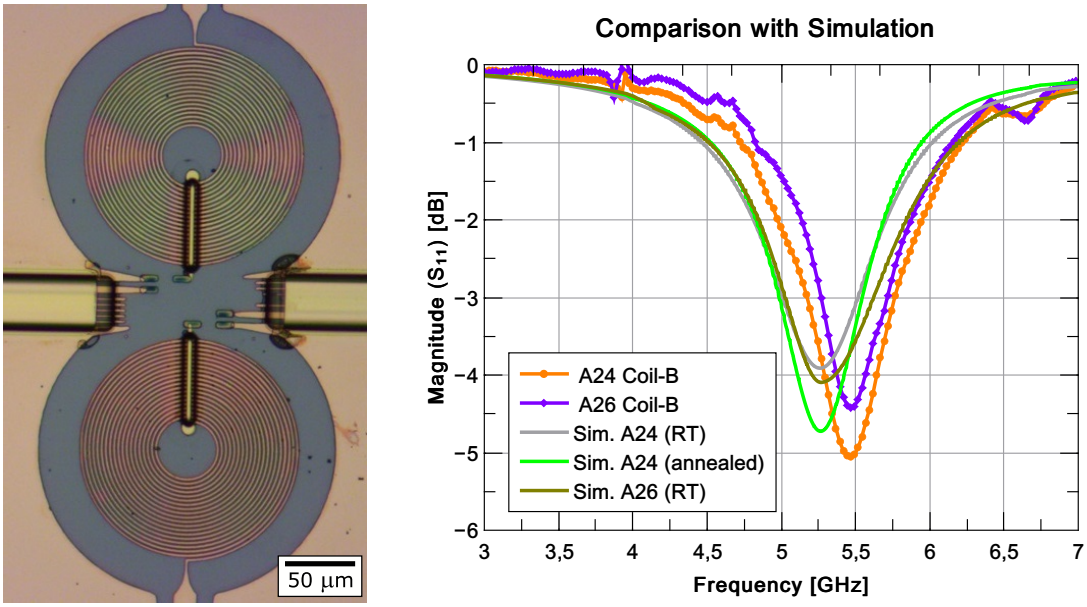

(a) (b)

Figure i.8: (a) Fabrication de l'échantillon d'essai A24: Achèvement de la fabrication des bobines résonantes (15 nm Ti / 500 nm Cu / 15 nm Au) avec des ponts entre les bobines et les lignes CC. Les ponts métalliques (15 nm Ti / 300 nm Cu / 15 nm Au) sont déposés sur des supports BCB diélectriques de 3 μm d'épaisseur. (b) Comparaison des courbes de réflexion simulées pour les bobines avec et sans ponts à résistivité arbitraire (gris & brun) à nos résultats de mesure VNA pour les bobines avec pont (A24, orange) et les bobines sans pont (A26, violet). Les mesures ont été effectuées à température ambiante tandis que les simulations utilisent des résistivités prédites basées sur des mesures de RRR. En comparant les deux mesures, nous n'observons aucun décalage de fréquence dû aux shunts capacitifs causés par le pont de 3 μm. Cependant, par rapport à la simulation, nous constatons un décalage de la fréquence de résonance de 200 MHz. Le changement de l'amplitude des mesures est attribué au recuit thermique qui réduit les pertes internes de la bobine pour A24. Comme montré, le remodelage direct avec les résistivités prévues ne correspond pas en magnitude mais après avoir considéré le recuit effectif de A24 (recuit - vert) il montre l'évolution correcte.

Pour réaliser la géométrie envisagée, les bobines sont fabriquées par une lithographie optique à trois niveaux qui atteint une résolution d'un micron à l'aide d'une bicouche de résist négatifs et de couches de décollage. Nous définissons d'abord la géométrie de la bobine avant de deposer un métal à haute conductance. Plusieurs choix différentes existent avec Cu, Ag et Au qui fournissent de petites résistances d'environ 12 Ω à basse température après recuit. Les bobines sont connectées via un pont métallique créé par la même technique sur une entretoise de support de pont BCB. Le BCB s'agit d'un polymère diélectrique avec une petite constante diélectrique, qui est façonné par lithographie optique et peut être complètement durci pour former une structure de support mécaniquement stable avec de faibles pertes RF.

Nous avons réussi à fabriquer et à tester les paramètres caractéristiques des résonateurs fabriqués sur des substrats de GaAs à température ambiante, avec (voir figure i.8a) et sans pont (non représenté). Nous avons mesuré la réflectance du signal de la bobine avec un analyseur de réseau vectoriel et comparé les résultats à des simulations (figure i.8b). Les résultats obtenus sont en accord avec la simulation et confirment la réussite de la fabrication de résonateurs d'impédance 1 kΩ à 5,5 GHz et 400 MHz bande passante avec un shunt capacitif négligeable du pont.
Avec la bobine planaire comme transformateur d'impédance, il est possible de mesurer l'échantillon avec une chaîne d'amplification en GHz et différents détecteurs, par exemple un analyseur de réseau vectoriel (VNA), des diodes de puissance et des analyseurs de spectre qui peuvent être placés à température ambiante. Malheureusement, la fabrication d'un échantillon complet sur un 2DEG n'a pas pu être terminée dans le délai de la thèse de doctorat en raison de problèmes de fabrication. Malgré tout, nous avons réussi à mettre au point la méthodologie qui permettra de réaliser une série d'expériences étonnantes dans un avenir proche.

Chapter ii

Summary of the thesis - English version

Contents

Over the last decades there has been a constant progress in the development of high mobility semiconducting materials and in the fabrication of micron- and sub-micron scale electrical conductors in the pursuit of the miniaturization of electrical devices. However, with this progress came new challenges and questions for electrical engineers and physicists alike. When electrical conductors become small and cold enough, the common macroscopic laws of electricity do not hold true anymore as was found for the addition of series [1–3] and parallel resistances ([4, 5] and experimentally [6–8]). This is the domain of mesoscopic physics that is at the crossover from the classical macroscopic physics towards the quantum mechanics developed for microscopic systems. It appears that, when conductors have a size that is comparable to the so called electronic phase coherence length L_Φ, electrons can not be described as particles anymore but have to be considered as waves. The phase coherence of the electronic waves, like in other wave related fields of physics, leads to interference phenomena which give rise to many quantum effects. This phase coherence is typically lost due to phonon interaction or electron-electron interaction so that quantum effects are only observable under the condition of sub Kelvin temperature when phonons and electrons are

effectively "frozen".
Due to charge granularity and the probabilistic character of the transmission through the conductor, reflecting the wave nature of the electrons, such quantum microscopic currents will couple to the macroscopic electromagnetic modes of the surrounding circuit. At frequencies $hf \gg k_B T$, the dynamics of these modes are dominated by quantum fluctuations and thus behave quantum mechanically as well. Because of this coupling, the transport properties of a quantum conductor are not intrinsic anymore, but depend on the circuit that it is embedded in [3, 9–13]. It is thus necessary to develop a physical understanding of these quantum effects, for quantum conductors ($L < L_\Phi$) and quantum EM-fields ($hf > k_B T$), and the underlying fundamental principles in order to define the quantum laws of electricity that will allow the engineering of nano-electronic circuits. To conduct those kind of experiments it is necessary to fabricate mesoscopic conductors in state-of-the-art clean rooms facilities that are then probed within a cryogenic cooling system equipped with a low noise electronic measurement setup. This can be realized by using a dilution refrigerator, reaching temperatures of typically 20 mK, and commercially available low noise electronics for the corresponding GHz frequency of the electronic signals.

ii.1 Emission, absorption and dissipation in a quantum conductor

A key feature of quantum mechanical systems is that their physical observables display quantum fluctuations [14]. This means that on top of a deterministic response of a quantum conductor, characterized by an impedance or a I(V) characteristic, the current flowing through will display stochastic fluctuations, even in equilibrium and at zero temperature [15]. A direct consequence of such vacuum noise floor is that the power spectral density (PSD) of fluctuations is generically different at positive and negative frequencies [15]. Thus the classical picture relating the PSD of a physical signal's noise to its energy content (Wiener–Khinchin theorem [16–18]) needs to be refined to account for such a difference. Linear response theory [19] provided a first step in this direction, as it related the frequency asymmetry of the PSD to the real (dissipative) part of the system's linear response to an externally applied force. This formal relation was further stressed by Caldeira and Leggett [20] who showed that mechanical viscous damping, or electrical Joule losses, could be modeled quantum mechanically as a linear coupling to a bath of harmonic oscillators simply characterized by their (mechanical or electrical) impedance. Finally, the tools developed in the 80's to describe open quantum systems [21, 22] could be used to model efficiently not only the physical quantum system, but also its (quantum) interaction with a measuring apparatus. It results that for a system linearly coupled to a meter, to lowest order in this coupling, the power absorbed by the system from its meter is proportional to the positive frequency PSD of the coupling operator, while the power emitted by the system to its meter is proportional to the negative frequency PSD [23]. This result not only provides a physical meaning to the positive and negative frequency PSDs

named consequently absorption and emission noise, but also, combined with the Kubo relation [19], provides a quantum framework to Joule dissipation. In the first part of this thesis we present an experiment where we extract the emission and absorption noise of a superconductor-insulator-superconductor (SIS) tunnel junction from measuring the energy exchanged with a linear electromagnetic environment whose energy content is externally controlled. Complemented with a phase-sensitive linear response measurement we experimentally close the Kubo formula, as we can compare the three quantities related by the formula. We chose the SIS junction in order to stress that such relation holds for a genuinely non-linear conductor, even when biased far from equilibrium.

ii.2 Finite frequency noise, an experimental platform for strongly correlated fluids

Measuring quantum fluctuations is also interesting since they convey information on microscopic details of the physical system they originate from. Current fluctuation in a quantum conductor results from the granularity of charge carried which, combined with the probabilistic character of quantum dynamics, gives rise to quantum shot-noise [24, 25]. This allows to measure the charge in a dilute fluid, when the probability for an electron to be transmitted through the circuit is small, and their statistics when the probability goes towards one. Then, Fermi-Dirac statistics tend to regularize the electronic flow and diminish the amplitude of shot-noise. Furthermore, making the conductor dimensions small not only allows to probe wave-like electronic phenomena, it can also increase the effects of Coulomb interactions. Quantum conductors can therefore be engineered to implement the physics of strongly interacting quantum fluids. Whether the electronic fluid is constrained by quantizing magnetic fields as in the quantum Hall effects [26–29], or by geometry to generate small electronic droplets [30, 31] with a high electrostatic charging energy, a common feature of such fluids is that their low energy excitations might display non-Fermi liquid behaviour with exotic properties such as renormalized electronic charges [32, 33] and even fractional statistics. While their ground state and equilibrium properties are quite well established, notably thanks to the exact results that quantum field theory can produce in one dimension [42], their dynamics are far less understood mainly for two reasons: on the theoretical side they are notoriously hard to predict, while on the experimental side, as one drives a system out-equilibrium, it is more likely that energy is sent to unanticipated degrees of freedom, making it difficult to interpret the experimental outcomes.

As it filters temporal channels, measuring high frequency current fluctuations provides meaningful statistical information on such correlated fluids even in the absence of fitting theory. The physical picture is the following: the maximum amount of energy the quantum fluid can release upon its detection circuit after a scattering event is qV, with q the charge carried by the scattered excitation and V the DC-bias applied to drive the fluid out-of-equilibrium. Thus high frequency photons at frequency f can

only be emitted for a scattering event at biases larger than the electromagnetic energy quantum at the detection frequency $qV > hf$. Contrary to low frequency noise, which reveals the average scattered charge [43], measuring high frequency noise conveys spectroscopic information on the different charges characterizing the excitations of the fluid, and on the order of their scattering processes.
However, accessing this information is an experimental challenge: We want to probe as few scattering channels as possible in order to facilitate the analysis of the system's noise data. Thus a single electronic channel is the ideal case of a 1D limit in which the sought after interaction effects are the most dominant, but may be hard to detect because of its high impedance Z that is about $R_{\mathrm{K}} = 25.8\,\mathrm{k}\Omega$. This is problematic because in order to be within the quantum regime, where $hf > k_B T$, we have to measure signals at a few GHz and commercially available GHz measurement equipment is standardized to $50\,\Omega$ impedance which leads to a poor power transfer when connected to a high impedance. It is thus necessary to transform the detection impedance to match R_{K}. Not the least, a consequence of measuring with a high detection impedance is that the conductor strongly interacts with its detection circuit. Indeed, a high impedance environment gives rise to a sizeable voltage pulse which adds to the voltage biasing the conductor, as a charge pulse is thread through the circuit. When the detection impedance is comparable to R_{K}, this measurement back-action modifies the transport properties of the conductor giving rise to inelastic scattering events. While physics are well understood in the tunnel limit [44, 45] , they are only partly understood for a finite transmission impurity mostly in equilibrium [3, 12, 13, 46].

In the second part of the thesis, we present an experimental platform which allows to perform these kind of experiments. We have realized and tested an RF-measurement system in a dilution refrigerator equipped with a magnetic coil providing up to 14 T. Therefore we have developed impedance matching techniques compatible with high applied magnetic fields which provide a detection impedance of about $15\,\mathrm{k}\Omega$ at 5 GHz with a bandwidth of around 400 MHz. Even though we were not able to utilize the system within the time-frame of this thesis, the developed tools and methodologies will allow us to realize a series of experiments in the near future.

The primary goals of this thesis are the measurement of emission and absorption noise with an externally controlled electromagnetic environment and the development of an experimental testing platform for the measurement of high frequency current fluctuations across mesoscopic conductors at low temperatures and high magnetic fields. Thereby creating the possibility to probe the strong correlations of a single electronic channel to a single electromagnetic mode and other environments.

ii.3 Detection of absorption noise

In the first part of the thesis we describe an experiment giving access to the so called absorption and emission current noise of a quantum conductor from electromagnetic power measurements.
Previous experiments, that attempted to separately measure the absorption and emission noise of a non-linear out of equilibrium quantum conductors, created specific on-chip detection techniques that allow to measure the high frequency noise signals by exploiting the photon-assisted transport effect (PAT) [47, 48]. The current fluctuation spectra are imprinted on the I(V) curve of a coupled non-linear conductor e.g. a superconducting-insulator-superconducting (SIS) tunnel junction and are thus readable with standard low frequency measurement techniques. This was shown successfully for different conductors e.g. Josepshon junctions and quantum dots [49–52]. While it is much easier to probe the fluctuations by measuring their imprint on the current across the detection conductor, this approach also has disadvantages: When sample and detector are in close proximity, as is the case for the on-chip detectors used in [49–52], it is possible to measure the phonon excitations [53] caused by the Joule heating in addition to the electromagnetic fluctuations. Thus it is necessary to calibrate the system for this coupling, which has so far only been demonstrated for Josephson junctions [51, 52]. On the other hand, an advantage of the SIS detector is that it has been proven to measure both emission and absorption noise. The results of [51] and [54] do show the asymmetry of noise even though their results are not quantitative. For a SIS detector to be able to measure absorption noise, it needs to be voltage biased, this means that the system can emit energy towards the measured conductor that can then modify the transport properties of the conductor via (a reverse) photo assisted transport effect. This detection back action, in the case of [51], [55] and [54], was of the same order as the absorption noise so that the signal could not be extracted because sample and detector had symmetrical coupling.
We have implemented and validated a radically different detection setup, which was proposed by Lesovik and Loosen [23]: We simply measure the power exchanged between a quantum conductor and a finite frequency linear resonator whose photon occupation number n_B can be externally tuned. The idea being that an empty resonator can only absorb power and thus couples to emission noise S^e, while a finite population couples unequally to the emission and absorption noise S^a. A careful calibration of the population of the resonator thus allows extracting both quantities from power exchange measurements at different populations. The exchanged power spectral density is written as:

$$P_{exch.} = Re[Z_{Detection}]((n_B + 1)S^e - n_B S^a)), \tag{ii.1}$$

which is valid within the current source limit [56] where $Z_{Source} \gg Z_{Detection}$. To fulfil this limit, we have performed several experiments with Z_{Source} in the few kΩ range and a detection scheme of about 50 Ω. The low detection impedance makes dynamic Coulomb blockade (DCB) effects (vacuum back-action effects) negligible as well as photon-assisted transport (PAT) effects when the resonator is energized (incoherent

PAT). It is thus a scheme with vanishing back-action.

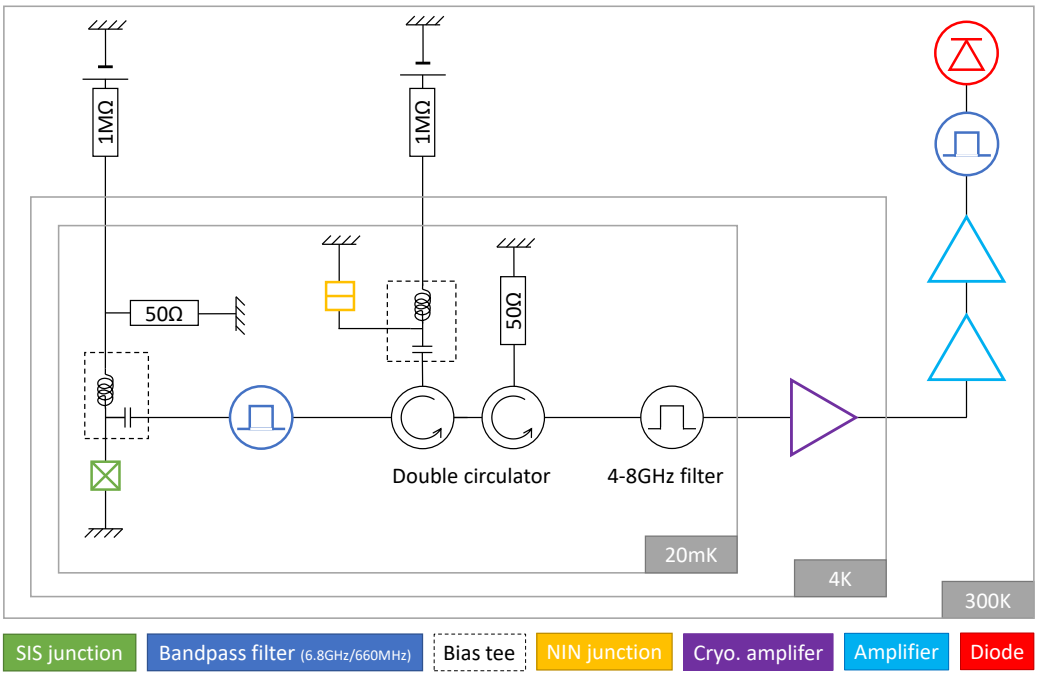

Figure ii.1: Block diagram of the DC biasing and RF-detection setup for the exchange power measurement between a SIS junction and a linear resonator within our dilution refrigerator. The resonator's photonic occupation is adjusted with the noise power that is generated from a DC biased NIN junction. The DC biasing signals are separated from the AC measurement signal via bias tees that guide the RF signal along our detection line including several amplifiers and a rectifying diode. The circulators are chiral elements that pass the initial RF-signal on to the detection line but route the noise coming from the amplifier to the ground via 50 Ω terminations. In addition to the circulators a 4-8 GHz filter is added before the detection line that reduces the power transfer to the amplifier in order to avoid its saturation.

The experimental setup is illustrated in figure ii.1: Within the dilution refrigerator on the low temperature stage, we use a SIS junction as test conductor. An SIS-junction is chosen not only because it is remarkably simple to fabricate, but also because it is eminently non-linear and thus gives a stark difference between its emission and absorption noise. It is capacitively coupled via a bias tee to the RF-resonator and to the RF-detection scheme. The resonator is a band-pass cavity filter with a resonance frequency of $f_0 = 6.8\,\mathrm{GHz}$ and a bandwidth of 600 MHz. The photon occupation of this resonator can be tuned by the noise power emission of a DC-biased NIN junction. Depending on the population of the resonator, it will be possible to observe the interaction between the SIS junction and the resonator that will be imprinted in the exchanged power when the SIS junction is DC-biased. To measure this RF-signal of the power exchanged, we are using an RF-measurement line consisting of a cryogenic pre-amplifier at the 4 K stage and two low noise amplifiers at room temperature to further amplify the signal. A cavity filter, having the same properties as the one seen

by the SIS junction, removes the added amplification noise contributions before the signal is rectified by a diode and the DC voltage signal recorded. In order to obtain the correct values of the exchanged power it is necessary to convert this voltage, which is proportional to the power, by determining the proportionality factor. The factor includes the amplifier gain and any additional amplification or attenuation of the detection line which we get by calibrating our setup.

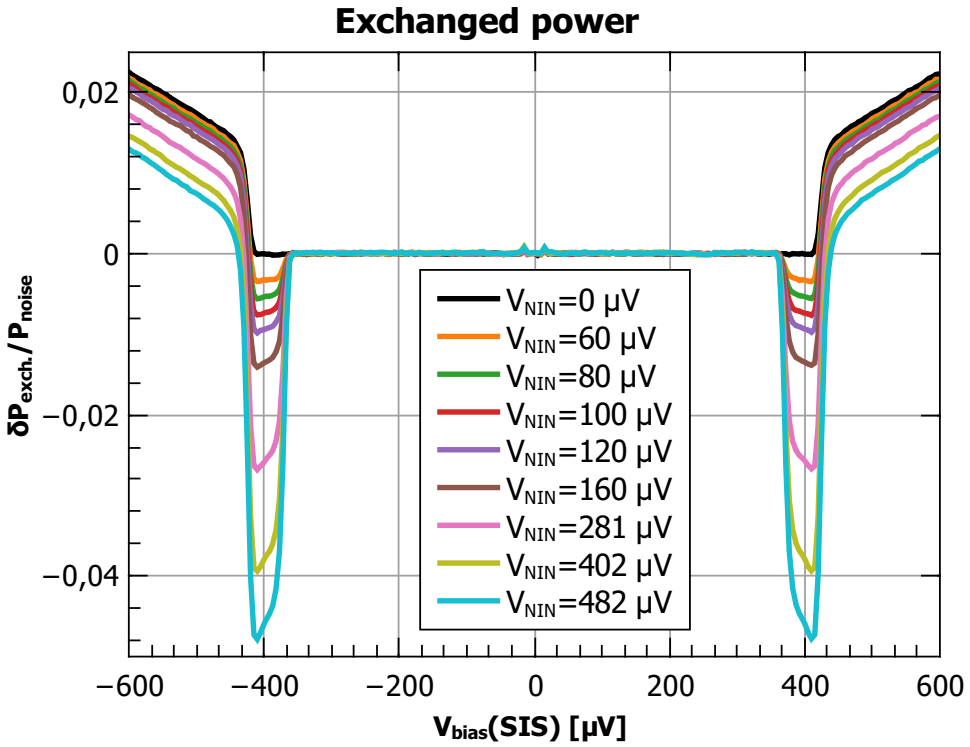

Figure ii.2: Plot of the exchanged power between the SIS junction and its surrounding circuit as a function of the SIS junction's DC bias. Different curves correspond to a different NIN-junction bias, thus to different photon occupation number of the RF-resonator.

The SIS-junction is then DC-bias swept for different biasing conditions of the NIN-junction, corresponding to different photon occupation numbers of the resonator, and the total power emission $P(V_{SIS}, V_{NIN})$ of the system is detected in the RT diode. To retrieve the pure noise signals, several corrections need to be applied. Firstly, we correct the temporal drift of the gain of the measurement line by subtracting a zero bias measurement $P(V_{SIS} = 0, V_{NIN} = 0) = P_{noise}$ for every data point recorded. P_{noise} is the noise background emitted from the 4 K pre amplifier which is also used to normalize our measurements. Secondly, since we are interested in the power exchanged between the SIS junction and the finite energy oscillator only, we have to subtract the power that is used to tune the oscillator's occupation: $\delta P_{exch}(V_{SIS}, V_{NIN}) = P(V_{SIS}, V_{NIN}) - P(0, V_{NIN})$. The then obtained exchanged power δP_{exch} is shown in figure ii.2. For $V_{NIN} = 0$, one observes the characteristic SIS behaviour with zero noise emission below the superconducting energy gap and the

onset thereafter at $2\Delta+hf_0 \approx 428\,\mu$eV where the junction starts to emit an RF-signal. This is the pure emission noise of the system as the resonator is unoccupied and the SIS-junction can thus not absorb any power from the resonator. Hence for all other measurements with finite applied bias on the NIN-junction $V_{NIN} > 0$, the occupation of the resonator modes becomes finite and part of its energy can be absorbed by the SIS junction. As the onset of absorption noise $eV - hf_0$ occurs sooner than that of emission, the exchanged power is negative in the interval $eV + hf_0 > eV > eV - hf_0$ where the SIS junction can only absorb energy form the resonator. Then, for biases higher than $eV + hf_0$, the detected exchanged power is a combination of emission and absorption noise power.

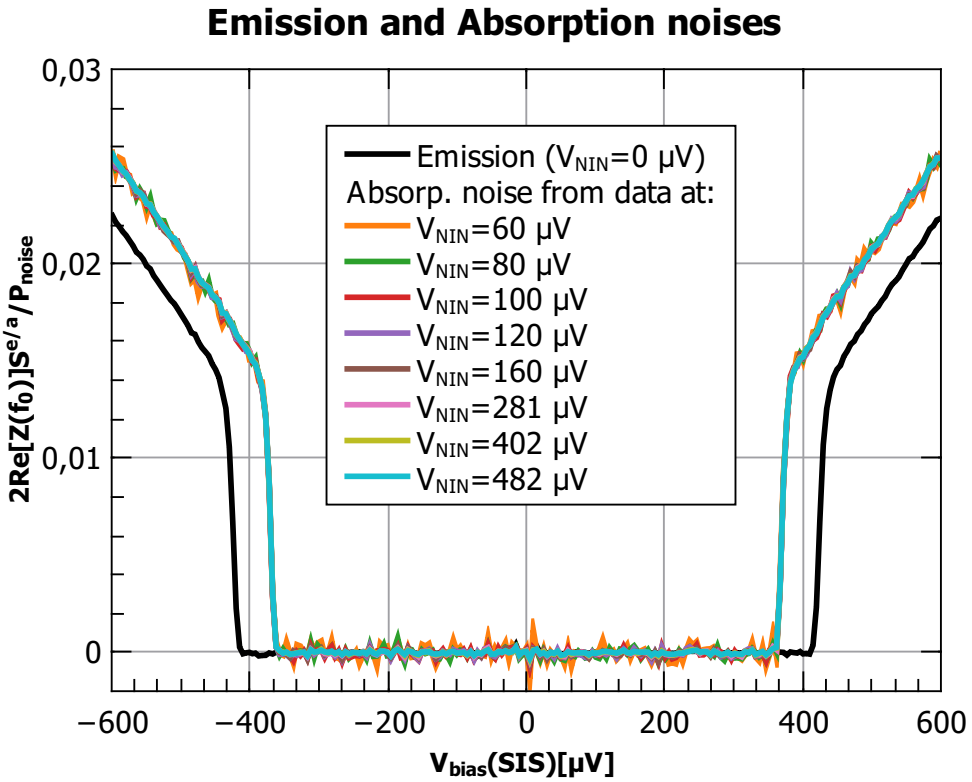

Figure ii.3: Comparison of the measured emission noise of a SIS junction as recorded for zero occupation of the resonator (black) and the calculated absorption noise from measurements with finite occupation of the resonator set by the NIN voltage V_{NIN}.

We can separate these two noise contributions, based on the exchanged power description by Lesovik and Loosen, with equation ii.1 [23] to obtain an expression of the absorption noise for finite resonator occupation measurements. The emission noise S^e can be expressed by the exchanged power measurement P_0 at V_{NIN}=0, for which the occupation number n_B and the absorption noise are zero, to obtain:

$$S^a = \frac{(n_B+1)P_0 - P_{exch.}}{2Re(Z)n_B} = \frac{\Delta P}{2Re(Z)n_B} \tag{ii.2}$$

Knowing the precise occupation number n_B of the resonator, thanks to the calibration,

we have calculated the absorption noise for all measurements with different NIN bias. The results are plotted in figure ii.3 along with the emission noise measurement. We observe that the absorption noise curve is just the emission noise curve with a shift in the DC-bias of $2hf_0$. We have thus shown, that it is possible to separately measure the emission and absorption noise of a quantum conductor from measuring its energy exchanges with a linear resonator set close to its vacuum state. This detection scheme, as we have demonstrated using a SIS-junction as our test conductor, can be applied to any other mesoscopic conductor.

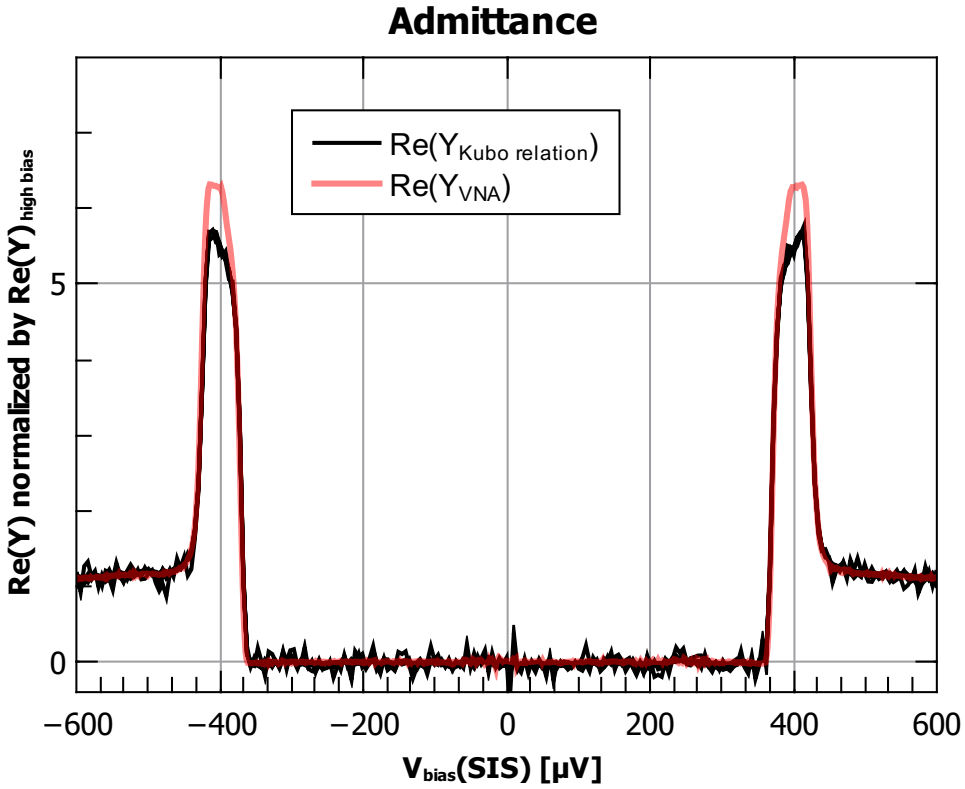

Figure ii.4: Calculated admittance of the SIS junction, using the Kubo formula, based on the measured emission and absorption noises (black), compared to the admittance obtained from a linear response measurement using a vector network analyser (red). We find a good agreement of the detected admittance over the voltage bias a discrepancy of 10% at the vicinity of the gap voltage at 400 μV. This is a rather satisfactory result given the complexity of the RF chain calibration procedure.

Even more, not only does this setup allow us to measure absorption noise of different systems but it also allows us to stress the physical meaning of the Kubo formula [19]:

$$S^a - S^e = 2hf \cdot Re[Y_{emitter}], \tag{ii.3}$$

which, coupled to this quantum description of the measurement setup, provides a quantum version of Joule's theorem: The Kubo formula simply states that the difference of the noise spectral densities is linked by the real part of the admittance.

Coupled to ii.1, one can see that the rate at which energy is taken from the environment and dissipated in the source conductor is proportional to admittance of the source $Re[Y]$ in agreement with the classical intuition of the Joule effect.
We have tested the Kubo formula by calculating the admittance of the system from the measured emission and absorption noise and comparing it to the admittance as obtained from a direct phase sensitive linear-response measurement. For comparison we show in figure ii.4 our results and the admittance as measured with a vector network analyser (VNA). The result of our detector measurement aligns well with the VNA reference and provides the first experimental closure of the Kubo relation for a non-linear quantum conductor[1]. Doing so for a genuinely non-linear conductor driven far from equilibrium stresses the generality of such a relation.

ii.4 Building an experimental platform for performing RF measurements on high impedance conductors at high magnetic fields

In the second part of the thesis we develop and realize an experimental platform for the high frequency noise measurement of mesoscopic conductors at low temperatures and high magnetic fields. The core of our mesoscopic test system, the single electronic channel (and possibly other mesoscopic conductors), will be defined in a 2-dimensional electron gas (2DEG) in a AlGaAs/GaAs heterostructure. This material is ideal for the creation of our mesoscopic test platform because it can be used in several different physical regimes, made possible with the help of magnetic fields and electrostatic gates.
The planar conductor can be physically shaped to create a confinement for the 2DEG which its connected via ohmic contacts. All together a sample geometry as shown in figure ii.5 can be defined by common optical and e-beam lithography fabrication techniques to serve as a base for different experiments. By applying a high enough perpendicular magnetic field, electrons enter the so called Quantum Hall regime, where the current through the sample is carried by chiral edge channels located in the vicinity of the edges of the sample while bulk electrons are localized. Furthermore it is possible to electrostatically manipulate the 2DEG so that we can define different mesocopic conductors or configurations that are needed for different experiments. Therefore metallic gates are defined by e-beam lithography and deposited onto the heterostructure. By negatively polarizing these gates, the electronic density in the 2DEG is locally depleted due to the repulsive Coulomb interaction. By using two split gates that taper down to fine tips with a gap of few hundred nanometers in between, it is possible to define a quantum point contact [57, 58]. Its transmission can be precisely adjusted even for a single electronic channel [59–61] which can be utilized to control the channel's interaction in our experiment (see figure ii.5b).

[1]The proof for a linear ohmic environment was already presented in [54]

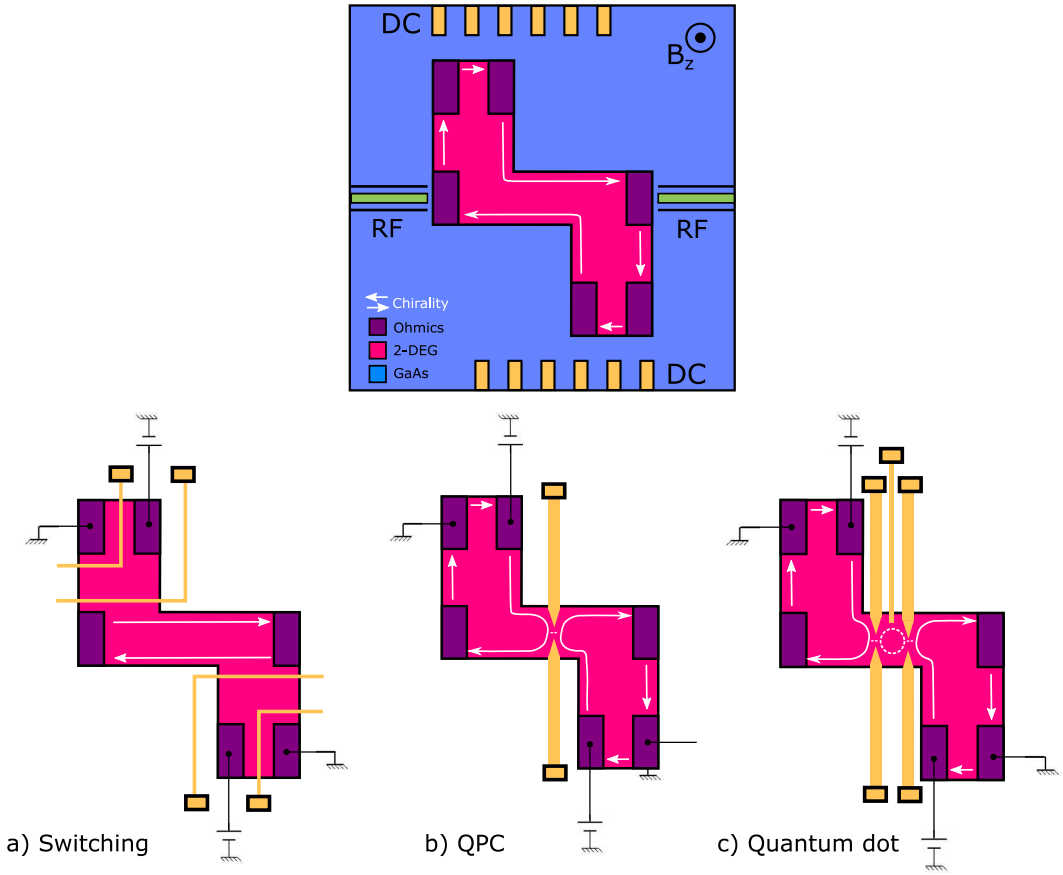

Figure ii.5: (left) Schematic illustration of the basic mesa layout. The chirality of the electronic edge currents for the given magnetic field orientation is indicated in white. The mesa (pink) is contacted via ohmic contacts (purple) of which two are dedicated for the RF- connections (with coplanar wave guides on chip that are required for RF signals) and a total of 4 multi-use contacts to be accessed via DC-lines. The basic mesa can be shaped electro-statically for different experiments by defining different metallic gates that can be biased from the DC ports as shown below: a) gates are used to disconnect the 2DEG around the additional ohmic contacts functioning as an on/off switch. With all contacts off the sample is in a 2-point geometry in which voltage fluctuations of the high impedance detection circuit bias the sample, thus giving rise to detection back-action effects [44]. Adding ohmic contacts to the system, a Hall bar geometry is realized that can be used to characterize the 2DEG properties. With all contacts used, an intercalated ground geometry enables to DC-bias an RF measurement with vanishing DCB effects. b) split gates can be created which taper into fine points with a narrow gap of few hundred nano-meter to create quantum point contacts when polarized; c) creation of a quantum dot in between to QPCs created by split gates. A fifth gate is able to adjust the energy level of the dot.

Likewise we can use the same approach to define other structures like a quantum dot (see figure ii.5 c) or use simple gates as switches (see figure ii.5 a) to connect and disconnect parts of the mesa like additional ohmic contacts that can be used to either ground or DC bias. Therefore, the 2DEG is not only to be connected to the two required RF measurement lines (left and right ohmic contacts) but also by four more ohmics contacts. Twelve available DC connections can then be used to contact or create different experimental arrangements by shaping the mesa with gates.

ii.4.1 RF-measurement

Outgoing from the two RF designated contacts, coplanar wave guides connect the mesoscopic system to the high frequency noise detection setup. With the temperatures reached in the dilution fridge where the experiment will be performed (T_{base} about 15 mK) the requirement $hf \gg k_B T$ is fulfilled for frequencies starting in the few GHz range[2]. Commercially available detection instruments in the GHz range are designed to match to 50 Ω circuits and will have considerable mismatch resulting in an ineffective power transfer when connected to an electronic channel with its intrinsic impedance in the order of $R_K = 25.8\,k\Omega$. The main challenge for the measurement of the noise is thus to establish a sufficient coupling between the sample and the detection setup.
One solution is to simply increase the time over which the signal is integrated. This however leads to a poor signal to noise ratio as was demonstrated for noise measurements in the fractional quantum Hall regime [62] even though using advanced signal analysis techniques. In order to achieve a better resolution, providing us with finer features, and a shorter measurement time, it is necessary to use an impedance transformer that allows to convert the standard 50 Ω detection impedance into a higher detection impedance that can couple well to the high impedance electronic channel. The simplest transformer is the LC-tank circuit (figure ii.6) which is a parallel circuit of a capacitor C and an inductor L. The output impedance or detection impedance $Z(f)$ scales as $ReZ(f) \sim Z_c^2/R$, where $Z_C = \sqrt{L/C}$ is its characteristic impedance that it is proportional to the inductance and inversely proportional to the shunting capacitance.
In order to achieve a detection impedance that is comparable to R_K, a characteristic impedance of 1 kΩ is necessary. Transformers can not only be made from lumped elements e.g. dense planar coils (see [63, 64]) but also from wave guides like the $\lambda/4$ resonators [65–67], also known as quarter wave transformer. While lumped elements need to be specifically designed as the frequency $f = 1/2\pi\sqrt{LC}$ is dependent on inductance and capacitance, the quarter wave transformer's frequency can be set freely by adjusting its length. The later approach was demonstrated by E. Zakka-Bajjani et al. [66] for the measurement of shot noise at a QPC with 200 Ω characteristic impedance. These moderate impedances already allowed for a quantitative measurement of the emission noise. Higher impedances were achieved by [68–72] using a chain of superconducting SQUIDs as quarter wave transformer that generate sev-

[2]For a temperature $T_{mc} = 15$ mK the corresponding frequency threshold is about 300 MHz

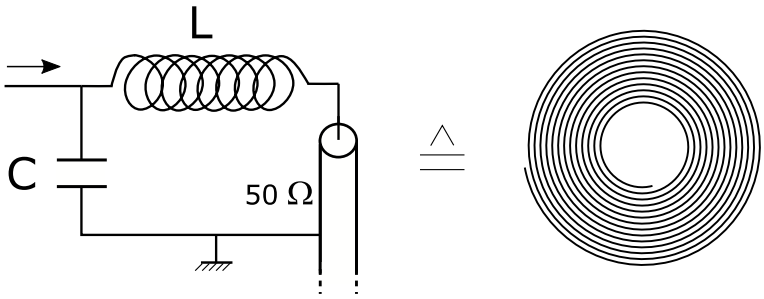

Figure ii.6: Schematic illustration of a lumped element resonator with parallel inductance L and capacitance C. The internal losses are represented as resistor R in series with the inductance. Such a LC-resonator can be realized as a planar coil.

eral kΩ of characteristic impedance. The strong coupling was demonstrated between an EM mode and a tunnel junction [72] as well as a quantum dot [73]. Even higher characteristic impedances were achieved for coplanar wave guide resonators with high kinetic inductance of more than 3 kΩ for Niobium-Tungsten hybrid systems [74] and reaching up to 5 kΩ for disordered superconducting aluminium films [75]. Even though these methods would provide the required characteristic impedance, they are not suitable for our experiments as we wish to work with a single electronic channel which requires strong perpendicular magnetic fields where any common superconductor becomes normal conducting[3]. Instead, we found it to be possible to achieve sufficiently high characteristic impedances with lumped resonators where the inductance originates from the magnetic influence only and does not depend on kinetic inductance. A benefit of this choice is that the platform can then also be used for perpendicular fields far beyond 2 T so that experiments in the fractional Hall regime are possible. The added intrinsic losses of the normal conducting material, in comparison to superconducting resonators, are negligible since radiative losses into the 50 Ω detection circuit are dominant.

ii.4.2 High impedance matching at high magnetic fields

We have thus designed a lumped element resonator, a densely packed micron-scale planar coil that can be fabricated on chip with the sample by means of optical lithography. The resonating coil was designed by simulating its properties with the EM-Solver software Sonnet®, closely following the previous designs by C. Rolland for spiral inductors etched in Niobium on quartz substrates that achieved a characteristic impedance of 1.97 kΩ at 4.4 GHz resonance frequency [77]. We optimized the coil design to be fabricated on GaAs/AlGaAs hetero-structures. The GaAs substrate's higher permittivity leads to a stronger capacitive shunt that decrease Z_c and f, thus imposing more constraints on the allowed capacitance of the design. A second constraint is given for the frequency by our detection circuit components. The key elements, the cryogenic amplifier, circulators, couplers and filters operate between 4-8 GHz, hence the resonance frequency of the resonator has to be within this limit with

[3]Some material choices exist that remain superconducting for in-plane field of $B > 2$ T [76]

a characteristic impedance Z_c of few kΩ. To facilitate the analysis, we wish to keep the bandwidth of the resonator smaller than $k_B T/h$. However, the larger the coupled bandwidth, the faster the experiment. Thus a compromise has to be made between the signal to noise ratio and the energy resolution so that we aim for a Quality factor (Q-factor), the ratio of the frequency to the resonator's bandwidth, of approximately 10. The goal for the resonance frequency was set to 5 GHz which leaves a buffer to the bandstop so that unexpected additional capacitive shunts can be tolerated.

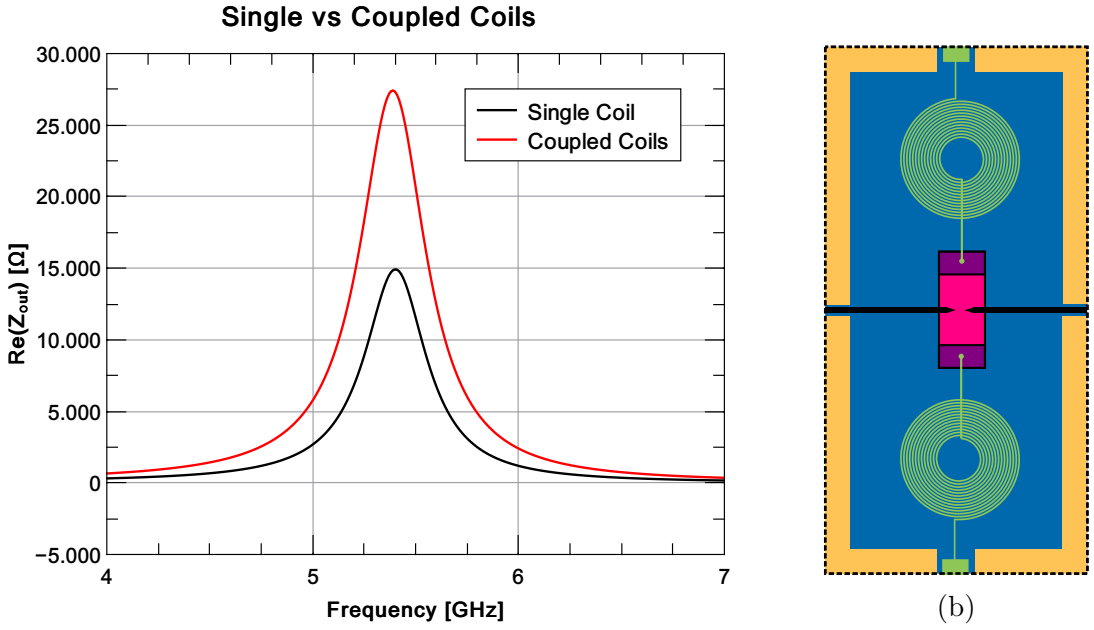

(a) (b)

Figure ii.7: (a) Comparison of the output impedance Z_{out} as plotted for the simulation of 2 planar coils in series connected to the mesa. A schematic illustration of the sample layout for the simulation is shown in (b). By coupling the coils in series in a symmetric arrangement around the QPC, the characteristic impedance is roughly doubled from 1 to 2 kΩ which increases the detection impedance from 18 to 27 kΩ, with a tolerable shift of the resonance frequency due to added capacitive shunts.

The last constraint, regarding minimal dimensions of the conductor, are given by the choice of the fabrication method. To be able to quickly fabricate large area resonators, we optimized the design to be fabricated by optical UV lithography so that the conductors line width and spacing can not fall below a micron. The final coil design is a 19.5 times wound conductor of 2 μm width with 1 μm spacing and achieves a 1k Ω characteristic impedance at 5.4 GHz with Q=15. We will use a series configuration of the QPC in between two coils (see figure ii.7) that gives a detection impedance of 27 kΩ that couples sufficiently well to a single electronic channel.
To realize the envisioned geometry, the coils are fabricated by a three level optical lithography that achieves a one micron resolution using a bilayer of negative resist and lift-off layers. We firstly define the coil geometry and then deposit a high conductance metal. Different choices exist with Cu, Ag and Au who provide small resistances of

about 12 Ω at low temperature after annealing. The coils are connected via a metallic bridge that is created by the same technique on a BCB bridge support spacer. BCB is a dielectric polymer with a small dielectric constant that is shaped by optical lithography and can be completely hardened to form a mechanically stable support structure with low RF-losses.

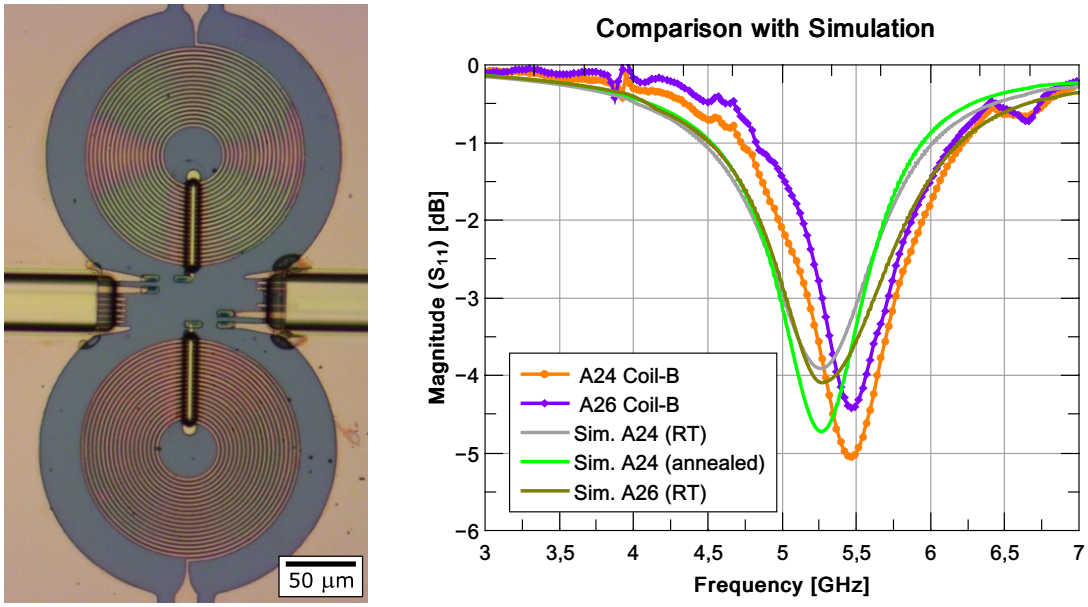

(a) (b)

Figure ii.8: (a)Fabrication of test sample A24: Completed fabrication of the resonating coils (15 nm Ti/500 nm Cu/15 nm Au) with bridges across coils and DC-lines. The metallic (15 nm Ti/300 nm Cu/15 nm Au) bridges are deposited on 3 μm thick dielectric BCB supports. (b) Comparison of the simulated reflection curves for coils with and without bridges with arbitrary resistivity (grey & brown) to our VNA measurement results for coils with bridge (A24, orange) and coils without bridge (A26, purple). The measurements were done at room-temperature while simulations use predicted resistivities based on RRR measurements. Comparing the two measurements we observe no frequency shift due to capacitive shunts caused by the 3 μm thick bridge. However compared to the simulation, we do see a shift of the resonance frequency by 200 MHz. The change of the magnitude of the measurements is attributed to the thermal annealing that reduces the internal losses of the coil for A24. As shown, the direct remodelling with the predicted resistivities does not match in magnitude but after considering the effective annealing of A24 (annealed - green) it shows the correct evolution.

We have successfully fabricated and tested the characteristic parameters of the resonators fabricated on GaAs substrates at room temperature, with (see figureii.8a) and without the bridge (not shown). We measured the signal reflectance of the coil with a vector network analyser and compared the results to simulations (figure ii.8b). The obtained results are in agreement with the simulation and confirm the successful

fabrication of 1 kΩ impedance resonators at 5.5 GHz and 400 MHz bandwidth with negligible capacitive shunt from the bridge.
With the planar coil as impedance transformer it is possible to measure the sample with a GHz amplification chain and different detectors e.g. vectorial network analyser (VNA), power diodes and spectrum analyzers that can be placed at room temperature. Unfortunately, the fabrication of a full sample on a 2DEG could not be finished within the time-frame of the PhD thesis due to fabrication issues. However, we have successfully built up the methodology which will make it possible to perform amazing a series of various experiments in the near future.

Chapter 1

Introduction: Noise in mesoscopic conductors

In this introductory chapter, we are about to present the fundamental concepts of electronic transport and physics of noise in mesoscopic circuits. Mesoscopic circuits are based on micron- and sub-micron scale electrical conductors that when probed at low temperatures do not obey the classical laws of electricity anymore [1, 2] but have to be described quantum mechanically. This crossover from the classical macroscopic physics towards the quantum mechanics arising in for microscopic systems gave rise to the field of mesoscopic physics that studies a large range of systems, including insulators, semiconductors, metals, and superconductors, which are typically defined in scales ranging from few nanometers to several μm. As the studied macroscopic circuits are made so that the current is forced through a bottleneck of the size of the electronic wavelength, electrons have to be considered as quantum mechanical waves. As a result, if the system is smaller than the phase coherence length, the electronic waves maintain a well-defined phase which leads to the appearance of quantum interference phenomena which modify the properties of system.
The granularity of charge, combined with the probabilistic character of quantum dynamics, naturally gives rise to current fluctuations. Such fluctuations are highly informative as they convey information on microscopic aspects of the conductor: the charge of the carriers, their statistics, dwell time in scattering region and interactions [39, 40, 78–80]. Such current fluctuations couple to the electromagnetic modes of the detection circuit, and for frequencies larger than the thermal agitation $hf \gg k_BT$, one enters the quantum optical regime in which one needs not only a quantum description of the electrons flowing through the quantum conductor, but also for the electromagnetic signals propagating in the detection scheme [14, 21].

In this thesis we are concerned with the measurement of the temporal correlation of electrons in mesoscopic conductors that are observable at high frequencies and low temperatures in the quantum regime ($hf > k_BT$). Therefore, in this chapter, we give a brief introduction to electronic transport in mesoscopic conductors and electronic noise. We will shortly introduce noise in the classical regime and highlight the differences to quantum noise. The main difference being a frequency asymmetry

in the power spectral densities [14, 15, 19], incompatible with classical interpretations but baring deep meaning in terms of power exchanged between a weakly coupled measurement apparatus and the system.

Contents

1.1 Quantum transport in mesoscopic conductors

In mesoscopic systems that have constrictions of the order of the electronic wavelength, the electron needs to be considered as a wave whose propagation is described by a wave function $\Psi(x,t) = Ae^{-i(kx-\omega t)}$, with wave vector k and phase $kx - \omega t$. As long as phase coherence is preserved, the electronic waves may interfere with themselves which results in different quantum effects. However this coherence is lost, for example due to scattering events of the electrons, so that the coherence length L_Φ is defined as the distance in a system that electrons can travel before their phase is randomized.

For large conductors with $L > L_\Phi$ physics are mostly classical or semi-classical physics as described by the Drude-Sommerfeld model [81]. For devices with smaller dimensions $L < L_\Phi$, we are in the electronic quantum transport regime in which quantum interference phenomena are observable. Here two transport regimes are to be differentiated: Firstly, if the conductor's dimension is smaller than the mean free electronic path $L < L_{mean}$, electronic trajectories maintain a well-defined velocity as the system is scatter-free. This is the ballistic transport regime for which the coherence length is described as $L_\Phi = v_F\tau_\Phi$, with v_F being the electronic velocity. Ballistic transport is typically observed in physical systems such as clean semiconductors, two dimensional electron gases, graphene etc. Secondly, for larger conductor dimensions $L > L_{mean}$, the electron transport is dominated by their scattering with impurities causing a diffusive electronic motion. In this diffusive transport regime the coherence length is thus given as $L_\Phi = \sqrt{D\tau_\Phi}$ where D is the diffusion constant. Typically systems would be sputtered metals in different shapes like e.g. wires.

Thus in both cases, the coherence length can be linked to a dephasing time, $\tau_\Phi = L_\Phi/v_F$ or $\tau_\Phi = L_\Phi^2/D$, that captures the dephasing due to interactions with the physical environment of the electronic system. So regardless of the transport regime, the electronic current is coherent as long as $\tau < \tau_\Phi$. To estimate τ_Φ the three main sources

of inelastic scattering, that cause dephasing, need to be considered: electron scattering, phonon scattering and scattering with impurities/defects. In a given system at finite temperature T, we have thus a superposition of these scattering mechanisms that amounts to a total inelastic scattering time following the Matthiessen's rule:

$$\tau_{inel.}^{-1} = \tau_{e-e}^{-1} + \tau_{e-ph}^{-1} + \tau_{imp.}^{-1} \tag{1.1}$$

In general multiple scattering can be present in a system for which one or two are dominant depending on the dimensionality of the system, the level of disorder and the measurement temperature [82]. For example: in impurity free systems scattering can occur between electrons or by exciting phonons in the lattice. While the phonon process is dominant at high temperatures or 3D systems in general, electron scattering is dominant at low temperatures below 1 K, as phonons are effectively frozen, and for low dimensional systems. In our case, working with two dimensional electron gases (2DEG) in GaAs/AlGaAs heterostructures at low temperature ($T < 1\,\mathrm{K}$), electron-electron scattering is the dominant mechanism with scattering rates found to be of the order 2.5-2500 GHz which is equal to coherence lengths of several hundred nanometer in the diffusive regime [83] and up to few hundreds of μm in the ballistic regime [84]. The third scattering mechanism is relevant for disordered conductors as now electrons scatter predominantly with static impurities in the conductor rather than dynamically with other electrons. These impurities in the conductor may have magnetic or electrostatic properties as found for many crystals grown using advanced growing techniques, such as e.g. molecular beam epitaxy (MBE) and metalorganic chemical vapour deposition (MOCVD), or simple grain boundaries in heterogeneous systems cause electrons to be scattered due to a spin-flip interaction as well as spin-orbit coupling. The dephasing rate is thus nearly temperature independent and depends only on the impurity concentration. In the case of GaAs/AlGaAs 2DEGs, the impurity scattering may be dominant, if the impurity concentrations is high enough, which results in a linear relation of the concentration and scattering rate at low temperatures. This scattering is dominated by the ionized donors that are implanted into the AlGaAs layer in order to increase the amount of charge carriers, while other contributions are negligible. Based on the impurity scattering limited mobility measurements of Tsui et al. [85] the scattering rates can be approximated as 20 GHz, however advanced high mobility 2DEGs strongly reduce the influence of impurity scattering by spatially separating donors from the 2DEG. With a spacing layer in place, the scattering rates are typically decreased into the MHz range which makes them negligible in comparison to the electron-electron scattering, except at temperatures in the milli-Kelvin range. Quantum conductors are electrical conductors with a bottleneck smaller than L_ϕ. In order to reach such regime we work with dilution refrigerators, reaching temperatures as low as few mK (typical commercial fridges reach about 7-15 mK), and fabricate circuits in the clean-room in order to create sub micron-scale patterns. In the following sections we introduce the two quantum conductors that we will be using in the thesis: The tunnel junction and the quantum point contact (QPC).

1.1.1 The tunnel junction

In the experiments that are performed and outlined in this thesis, we will be working with different mesoscopic conductors. The simplest and oldest physical system upon which experiments of quantum transport have been conducted, starting with Giaever in the early 1960s [86], are tunnel junctions. Due to their simple design, tunnel junctions are an easy to fabricate structure and have found many applications in different mesoscopic electric systems. It is constructed from two metallic and/or superconducting leads that are separated by a thin insulating barrier.
Following a classical intuition, two separated leads of a metal to metal (NIN) junction for example should not be electrically conducting for low bias voltages V, smaller than the dielectric breakdown field of the insulator, or the work function of the conducting material. However, a finite conductivity across the barrier with an ohmic behaviour is measurable when the insulating film is thin enough. In quantum mechanics, it is possible for electrons at energies E smaller than the potential energy U, characterizing the insulating gap, to be transmitted as a quantum wave with a finite tunneling amplitude $\tau(E) \sim \exp\left(-[(2m^*/\hbar^2)(U-E)]^{1/2} \cdot d\right)$, where d is the width of the potential barrier and m^* is the effective electronic mass, that leads to a finite transmission probability $T_P = |\tau(E)|^2$. So even though the metallic conductors are physically separated by an insulator, the electronic waves are able to tunnel through with a transmission probability T_P that is typically $T_P \ll 1$. This applies even at zero bias when the electrons can tunnel through the barrier but at the same rate in both directions, so that the conductance is finite even though the net current is zero. A finite net current is achieved when a bias is applied to the Fermi levels so that the transmission rate across the junction is increased in one direction. In the case of small biases that are way smaller than the potential barrier U and E_F this current is linear to the applied bias and proportional to the tunneling resistance of the junction that increases exponentially with the insulating layer thickness.
Tunnel junctions, as short coherent conductors, have been a useful tool in understanding and exploiting many quantum effects: Very soon the technology developed by Giaver on metallic and superconducting junctions [87] enabled the observation of supercurrents in SIS junctions [88] as predicted by Josephson [89], and concomitantly Esaki developed semi-conducting tunneling junctions [90]. Superconducting junctions where intensively used as current or flux amplifiers (SQUIDs) onwards from the 70s [91, 92] and also as quantum limited mixers for microwaves widely used in radio-astronomy starting in the 80s [93]. By now tunnel junctions have appeared to be one of the most widely adopted physical platforms for quantum computing [94] , whereas semiconducting tunneling structures have also found many applications ranging from Esaki diodes [95] to quantum cascade lasers [96].

1.1.2 The quantum point contact

Despite the tremendous amount of applications and explorable physical effects, tunnel junctions only encompass a small subset of the physics one can obtain in a quantum circuit. The tunnel junction is limited by definition to the low transparency regime

($T_P \ll 1$) as it can only weakly couple the electrons on both sides of the barrier. Such weak coupling is unable to capture more complex correlated motion that can only be obtained with larger transmission probabilities.
Those finite transmission values can be achieved and controlled within a more advanced mesoscopic structure, the quantum point contact (QPC). The QPC, in the design that was created by Thornton et al. [57] and Zheng et al. [58] in 1986, is a nanometer-scale constriction in a 2-dimensional electron gas (2DEG) [1] that is created at the interface of a selectively doped GaAs–AlGaAs hetero-structure. This planar conductor can then be shaped electro-statically via metallic gate electrodes that are fabricated on top of the hetero-structure. Charging these gates then causes a local depletion of the 2DEG due to Coulomb repulsion interactions. A constriction is created by two split gates that are commonly 250 nm apart and taper down to nanoscopic tips. Depending on the applied voltage the depletion field is enlarged so that it is possible to tune constriction width W between 0-250 nm. If a constriction's size is of the same order as the Fermi wavelength $W < \lambda_F$, where $\lambda_F = 40\,\text{nm}$ for GaAs/AlGaAs hetero-structures with a sheet density of $4 \cdot 10^{11}\text{cm}^{-2}$ [97], this will give rise size quantization effects due to the quantum wave nature of the electrons, as observed in the first conductance measurements of a quantum point contact as done by Van Wees et al. [59] and Wharam et al. [60] in 1988. The measured conductance through the QPC for different constriction sizes, driven by the gate voltage, exhibits a step like function of the conductance (see figure 1.1a). The plateaus appear at multiples of the quantum of conductance $2 \cdot G_0 = 2e^2/h$. These features can be understood as a quantization of the transverse motion into modes that each carry a quantum of conductance G_0. As the width of the constriction is enlarged, more and more transverse modes at the Fermi energy can be filled. For a voltage V applied across the QPC, then every open mode carries the current $I_{open} = G_0 \cdot V$. If a channel is however not fully open or closed, it carries a reduced current proportional to its finite transmission coefficient T_P, which we assume to be energy independent, so that $I_{pinched} = G_0 \cdot V \cdot T_P$. The conductance of the QPC is then simply the sum over the modes with a factor of 2 for corresponding to the spin degeneracy:

$$G = \frac{2e^2}{h} \sum_N T_{P,N} \tag{1.2}$$

The simplest model explaining such features is regarding electrical transport as a scattering process for non-interacting quantum waves. Initiated by Landauer in the 50s [98], this point of view was enriched and extended in the 80s to account not just for the average current, but also the statistical properties of the current fluctuations by Büttiker [24, 99–101] and many others [102–106]. The main idea is to look at quantum transport as a scattering mechanism of the electronic waves that are linked by a forward transmission given by the transmission coefficient T_P and likewise a backward reflection with the reflection coefficient $R = 1 - T_P$.
We will illustrate this model starting by assuming two macroscopic leads (see figure 1.2). The left and right reservoirs have electrochemical potentials $\mu_{L/R} - eV_{L/R}$, with

[1] for more details refer to section 5.1.1

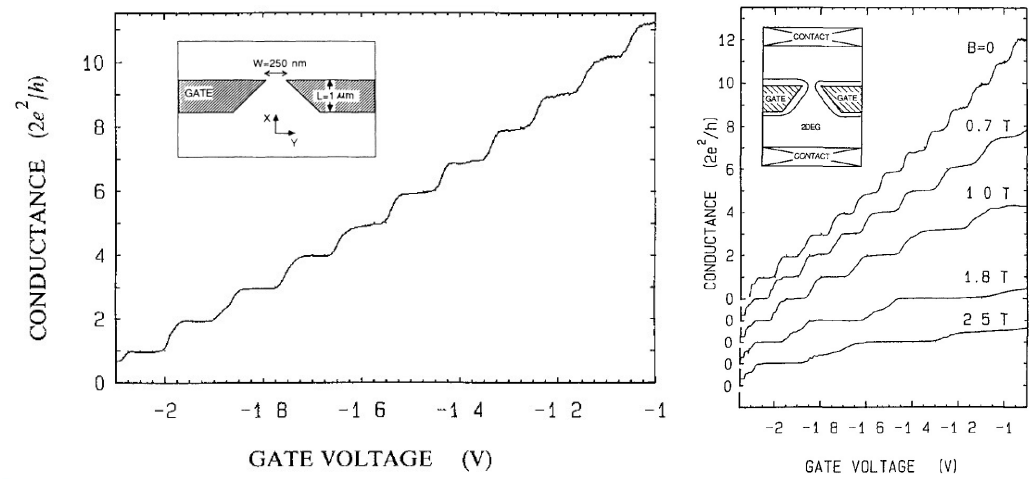

(a) (b)

Figure 1.1: (a) Measured quantum point-contact conductance as a function of the applied gate voltage at 0.6 K and after subtracting the lead resistance (400 Ω, taken from [59]. The plateaus occur at multiples of $2e^2/h$. The inset shows the layout of the QPC split-gates; (b) Measured quantum point-contact conductance for different applied magnetic fields [61]. For increasing fields the plateaus are extended and the number of plateaus per voltage interval decreases, until for high magnetic fields spin degeneracy is lifted, so that additional plateaus at odd multiples of e^2/h appear.

corresponding voltages V_L, V_R and chemical potentials μ_L, μ_R and are assumed to be incoherent (in their own thermal equilibrium). In between we assume an impurity-free one-dimensional conductor, which is effectively a single electronic channel, that is connected to the reservoirs. If we now assume a more realistic mesoscopic conductor, resistance in form of impurities or other scattering sources have to be added as a potential barrier into the mesoscopic channel, represented as the scattering region QC in figure 1.2. As for the tunnel junction barrier, the electron waves can quantum mechanically tunnel through this barrier at any energy with a finite transmission probability $T_P(E) = |\tau(E)|^2$, with $\tau(E)$ being the transmission amplitude.
For an applied bias $eV_{bias} = \mu_L - \mu_R$ we are shifting the chemical potential on one side so that a net current $I = I^L_{in} - I^L_{out}$ flows. Therefore we firstly define the in- and output currents based on the electron's Fermi-distributions, describing the occupation of the electrons fed by the reservoirs: $f_{L/R}(E) = (1 + \exp((E - \mu_{L/R})/k_B T))^{-1}$. The obtained equations 1.3 and 1.4 are universal expressions, independent of microscopic details, because the 1D density of states of free electrons cancels the electron velocity out $\rho_{1D}(E) \cdot v(E) = 1/h$ in the absence of interaction:

$$I^L_{out} = \frac{2e}{h} \int_0^\infty dE[(1 - T_P(E)) f_L(E) + T_P(E) f_R(E)] \tag{1.3}$$

$$I^L_{in} = -\frac{2e}{h} \int_0^\infty dE f_L(E) \tag{1.4}$$

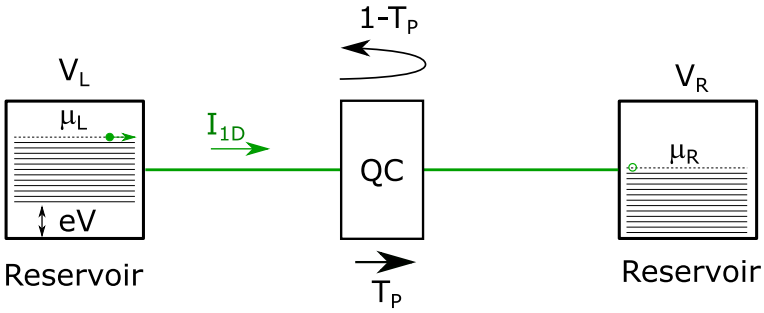

Figure 1.2: Schematic representation of the current transport through a 1D single channel quantum conductor (QC) in between two macroscopic electron reservoirs. The electrons have a finite transmission probability T_P across the QC potential barrier or are reflected with the reflection probability (1-T_P).

Both input and output current are obtained by integrating their Fermi functions. While the input current includes only the Fermi function of the left reservoir, the output current is a superposition of the transmitted and reflected currents originating from both leads, thus including the Fermi functions of the left and right reservoirs. With equation 1.3 and 1.4 the net current is calculated as:

$$I = \frac{2e}{h} \int dE T_P [f_L(E) - f_R(E)], \tag{1.5}$$

and, if the energy dependence of the transmission T_P can be neglected in the transport window, it then simplifies to:

$$I = \ G_0 \cdot T_P \cdot V, \tag{1.6}$$

where $G_0 = e^2/h$ is the quantum of conductance, whose inverse is also known as the quantum of resistance $R_K \simeq 25.8\,\mathrm{k}\Omega$. One can see in figure 1.1 that for perfect transmission $T_P = 1$ (no impurity scattering), there is a finite two point conductance given by G_0. This is in stark contrast with the Drude model for which impurity free systems give zero resistivity. The physical meaning of this is that, even though there is no impurity scattering, the Pauli exclusion limits the amount of charge carriers which can be conveyed in a 1D channel in a finite energy window, thus giving a finite conductance. It can also be shown that the dissipation related to this resistance of the electronic channel is found at the macroscopic leads. Since there is no backscattering, the chemical potential of the 1D wire is conserved along it, thus the channel's resistance as well as applied voltage drop have thus to be at the terminations of the channel, in the macroscopic leads. The quantum of resistance is thus found as the contact resistance from the macroscopic lead to the channel with the dissipation occurring mainly in the reservoirs. Thus the resistance of a coherent conductor is non-local, which is the reason why macroscopic rules for electronic circuits can not be applied to mesoscopic conductors.
Equation 1.6 presents the general case of energy independent scattering, the conductance is simply obtained by multiplying the conductance quantum with the transmission probability, so that the total conductance G across the channel is reduced

for $0 < T_P < 1$. By summing incoherently over the transmission probabilities for every channel, one obtains a formalism that allows to calculate G for multi-channel scattering [99, 107]:

$$G = \frac{2e^2}{h} \sum_N T_{P,N} = 2G_0 \sum_N T_{P,N}, \tag{1.7}$$

where the factor 2 accounts for the spin degeneracy.

1.2 Quantum noise in mesoscopic systems

For any measurement of electronic systems and their properties, be it current, voltage, etc., one observes fluctuations of the measured property. These fluctuations also known as noise can have multiple origins that include the electronic circuit, impurities in the conductor but also quantum effects. For example, because electrons carry a quantized value of electrical charge and are scattered individually, their transfer process is random. Thus, the measurable electronic current across the mesoscopic conductor exhibits fluctuations that provide statistical information about the charge transport mechanisms of the conductor. Hence the measurement of noise within the quantum transport regime allows to probe fundamental aspects of the charge transport and physical responses of these systems that are not accessible otherwise. We will introduce the fundamentals needed to understand noise in the classical and quantum regime as well as the fluctuation dissipation relation and theorem that links the fluctuation within a system to its physical response to an external driving force.

1.2.1 Electrical noise in classical physics

In the simple case of a random current signal through a resistor with impedance R, we observe a fluctuation of the current signal $\Delta I(t)$ that has a zero mean value $\overline{I(t)} = 0$ and can be described by its auto-correlation function C_{II} (ACF). The classical case is described as:

$$C_{II}(t, t') = E(I(t)I(t')), \tag{1.8}$$

where $E()$ designates the statistical ensemble average. At equal sampling times, $t = t'$ the ACF gives the variance of $I(t)$, and in the case of stationary noise, when the fluctuation is time-translation invariant, so that the ACF has to obey $C_{II}(t, t') = C_{II}(t - t', 0)$.
A very important related quantity is the Fourier transform of the auto-correlation function, the power spectral noise density (PSD):

$$S_I(f) = \int_{-\infty}^{\infty} dt \cdot e^{i2\pi ft} C_{II}(t, t') \tag{1.9}$$

This expression can be linked to the ensemble average of $E(I(f)I(-f))$, thus to the energy content of the classical signal, by the Wiener-Khintchine theorem [16–18].

Another consequence of the signal $I(t)$ being classical is that $I(t)I(0) = I(0)I(t)$, so that the ACF is real as well, resulting in the classical PSD being frequency symmetric $S(f) = S(-f)$.

1.2.2 Low frequency noise in mesocopic conductors

Since fluctuations arise for different reasons, here we elaborate on the most relevant contributions for mesoscopic conductors in the low frequency limit, $hf \ll k_B T$ (thus $f \ll 300\,\mathrm{MHz}$ in a 15 mK dilution fridge): Thermal noise and shot noise. Since the early 20th century we know of the existence of thermal fluctuations of electrons, characterized by Johnson [108] and modelled by Nyquist in 1928 [109], in a conductor which we refer to as thermal electrical noise (or Johnson-Nyquist noise). A conductor of conductance G at thermal equilibrium will give rise to a variance of its current I that increases with the temperature T due to the thermal agitation of electrons:

$$\overline{i^2} = 2k_B T \Delta f G, \tag{1.10}$$

where k_B is the Boltzmann constant and Δf is the bandwidth over which the current fluctuations are averaged. The corresponding power spectral density [2] is frequency independent and is thus referred as "white noise":

$$S_I(f) = 2k_B T G \tag{1.11}$$

When driven out-of-equilibrium, conductors might display other sorts of fluctuations. The most relevant to us is the shot-noise that arises from the granularity of the charge carriers. This was firstly discovered by W. Schottky in 1918 [110] who measured electron transport in vacuum tubes. Unlike thermal noise, shot-noise is driven from the current itself. Due to the discreteness of the electronic charge, electrons tunnel individually as a "shot" whenever they are extracted from the hosting electrode and injected in the vacuum tube, causing a statistical fluctuation of the current. Because electrons tunnel individually, as a "shot", they are uncorrelated and the process can be modelled with a Poisson distribution, hence shot-noise is also known as Poisson noise. Thus the variation of the current depends on the current I itself and also the bandwidth of the measurement Δf.

$$\overline{i^2} = Ie\Delta f \tag{1.12}$$

Based on equation 1.12 we obtain the Schottky Formula for the spectral noise density, which is a white noise spectrum proportional to the applied current and the charge transported by the microscopic carriers

$$S_I(f) = eI, \tag{1.13}$$

[2] This general equation should not be confused with the different but commonly used definition of the power spectral densities of the Johnson-Nyquist noise as $S'_I(f) = 4k_B TG$, which is typically used when describing low frequency noises. Since $S(-f) = S(f)$ in this case, the signal's variance can be written as $\delta I^2_{rms} = \int_0^\infty S(f) + S(-f) = \int_0^\infty 2S(f)$, with the 2 factor being incorporated in $S' = 2S(f)$ such that $\delta I^2_{rms} = \int_0^\infty S'(f)$

In the case of quantum conductors, the granularity of the charge carriers combined with the probabilistic character of quantum scattering naturally gives rise to quantum shot-noise. For non-interacting conductors, shot-noise is completely characterized by the set of transmission probabilities of the electronic channels defining the conductor. The main difference as compared to classical Schottky noise, is the appearance of additional correlations induced by the Pauli principle which tends to regularize the electronic flow. In the low frequency and low temperature limit, $hf, k_BT \ll eV$ [102], the spectral density of current fluctuations reads:

$$S_I(f=0) = \frac{2e^2}{h} eV \sum_N T_{P,N}(1 - T_{P,N}), \tag{1.14}$$

where $T_{P,N}$ is the transmission probability of channel N, and $2e^2/h$ is the spin degenerate conductance quantum ($G = 2G_Q$). In the tunnel limit , $T_P \ll 1$, one could expect that electron transfers are scarce and uncorrelated so that the Schottky formula applies. However, at finite transmission T_P the noise is reduced as compared to the Poissonian value. The measure for deviations from the Poissonian description is expressed as the Fano factor F, the ration of sub-Poissonian to Poissonian noise:

$$F = \frac{S_I(f)}{eI} = \frac{\sum T_P(1 - T_P)}{\sum T_P} \tag{1.15}$$

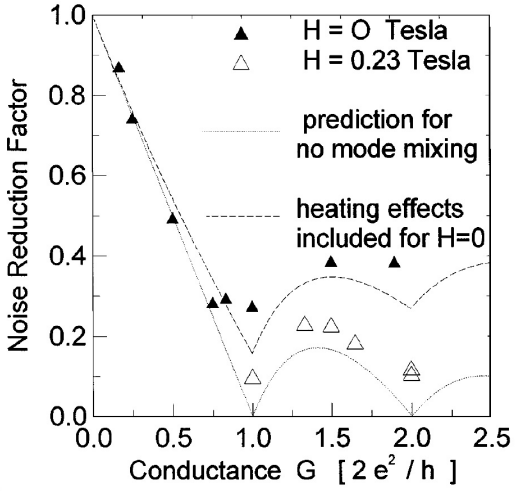

Figure 1.3: Measurement of the Fano factor as defined by equation 1.15 (triangles) for a QPC at different magnetic field, plotted over the conductance. The measurement is compared to predictions without and with heating effects. The system tends to be noiseless when all channels are ballistic ($T_P = 1$). Figure taken from [78].

The Fano factor takes values between 0 and 1, where it is noiseless for values of $F = 0$. By inspecting equation 1.14, one sees zero temperature quantum shot noise is strictly zero when a conduction channel has transmission values of 1 as a non-partitioned channel does not give rise to shot-noise, while the noise is maximal for $T_P = 1/2$.

The suppression of shot-noise was shown experimentally for a QPC by Kumar et al. [78] and Reznikov et al. [79], where the shot noise was recorded as a a function of the current bias for different transmission coefficients of a QPC. The resulting Fano factor from [78] is shown in figure 1.3, it shows that the noise is suppressed for integer numbers of open/closed conduction channels and that the measured Fano factor approaches the non-interacting theory: $\sum_N T_{P,N}(1-T_{P,N})/\sum T_{P,N}$ when heating effects are mitigated by applying a perpendicular magnetic field.
Of course, quantum conductors are also subject to thermal fluctuations as well. The non-interacting scattering approach states that in the low frequency limit, $hf \ll k_BT, eV$, there is a smooth crossover from thermal fluctuations to quantum shot noise as eV becomes larger than k_BT [24]:

$$S_I(f=0,V,T) = \frac{2e^2}{h}[2k_BT\sum_N T_{P,N}^2 + eV\coth\left(\frac{eV}{2k_BT}\right)\sum_N T_{P,N}(1-T_{P,N})] \quad (1.16)$$

The power spectral density is shown as a simplified plot in figure 1.4 with $T_S = S_I(f=0,V,T)/(4G_0k_BT\cdot\sum_N T_{P,N})$. At low biases $eV \ll k_BT$, we expect the constant equilibrium thermal noise (equation 1.11) which transitions to the complex superposition of thermal noise and shot noise at $eV = k_BT$ while the shot noise limit of equation 1.14 is approached asymptotically for $eV \gg k_BT$.

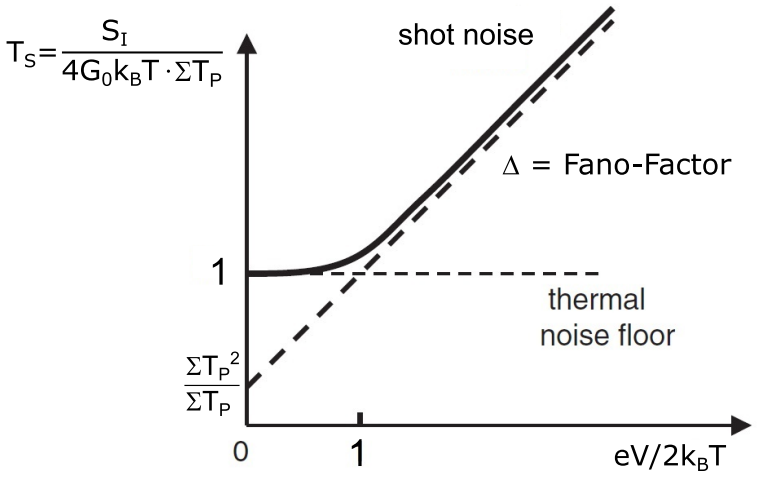

Figure 1.4: Simplified plot of the transition from thermal to shot noise by increasing the applied bias across the system for arbitrary transmission T_P. In the chosen units the slope of the shot noise is the Fano-Factor $\sum_N T_{P,N}(1-T_{P,N})/\sum T_{P,N}$ and the extrapolation intersects the y-axis at $\sum_N T_{P,N}^2/\sum_N T_{P,N}$. Modified figure taken from [111].

1.2.3 Quantum noise at finite frequency

The zero temperature features described in the precedent section can be captured within a semi-classical model where electronic wave packets, each carrying the same

charge e, are regularly emitted by the reservoirs in time intervals of h/eV and are independently scattered by the mesoscopic conductor [103]. Thus even though the dynamics are dictated by quantum tunneling and one can observe quantum statistical features leading to subpoissonian noise, the phenomenology is similar to that of classical noise. However, such approach ignores the finite quantum coherence existing between successive wave-packets (due to a spatial overlap of their corresponding wave-functions). In order to capture this coherence, one needs to probe shorter time scales such that $hf \gg k_B T$. In this regime, one deals with genuine quantum fluctuations without any classical counterpart: Notably, in the limit of zero temperature and bias, zero point motion gives rise to finite quantum fluctuations, contrary to classical systems which become completely frozen (noise free) at zero temperature. A consequence of this finite quantum noise floor, is that the spectral density of current fluctuations is frequency asymmetric $S(f) \neq S(-f)$, making it difficult to understand using classical signal analysis tools.

1.2.3.1 Vacuum fluctuations

Zero-point fluctuations or vacuum fluctuations are a consequence of the Heisenberg uncertainty relations, which imply that the ground state of a physical system is not completely inert, and contains indeed a finite amount of energy. We can observe these quantum fluctuations for $hf > k_B T$ which we refer to as the quantum regime. To illustrate their origin: we will follow Nyquist [109] and consider an electrical conductor of conductance G in thermal equilibrium with a transmission line of matching impedance. The electromagnetic modes of the line are thus perfectly absorbed by the matching conductor, and conversely the fluctuations of the conductor are perfectly transmitted to the line. Since it is easy to predict the transmission line dynamics, being those of an infinite sum of itinerant harmonic oscillators, one deduces the fluctuations of the matched conductor by current conservation. The key point of this approach is that kinematic constraints (Kirchhoff's laws) on the circuit make the current fluctuations computed in the line to be the same as those flowing through the matched conductor. The quantum mechanical calculation [15] gives that the power spectral density at positive and negative frequencies is no longer symmetric as we can see following equation 1.9 and 1.8 because the current operators $I(t)$ and $I(0)$ do not commute anymore. Hence the zero temperature equilibrium fluctuations for positive and negative frequencies are given as:

$$S_I(f, T = 0, V = 0) = \begin{cases} hfG, & \text{for } f > 0 \\ 0, & \text{for } f < 0, \end{cases} \tag{1.17}$$

with G equal to $2G_0 \sum_N T_{P,N}$. At finite temperature this stark frequency asymmetry is smoothed by thermal agitation. The combination of equilibrium Johnson-Nyquist noise and zero-point-fluctuations is referred to as Callen-Welton noise [15]:

$$S_I(f, T, V = 0) = \begin{cases} hf(1 + n_B(hf))G, & \text{for } f > 0 \\ hf n_B(h|f|)G, & \text{for } f < 0, \end{cases} \tag{1.18}$$

where $n_B(hf) = 1/(e^{\beta hf} - 1)$ is the Bose occupation factor at temperature T: $\beta = 1/k_B T$. This expression does not make any hypothesis on the microscopic properties of the resistive element other than being at thermal equilibrium, it respects the detailed balanced symmetry $S_I(f) = e^{\beta hf} S_I(-f)$, and reproduces Johnson-Nyquist noise (see equation 1.16) in the low frequency (high temperature) limit $\beta hf \ll 1$: $S_I(f) = S_I(-f) = 2k_B TG$ and otherwise vacuum noise (see equation 1.17).

1.2.3.2 Finite frequency shot noise

However, when the quantum conductor is driven out of equilibrium, one cannot rely on such general considerations anymore and needs a derivation from a microscopic model. While other techniques give the same result, see for example [112], the scattering approach enables the computation of the finite frequency noise of non-interacting electrons that are being scattered upon the quantum conductor [102, 113].

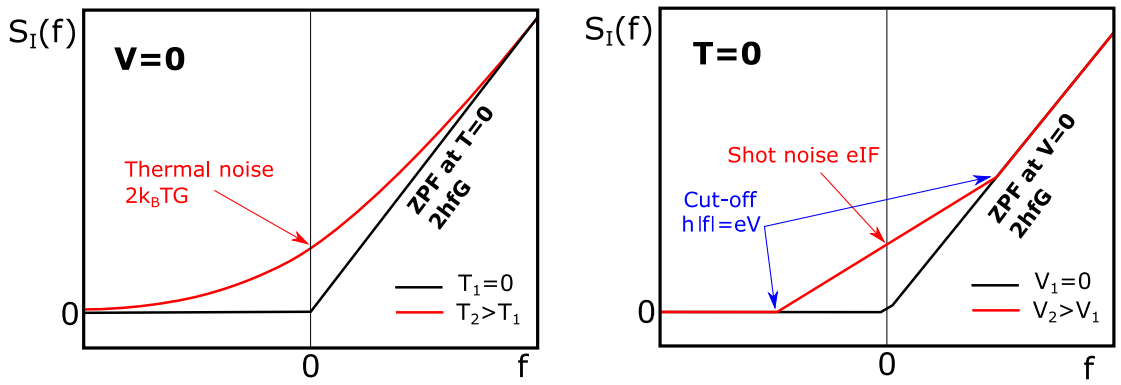

Figure 1.5: (a) Schematic frequency dependence of the equilibrium voltage noise of a resistor at different temperatures T_1 and T_2. For $T_1 = 0$ (black), the PSD for negative frequency is zero while it increases linearly for positive frequencies due to the zero point fluctuations. At finite temperature T_2 (red) thermal noise is observable and blurs out the ZPF transition. The zero frequency value at finite temperature is obtainable by the Johnson-Nyquist formula; (b) Schematic frequency dependence of the out-of-equilibrium current noise at different bias voltages V_1 and V_2 at zero temperature. For zero bias voltage (black), the PSD is again zero for negative frequencies and increases linearly for positive frequencies due to ZPF. At higher bias voltages (red), shot noise is observable within the energy cut-off (blue arrows) for negative and positive frequencies, whose zero frequency value is predicted by the shot noise formula.

In the zero temperature case, where the thermal fluctuations are suppressed, the solution is discontinuous for the two regimes where either shot noise (for $hf < eV$) or the vacuum fluctuations (for $hf > eV$) is dominant. For an energy independent transmission coefficient T_P, and at zero temperature, we obtain:

$$S_I(f, T=0, V) = 2G_0 \cdot \begin{cases} hf \sum_N T_{P,N}^2 + \Theta(eV - hf) eV \sum_N T_{P,N}(1 - T_{P,N}) & \text{for } f > 0 \\ 0 + \Theta(eV - h|f|) eV \sum_N T_{P,N}(1 - T_{P,N}) & \text{for } f < 0, \end{cases} \tag{1.19}$$

with Θ as the Heaviside function. We have plotted in figure 1.5 the quantum current fluctuations appearing in two illustrative limits. Firstly in figure 1.5a we show the evolution of the spectral noise density for different temperature at zero voltage bias and in figure 1.5b for different voltage biases at zero temperature.
Considering that even though the transition of equation 1.19 is discontinuous in theory, it will always be smeared out by the remaining thermal fluctuations as absolute zero temperatures can not be practically achieved. This leads us to the formulation of the final equation for the PSD by taking into account the three ingredients introduced before: zero-point motion, thermal noise and shot noise. The total quantum noise for arbitrary voltages, temperatures and for a quantum conductor [102, 112, 113] with N channels with a transmission coefficient $T_{P,N}$ for negative frequencies is:

$$\begin{aligned} S_I(f < 0, T, V) =& 2G_0 \sum_N T_{P,N}(1 - T_{P,N}) \cdot \{(h|f| + eV) n_B(h|f| + eV) \\ &+ (h|f| - eV) n_B(h|f| - eV) - h|f| n_B(h|f|)\}, \end{aligned} \tag{1.20}$$

while for positive frequencies $S_I(f > 0)$ the finite frequency equilibrium noise has to be added, thus $S_I(f > 0) = S_I(f < 0) + 2G_0 \sum_N T_{P,N} hf n_B(hf)$, giving:

$$\begin{aligned} S_I(f > 0, T, V) =& 2G_0 \sum_N T_{P,N}(1 - T_{P,N}) \cdot \{(hf + eV) n_B(hf + eV) \\ &+ (hf - eV) n_B(hf - eV)\} + \sum_N T_{P,N}^2 \cdot hf n_B(hf) \end{aligned} \tag{1.21}$$

1.2.3.3 Fluctuation dissipation theorem (FDT)

Furthermore, by inspecting the expression of the finite frequency noise predicted by the scattering approach in the limit of energy independent scattering matrix elements, one can check that the frequency asymmetry of both quantum thermal noise and quantum shot-noise are simply related to the DC conductance G as: $S_{II}(f) - S_{II}(-f) = 2hfG$. Such fluctuation dissipation relation (FDR) is not accidental, as Kubo demonstrated it generically in the frame of linear response theory [19]. Fluctuation-dissipation theorems, relating the fluctuations of a system to its physical response to a driving force, are powerful results of statistical physics. The first of them, proven by Einstein in 1905 [114] relates the diffusion constant D, characterizing the fluctuations of Brownian motion ($\langle x^2 \rangle = 2Dt$ in a given observation time t), and the mobility μ of a particle, describing its response to an external force F with $\mu = \langle \dot{x} \rangle / F$:

$$D = \mu k_B T \tag{1.22}$$

This FDR is simply a linear response theory for a system in equilibrium, where a small perturbation drives the system out of equilibrium. When there is a process that allows a system to dissipate energy into the environment, then a reverse process must exist for the system to absorb energy which creates fluctuations.
This can be applied to other systems as for example in the case of the Johnson-Nyquist noise. The dissipative part of the impedance $Re[Z(f)]$ of a conductor allows a power dissipation by Joule heating, while in reverse the thermal energy of electrons leads to fluctuations of the current (see equation 1.10) The quantum mechanical version of equilibrium FDR was provided by Callen & Welton. When applied to an electrical conductor, the Callen-Welton noise is given by equation 1.18.
It can be seen that this expression is not frequency symmetric $S(f) \neq S(-f)$ and that it satisfies the detailed balance of equilibrium quantum fluctuations $S(f) = e^{\beta h f} S(-f)$. This is starkly different from classical correlation function of real signals and Kubo showed in 1957 [19] that this very quantum asymmetry of spectral density is directly proportional to the real part of the admittance:

$$S_{asym.} = S(f) - S(-f) = 2hfRe(Y(f)) \tag{1.23}$$

Kubo showed that this result is valid generically, not having to make an hypothesis of thermal equilibrium but just asking the system to be in a stationary state [19]. This formal relation was further stressed by Caldeira and Leggett [20] who showed that mechanical viscous damping, or electrical Joule losses, could be modeled quantum mechanically as a linear coupling to a bath of harmonic oscillators simply characterized by their (mechanical or electrical) impedance. Finally, the tools developed in the 80s to describe open quantum systems [21, 22] could be used to model efficiently not only the physical quantum system, but also its (quantum) interaction with a measuring apparatus.

1.2.3.4 Tunneling FDR

Kubo formula links the emission and absorption noises to the linear response of the quantum conductor. Yet it does not help computing either one of them unless the other one is already known. More predictive formulas can be derived for simple conductors where the current flows according to instantaneous tunneling events and where no memory effects build up so that perturbative techniques are valid. These formulas were originally derived by Rogovin and Scalapino [118] in order to understand the finite frequency phenomena in Superconducting-Insulator-Superconducting (SIS) junctions. They found that both the current fluctuations, and thus the admittance, can be simply expressed in terms of the DC current voltage characteristic I(V) only:

$$S_I(V,f,T) = e\left[\frac{I(V+hf/e)}{1-exp\left(-\frac{V+hf/e}{k_BT}\right)} - \frac{I(eV-hf/e)}{1-exp\left(\frac{eV-hf/e}{k_BT}\right)}\right] \tag{1.24}$$

$$Re[Y(V,f)] = e\frac{I(V+hf/e)-I(V-hf/e)}{2hf} \tag{1.25}$$

In their original article, they found them to describe several regimes of correlated charge transport that one can observe in SIS junctions: they describe the quasiparticle tunneling above the gap as well as the Fisk resonance associated to the AC Josephson effect in the presence of an electromagnetic mode (in this case replacing e with the Cooper pair charge $2e$, in the above expression). These relations where further acknowledged to be extremely general by Sukhorukov, Burkard and Loss in 2001 [139]. Which was indeed confirmed by Safi and co-authors by building a general tunneling model based on tunneling operators of arbitrary charge q acting on arbitrary systems [115–117].
Interestingly, they fail to apply to systems where the tunneling time scale is relevant as recently showed experimentally by Février & Gabelli [119]. Indeed such relations are based on a single tunneling operator model, which by construction imposes equal currents on both electrodes, and thus they cannot capture dwelling time dynamics.

At this point we have introduced some tools in order to describe the current fluctuations flowing in quantum electrical conductors. Yet, we still do not know how to access them experimentally. In the next chapter, we will focus on the experimental strategies used to measure quantum noise and we will introduce a new experiment extracting both the positive and negative frequency noise of a non-linear conductor driven far from equilibrium.

Part I

Measurement of emission and absorption noise by energy exchanges between a non-linear conductor and a linear electromagnetic environment

Chapter 2

Introduction to Absorption noise detection

The measurement of classical electric noise has become a simple task with many detectors and measurement systems available. However, the measurement of quantum noise, with all its new properties as compared to classical noise, still remains a challenge. A common strategy is to measure the excess noise: A typical measurement records the noise of an applied current across a mesoscopic conductor over a certain frequency range. The noise signal is amplified, squared and then averaged to obtain power spectral density (PSD). The PSD will be recorded in two conditions: for the system at equilibrium and out-of-equilibrium, in which case the sample is DC-biased. The excess noise is defined as the difference between the two measurements which is, put in other terms, the energy that is transferred between the conductor and the detector [120]. While this excess noise is fundamentally independent of the measurement setup, quantum features may not be detectable depending on the detector used. An ideal classical detector is generally a passive element that can only absorb energy which limits it to the measurement of emission noise, even though for some detectors, as for example a voltage amplifier, a back-action noise exists that may excite the system so that an uncontrolled mixture of emission and absorption noise is probed instead. The ideal classical detector provides the correct results when the noise is symmetric as is the case in the classical regime but does not allow to measure the asymmetrical quantum noise. For this a dedicated quantum detector is needed, that is able to absorb energy coming from the conductor and to emit energy towards the conductor by a de-excitation, in order to measure both the emission noise and absorption noise. Such a detector that can be set to a passive or active mode is often referred to as "quantum spectrum analyzer" (QSA). The concept of a QSA by the use of an LC-resonator circuit as a quantum detector has been proposed by Lesovik and Loosen in 1996 [23] but not yet been realized as it is technically challenging to measure these energy exchanges. Instead current detection schemes relied on a direct power measurement by which it is possible to measure the emission noise of a conductor. Later developed on-chip detectors circumvent the difficulty of the noise measurements based on the utilization of photon assisted transport effects. PAT effects allow to imprint the amplitude of the fluctuations in another observable like the

DC-current across the used detector, which can be easily red-out. These detectors allow in principle to measure both emission and absorption noise without directly measuring the energy exchanges.
In the following sections we give a short overview of the most common detection methods: We firstly introduce the basic concept of a detector based on an LC-resonator and then present the different already established detection techniques including direct power measurements and on-chip techniques relying on PAT effects for quantum dots and the SIS tunnel-junction.

Contents

2.1 Quantum noise detectors

It is a direct consequence of the ZPF that the power spectral density (PSD) of fluctuations is generically different at positive and negative frequencies [15] as the ZPF themselves are asymmetric. In a simplified picture, this asymmetry can be understood by looking at the energy exchange an electromagnetic source with the electromagnetic vacuum: for positive frequencies the vacuum acts as a thermal bath that can absorb energy from the source which enables to fluctuate and dissipate energy. The reverse energy process, corresponding to the negative frequency range, however, is not possible as no energy can be taken from the vacuum. One can see that vacuum couples only to the ability of the source to emit energy, however, the source itself might absorb some, should it be present in its environment. A detector being able to measure both the ability of a source to emit and absorb energy is a QSA. We will see that while passive devices can always be used to detect emission processes, one needs an active device in order to measure absorption processes. Since conductors naturally couple to EM fields, a simple scheme to detect the power conveyed by the current fluctuations is to measure the power it can deposit in a single electromagnetic mode. In quantum circuits, this is an LC mode. Since its dynamics are simple enough, we can derive its fluctuations without the need of any fluctuation dissipation relation. As they will be important in the next section, we quickly present their derivation here.
We compare the classical and quantum solutions of the PSD for analogue model of a quantum harmonic oscillator. We assume a harmonic oscillator whose mass m corresponds to the resonators capacitance C and its spring constant k to its magnetic reluctance $1/L$, thus resulting in its resonance frequency given as $\omega = 1/\sqrt{LC}$. We

can then express the resonators voltage $V = d\phi/dt$ and its flux ϕ as velocity v and position $x(t)$ respectively which is given by the Hamilton's equation with p representing the charge q:

$$x(t) = x(0)\cos(\omega t) + p(0)\frac{\sin(\omega t)}{m\omega} \tag{2.1}$$

We then obtain the auto-correlation function as:

$$C(t) = \langle x(t)x(0)\rangle = \langle x(0)x(0)\rangle\cos(\omega t) + \langle p(0)x(0)\rangle\frac{\sin(\omega t)}{m\omega} \tag{2.2}$$

In a classical system at thermal equilibrium p and x do not correlate (=0), hence the second term vanishes. We then obtain the ACF by replacing $\langle x^2\rangle$ by the equipartition theorem:

$$C(t) = \frac{k_B T}{m\omega^2}\cos(\omega t) \tag{2.3}$$

The auto-correlation function is thus symmetric and real which also leads to a symmetric noise spectral density:

$$S(\omega') = \pi\frac{k_B T}{m\omega^2}[\delta(\omega' - \omega) + \delta(\omega' + \omega)] \tag{2.4}$$

To describe an oscillator in the quantum regime, we replace x and p in equation 2.2 by their associated quantum operators $\widehat{x}$ and $\widehat{p}$, which do not commute as $[\widehat{x}, \widehat{p}] = i\hbar$. After few calculations, we find the complex ACF [121]:

$$C(t) = \frac{\hbar}{2m\omega}[n_B(\hbar\omega)e^{i\omega t} + [n_B(\hbar\omega) + 1]e^{-i\omega t}], \tag{2.5}$$

with the Bose-Einstein occupation factor

$$n_B = \frac{1}{\exp\left(\dfrac{hf}{k_B T}\right) - 1}, \tag{2.6}$$

and obtain an asymmetric spectral noise density after Fourier transformation:

$$S(\omega) = \frac{h}{2m\omega}[n_B(\hbar\omega)\delta(\omega' + \omega) + [n_B(\hbar\omega) + 1]\delta(\omega' - \omega)] \tag{2.7}$$

Based on equation 2.7 we can see, that the spectral density is asymmetric but becomes symmetric again in the high temperature limit $k_B T \gg hf$ as $n_B \approx n_B + 1 \sim \dfrac{k_B T}{hf}$, so that we obtain the classical solution.

2.2 Measurement of equilibrium noise

The first experiment we are aware of measuring quantum noise of an electrical conductor was performed in the 80's in Clarke's group [122]. Their idea was to measure how the high frequency quantum noise of a shunting resistor influenced the dynamics of a Josephson junction, that is a superconducting-insulating-superconducting junction operated in the superconducting regime. Such a device has a strongly non-linear constitutive relation: $I = I_c \sin(2\pi\Phi/\Phi_0)$, with I_c the supercurrent of the junction, Φ the electromagnetic flux threading the junction related to its voltage drop as $\Phi = \int dt' V(t')$, and Φ_0 the superconducting phase quantum $\Phi_0 = h/2e = 2{\cdot}10^{-15}$ Wb. In the experiment, such a strong non-linearity is essentially used to selectively down-convert the high frequency current noise arising from the shunting resistor to a low frequency band, which is filtered, amplified and measured. In figure 2.1 we reproduce a figure from their article showing the frequency dependence of the spectral density of symmetric current fluctuations arising from a resistor as extracted from their experiment at two different temperatures. Not only could they resolve quantitatively the Johnson-noise limit ($hf \ll k_B T$), but could also show how the symmetrized equilibrium noise increases with frequency (due to zero point motion) with a thermal rounding well described by Callen-Welton theorem.

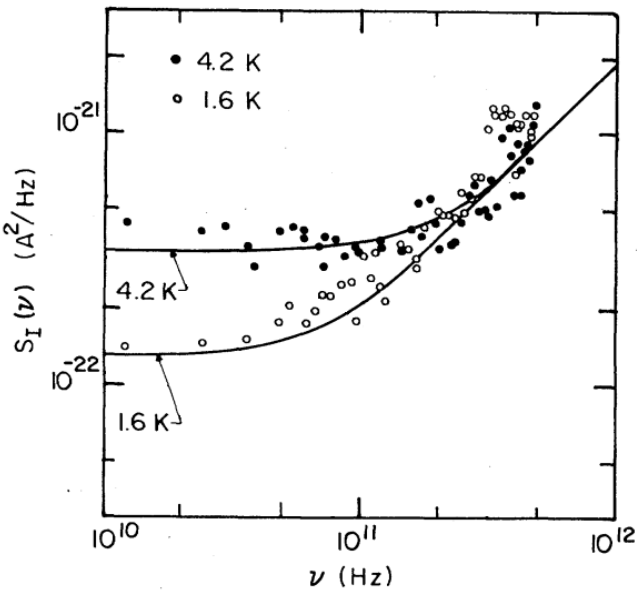

Figure 2.1: First experimental measurement of Callen-Welton noise, measured in a resistively shunted SQUID at different temperatures. The high frequency current noise of the shunting resistor is down converted by the SQUID's non-linearity and gets imprinted onto the measured low frequency current noise. The measured data (dots) is compared to the theoretical prediction (line). Modified figure taken from [122]

2.3 Measurement of out-of-equilibrium noise

Experiments aiming at measuring the quantum current fluctuations of electrical conductors driven out-of-equilibrium have followed essentially two different experimental paradigms. One of them is photon assisted transport experiments where, in a similar way to Clarke's group experiment, the high frequency spectra of the quantum noise is fed on-chip to a non-linear quantum conductor which essentially rectifies it and thus the high frequency noise can be read via low frequency conductance measurement. The theory of rectification of (classical) electromagnetic signals by tunneling junctions was introduced by Tien & Gordon in the 60's [47], and extended to develop mm-wave mixers in the 80's [93]. It was only in 2000 when Aguado & Kouwenhoven realized that such a scheme could be used to measure separately the non-symmetrized current fluctuations. A second experimental approach has been to collect the high frequency current fluctuations in a transmission line, amplify them and measure them at room temperature. In order to understand the measured quantities, one needs a quantum description not only of the conductor at the origin of these fluctuations, but also of the electrodynamic coupling between the conductor and the electromagnetic modes of its detection circuit. Such tools where introduced in the 80's (Input-output theory Yurke & Denker, quantum Langevin equations Gardiner & Collet) in order to understand quantum dynamics in open systems and/or in the presence of dissipation. In the late 90's Lesovik & Loosen used such tools to analyse the power exchanges of quantum conductor weakly coupled to a harmonic oscillator (e.g. one mode of the detection circuit), and found that the non-symmetric noise can be extracted from such measurements.

2.3.1 Direct power detection

The main idea of this scheme is to couple the current fluctuations of the quantum conductor to a transmission so that the RF signals are conveyed to a room temperature RF detection circuit. This approach is seducing because once it possible to do so, one can exploit the arsenal of RF signal acquisition and processing techniques (either digital or analogue) in order to measure and analyse it. In principle, one could completely characterize the statistical properties of the emitted radiation by sampling the field in real time and computing all the relevant time correlation functions (see e.g. [77, 123–125]). In practice, even though the signal is pre-amplified by a cryogenic low noise amplifier, it still adds some noise, making it the more and more difficult to measure higher order correlations. A full review of the possibilities offered by such scheme lies out of this dissertation, so we will directly focus on the scheme relevant for the experiments showed in the next section, which is the current source limit.

2.3.1.1 Energy exchanges between a quantum conductor and a LC circuit

In order to measure the non-symmetrized noise we need a detector able to absorb energy coming from the conductor and to emit energy towards the conductor by a de-excitation. We will follow Lesovik & Loosen [23], and analyse the energy exchanges

between a quantum conductor and an LC circuit held at finite temperature when linearly coupled through the current operator of the quantum conductor. As illustrated in figure 2.2 any quantum conductor can be coupled to a resonator who, depending on its photon occupation corresponding to n_B, is able to either emit or absorb photons from the conductor.

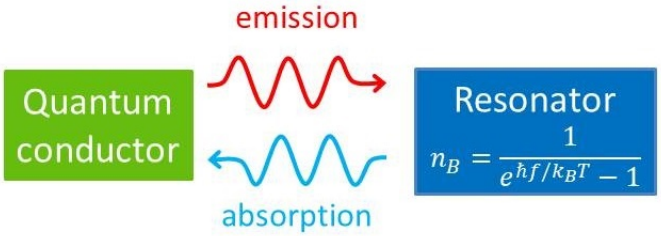

Figure 2.2: Schematic illustration of the interaction between a quantum device and a detector.

Indeed, the simplest quantum electrodynamic coupling is linear $H_c = \hat{I}\hat{\Phi}$ with $\hat{I}$ the current flowing through the conductor, and $\hat{\Phi}$ the EM fluctuations imposed by the LC mode. Lesovik & Loosen analysed the dynamics resulting from such linear coupling under the hypothesis that no memory can build in the system, which is expected to be the case when the coupling is sufficiently small and the mode has a finite quality factor. They found that the power exchanged between the conductor and the mode (with the convention that positive power increases the mode energy) reads as:

$$S_{Power} = K((1 + n_B) \cdot S(-f_0) - n_B \cdot S(f_0)]), \tag{2.8}$$

with the Bose occupation number

$$n_B = \frac{1}{e^{hf_0/k_B T_{LC}} - 1}, \tag{2.9}$$

and the effective coupling constant K of the mesoscopic conductor to the resonator

$$K = (\frac{\alpha}{2L})^2 \frac{1}{2\eta}, \tag{2.10}$$

where η is the width of the resonance of the LC-resonator, T_{LC} its temperature and L its inductance. α is the inductive coupling coefficient of the harmonic oscillator coupled linearly to the time derivative of the current.
Equation 2.8 links the two exchange contributions: Following our convention positive exchanges are proportional to $S_I(-f)$ and negative exchanges proportional to $S_I(f)$. This means that $S_I(-f)$ triggers the energy emission from the conductor into the environment, while $S_I(f)$ triggers absorption from it. This result led to the coining of the more physical terms "emission and absorption noise" in order to describe the negative and positive current spectral densities. Importantly, equation 2.8 says that the oscillator couples unequally to the emission and absorption noise, depending on the resonator state. Indeed, at zero temperature $n_B = 0$ and the only possible energy

exchanges are power being emitted into the oscillator (equation 2.11) which describes the spontaneous emission into vacuum.

$$Power_{sponteaneous} = P(n_B = 0) = K \cdot S_I(-f_0) \tag{2.11}$$

At finite occupation, a stimulated emission term proportional to $n_B S(-f)$ adds to the emitted power, but also the time reversed process of stimulated absorption proportional to $-n_B(f)S(f)$ takes energy from the environment, resulting in equation 2.8.
The LC resonator is thus a detector coupling to non-symmetrized noise, and thus a genuine quantum detector. Despite having an evenly spaced spectrum, when sitting close to vacuum, the oscillator has very asymmetric properties as it can be excited but is hardly able to emit energy.
However, in the (classical) high temperature limit ($k_B T \gg h f_0$) equation 2.8 can be simplified by the approximation of $1 + n_B \simeq n_B \simeq k_B T / h f_0$. Thus the resonator only measures the difference of noises, that is equal to the real part of the admittance, following the Kubo formula (equation 1.23), as in a classical experiment:

$$S_{meas} = K(-2Re(Y)k_B T_{LC}) \tag{2.12}$$

While the main physics are already present in Lesovik & Loosen's article, an input -output analysis of the power exchanged between the conductor and the electromagnetic modes of its surrounding circuit by Mora et al. [56] showed that the no-memory assumption in Lesovik & Loosen's derivation is fulfilled in the current source limit (when the impedance of the quantum conductor is larger than the impedance Z_{det} of the detection circuit). They found that in this limit, the power exchanged per unit bandwidth between the conductor and the detection circuit reads:

$$\frac{\delta P}{\delta f}(f_0) = 2Re[Z_{det}(f_0)][(1 + n_B(f_0)S_I(-f_0) - n_B(f_0)S_I(f_0)] \tag{2.13}$$

To be exhaustive, let us say that when there is not a large difference in impedances, one needs to take into account how the current fluctuations arising from the current source gives rise to voltage fluctuations in the detection circuit thus modifying the biasing conditions of the source at their origin. There is no general method to solve such a self-consistent problem, even though some results have been obtained when treating the quantum conductor within a linear response approach [126] and in the case of a $50\,\Omega$ transmission line matched to a $50\,\Omega$ tunnel junction [127].
Some experiments have demonstrated the ability to extract the emission noise from such a scheme (see next section) but we are not aware of experiments exploiting it in order to extract the absorption noise. Doing so is more involved, since it requires to control quantitatively the occupation of the mode. In the next chapter we will present an experimental realization of it. Beforehand we give a short review of different noise detection techniques in the following sections that have been used experimentally probing the asymmetry of quantum noise under certain conditions and limitations.

2.3.1.2 Some experimental realizations

Starting with the simplest technique which is the direct measurement of the emitted noise power with simple RF-electronics relying on amplifiers, filters and rectifying diodes. Firstly we present the results for linear mesoscopic conductor, meaning that they either have an intrinsically constant admittance or were operated under the required condition so that the admittance did not vary with the frequency. Secondly, we present measurement of shot noise of non-linear conductors which went further to give the first experimental signature of the excess noise and thus the emission noise of the system.

A) Power emitted by a linear conductor:

The first experiments we are aware of probing finite frequency non-equilibrium noise of a quantum coherent conductor driven out-of-equilibrium where performed in Dan Prober's lab [128]. The idea was to measure the noise power emitted by the finite frequency shot noise of a diffusive wire when DC biased. They had two good reasons to choose such a noise source:

- On the one side, it is a many channel coherent conductor where the channels have essentially either a very poor transmission probability to be transmitted, or a transmission very close to one. The weakly coupled channels contribute to the noise with a shot noise close to the Schottky limit, however the well transmitted channels poorly contribute to noise and give a global Fano factor lower than one. In the universal limit of disordered wires, the scattering theory predicts a resulting Fano factor of 1/3. Thus, a diffusive wire is an easy to fabricate quantum shot noise source.

- On the other side, having many channels in parallel provides the wire with a resistance way smaller than the resistance quantum. In the experiment, the wires had an impedance close to $50\,\Omega$. This way, the source is essentially perfectly matched to the detection circuit (a $50\,\Omega$ transmission line) enabling a very large band coupling, of about 20 GHz.

The authors exploited such a wide band coupling to measure the finite frequency power emitted by the diffusive wire as a function of the DC voltage bias V for several detection frequencies f ranging from 1.5 GHz to 20 GHz. To be more specific, the experiment amplified the RF signal conveyed by the coupled transmission line, guided it to a room-temperature detection scheme where it was multiplexed into detection bandwidths centred on different adjustable carrier frequencies, and finally the noise power P of each band was detected by square law power detectors (RF diodes). In figure 2.3 we reproduce their measurements of the differential noise power: dP/dV, expressed in units of noise temperature $T_n = P/k_B$. One can see that at sufficient high voltage bias the emitted noise power has a constant slope given by the Fano factor of disordered wires ($S_I = 2eI/3$) as predicted by the scattering theory of diffusive conductors in the low frequency limit ($k_BT \,\&\, hf \ll eV$). We note that for figure 2.3 the Fano factor has not been determined directly, but that the data is normalized by the high current value. At high enough detection frequencies $hf > k_BT$ a clear onset

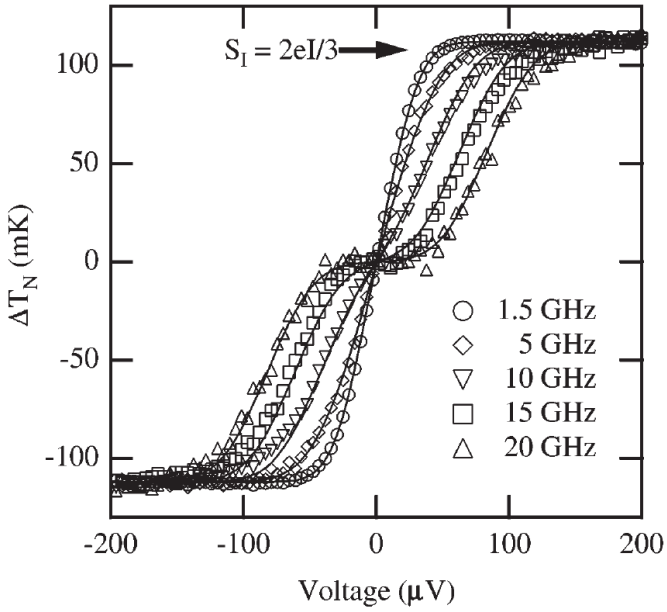

Figure 2.3: First experiment measuring the non-equilibrium noise in the quantum regime at 40 mK. The high frequency current fluctuations are amplified and rectified after band-pass filtering at room temperature to directly obtain the PSD. The differential noise is measured at 1.5, 5, 10, 15, and 20 GHz (Symbols) and compared to theoretical predictions (solid line). The measured noise transitions from voltage independent ZPF at zero bias to shot-noise past the threshold bias voltage of $V > hf/e$. Figure taken from [128].

of noise emission appears at $eV = hf$, in agreement with the finite frequency noise predictions introduced in section one.
We would like to stress that the experimental protocol used here measured essentially the excess noise as introduced by the noise source, that is the difference between the noise power detected by the RF circuit when biasing the device at finite voltage and the noise detected at zero bias: $P = P(V) - P(V = 0)$. Such an approach cannot discriminate between symmetrized and non-symmetrized noise when the admittance of the noise source is voltage independent. Indeed, the only difference between emission and absorption noise is $2ReY(V)hf$ as predicted by Kubo formula, thus symmetrized noise can always be written as $S_{sym}(V, f) = S_e(V, f) + S_a(V, f) = 2S_e(V, f) + 2ReY(V, f)hf$. From this equation, one can see that for a linear conductor the excess symmetrized noise is just twice the excess emission noise $S_{sym}(V, f) - S_{sym}(V = 0, f) = 2[S_e(V, f) - S_e(V = 0, f)]$.

B) Power emitted by a non-linear conductor:

The first experiment we are aware of directly measuring the power emitted by the finite frequency noise of a non-linear conductor was performed in Fabien Portier's lab [72]. The authors implemented a very similar RF noise-power detection scheme as in the precedent experiment, with the important differences that firstly, the source of current fluctuations is now a high impedance tunnel junction, and secondly the

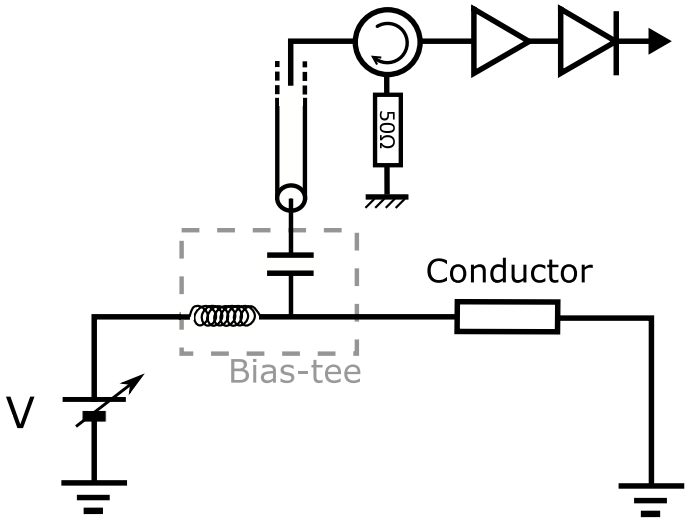

Figure 2.4: Simplified electrical scheme of a finite frequency noise measurement for a conductor that is connected to a DC biasing voltage V through the inductive port of a bias-tee and a microwave measurement line through its capacitive port. The measurement line consists of a transmission line, circulator, amplifier and a matched quadratic detector. The circulator protecting the sample from the emitted noise of the amplifier by redirecting its signal to ground. The conductor may either be directly matched [128] or contain a matching circuit on chip as in the experiment realized in [72], where a high impedance RF resonator is placed in series with a high impedance tunnel junction.

impedance of the transmission line collecting the emitted radiation is transformed around the detection frequency by a high impedance RF resonator (see figure 2.4). The experiment was designed to be in the current source limit, namely the impedance of the junction is larger by an order of magnitude than that of its detection circuit, so that it can be seen as a current source of fluctuations being fed into the detection line.
Such a scheme seems extremely inefficient regarding RF measurements as compared to the precedent one, as it only couples efficiently the emitted radiation in a few 100 MHz detection bandwidth around the resonator frequency of about 6 GHz, as compared to the precedent 20 GHz bandwidth. However, it gives rise to new physics: As we will see in Chapter 4, the vacuum voltage fluctuations arising from the high impedance resonant detection circuit give rise to a strong detection back-action on the dynamics of the tunnel junction, triggering inelastic tunneling events that make the transport properties of the junction non-linear. Thus, the admittance of the tunnel junction becomes voltage dependent, and there is an observable difference between the excess noise of symmetrized current correlations, and the excess emission noise. In figure 2.5 we reproduce the findings of Altimiras et al. [72], in the upper panel the authors present the differential DC conductance of a tunnel junction as function of its DC bias when coupled to three different high impedance resonant detection schemes (with characteristic impedances and resonant frequencies described in the

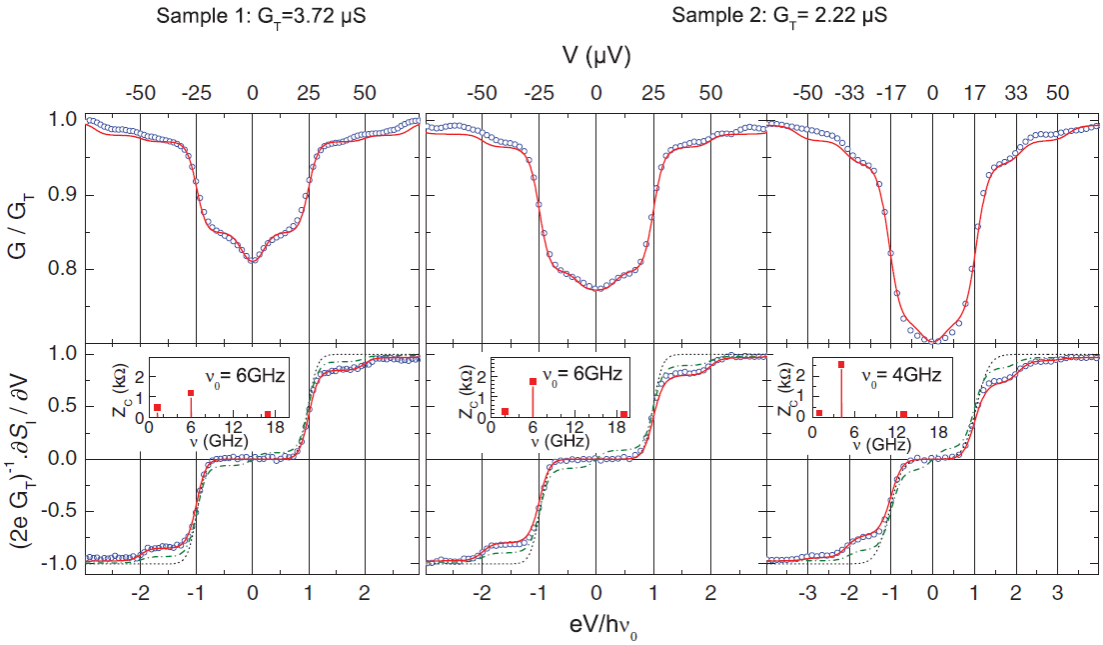

Figure 2.5: Plot of the normalized differential conductance (top) and current noise spectral density (bottom) for different samples: Sample 1 in the left panel with $\nu_0 =$ 6 GHz and Sample 2 in the center and right panel with ν_0 =6 and 4 GHz, respectively. Experimental measurement data is recorded at 15 mK and presented as open circles. The solid red lines result from an analytical fit to the data involving series impedance made of three discrete modes shown in insets and the dotted black curve shows the non-interacting, finite frequency shot noise prediction. The green dot-dashed line represents the DCB expression for the current noise density symmetrized with respect to frequency. Figure taken from [72].

inner panels). Clear steps are visible at multiples of the resonant condition $eV = nhf$ with n an integer, and f the resonant frequency of the high impedance resonator, demonstrating the onset of inelastic tunneling channels. On the lower panels, the authors present the voltage derivative of the noise power emitted in the resonator as a function of the applied voltage bias, again showing a step like shape at the onset of inelastic channels. The important aspect of these measurements regarding our discussions is that the authors could compare their measurements to the predictions of noise symmetrization made using Dynamical Coulomb Blockade theory. The quality of their predictions was first tested on the DC conductance data, and then it was used to predict the finite frequency noise. The emission noise prediction (red line), was found to reproduce well the measured excess noise power, however the prediction of the symmetrized correlator green dashed-dotted line failed to reproduce it, thus confirming the physical picture of emission noise triggering energy emission in linearly coupled environments as introduced by Lesovik & Loosen theory.

2.3.2 Photon assisted transport

2.3.2.1 Photon assisted transport in non-linear conductors

On-chip detectors are created based on the principle that current transport across a mesoscopic conductor is modified by its interactions with an electromagnetic field. By irradiating a conductor with microwave photons, an inelastic tunneling current is induced in the conductor when tunneling electrons exchange photons with energy hf with the microwave field. The effect is thus named photon-assisted tunneling (PAT or Tien-Gordon effect [47] in the case of a monochromatic coherent irradiation) and Aguado & Kouwenhoven showed in 2000 that it can be utilized to probe photon energy exchanges discriminating absorption from emission processes [48].
To allow for this discrimination in the direction of energy exchanges, it is mandatory to use a non-linear conductor, which we will quickly illustrate: Assume a non-linear conductor with a potential barrier U across which the electronic transport is suppressed for low DC-bias $eV < U$ and finite for $eV > U$. For simplicity, let's assume a toy model where the transmission $\tau(V) = 0$ for $eV < U$, and $\tau(V) = 1$ for $eV > U$. That gives a current voltage characteristic $I(V)$ equal to zero up to $eV = U$, and then having a linear increase with voltage. This looks like a diode, and an incoming electromagnetic field providing a time dependent voltage bias $\delta V(t)$ should be rectified by it. Classically, one expects the rectified current to be given by the time average of $I(V + \delta V(t))$. However, Tien & Gordon showed [47] that when such a non linear I(V) results from the quantum tunneling of electrons, the rectification of a classical AC field is nevertheless "quantized", namely the rectified current is the sum of the original I(V) curve shifted by multiples of $\pm nhf/e$ with f the frequency of the microwave tone used to irradiate the conductor, weighted by a factor depending on the tone amplitude $I_{rectified}(V) = \sum_{n=-\infty}^{n=+\infty} J_n^2(e\delta V/hf) I(V - nhf/e)$ with J_n being Bessel functions of the first kind of order n. For a classical driving field its voltage time correlations are time symmetric, and the amplitude of positive and negative shifts of the same order are equal. However, Aguado & Kouwenhoven [48] realized that when the electromagnetic field sent to the conductor originates from the quantum mechanical dynamics of another quantum conductor, such weighting factor should be different. They proposed a protocol where the current fluctuations of a source conductor $\delta I_s(t)$ are transformed on-chip into a voltage fluctuations at the input of a detection non-linear conductor $\delta V_{det}(t)$, via a linear coupling circuit characterized by a transimpedance $Z_T(f) = \delta V_{det}(f)/\delta I_s(f)$ (see figure 2.6). Up to lowest order in such electrodynamic coupling, they indeed found that the resulting photon assisted current of the detection conductor is the sum of its original I(V) curve translated by hf/e with f the coupled frequency weighted by the emission noise of the source conductor for positive shifts and its absorption noise for negative shifts. Depending on the detector used and its operation point, the rectified signal might be proportional to emission noise only, or to a combination of emission and absorption noise. One can convince oneself easily that, when the toy model conductor introduced before with zero current for $eV < U$ is used as a PAT detector, the emission noise spectra of the source will be imprinted in the $eV < U$ part of the I(V)-curve, while for $eV > U$ the

PAT will be a weighted sum of emission and absorption noise.

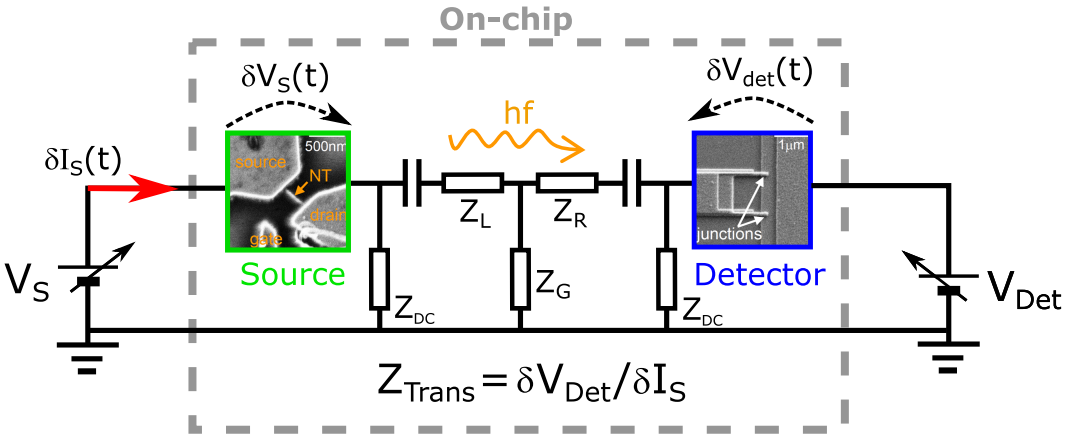

Figure 2.6: Electrical scheme of the PAT detection scheme: a linear network couples the current fluctuations flowing through the source to the non-linear detector. Such a circuit can be realized as in [129] with an SIS-junction as detector for the noise emitted from a carbon nanotube. The DC biasing and measurements are done separately for source and detector, through the respective DC-branches of the circuit, while high frequency currents are coupled via an RF-network. Its finite transimpedance Z_{trans} gives rise to voltage fluctuations at the detector input, which are rectified by it according to PAT effects [47, 48]. However, detection back-actions may appear in the case of symmetric circuits and coupling networks ($Z_L = Z_R$): because the transimpedance from source to detector is the same as from detector to source, PAT effects arise in both directions provided that both conductors are biased.

The noise is thus imprinted on the detector's recorded I(V)-curve which allows to measure the high frequency noise with standard low frequency noise measurement equipment. One can express this modification of the electrical transport as the difference of the modified I(V)-curve as compared to the I(V)-curve in the absence of irradiation, labeled as I_0. The modified current is obtained by simply multiplying the current I_0 with the probability to exchange energy with the environment $P(E)$:

$$I_{mod}(V_{bias}) = \int dE'\, P(eV_{bias} - E') \cdot I_0(E'/e) \tag{2.14}$$

When the voltage fluctuations at the detector input give phase excursions smaller than 1, then the probability to exchange an energy quanta with the environment $P(E)$ can be expressed in terms of the noise spectral density of current fluctuations $S_I(f)$ which are coupled to the voltage fluctuation of the environment via the transimpedance $Z(f)$ ($S_V(f) = |Z(f)|^2 S_I(f)$) as lowest order expansion [48]:

$$\begin{aligned} P(E) \simeq & \left(1 - \frac{1}{hR_K}\int_{-\infty}^{\infty} df \frac{|Z(f)|^2}{f^2} S_I(f)\right)\delta(E) \\ & + \frac{1}{R_K}\frac{|Z(E/h)|^2}{E^2} S_I(E/h) \end{aligned} \tag{2.15}$$

The first half of this equation, the δ-contribution, renormalizes the elastic current at zero energy ($E = 0$). The second half corresponds to the inelastic current flowing across the detector. At positive energy $P(E)$ is proportional to the source absorption energy and the corresponding inelastic current witnesses processes where the energy E is sent from the detector to the source. At negative energy $P(E)$ is proportional to the source emission noise, and the resulting inelastic current witnesses the opposite processes.
Quantum current noise has been measured exploiting PAT effects on essentially two kinds of non-linear conductors used as quantum detectors: SIS-junctions [49,51,52,54, 55] and semiconducting quantum dots [48,50,130]. In the following sections we briefly introduce them and highlight the drawbacks of the implemented circuits which have prohibited them, up to now, to measure the absorption noise of a driven conductor.

2.3.2.2 PAT detection

A) Using Quantum dots

A semiconducting quantum dot (QD) is a small electronic islands of the order of 100 nm [131] that can be formed in different systems like 2DEGs, graphene sheets, carbon nanotubes, nano wires etc. When confined to such small dimensions, the kinetic energy of the charge carriers is quantized by the boundary conditions giving rise to a single particle discrete energy spectrum. Because of this, quantum dots are also sometimes labelled as artificial atoms. Another consequence of such reduced dimensionality is that the electronic island has a small capacitance to ground. This means that in order to change the number of the electrons in the box, one does not only need to pay the energy difference as predicted from the single particle spectrum, but also an electrostatic cost which might be even greater than the single particle energy scale. Regarding our discussion on PAT detectors, the important feature of quantum dots is that when tunnel coupled to electron reservoirs they act as genuine electron energy filters, with a very non-linear I(V) having spikes each time the bias voltage matches the charge addition potential, and zero otherwise.
Usually, the electronic island is made by confining the electron fluid via negatively biased electrostatic gates, but also etching or even growing the conducting material at the nano-scale. In order to perform electrical transport through the dot, it is tunnel coupled to electronic reservoirs, so that electrons can enter and leave the island through two different ports. We present a general lateral arrangement in figure 2.7a where an electro-statically defined QD is connected to the reservoirs (source and drain) via two QPCs, so that electrons can be transferred between the dot and the reservoirs, and capacitively coupled to a central gate. The central gate or plunger gate can be polarized with bias V_g in order to continuously change the electrochemical potential μ of the island by charge influence. When the kinetic energy is neglected, the electrochemical potential reads as $\mu(N, V_g) = (Ne + V_g C_g)^2/2C_{sum}$, where N is the number of electrons in the dot, C_g is the dot to gate capacitance, and C_{sum} is the total capacitance of the dot to ground. Thanks to that the dot can be tuned to the charge degeneracy point where states with different number of electrons have the

same potential $\mu(N) = \mu(N+1)$, so that electrons can transit through the dot giving rise to a zero bias conductance. For other values of the plunger gate voltage, the voltage bias needs to supply the potential difference $eV = \Delta\mu = \mu(N+1, V_g) - \mu(N)$, in order to have a finite current.

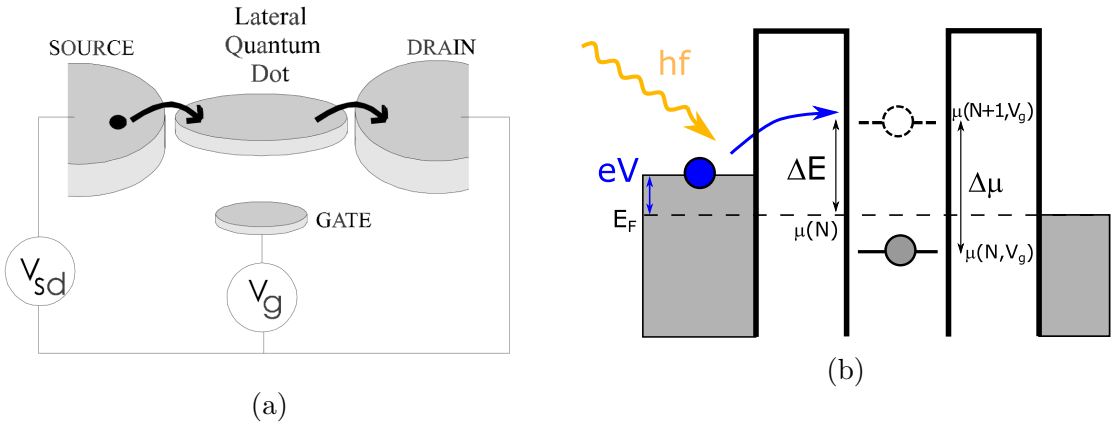

(a) (b)

Figure 2.7: a) Schematic illustration of a quantum dot connected to an electronic circuit via tunneljunctions/QPC and capacitively to an electrostatic gate. Figure taken from [132]; b) Schematic representation of energetics of a QD as quantum detector for emission noise. The chemical potentials for the dot to have N and $N+1$ charges are influenced by the gate voltage so that the N state potential lies below the Fermi energy, while the $N+1$ potential lies above the available energy provided by the DC bias eV. The dot is able to measure the emission noise, as electrons from the reservoir can only pass through the dot by tunneling to the $N+1$ state, if the missing energy is provided by a photo-emission process so that $eV + hf = \Delta E$.

Such an non-linear characteristic makes that QDs can be used as PAT detector of radiation, as this blockade can not only be lifted by increasing the bias but also by an external energy excitation through the emission of photons $eV + hf = \mu(N+1, V_g) - \mu(N)$. Therefore, as illustrated in figure 2.7b, a QD is tuned so that the potential energy of the dot containing N electrons lies beneath the Fermi energy, and the chemical potential having $N+1$ electrons has a higher energy. The applied bias eV is lower than the chemical potential difference of the $N+1$ state to the Fermi energy, labeled as ΔE so that electrons from the reservoirs can not enter the dot and the current flow is zero. Upon irradiating the dot with an electromagnetic field, electrons can nevertheless tunnel in by taking the energy hf from the applied field provided $eV + hf = \Delta E$. Such a configuration is thus sensitive to emission noise of the incoming field.
Experimental implementations of such scheme sensitive to emission noise only have been performed on QDs formed in carbon nanotubes by Onac et al. [50,130], QDs in 2DEGs by Gustavsson et al. [133] and also on nanowire QDs [134]. In the latter case, they measured the current fluctuations of a QPC in direct proximity to the quantum dot at 2 K. Having two different crystallographic systems, they eliminated the phonon coupling that occurred for the AlGaAs QPC-QD system in [133]. Even though in

the original proposal of Aguado and Kouwenhoven made explicit calculations of the absorption noise being imprinted in the PAT of a double quantum dot, where are not aware of any experiment demonstrating it. However, such quantum dot based detectors have been successfully used to measure the High-frequency noise emitted by QPCs testing the $\tau(1-\tau)$ prediction for the noise power and $eV = hf$ onset of emission.

B) Using SIS junctions

SIS-junctions are built up with two superconducting contacts separated by an insulating barrier. SIS junctions are characterized by a non-linear current-bias relation originating from the formation of Cooper pairs in the superconducting state. The first feature of the SIS's I-V curve (shown in figure 2.8), that originates from superconducting effects, is a super current of Cooper pairs that flows at zero bias. One can then observe a current of bosonic cooper pairs, that is driven by the phase difference ϕ of their wave equation on both sides of the barrier that is given by the first Josephson equation [89]:

$$I_J = I_c \sin(\phi), \tag{2.16}$$

with I_c being the critical current of the super conductor which at zero temperature is given by $I_c = \pi\Delta/2eR_T$, with Δ as the superconducting gap and R_T the normal state tunneling resistance, and is thus proportional to the energy gap and inversely proportional to the normal state tunneling resistance. If I_c is exceeded, superconductivity breaks down and the junction becomes normal conducting. The relation between the phase difference and the voltage across the junction is given by the second Josephson equation [135]:

$$\frac{d\phi}{dt} = \frac{2e}{\hbar}V(t) = \frac{2\pi V(t)}{\Phi_0}, \tag{2.17}$$

where $h/2e = \Phi_0 = 2 \cdot 10^{-15}\,\mathrm{Wb}$ is the magnetic flux quantum. From this we see that for $V = 0$ the phase difference is constant so that the current of equation 2.16 is also constant which is known as the DC Josephson effect. For a finite applied bias the phase difference increases linearly with time, resulting in an alternation of the Josephson current (known as AC-Josephson effect) based on the shown phase dynamics. The applied bias causes an oscillation across the junction at frequency $f_J = 2eV/h$ and, since $2eV$ must be smaller than 2Δ (see next section), it results typically in frequencies in the GHZ range (e.g. for Aluminum $2\Delta \simeq 360\,\mu\mathrm{eV} \simeq 88\,\mathrm{GHz}$):

$$I_J = I_c \sin(\omega_J t) = I_c \sin(2\pi V/\Phi_0 t) \tag{2.18}$$

The second feature is observable as a suppression of electronic current for finite voltages up to a threshold, at which the junction becomes normal conducting. The reason for this is the existence of an energy gap Δ between the ground state and the excited electronic states (see figure 2.8b). As a result, if we shift the bands with a bias that

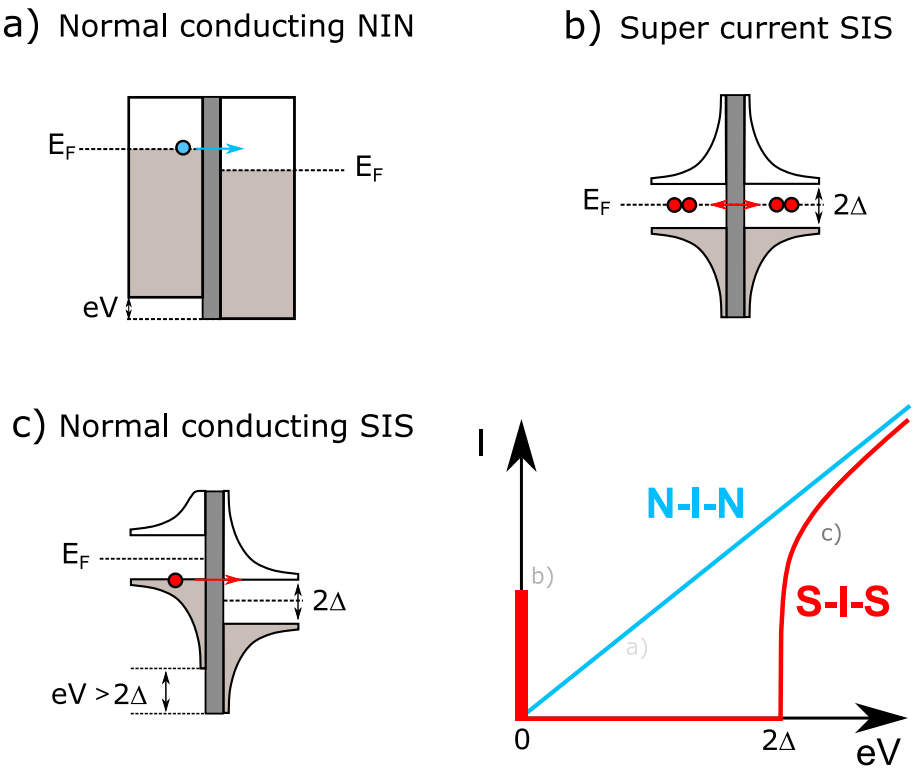

Figure 2.8: Illustration of the band-diagrams and I-V curve for a SIS-tunnel junction in the normal conducting state (NIN) (a) and the superconducting state (SIS). In the super-conducting state the current is zero, except for the super current at zero bias (b), until the applied bias is larger than the superconducting energy gap $eV > 2\Delta$ and the I-V asymptotically approaches the I-V of the normal state.

is smaller than 2Δ, there are no available electronic states within the transport window, and DC transport is suppressed. This is lifted for biases that are larger than 2Δ, when the valence band on the left and the conduction band on the right finally align (see figure 2.8c). The I-V curve then jumps from zero to a finite value and asymptotically approaches the linear non-interacting regime of normal junctions for higher energies.

It is this very non-linear I-V profile of the SIS-junction that allows it to be used as a quantum spectrum analyser exploiting PAT effects. When the junction is biased within the gap ($0 < eV_{bias} < 2\Delta$) electron transport is only possible if the junction is provided the missing energy by photon absorption of frequency ν that comes from the environment. This way one can detect the emission noise as an increase in the current within the gap $h\nu > 2\Delta - eV_{bias}$ (see figure 2.9). Fortunately it is also possible to measure the absorption noise of the environment when the junction is at biases for which $h\nu > 2\Delta + eV_{bias}$. The situation is reversed and tunneling electrons can emit their excess energy as photons by inelastic scattering. The absorption noise is then observable as a reduction, with respect to the case without irradiation, of the electrical current in the interval of $[2\Delta, 2\Delta + h\nu]$ where electrons do not have sufficient energy to excite the environment.

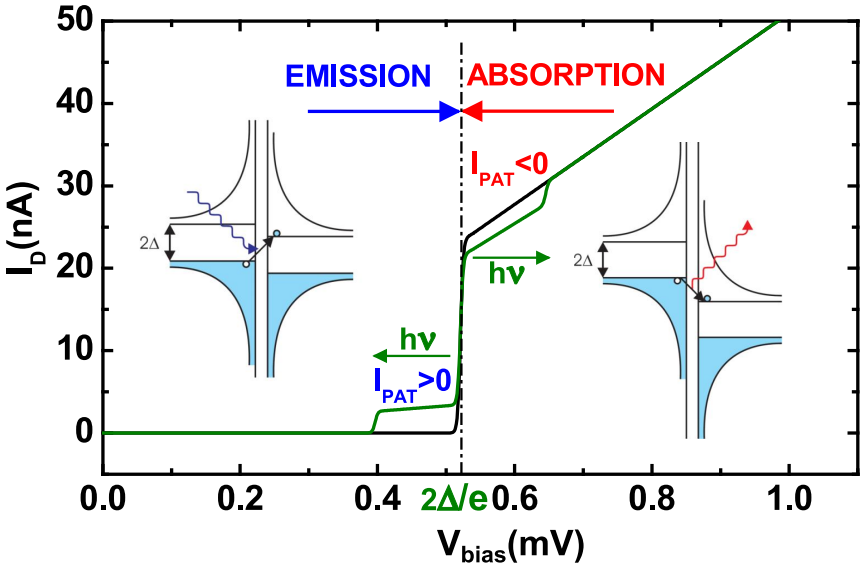

Figure 2.9: I(V)-curve of a SIS junction without (black) and with a noisy environment (green) that includes the increase in current due to PAT events. The PAT current is obtainable as difference of the two curves, taken from [129]. Below the gap $V_{bias} < 2\Delta/e$ the junction is sensitive to emission noise and to absorption noise when $V_{bias} > 2\Delta/e$.

The SIS junction is thus able to individually detect the imprints of specific energy exchange processes with an environment on its I(V)-curve, depending on its biasing condition. While for low voltage biases ($V_{bias} < 2\Delta$) the junction is only sensitive to emission noise, it measures a combination of emission and absorption for $V_{bias} > 2\Delta$, that can be disentangled in principle, by subtracting the emission noise as measured within the gap, in order to obtain the absorption noise.
The first experimental implementation of a SIS junction as a QSA was performed in Leo Kouwenhoven's lab [49], where the authors report on several experiments where the SIS detector detects the emission spectra of another SIS junction operated both in the AC Josephson regime and in the dissipative regime. They also present an experiment where the source is a Cooper pair box. Notably, this experiment established that the high frequency emission noise of a tunnel junction is indeed $S_I(f) = eI$ and not the symmetrized $S_I(f) = 2eI$. Easy to fabricate and operate, SIS junctions have proven to be versatile QSA by detecting the noise emitted from many different sources. Probed systems range from metallic sources such as in [49, 51, 52, 54, 55], but also semiconducting based circuits [136, 137]. Thus such detectors have revealed many physical effects such as electron bunching effects in electron co-tunneling in quantum dots [130], high frequency dynamics of the Kondo ridge [136] or the competition between superconductivity and Kondo physics in a proximitized carbon nanotube [137].
SIS detectors have proven to measure not only the emission noise, but also the absorption noise. Indeed, in Richard Deblock's lab, quantitative experiments with an SIS

detector where made [54, 55] measuring the high frequency emission and absorption noise of an electromagnetic linear oscillator, clearly following the non-symmetrized prediction of Callen-Welton noise. However, when aiming at measuring the absorption noise of non-equilibrium quantum conductors [51, 52, 54] the circuits used introduced to much detection back-action prohibiting to extract quantitatively the absorption noise. The reason for this is that when biased under the gap, the SIS junction behaves essentially as a silent (infinite impedance and noise-less) detector, so that emission noise can be quantitatively measured. However, when aiming at measuring the absorption noise, the detector must be biased above the gap giving rise to finite fluctuations (arising from the finite admittance and the finite emission noise). Thus in a symmetrically coupled scheme, where source and detector have similar impedances and the coupling transimpedances are symmetric as well, the detector gives rise to a measurement back-action imprinting PAT effects on the source, thus modifying the noise to be measured.

2.4 Summary

In this section we have introduced the fundamental principles of quantum detectors for a quantitative measurement of the asymmetric absorption and emission noise of a quantum conductor coupled to an environment. We have introduced the concepts and schemes implementing direct noise power measurements and photo assisted transport detection. While emission noise has been measured efficiently in both schemes, only SIS based PAT detectors have been exploited to measure absorption noise. However, the implemented schemes gave too much detection back-action when coupled to non-linear quantum conductors driven out-of-equilibrium, prohibiting to extract their absorption noise quantitatively. In the following chapter we describe the first implementation of the Lesovik & Loosen scheme [23], where both the emission and absorption noise of quantum conductor can be extracted by measuring the power exchanged with a linear environment having a tunable population.
We thus want to apply this concept to create a detection setup, using a bulk commercial RF filter, to measure the emission and absorption noise of a sample. The creation and experimental test of this detection scheme are presented in the following chapter 3.

Chapter 3

Measurement of emission and absorption noise

As introduced in chapter 1, the power spectral density of current fluctuations flowing through a quantum conductor is different at positive (absorption noise) and negative (emission noise) frequencies, this difference is linked by Kubo's formula (Equation 1.23) to the real part of the conductor's admittance. Most attempts aiming at measuring separately the absorption and emission noise of a non-linear conductor driven out of equilibrium were based on exploiting photon-assisted transport effects [48–52, 54, 55, 130], thus imprinting the current fluctuations spectra to be measured on the I-V curve of a non-linear conductor.
Here instead, we follow directly the proposal of Lesovik & Loosen [23], and implement a different experimental approach: We simply measure the electromagnetic power exchanged between a quantum conductor and a low impedance radio frequency linear resonator whose occupation number can be externally tuned. The idea being that an empty resonator can only absorb power, and thus couples to emission noise, while a finite population of it couples unequally to the emission and absorption noise of the junction. A careful calibration of the population of the resonator thus allows extracting both quantities from power exchange measurements at different populations.
A benefit of the implemented setup is that it generates negligible back-action, thus enabling for the first time a quantitative measurement of the absorption noise of a non-linear active conductor. Such setup allows as well to perform phase sensitive reflectometry measurements with a vector network analyser, giving access to the admittance of the conductor. We could thus independently measure the three physical quantities linked by Kubo formula, and provide an experimental test of it for a non-linear system driven far from equilibrium.

Contents

3.1 Experimental setup

We want to measure the power exchanged between a quantum conductor and a radio frequency resonator in a regime where the emission and absorption noise of the conductor are simply related to these energy exchanges (see Chapter 2). We chose a SIS junction made from thin layers of aluminium as a test quantum conductor, since it is a genuine non-linear conductor that we could easily fabricate within the lab's clean-room.

In practice, we used a SQUID geometry so that we could frustrate the supercurrent flowing through the junction and couple only to the non-linear dynamics of the quasiparticle excitations. Constraints on the electrical properties of the junctions are firstly given by the simple link between exchanged power and noise, as predicted by Lesovik & Loosen, that only arises in the current source limit: thus we need the junction's resistance to be larger than the detection impedance $R_T \gg Z_{det}$. Secondly, by keeping the characteristic impedance of the detection scheme much smaller than R_K ($Z_{det} \ll R_K$) we ensure a negligible back-action in the QED coupling from vacuum fluctuations, DCB or PAT of the resonator at finite population. However, as the emitted power scales with Z_{det}/R_T one needs a compromise: We chose the parameters R_T about $6\,\mathrm{k}\Omega$ and $Z_{det} = 50\,\Omega$, fulfilling both earlier requirements at the % level. The advantage of having $Z_{det} = 50\,\Omega$ is to make use of commercial elements to define the RF environment: we used a cavity filter, centred at 6.8 GHz ($hf_0/e = 28\,\mu\mathrm{V}$) with a flat 600 MHz bandwidth.

The photon occupation of this resonator can be tuned by the noise power emission of a noise generator, a NIN junction, that is converted from a SIS junction that is physically attached to a permanent magnet on the backside of the chip. The magnetic field is stronger than the critical magnetic field of the superconducting state, rendering the junction normal. The junction is also chosen to have a low impedance, close to the detection impedance, in order minimize both the Joule heating and the RF signal reflection towards the resonator. When the NIN junction is DC-biased, it generates a shot noise signal whose power emission increases with the applied bias and can be used to control the amount of photons present in the resonator. Depending on

the population of the resonator, it will be possible to observe a different interaction between the SIS junction and the resonator that will be imprinted in the exchanged power when we DC-bias the SIS junction (Equation 2.8).

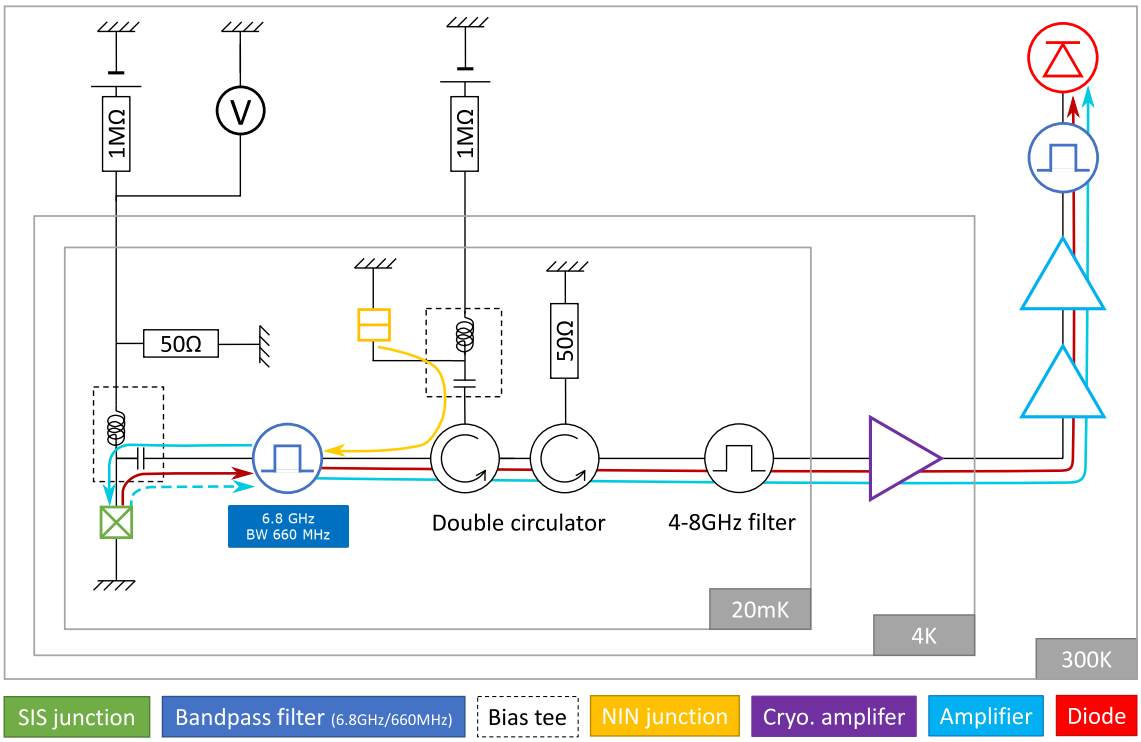

Figure 3.1: Block diagram of the DC-biasing and RF-detection setup for the exchange power measurement between a SIS junction and a linear resonator within our dilution refrigerator. The emission and absorption noise signals are indicated as red and cyan coloured arrows. The corresponding photonic occupation of the resonator is adjusted with the noise power (yellow arrow) that is generated from a DC-biased NIN junction. The DC-biasing signals for NIN and SIS junction are separated from the AC measurement signals via bias tees that guide the RF signal along our detection line including several amplifiers and a rectifying diode. DC-voltage measurements of the SIS junction are done in a three wire configuration.

To measure the power exchanged in the coupled band, we are using an RF-measurement setup as shown in figure 3.1. Both junctions are mounted at the low temperature stage (12-15 mK) of a dilution refrigerator and connected to the RF- measurement setup at room temperature via co-axial cables. The SIS junction is placed inside a superconducting magnet that enables us to apply a small flux to tune the Jospehson coupling of a SQUID and to apply larger fields to make the electrodes transit to the normal conducting state.
Both junctions are biased via a bias tee, which has an inductive branch, that is only passable for DC signals, and a capacitive branch (high frequency pass) that only allows RF signals to pass. Its purpose is thus to have a specialized circuit for the DC bias of the junctions and a separated specialized circuit for the RF detection coupled

to the capacitive port. The DC biasing line for the SIS junction includes a DC voltage source and a 1 MΩ polarizing impedance connected via the inductive (low frequency pass) port of a bias tee. The polarizing impedance converts the voltage signal to a current bias so that thermoelectric fluctuations of the voltage can be avoided that would be of the order of μV at the junction. This well-defined polarization current is the re-transformed into a voltage bias, via a 50 Ω shunting resistor, because in its superconducting state the junction does not conduct electronic currents unless the applied bias is larger than the energy gap $2\,\Delta$. The DC biasing line for the NIN junction is a simple current bias with a voltage source and a 1 MΩ polarizing impedance at room temperature via the inductive port of a bias tee to ground.
The NIN's noise signal is guided through the capacitive port of the bias-tee into the main RF-measurement line and directed to the resonator by a circulator. A second circulator in series dissipates the radiation coming from the HEMT noise into a 50 Ω matched resistor and replaces it with the black body radiation at the temperature of the matched resistor. Since the NIN junction is close to 50 Ω as well, it provides an additional stage of isolation as well. The noise signal emitted from the NIN junction increases the photonic occupation of the resonator coupled to the SIS junction. When DC biasing the SIS junction, it can absorb some of energy present in the resonator, or emit into it. This exchanged power signal is guided through the circulators into the amplification chain and measurement setup. It consists of a bandpass filter (4-8 GHz), that reflects noise out of the band for which the RF elements (circulators, amplifier, etc.) are specified, at the low temperature stage and a cryogenic pre-amplifier at the 4 K stage. The signal is further amplified at room temperature by two low noise amplifiers and again filtered with a band pass filter, nominally identical to the cavity filter used to define the resonator seen by the SIS junction. The signal is then rectified by a diode and the converted DC voltage signal is recorded. This recorded signal is proportional to the exchanged power but includes a signal modification due to the amplifier gain and any additional amplification or attenuation of the detection line. In order to retrieve the exact exchanged power values it is necessary to determine the proportionality constant via a calibration measurement for the setup.

3.1.1 Tunneling junction fabrication and characterization

The used SIS-junction(s) are Al-Al_2O_3-Al junctions in different designs. For the NIN-junction we use a single junction with a normal state impedance of 40.2 Ω while the SIS junction is a SQUID made from two junctions in parallel. Both are fabricated on SiO/Si substrates by e-beam lithography and angle evaporation techniques[1]. To create the mask for the deposition of the conductor, a 800 nm thick PMMA resist layer is exposed with the e-beam to define a 100 nm thin suspended PMMA bridge which will create a gap within the deposited metal strips. This resist mask is then used for a multi-layer physical vapour deposition: The first deposition of the 30 nm Al bottom layer creates a gapped conductor that is statically oxidized in the second step. Exposing the layer to 50 μbar Ar/O_2 for 10 min creates a surface oxide layer

[1] All junctions were fabricated by Z. Iftikhar

of $\simeq$1 nm thickness. Before adding a second aluminium layer of 60 nm, the sample is rotated by an angle of 30 degrees. This deposition angle effectively shifts the position of the top layer so that the conductor gap is covered. The newly created overlap creates the SIS junction on one side.

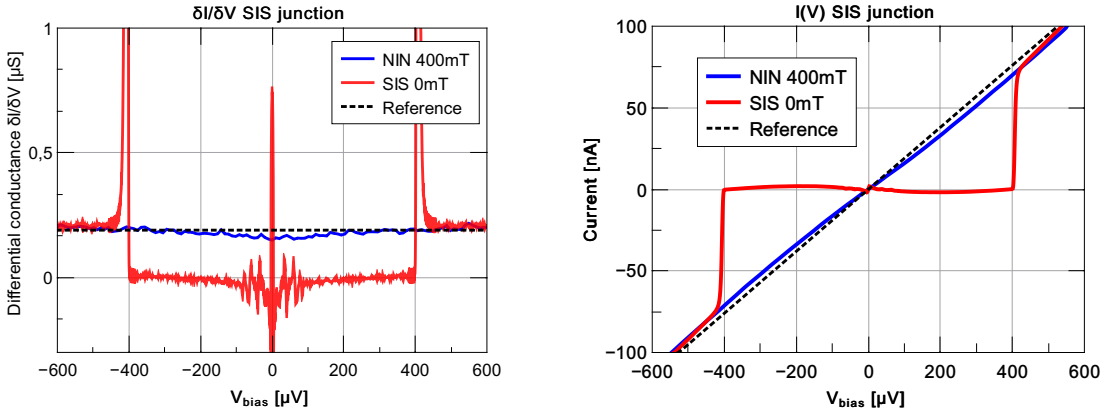

(a) (b)

Figure 3.2: (a) Plot of the measured differential conductance for an aluminium tunnel junction in the normal conducting state (400 mT, blue) and the superconducting state (0 T, red). The SIS measurement has been corrected for the 50Ω parallel resistor. In both cases the differential conductance shows a non-zero slope for increasing bias voltages we presume due to heating up of the shunting resistor.; (b) I-V curve extracted from the numerical integration of the $\partial I/\partial V$ of the SIS-junction in the normal and superconducting state (blue and red). The black reference in both figures serves as a guide to the eye. A supercurrent peak is visible at zero bias and the transport gap threshold is found at $V_{bias} = \pm 400\,\mu$V.

To characterize the fabricated junctions we directly measure the resistance in the normal conducting regime as 6.1 kΩ at room-temperature with a 2-probe measurement. To measure its resistance in the superconducting regime it is mounted and cooled-down within the dilution refrigerator and measured using the electrical scheme of figure 3.1. We apply a current bias through the resistor and record the voltage bias across the parallel composition of the SIS junction and the 50 Ω shunting resistor and measure the differential conductance of the junction in both the normal- and superconducting state at sub-Kelvin temperature with a lock-in amplifier as voltage detector. The calculated resistances from the measurement data are plotted in figure 3.2a. The data for the normal conducting state is recorded with an applied magnetic field of 400 mT and 0 T in its superconducting state. The obtained results for the SIS-state were corrected for the 50 Ω parallel resistance that itself is extracted as the resistance read in the superconducting state when the bias is between 200 and 300 μV, when the SIS acts as an open circuit. We have to emphasize that this is not an accurate determination of the junction's DC properties, because the signal is highly shunted by the 50 Ω resistor. Thus any inaccuracy in the determination of its exact resistance will have a strong impact on the extracted tunneling resistance.

As shown in figure 3.2a, we observe the supercurrent peak at zero bias and an average zero conductance for the SIS junction within the gap $eV_{bias} < 2\Delta$ with some fluctuations around zero bias due to the coupling of the supercurrent to the electromagnetic environment. We find the transport gap $2\,\Delta$ at $400\,\mu$V, where the differential conductance peaks before falling off to the same constant value obtained in the normal state regime. In the normal conducting regime however, the measured resistance shows an unexpected non-monotonous behaviour where the resistance is slightly dips at low biases which can also be seen within the low bias fluctuations of the superconducting state. The cause is most probably a tiny variation of the shunting resistance value with the applied bias due to Joule heating. Indeed, no particular precautions were taken to thermalize the resistor even though the applied bias of $200\,\mu$V across the $50\,\Omega$ resistance yields a considerable Joule power of about 400 pW to be dissipated. The corresponding I(V) profile of the junction in its superconducting state was obtained by numerical integration of the $\partial I/\partial V$ data, as shown in figure 3.2b. The I-V curve confirms the same characteristic peaks and transitions at zero bias and $400\,\mu V$.

3.1.2 Calibration of the measurement

In order to quantitatively measure the exchanged power between SIS and the resonator one has to calibrate the measurement system first. A noise measurement without biasing the NIN or SIS junction yields the background noise that is emitted from operating the cryogenic amplifier $P_{noise} = P(V_{SIS} = 0, V_{NIN} = 0)$. We calibrate it via a $P_{noise}(T)$-curve that is recorded while changing temperature of the mixing chamber between 15 mK and 1 K (as shown in figure 3.3) and fitting it with the Callen-Welton noise formula. In this experimental setup we effectively measure the rms voltage noise power of a matched source, thus the noise is symmetrized as can be obtained form the added emission and absorption noise of equation 1.18:

$$\begin{aligned} P_{noise} &= S_I(f,T,V=0) + S_I(-f,T,V=0) \\ &= hf \cdot Re(Y(f))[(1+n_B(hf) + n_B(h|-f|) \\ &= 2hf \coth\left(\frac{hf}{2k_BT}\right) Re[Y(f)] \end{aligned} \tag{3.1}$$

Based on the fitting, we determine the background noise $P_{noise} = k_B T_N$ with an equivalent noise temperature of T_N =2.9 K.
Then we need to calibrate the attenuation of the RF lines used to measure the junctions. For this, we will use the well known high bias limit of current shot noise in the normal state [67]: We first bias the NIN junction, while the SIS junction is at zero bias and thus reflects all RF signals. We measure the power on top of the amplifier noise in this condition in order to calibrate the global gain between the NIN junction and the cryogenic amplifier. This power is given by equation 3.2, where we identify the emitted noise power ($\simeq (eV - hf_0)/2$), the RF transmission coefficient between the junction and the line $1 - \Gamma$, with Γ being the microwave reflection coefficient at the output of the junction 3.3, and an attenuation factor α due to insertion losses of the RF elements (bias tee, circulators, coaxial cables):

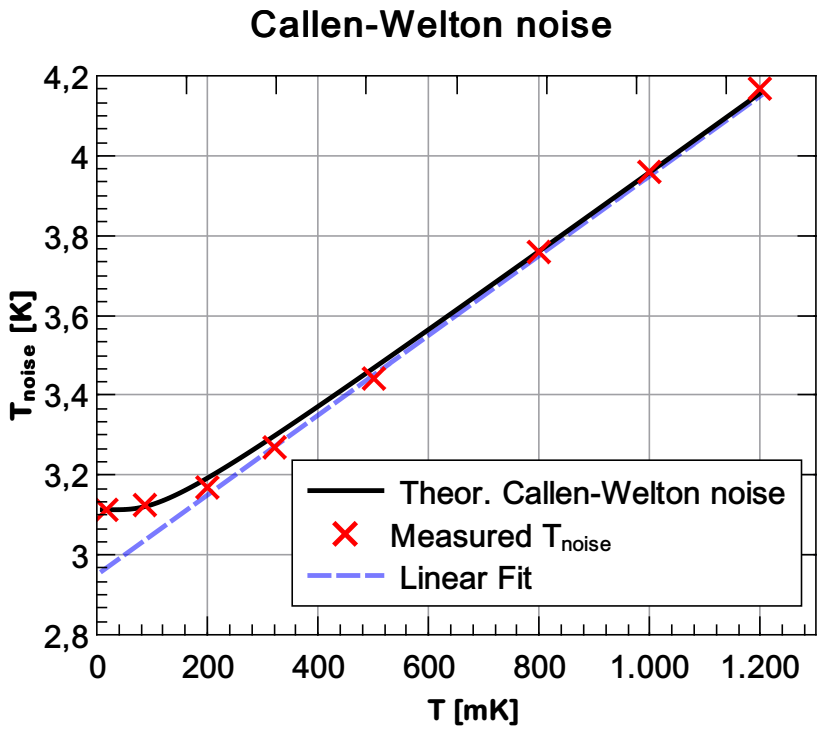

Figure 3.3: Calibration measurement of the noise power emission of the detection chain. The measured noise emission (red) is measured at temperatures of 18, 86, 200, 320, 500, 800, 1000 and 1200 mK and compared to the theoretical prediction (black) following the symmetrized Callen and Welton formula (see equation 3.1) with the noise transition found at $T = hf/(2k_BT) = 170\,\mathrm{mK}$. From the fitting of Callen and Welton plot, as well as from the linear fit of the measurement data (blue), we extract a noise temperature of around 2.9 K.

$$\frac{\delta P}{P_{noise}} = \alpha(1-\Gamma)\frac{eV - hf_0}{2}\frac{1}{k_B T_N}, \tag{3.2}$$

$$\Gamma = \left(\frac{Z_{NIN} - 50\Omega}{Z_{NIN} + 50\Omega}\right)^2 \tag{3.3}$$

For the NIN-junction, with its resistance of 40.2 Ω, Γ is 0.012, so that the last unknown variable, the attenuation α_{NIN}, can be determined from the measured power emission via equation 3.2. The obtain an attenuation $\alpha_{NIN} = 0.086$ in absolute value, corresponding to -10.66 dB, for the recorded data shown in figure 3.4a.
We repeated the same calibration for the SIS junction in its normal conducting state at an applied magnetic field of 200 mT with zero applied bias for the NIN junction (see figure 3.4b). This high impedance junction, $R_n = 6.1\,\mathrm{k}\Omega$, gives a larger reflection coefficient of $\Gamma = 0.968$ and thus we obtain an attenuation α_{SIS} of 0.35 in absolute value equal to -4.56 dB. The relative difference in attenuation for the SIS and NIN junction of about 6 dB originates mostly from our measurements setup: The calibration signal of the NIN has to travel an additional distance to the SIS where it is reflected and

then sent to the detector. Hence it is to be expected that the attenuation is roughly doubled for the NIN.
We also compare both calibration measurement to a theoretical plot of the shot noise, driven by a DC bias, to determine the electronic temperature. We obtain a good agreement with the measurement by fitting an electronic temperature of 30 mK, while the mixing chamber plate is at about 20 mK (see the red curves in figure 3.4a) and b)).

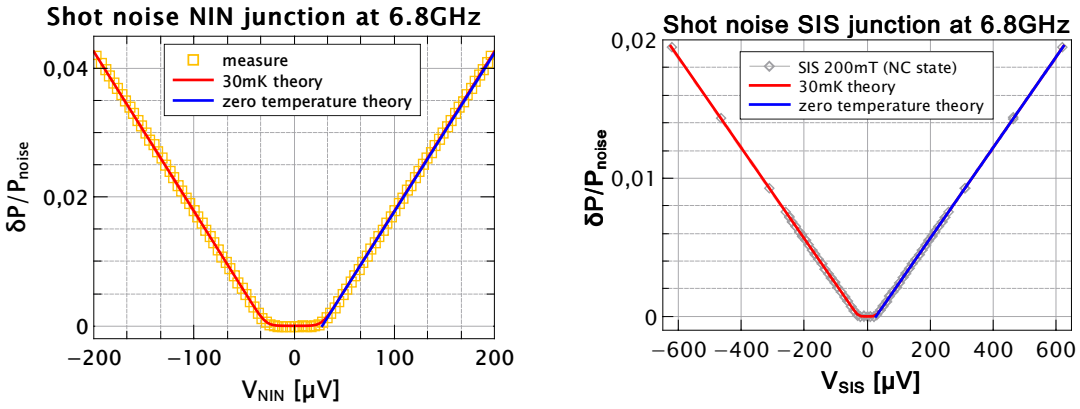

(a) (b)

Figure 3.4: Calibration measurement of the noise power emission of the NIN junction (a) and the SIS junction (normal and superconducting in b) as normalized by the amplifier noise temperature. The drift of the amplifiers was corrected by subtracting a zero bias measurement for every point taken. The measurement data is modelled theoretically to determine the electronic temperature (red curve) and for reference for the zero temperature case (blue curve). The intercept of the zero temperature fit gives $eV = hf_0$, thus validating the value of the polarization resistance used to determine the applied bias.

3.2 Measurement of emission and absorption noise

With both junctions calibrated, we can now start our measurement. The magnetic field is set close to zero in order to smooth the back-bending of the SIS junction dynamics observed at biases close to $eV = 2\Delta$. The large currents arising at the transport gap transition generate a depairing that decreases the size of the gap. This biasing instability close to the sharp non-linearity is observable as a negative dV/dI. To remove this effect, a small yet finite perpendicular magnetic field is required, giving some finite depairing and thus smoothing the features around 2Δ. The field value is chosen to smooth on the scale of $< hf_0$ so that the differences between emission and absorption noise can still be observed as a sharp feature. Additionally, we finely tuned the finite field, making sure that the SQUID was frustrated, in order to minimize the Josephson features around zero bias.

We then measure the power emitted by the junction in the superconducting state, plotted in figure 3.4b for zero bias being applied to the NIN. We can observe two peaks at -14 and 14 μeV that arise from the AC-Josephson effect ($2eV = hf_0$), on top of a zero flat emission until the bias reaches $\pm 428\mu\text{eV} = \pm(2\Delta + hf_0)$. At this value the emitted power suddenly jumps and asymptotically approaches the power recorded in the normal conducting state for larger biases.

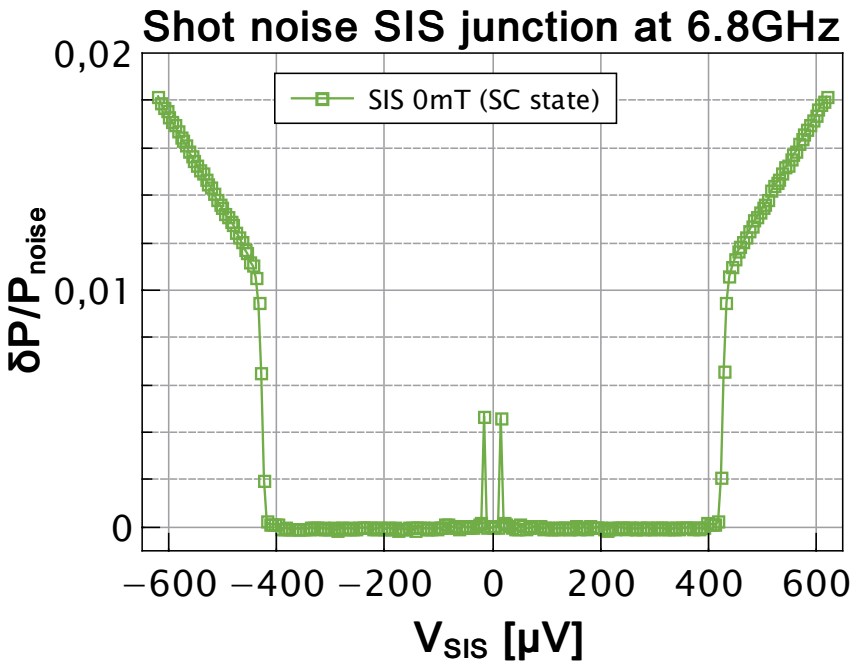

Figure 3.5: Plot of the emitted power of the SIS exhibiting its characteristic features that are shifted, due to the finite frequency of the measurement, as compared to the characterization measurement in shown in figure 3.2. We observe two peaks at $2eV = hf_0$, corresponding to the Josephson radiation, and a sudden increase of the emitted power at $2\Delta + hf_0$. The quasiparticles emit power when the bias surpasses the DC transport gap by more than hf_0.

This experiment was designed to access the quasi-particle dynamics (here at $2\Delta + hf_0$) but not to quantitatively study the domain of emissions caused by the Josephson effect. Thus we finely tuned the flux in the SQUID in order to minimize the Josephson effect contribution to the exchanged power which allows us to focus on the physics of the quasi-particle dynamics.
Under these conditions, we recorded the total power emitted from the junctions P(V_{SIS}, V_{NIN}) in addition to the amplifier noise P_{noise} =P($V_{SIS} = 0$, $V_{NIN} = 0$) and normalized by it in order to compensate temporal drifts of the detection chain gain:

$$\frac{\delta P}{P_{noise}} = \frac{P(V_{SIS}, V_{NIN}) - P_{noise}}{P_{noise}} \tag{3.4}$$

The data is presented figure 3.6 as a function of V_{SIS} for different values of V_{NIN}.

One sees, that indeed, the Jospehson peaks, observed in figure 3.5 at $V_{NIN} = 0$, are now barely visible and also that increasing V_{NIN} adds a power offset. Indeed, this offset is the plain NIN emission which follows the values measured in figure 3.4a. On top of this, a new feature appeared that is not visible at zero NIN bias: the power diminishes suddenly at $2\Delta - hf_0$, and then increases again at $2\Delta + hf_0$. The larger the NIN bias, the larger is this power depression.

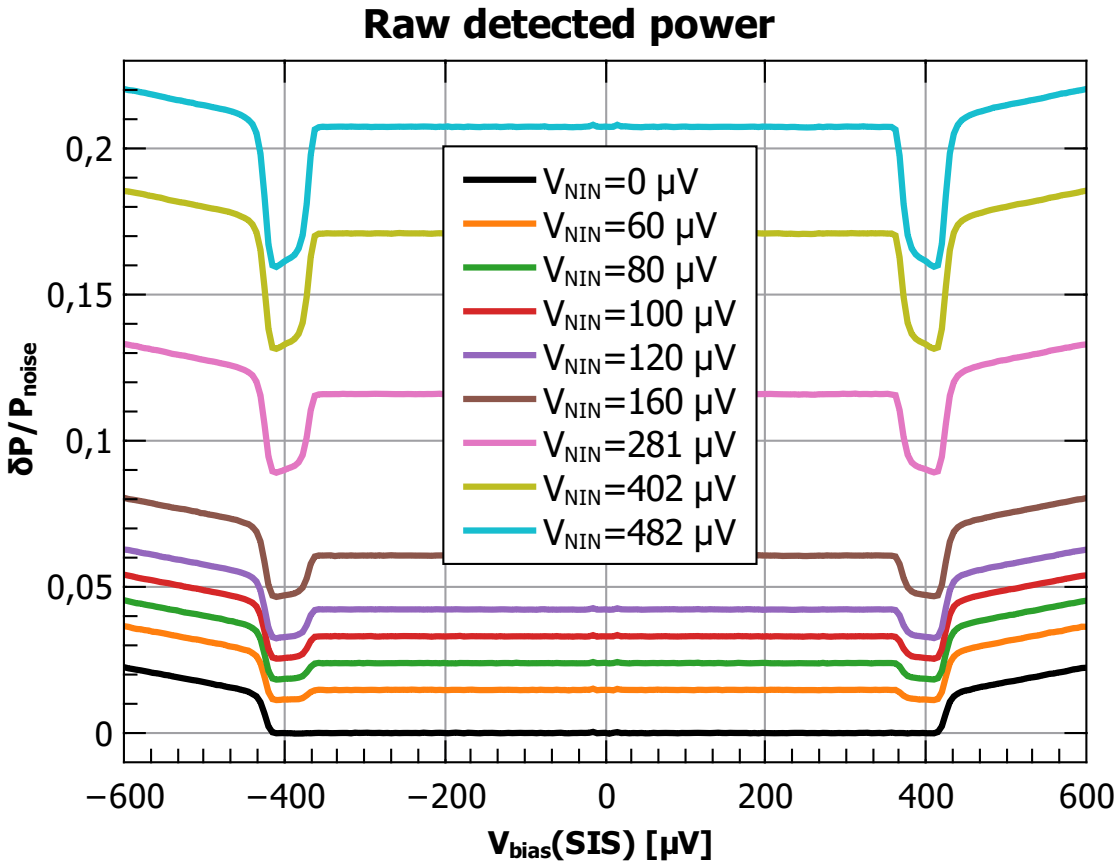

Figure 3.6: Plot of raw power measurement for different resonator occupation as controlled by the NIN bias voltage.

To see this new effect more clearly, we can remove the power offset, which corresponds to the power cost of providing the resonator with a finite population, by subtracting the power emission of the NIN-junction for the different biases. The obtained the exchanged power δP_{exch} is the amount of power exchanged between the SIS junction and the resonator held at a finite population:

$$\frac{\delta P_{exch}}{P_{noise}} = \frac{P(V_{SIS}, V_{NIN}) - P(0, V_{NIN})}{P_{noise}} \tag{3.5}$$

The plot of the exchanged power is shown in figure 3.7. The figure shows three regimes: The exchanged power is zero for biases smaller than $2\Delta - hf_0$. The exchanged power is negative for biases $2\Delta - hf_0 < eV < 2\Delta + hf_0$, meaning the SIS junction is extracting energy from the resonator in this regime. Finally, the exchanged power

becomes positive for biases larger than $2\Delta + hf_0$, meaning the SIS is sending energy to the resonator. Increasing the resonator population (increasing V_{NIN}), makes the absorption dip larger, while diminishing the net emitted power in the emission regime.

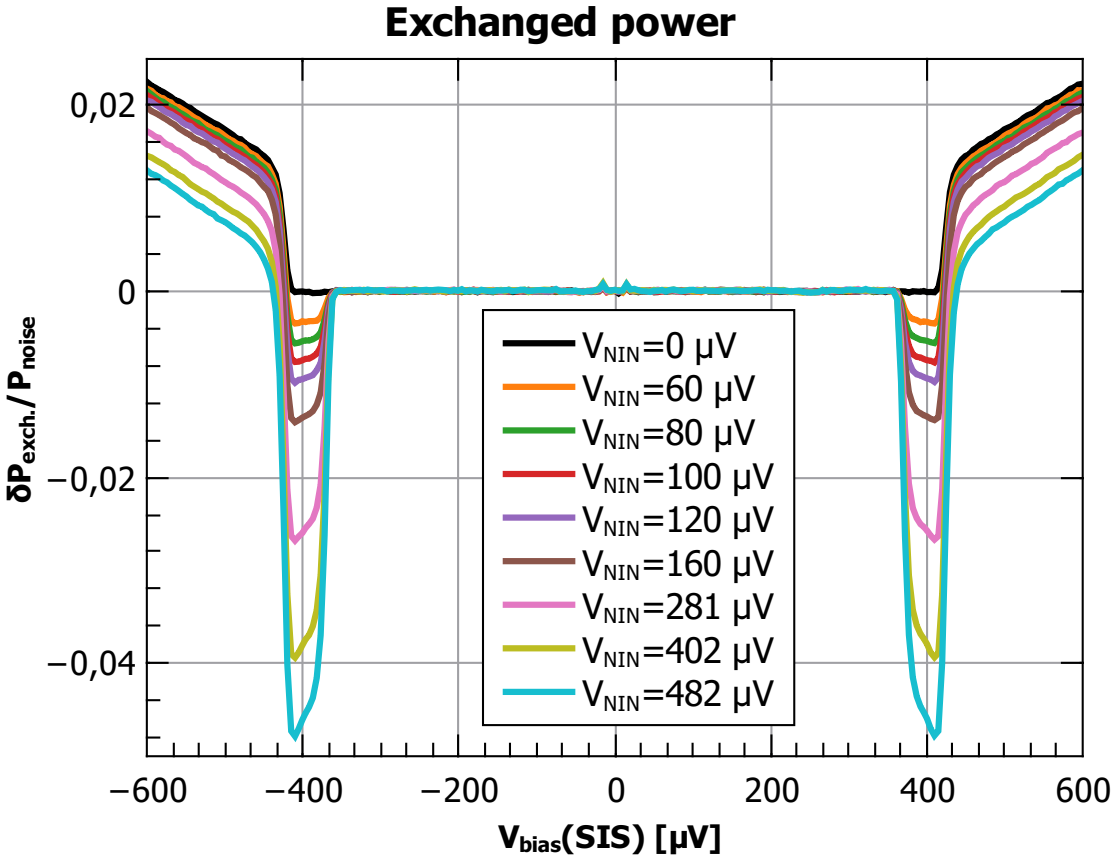

Figure 3.7: Plot of the exchanged power obtained from the raw power measurement data by subtracting the baseline power emission from the NIN junction that is used to populate the resonator with photons. It can be seen that a negative peak develops before the gap. This indicates the presence of absorption noise due to the finite photonic population of the resonator.

We can understand these features with the model of Lesovik and Loosen, generalized to a continuum in Mora et al. [56], the exchanged power per unit bandwidth reads:

$$\delta P_{exch.} = 2Re[Z(f)] \cdot [(1 + n_B(f))S^e(V_{SIS}, f) - n_B(f)S^a)] \tag{3.6}$$

We see that for a zero population resonator, the exchanged power is just proportional to the emission noise, which is indeed non-zero only for SIS biases larger than $2\Delta + hf_0$ ([54, 118]). At finite population photons can be absorbed by the junction with an absorption rate that is proportional to the occupation factor and the absorption noise. This explains why the absorption dip decreases with the NIN bias in the SIS bias window $[2\Delta - hf_0, 2\Delta + hf_0]$, where only the absorption noise is non-zero. Finally, at biases larger than $2\Delta + hf_0$, the exchanged power is decreased by a factor proportional

to the occupation as well, explaining why the emitted noise diminishes with the NIN bias.
We can separate the emission and absorption contributions based on the exchanged power description following equation 3.6. While S^e can be directly extracted from the exchanged power measurement at zero population ($(n_B = 0)$):

$$S^e = \delta P_{exch.}(V_{SIS}, V_{NIN} = 0)/2Re[Z(f_0)] \equiv P_0/2Re[Z(f_0)], \tag{3.7}$$

extracting the absorption noise requires the knowledge of the occupation of the resonator:

$$S^a = \frac{-\delta P_{exch.}(V_{SIS}, V_{NIN}) - (1 + n_B)P_0}{2Re[Z(f_0)]n_B} \tag{3.8}$$

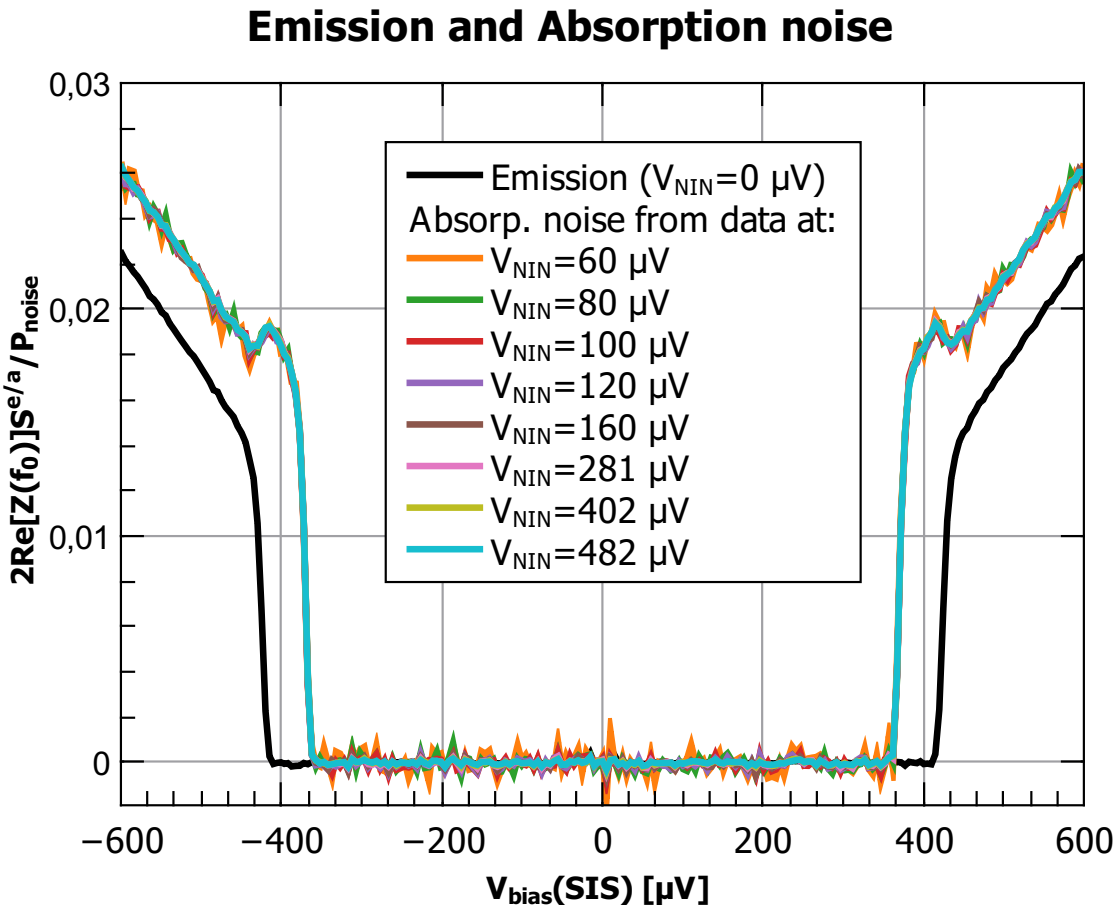

Figure 3.8: Comparison of the measured emission noise of a SIS junction as recorded for zero occupation of the resonator (black) and the calculated absorption noise from measurements with finite occupation using a simple calibration scheme for predicting the occupation of the resonator.

The amount of photons provided by the NIN is calculated as the ratio of the total power emission and the quantum of the resonator energy:

$$n_B = \frac{\alpha_{Coupling} P_{NIN,shotnoise}}{hf_0} = \frac{e \cdot V_{NIN} - hf_0}{2} \cdot \frac{1}{hf_0} \cdot \alpha_{Coupling}, \tag{3.9}$$

where the power emission is taken from our calibration measurement including the matching conditions and the coupling $\alpha_{Coupling}$ that accounts for the losses between the NIN junction and the SIS junction. Should there be no spurious reflection by any element, it should simply be $\alpha_{NIN}/\alpha_{SIS} = 0.246$. By inserting this occupation number into equation 3.8, the absorption noise for all measurements with different NIN bias can be calculated as shown in figure 3.8 with the coupling defined this way.

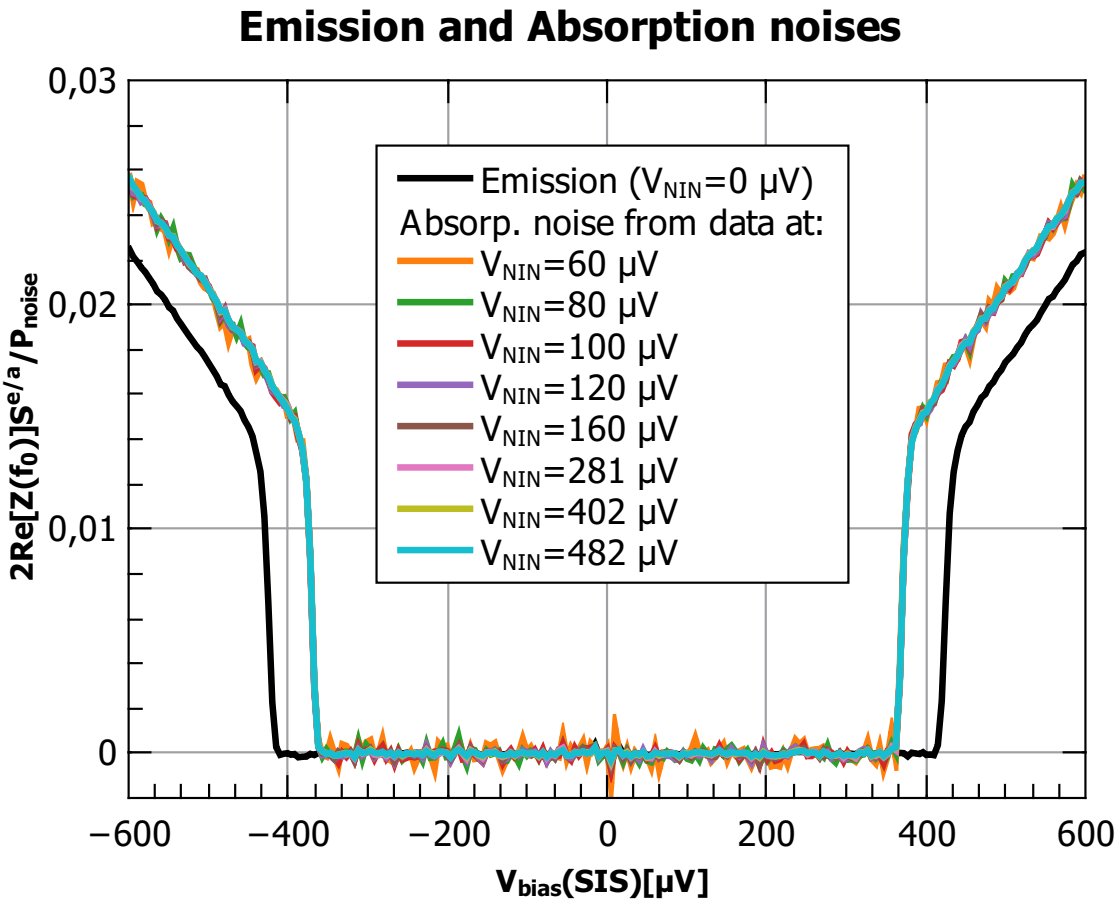

Figure 3.9: Measured emission (black) and absorption noise as measured for different occupation of the resonator. The absorption noise data has been corrected as compared to figure 3.8 by correcting for the spurious reflections of the measurement by an additional calibration.

The plot shows an unexpected bump: it result from an imperfect calibration because there are reflections in the path between the NIN and the SIS junction. Calibrating this spurious reflection requires an additional calibration step. The path that is described by α_{SIS} is split into two parts: one that is never reaching the SIS junction, it is thus free of spurious reflections, and another part that is connected to the SIS. Only the later part contributes to the occupation of the resonator. In order

to calibrate these two paths, one needs to input additional information: we assume the SIS junction to be fully reflecting the incoming radiation at $V_{SIS} = 0$, and we assume that it reflects it with a RF reflection coefficient given by the normal state resistance: $(R_n - 50\Omega)/(R_n + 50\Omega)$ in the large bias regime for $eV \gg 2\Delta$. We then obtain $\alpha_{Coupling}$ =0.222. Unfortunately this calibration is not sufficient to provide the necessary corrections. To fully remove the bump it was necessary to manually tweak the resonator populations by subtracting a linear-bias-dependent resistance from the 50 Ω resistors that are DC shunting the junction. With an applied correction of 13%, the absorption noise and the emission noise measurements are obtained as shown in figure 3.9. All absorption noise measurements collapse on to one another, showing that the absorption noise is independent of the NIN-power. In consequence, the SIS dynamics are not modified by the finite occupation of the resonator so that our measurement has no measurable PAT back-action effect. While the emission noise is only finite for biases $2\Delta + hf_0$, we see that the absorption noise is finite for biases larger than $2\Delta - hf_0$ [118, 138]. One curve can be recovered from the other upon a sis bias translation of $2hf_0$. We have thus shown that it is possible to separately measure the emission and absorption noise of a non-linear conductor driven far from equilibrium by detecting the power it exchanges with an electromagnetic resonator with a finite population close to zero.

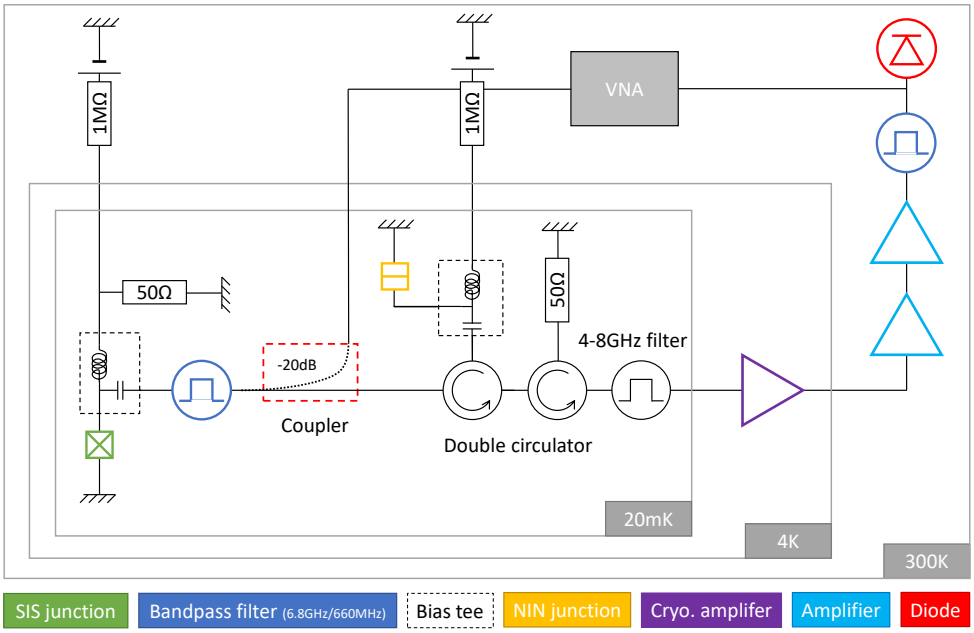

Figure 3.10: Block diagram of the modified experimental setup for the measurement of the admittance. The VNA detection port is directly connected to the detection chain output at room temperature while its output port is routed to the sample via a heavily attenuated dedicated line and a -20 dB coupler inserted in the measurement line, in between the cavity filter and the circulators.

3.3 Experimental closure of the Kubo relation

The Kubo relation [19] states a direct correspondence of the difference of absorption and emission noise to the conductor's admittance:

$$S^a(f) - S^e(f) = 2hf \cdot Re[Y_{emitter}(f)] \tag{3.10}$$

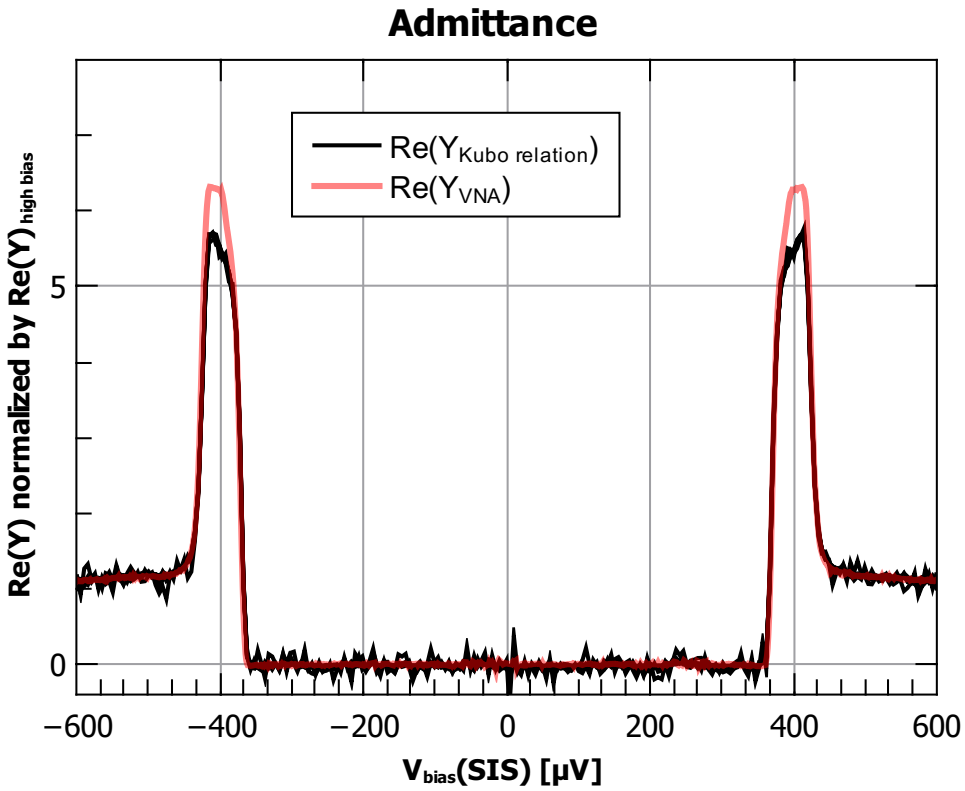

Figure 3.11: Comparison of the calculated admittance of the SIS junction using the Kubo formula, based on the measured emission and absorption noises, (black) and the admittance obtained from a linear response measurement using a vector network analyser (red). All admittance values have been normalized using their high bias value.

We can thus directly calculate the admittance of the junction using the measurement data for the emission and absorption noise. However, to directly test the validity of this formula, it is necessary to have a direct measurement of the admittance as well. Therefore we add a vectorial network analyser (VNA) to our measurement scheme, that is connected to the detection line and to the amplified signal output via a directional coupler (see figure 3.10).
This scheme enables the phase sensitive measurement of the reflection coefficient between the SIS junction and the 50 Ω transmission line. From this coefficient, we extract the real and imaginary parts of the SIS junction admittance. In order to make this measurement quantitative, we need to calibrate for the amplitude and the phase of the measured signal. For this we assume the SIS junction reflection coefficient at

zero bias is a specular reflection $\Gamma_{SIS}(V_{SIS} = 0) = -1$, and we assume the reflection coefficient in the large bias limit $eV \gg 2\Delta$ is given by the normal state resistance. We show in figure 3.11 the admittance as derived using Kubo formula on the incoherent emission and absorption noise measurements, and as measured from a phase sensitive linear response measurement. We find an agreement within 10% which is rather satisfactory given the complexity of the RF chain to calibrate. We thus validate Kubo relation for a non-linear conductor driven far from equilibrium.

3.4 Comparison to microscopic predictions

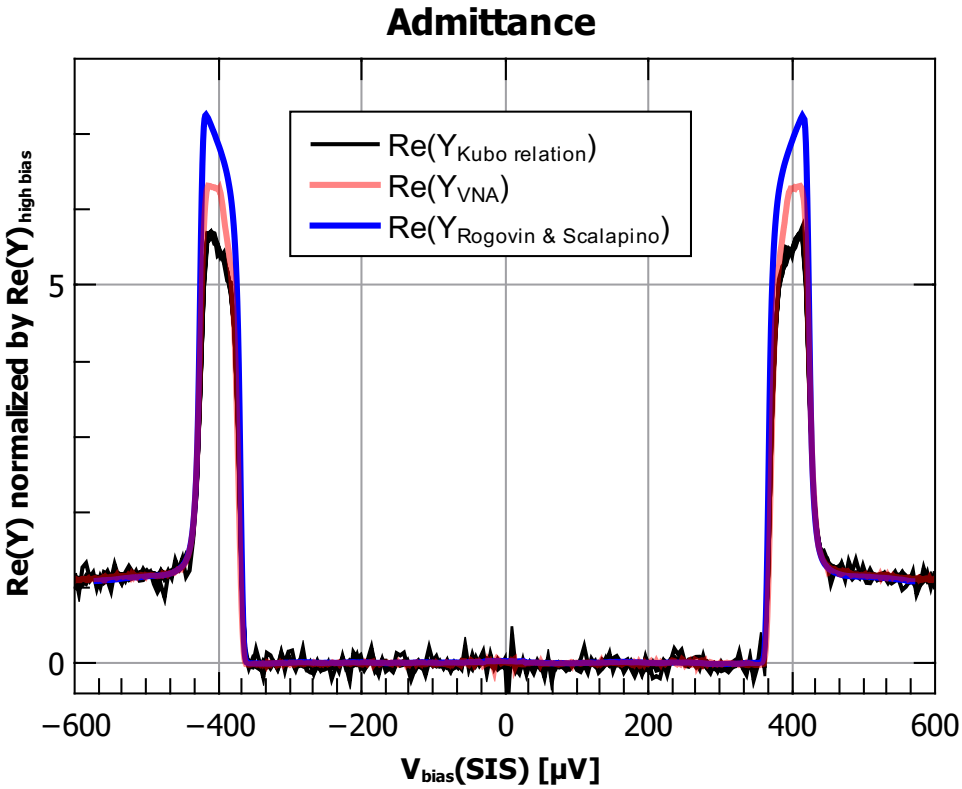

Figure 3.12: Calculated admittance of the SIS junction, based on the Kubo formula using the measured absorption and emission noise (black), compared to the admittance obtained from a direct VNA measurement (red) and the calculated admittance from the Rogovin and Scalapino formalism from the DC differential conductance measurement with a Lock-in amplifier (blue). All admittance values have been normalized using their high bias value.

For the sake of completeness, we now compare the different measured quantities: S^a, S^e and $Re[Y(V, f)]$ to microscopic predictions. We make use of the Rogovin and Scalapino formalism [118], which links all these quantities to the DC-I(V) curve:

$$Re[Y(V, f)] = e(I(V + hf/e) - I(V - hf/e))/2hf \tag{3.11}$$

$$S^a(V,f) = eI(V + hf/e) \tag{3.12}$$

$$S^e(V,f) = eI(V - hf/e), \tag{3.13}$$

where the shown equation for the emission noise (equation 3.13) is only valid if $2\Delta \gg k_B T, hf$, otherwise it has an additional temperature dependence.
The obtained admittance through equation 3.11 is plotted together with the previous admittance curves in figure 3.12. For all three methods the same average admittance is recorded for biases below and above the transition. Accordingly, the gap and the feature around the transition have the same position and width. The only visible difference between the graphs is the magnitude of the admittance and minor differences in the shape of the peak, for which the VNA measurement shows a rounder head than the very similar and sharp results of the measurement and the RS-calculation. With the measurements agreeing so well for the most part, it is assumed that the magnitude deviations are causes by minor deviations of the attenuation between measurement and VNA reference. A similar assumption is made for the used I(V) data, for which the attenuation at low frequencies may be less, so that the shown magnitude is over-exaggerated. Hence the comparison of magnitudes is not conclusive. But based on the otherwise perfect alignment of the feature we can infer that all methods are in good agreement

3.5 Conclusion

We have performed several experiments by measuring the power exchanged between a quantum conductor and an electromagnetic mode whose photon occupation number n_B is externally tuned close to vacuum. Doing so we are able to couple to emission noise S^e when the resonator is in its ground state and to couple unequally to the emission and absorption noise while the population is finite. Both quantities could be obtained from the measurements after calibration of the system.
This technique, as demonstrated for a SIS junction with a tunneling resistance of few kΩ and a cavity filter as detector, connected a 50 Ω detection scheme, showed neither DCB nor PAT back-action effects. We have thus proven it to be a back-action free measurement scheme that can be applied to any other mesoscopic conductor.
Performing a phase sensitive linear response measurement of the conductor, we could validate Kubo relation equating the difference between absorption and emission noise to the real part of the admittance. Doing so we provide the first experimental closure of the Kubo relation for a non-linear quantum conductor[2] that, as demonstrated for a non-linear conductor driven far from equilibrium, also stresses the generality of this relation.
We applied this experimental protocol to a SIS tunnel junction, and found the measured quantities can be constructed, within our experimental accuracy, from the independently measured I-V curve in agreement with the microscopic theory of Rogovin

[2]The experimental test for a linear conductor was already presented in [54]

& Scalapino of quantum tunneling through a single barrier. The method only relies in standard RF circuits and protocols, and can be used straightforward to characterize the non-equilibrium dynamics more complex quantum conductors.

Part II

Towards the measurements of time dependent RF-fluctuations in high magnetic fields

Chapter 4

Interaction effects in single electron channels

In order to understand the fundamentals of the quantum laws governing electronic transport phenomena one has to understand the basic building block of mesoscopic electrical circuits, the single electronic channel. A single electronic channel can be realized within state-of the art mesoscopic conductors like a QPC where the single channel is defined by an electro-statically defined constriction within the 2DEG of a semiconducting hetero-structure. This channel's transport properties, as introduced for non interacting electrons in section 1.1, will be modified when electronic interactions cannot be neglected. The simplest example occurs when placing a single electronic channel in an electrical circuit that includes a high impedance electromagnetic environment leads to the observation of the dynamical Coulomb blockade effect (DCB). The DCB effect is a charging effect that reduces the channel's conductance when strongly coupled to a dissipative environment. So far DCB effects are mostly well understood in the tunneling (low transparency) limit [44, 72], but a full understanding for channels with finite transmission is still missing. Even though (equilibrium) exact results from quantum field theory have shed new light in the particular case of a single channel QPC coupled to a an electromagnetic continuum (a resistor) [3,13,46,141], no predictions exist for the very building block of such dissipative circuit electrodynamics: a single channel interacting with a single mode. Because of this it is of interest to experimentally investigate the DCB effect resulting from the interaction of a single electronic channel with a high impedance electromagnetic mode.

Besides the aforementioned DCB effects arising from the interaction with an external circuit, local interactions can also dramatically modify the transport properties of single electron channels. For example, in the Quantum Hall regime, when a strong perpendicular magnetic field is applied to the 2DEG, one can tune the system to exhibit the fractional quantum Hall effect. There, the current is carried by strongly correlated 1D channels [142, 143] that exhibit non-Fermi liquid features like carrying fractional charges for the simple Laughlin fractions [34], which makes them prototypes of Luttinger liquids, or possibly showing non-abelian physics for more complex fractions [144, 145]. Thus their transport properties are starkly different from those

introduced in section 4.1.1. Another regime of strongly correlated motion attainable in a spin degenerate single electron channels is the Kondo effect, where the channel interacts with a localized magnetic impurity.

This is usually done by putting two quantum point contacts in series, thus forming a quantum dot used to trap an electronic spin. This magnetic impurity is screened by the conduction electrons of the single channel leads that are attached to it and causes a hybridization of states. This tends to delocalize the fluid, which is in conflict with the charging effects tending to localize it. A critical behaviour arises from this competition giving rise to markedly non-Fermi liquid features [146, 147].
In this chapter we give a general overview of some interesting research domains concerning the interaction effects arising in single electronic channels. We will point out current progress and the related challenges that we aim to overcome with the design of a novel experimental platform aiming at efficiently measuring their finite frequency dynamics that we present in chapter 5.

Contents

4.1 Single electronic charging effects

4.1.1 Introduction to Coulomb blockade effects

When a quantum coherent conductor, like a tunnel junction for example, is placed in an electric circuit, we can observe a reduction of the low bias electrical conductance that is known as the environmental or dynamic Coulomb blockade. This single electron charging effect (SEC) arises in circuits having a small capacitance and thus a high charging energy:

$$E_C = \frac{e^2}{2C} \tag{4.1}$$

In order to observe single electron charging effects the thermal energy of the electrons must be smaller than the charging energy $E_C \gg k_B T$, otherwise thermal fluctuations blur-out the blockade effect. For example: the charging energy $e^2/2C$ is about $1\,\mathrm{K}\cdot k_B$ for a capacitance of C= 1 fF. Thus SEC effects can be observed in dilution refrigerators for circuits having capacitances in the few 10s of fF.
SEC effects are traditionally distinguished, depending on the mesoscopic system used, as either static, for systems where the charge is localized, or dynamic, when the discharging time of the capacitance is limited by an external dissipative circuit. These SEC effects are known as the static Coulomb blockade (SCB) and the later discovered dynamical Coulomb blockade (DCB). Historically the SCB that was found firstly in metallic films by Lambeir et al. [148] and Mostovetch & Vodar [149] in 1950, with a full description given by Gorter in 1951 [150]. However the investigation of the underlying effect began much later when the creation of a metallic island in between micro-fabricated tunnel junctions was firstly realized by Fulton and Dolan [151] in 1987. The availability of these easy to fabricate samples led to extensive research on the blockade effects that was also continued for more advanced structures like semiconducting dots and quantum dots in the following decades. It also led to the investigation of charging effects for single mesoscopic conductors in a circuit environment as was firstly investigated for tunnel junctions by Devoret et al. [9] and Geerligs et al. [10] in 1990, thus starting the research of the dynamical Coulomb blockade.

Before explaining the DCB effect and its current research progress, we will start with the more simply to apprehend static Coulomb blockade. When we assume a quantum dot formed by two tunnel junctions, it is essentially an electrostatic island made by two series capacitances defined by the insulating layer of the tunnel junctions, yet electrons can tunnel in and out via the tunneling effect. As the electronic charge of the island is discrete, one can regard a tunneling current as a series of single electronic tunneling events. When an electron is transferred to the island, it increases its charge by an elementary charge and the biasing source thus needs to provide the electrochemical work of the single electron charging energy of the island $E_C = e^2/2C_\Sigma$, with C_Σ the sum of capacitances from the island to ground. Otherwise, for low biases $eV_{bias} < e^2/2C_\Sigma$, the electron transfer is blocked. The observed conductance is zero which is known as the static Coulomb blockade.
It turns out that it is not even necessary to have an electrostatic island to block or reduce charge transport, indeed the dynamic Coulomb blockade (DCB) occurs when any mesoscopic conductor of finite transmission, for this example a NIN-junction, is placed in series with an electrical circuit having a finite dissipative admittance (see figure 4.1). If the conductor, that we represent as a normal tunneling element in parallel to its charging capacitance C, was in a perfect voltage biasing circuit (zero series impedance), the charge accumulated at the capacitor's plates after a tunneling event would immediately relax and not perturb the tunneling dynamics. If we now add a resistor with impedance $Z(f) \simeq R$ into the circuit environment, we introduce a finite life time $\tau_{RC} = RC$ for the electric influence field trapped within the plates of the capacitor. Whether the single electron charging energy is well defined with respect to this relaxation dynamics, depends on its corresponding energy

uncertainty $\delta E_{RC} = h/\tau_{RC}$. Thus single electron charging effects become relevant when $\delta E_{RC} < E_C$, which is the case when $R > h/e^2$. It results in a suppression of the electronic transport similar to the static Coulomb blockade in the ideal case of zero temperature and small biases. This qualitative picture given above yields the right order of magnitude of the resistance necessary to observe sizeable reduction of the conductance at small but finite temperature: the conductance is not fully suppressed and also increases with the applied bias until the charging energy is reached and the blockade is lifted [44, 152]. However, at zero temperature and bias voltage, the conductance is expected to vanish for any non-zero value of the series resistance
In order to obtain a better microscopic picture, it is useful to exploit the Caldeira & Legget [20] representation of linear dissipative circuits as an ensemble of electromagnetic modes which is equivalent to a series of LC-resonators. Thus a macroscopic resistor is an infinite chain of resonators with different frequencies so that the resistor is able to absorb photons at any energy. Within this picture, the DCB corresponds to inelastic tunneling, i.e. tunneling electrons may spontaneously emit a number of photons into their environment. We illustrate this in figure 4.1: In situation a), for a perfectly shunted tunnel junction, all electrons tunnel elastically. However in situation b), when a resistor is added in series, electrons may tunnel inelastically with their energy being dissipated into the environment as a photon. Case b) in return implies that electrons can not pass the junction unless they carry the necessary energy to emit the photon, so that the conductance diminishes at low biases (dark red dashed line in figure 4.1) and vanishes at low temperature (red solid line in figure 4.1).
When the circuit attached to the junction consists of a single resonator of frequency f, as shown in c), one can observe a similar suppression of the conductance that is also lifted for increasing bias voltages. Having only one resonator mode in the environment, inelastic processes are only possible if the electrons have energies that are multiples of the resonator's energy and thus the blockade release occurs step by step at bias values $eV = n \cdot hf$. Hence one can observe plateaus for electronic tunneling events with multiple photon emissions (see figure 4.1 (blue)). Yet again, as is the case for the resistor, the sharp step-profile is only obtainable close to zero temperature $k_B T \ll hf$. At finite temperature the steps will be smoothed by the thermal fluctuations.

4.1.2 DCB effect for arbitrary transmission

The dynamic Coulomb blockade is well understood for the tunnel junction or any conductor where all electronic channels have a very small probability to be transmitted through the conductor ($T_P \ll 1$) [44], the reason for this is that in this limit the junction can be treated as a Hamiltonian perturbation to the circuit. At finite transmission however, there is no general theory that enables a prediction of the dynamics of an arbitrary quantum conductor embedded in an arbitrary linear circuit. Yet another breakthrough, came using exact results of low dimensional quantum field theory by mapping the dynamics of a single channel QPC embedded in a resistive circuit to the dynamics of a Tomonaga-Luttinger liquid [46].
The TLL model is a description of interacting electrons in a 1D conductor/wire with

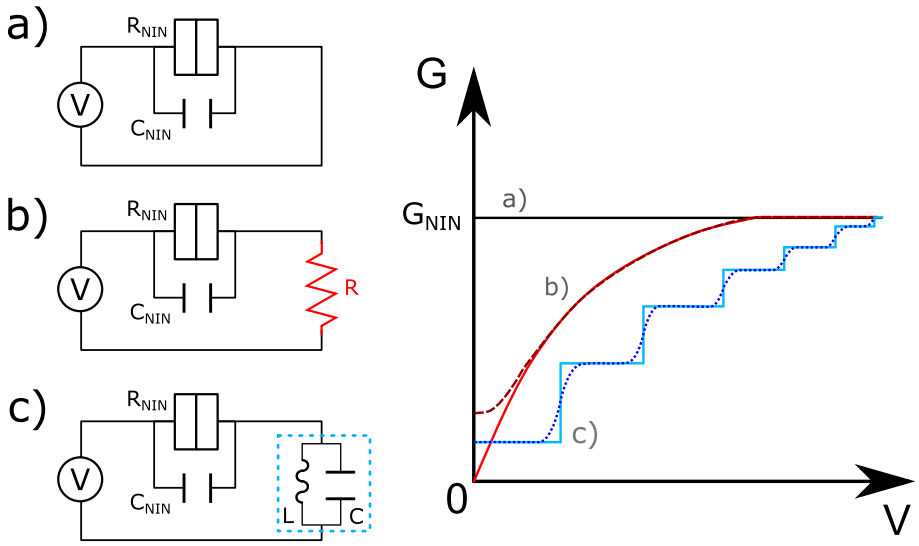

Figure 4.1: Illustration of the DCB effect for a tunnel junction in different electrical circuits: a) tunnel junction in a zero impedance biasing circuit; b) in series with a resistor; c) in series with a single LC resonator (1 EM-mode). The corresponding conductance curves are shown schematically for a) in black, for b) in red, for c) in blue. Solid lines illustrate the zero temperature limit, while dashed lines represent the finite, yet low, temperature behaviour where k_BT is much smaller than the characteristic energies of the environment: $E_{env.} = \hbar/RC$ for (b) and $E_{env.} = \hbar/\sqrt{LC}$ for (c).

short range interaction and a linear dispersion relation. The Fermi liquid model , which provides a remarkably good description for 2D and 3D conductors [153], breaks down in 1D [154] where the faintest interaction gives rise to collective dynamics. The TLL model solves this by modelling the electronic fluid as bosonic excitations. This simplified model was firstly proposed by Tomonaga [155] and Luttinger [156] with the final solution given by Mattis and Lieb in 1965 [157].
The TLL model characterizes the electrons with power-law correlation functions [158, 159] that have been shown via conductance measurements in semiconducting quantum wires [160–163]. When a scattering impurity is placed within the conducting channel or wire, a backward scattering is added that leads to a power law suppression of the transmission across the Luttinger Liquid $G(T) \sim T^{2(1-K)/K}$ [164]. In the TLL-model K is the interaction constant which is a dimensionless parameter representing a non-interacting Fermi-gas for $K = 1$, attractive interactions for $K > 1$ and repulsion for $K < 1$. Safi and Saleur [46] realized the action of describing a single channel QPC interacting with series resistor could be mapped to that of a TLL with $K = 1/(1 + R/R_Q)$, thus that of a repulsive liquid.
Independent of the TLL theory, some models for finite transmission values T_P were made for a weak impedance environment by Golubev [165] and Levy & Yeyati [166] in 2001 and Kindermann in 2003, predicting a a conductance suppression proportional to the shot noise reduction $F = 1 - T_P$. By now, their theories were experimentally proven by Cron et al. [11] and Altimiras et al. [12] for the weak blockade regime of a single channel of a QPC coupled to a different weak impedance environments.

Later on, the experimental work was also extended to high impedance environments, the strong blockade regime, by Parmentier et al. [3] and Jezouin et al. [13]. Such experiments could follow the temperature dependence of the zero bias differential conductance of a QPC probed for transmissions between 0 and 1 and the agreement between the recorded zero bias differential conductance [3,13] and TLL predictions for a span of QPC transmissions validated the mapping. Recent progress is put together, as illustrated in figure 4.2 for the case of a series impedance of $R = h/e^2$ (or $K = 1/2$), and extended on by Anthore et al. [141] who could even experimentally access the full energy dependence of the scaling law governing the universal properties of this impurity problem in several interaction strengths (resistive environments).

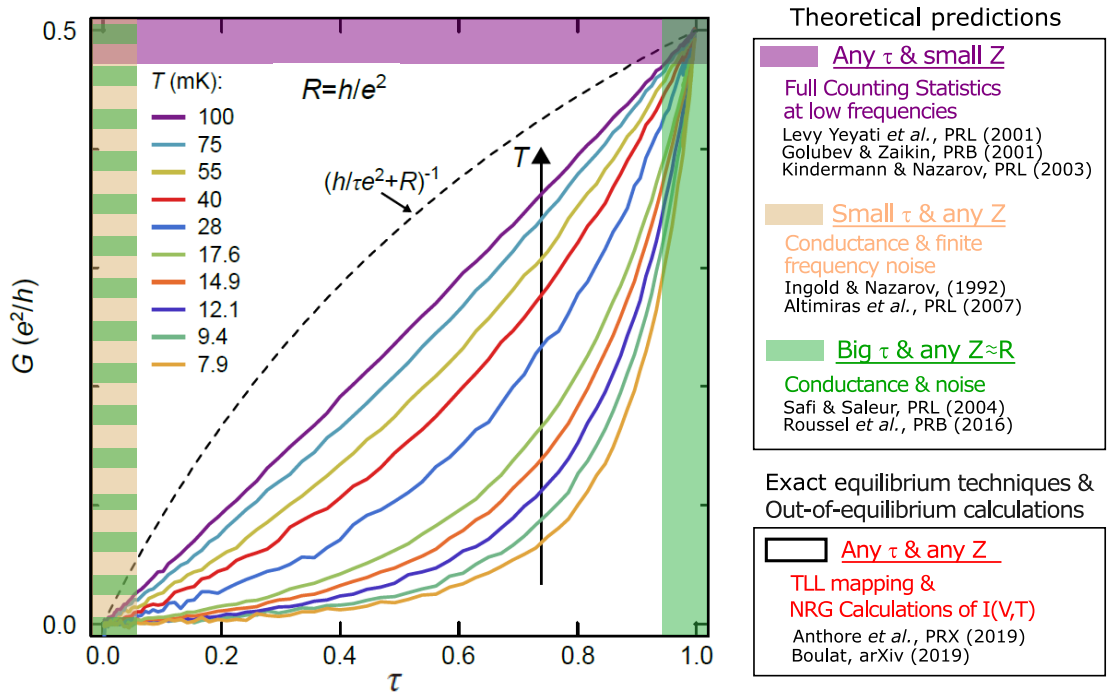

Figure 4.2: Measured zero bias differential conductance, as presented in [141], for a QPC in series with a resistor of $R = h/e^2$, as a function of the QPC transmission for a different temperatures and a charging energy of about 300 mK. At perfect transmission, the conductance matches the non interacting value since the QPC cannot couple to the electromagnetic environment, if it does not give rise to current fluctuations. A soon as the transmission is different from 1, the conductance is strongly reduced with respect to the non-interacting value (represented as a dashed line). Increasing the temperature brings the data closer to the non-interacting values. Modified figure taken from [141], highlighted areas represent suppression and transmission regimes for which previous measurement results or theoretical models exist [12, 44, 46, 140, 165–168].

But despite these successes, so far there is no known solution for such a simple system as a single QPC connected to a single (high impedance) mode. Coupling to a single mode should make it easier to grasp the fundamental dynamics of the DCB effect

and also gives an easier access to experimentally study non-equilibrium dynamics (e.g. high frequency noise). On the experimental level, one needs to couple a high impedance resonator of the order of $R_Q = 25.8\,\mathrm{k}\Omega$ in order to achieve non-perturbative DCB effects.
The first experiment introducing such scheme was performed in 2014 by Altimiras et al. [72], where a high impedance tunnel junction $R_T \gg R_Q$ was coupled to a RF resonator with a large characteristic impedance $Z_c \simeq 2\,\mathrm{k}\Omega$. The oscillator was made up from a Josepshon transmission line, a series of aluminium based SQUID's, that allows to tune the oscillators frequency and provided a large (superconducting) kinetic inductance in order to achieve sufficiently high characteristic impedance values. Such a scheme gave rise to a sizeable blockade as read from a 25% conductance reduction at zero bias (figure 4.3a), but also enabled the direct measurement of the finite frequency emission noise of the junction (figure 4.3b).
The core idea is to continue building on a similar architecture as in [72], but to replace the tunnel junction with a QPC, thus coupling it to a high impedance mode providing both DCB effects and an efficient RF detection scheme. This coupling is however challenging to achieve and will be further elaborated on in the next chapter.

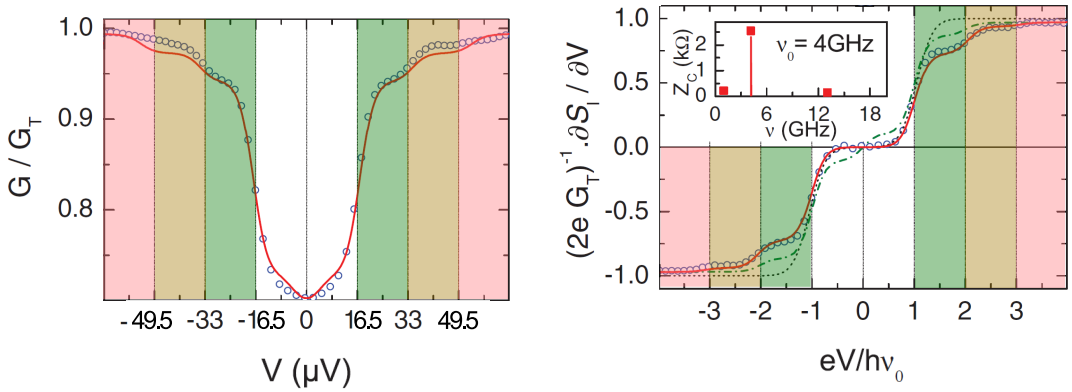

Figure 4.3: Measurement results of a normal tunnel junction interacting with a high impedance RF mode [72]: (a) dI/dV as a function of the applied bias. Conductance jumps are observed at multiples of the resonant frequency of the oscillator. b) High frequency emission noise power derivative measured at the frequency of the resonator, showing that the conductance jumps are indeed accompanied with jumps in photon emission. Highlighted areas mark the observable photon processes: green - single photon, orange - one and two photons, red - one, two and three photons. Measurements (open circles) are done at 4 GHz and 15 mK and fitted (red) with a series impedance as shown in the inlay. it is compared to the non-interacting, finite frequency shot noise prediction (black) and the symmetrized DCB expression (green, see equation 3 in [72]). Figures taken from [169] and modified.

4.2 Introduction to magneto-transport at high magnetic fields

We have already hinted at basic concepts of the integer Hall effect and the accompanying edge states. Here we will introduce the quantization effects that create the Landau Levels and lead to the development of quantum edge channels, to build a fundamental understanding before moving on to the fractional Hall effect.

4.2.1 2D conductors in high magnetic fields

If a magnetic field B_z is applied perpendicular to a 2D conductor (see figure 4.4a), the electronic current in the x-direction $I_x = n \cdot e/t = n \cdot eAv_x$, with n the number of the elementary charges e, the cross-section A and the drift velocity v_x, will be deflected perpendicular to the current direction by the Lorentz force F_L:

$$F_L = e \cdot v_x \cdot B_z \tag{4.2}$$

Charges thus accumulate on one side of the conductor creating an electric field E perpendicular to the original current. This field gives rise to a measurable voltage over the length d in the y-direction, known as the Hall voltage $V_H = E \times d$ after its discoverer Edwin Hall, who measured the Hall effect in 1879 on a thin gold sheet [170]. One can derive the Hall voltage from the equilibrium of the Lorentz force and the generated electric field:

$$e \cdot E = e \cdot v_x \cdot B_z \tag{4.3}$$

$$V_H = v_x \cdot B_z \cdot d \tag{4.4}$$

If we were to measure the resistivity of our conductor in the y-direction, we would now observe a change of the resistivity proportional to the magnetic field due to the shift of charges (see figure 4.4b). We can properly describe this phenomenon by using the Drude model with $E = \sigma \cdot j$, the current flow density $j = n_e \cdot e \cdot v$, and the drift velocity $v = e \cdot E \cdot \tau / m_e$, where n_e is the electronic density, τ the time between scatter events and m_e the effective mass of an electron. Based on this we can formulate the longitudinal resistivity ρ_{xx} and the Hall resistivity ρ_{xy} of the conductor.

$$\rho_{xx} = \frac{j_x}{E_x} = \frac{n_e \cdot e^2 \cdot \tau}{m_e} \tag{4.5}$$

$$\rho_{xy} = \frac{j_x}{E_y} = \frac{e \cdot v_x \cdot B_z}{e \cdot j_x} = \frac{B_z}{n_e \cdot e} \tag{4.6}$$

We see that the longitudinal resistance is independent of the applied magnetic field and thus remains constant while the Hall resistance is linearly proportional to the magnetic field. The proportionality constant $R_H = 1/(e \cdot n_e)$ is known as the Hall constant and allows for the measurement of the sign of the charge and the density of the carriers.

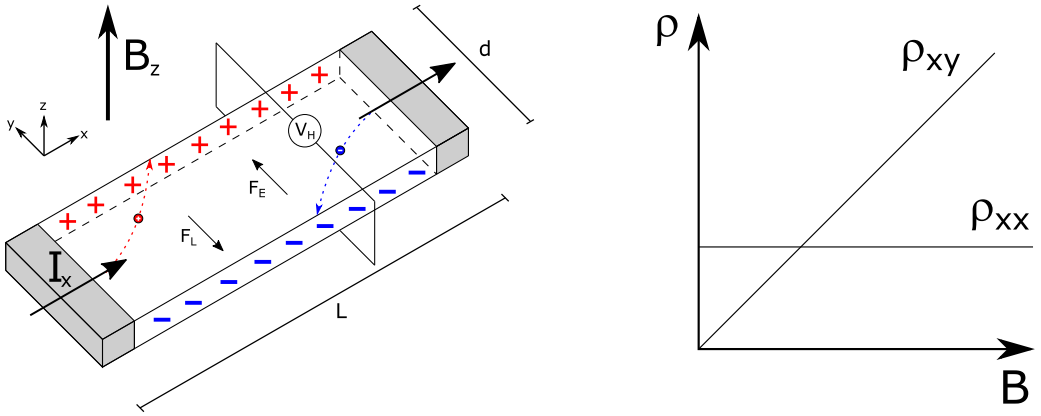

(a) (b)

Figure 4.4: (a) Illustration of the classical Hall Effect in a macroscopic but thin conductor. An applied magnetic field B_z exerts the Lorentz force F_L on the incoming current I_x. The deflected trajectories of the charge carriers cause a charge accumulation which creates an electric field (F_E) orthogonal to the current with voltage V_H. (b) Plot of the longitudinal and Hall resistivity of for a conductor in a magnetic field. The Hall resistivity increases linearly with the magnetic field.

This macroscopic description of the Hall effect changes if one transitions to a mesoscopic coherent conductor that we assume to be 2-dimensional. As the electronic mean free path is increased, electrons will be able to complete their cyclotron motion with the cyclotron radius r_c:

$$r_c = \frac{m_e \cdot v_x}{q \cdot B_z} \tag{4.7}$$

The novel aspect is that, if the cyclotron radius is of the order of the phase coherence length $r_c \simeq L_\phi$, the energy of the electronic states localized in cyclotron orbits becomes quantized. An electron wave can only form a closed path when the length of the path is a multiple of the electronic wavelength: $n \cdot \lambda = 2\pi r_c$. However, the cyclotron angular frequency $\omega_c = v/r_c = eB/m_e$ is independent of the cyclotron radius, thus the dynamics looks similar to those of a pendulum. Indeed, the quantum mechanical calculation of cyclotron motion, first obtained by L. Landau, gives rises to an evenly spaced energy spectrum $E_n = (n + 1/2)\hbar\omega_c$, reminiscent of that of an harmonic oscillator. So when a magnetic field is applied to a 2D electron gas, the continuous set of kinetic energy states collapses in a discrete set of states called Landau levels (see figure 4.5). The stronger the magnetic field the larger is the energy difference between Landau levels and, for an electron gas with fixed density, the more electrons collapse into fewer Landau levels. Since the eigenvalue doesn't depend on the center of the cyclotron orbit, these sites are delocalized.
So far, we assumed an impurity-free system that gives us these discrete Landau levels with smooth potentials and without any mixing of the Landau levels. For a true sample however, impurities e.g. defects or doping impurities are unavoidable. In the presence of scattering impurities, the path of an electron will be changed and it

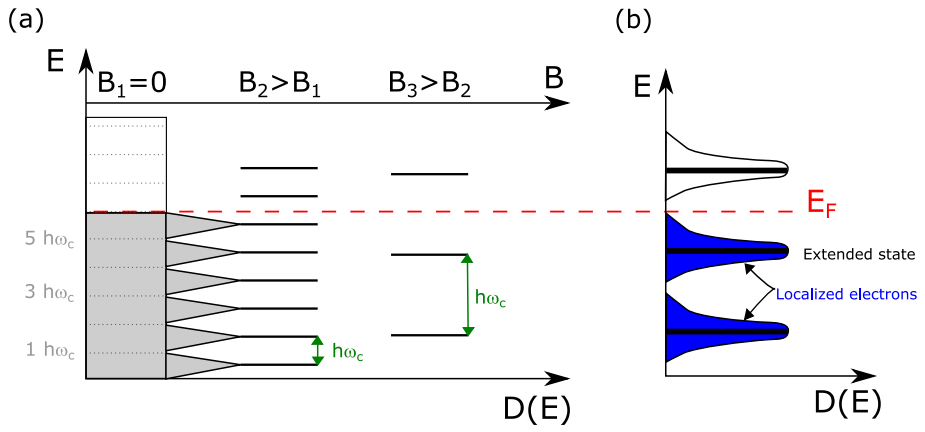

Figure 4.5: (a) Landau Level evolution with increasing magnetic field; (b) Broadening of Landau levels due to impurity scattering. The new states can be categorized as extended states where electrons are free to conduct across the sample and localized states, where the electrons are trapped by the scattering impurity's potential.

appears to have a different energy from the Landau level, hence the Landau levels will broaden [171] (see figure 4.5b). This broadening is independent of the number of the Landau level and typically follows a Gaussian distribution (see Gerhardts [172] and Wang [173]), unless an imbalance of positive and negative defects causes it to become asymmetric. Due to the broadening, the degeneracy of the Landau levels is lifted: whereas states close to the unperturbed Landau eigenvalue remain delocalized, localized states appear in the tail of the distribution While the extended states remain free to conduct across the sample, localized states are electrons that are trapped by the potential of the scattering impurity. Localized electrons are moving on equipotential lines around the impurity and do not contribute to any current conduction. Despite the different categorization of states, the total amount of electrons within a Landau Level does stay constant independent of the degree of broadening. The number of available states per unit area within each Landau Level corresponds to the amount of flux quanta per applied magnetic field and thus varies only with the applied magnetic field as $n_L = e \cdot B_z/h$. With this we define the filling factor v_L of the Landau Levels which is the ratio of the available electron density and the available states. For integer values of ν_L the equivalent amount of Landau levels are completely filled.

$$\nu_L = \frac{n_e}{n_L} = \frac{h \cdot n_e}{e \cdot B_z} \tag{4.8}$$

The presence of edge channels in a 2DEG or a general planar conductor in a high magnetic field can be easily understood, if we now look at a real sample where we have to add a potential $V(x)$ to the Landau levels as it represents the lateral confinement of the conductor. The Landau levels are thus bent at the edge crossing the Fermi potential, which will give rise to conductive edge channels in the 2DEG (see figure 4.6a). In the bulk, the potential might randomly fluctuate due to impurities but electrons are generally localized, trapped within the potential wells of impurities, and

do not contribute to the transfer of current. Referring to a semi-classical picture, using the cyclotronic electron motion, one can imagine that all electrons circulate, causing bulk electrons to move on the spot. Electrons near the edge however are not localized by impurities but collide with the potential barrier and are practically scattered forward. This is called a skipping orbit which forms a chiral electronic channel without backward scattering (Even if scattered at an impurity, at high enough fields the electron will continue its path), shown in figure 4.6b.

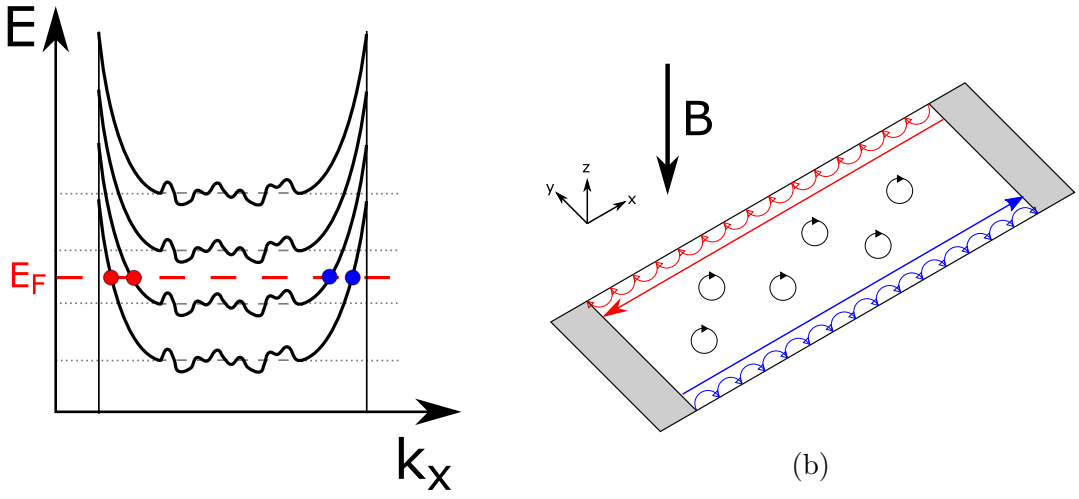

(a) (b)

Figure 4.6: (a) Bending of the Landau Levels due to the conductors confinement potential $V(x)$. For every filled LL a conductive edge channel on each side is formed; (b) Schematic drawing of the skipping orbitals of the edge channels. When the Fermi potential is within the localized states, electrons in the bulk are localized in place and do not conduct. However, electrons near the edge are reflected by the edge potential onto a forward trajectory creating the conductive edge channels while the bulk is insulating.

For non-integer filling factor $n < \nu_L < n + 1$, a number n of chiral channels are well defined close to the edge of the sample, equivalent to the number of bent Landau Levels that are within the Fermi-level (see figure 4.7a). All bulk electrons are localized and thus in an insulating state. In x-direction the conductance is then scatter free via the edge channels and ρ_{xx} is zero. In the y-direction a finite voltage V_H between the separated edge channels is built up and the Hall resistivity is finite. If the B-field is increased, the system does not change much as long as E_F is within the localized density of states. Once we reach the extended density of states, near the LL energy (figure 4.7b), the innermost edge channels percolates on paths that scatter in between the localized states and eventually backscatter on the opposite chirality channel. At this point the conductance in x-direction is not back-scatter free anymore and the longitudinal resistivity becomes finite. If B is increased further (figure 4.7c), the amount of LL's is reduced and the percolated edge channels are localized in the bulk. Conductance in x-direction is again scatter free, giving zero longitudinal resistivity. Again, a voltage between the edge channels of different direction builds up which has

increased compared to situation (a) because the current is now carried by a fewer number of channels so that R_H increases.

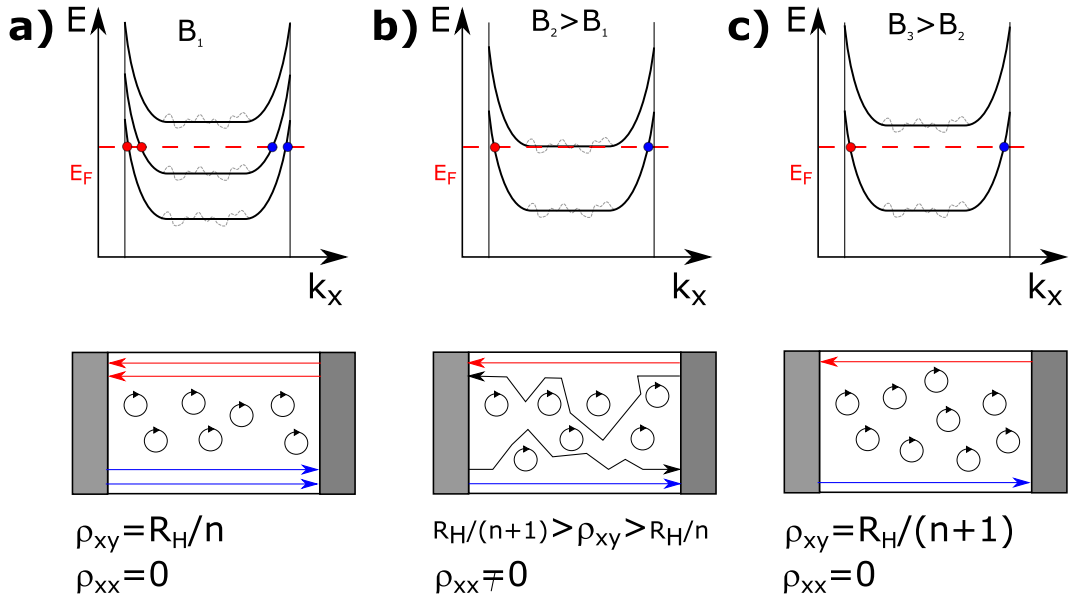

Figure 4.7: Illustration of the evolution of the Landau Levels (top) and the skipping orbitals of the edge states (bottom) for increasing magnetic fields. If the magnetic field is increased from a)-b) so that the Fermi energy is within the extended states, the inner edge channel becomes de-localized and percolates into the system before it may be trapped by the impurities c).

At this point, is should be clear that in order to access the transport regime dominated by edge channels, it is crucial to have a certain amount of impurities in the sample as they allow to localize the percolating edge channels. If a sample is too clean, the chemical potential is essentially pinned in Landau levels, where the bulk conduction shunts the edge channel contribution. On the other hand, it should also be avoided to have too many impurities which would promote an overlap of different Landau states so that a direct y-conductance due to thermally assisted interband hoping would be possible.

4.2.2 Magneto-transport measurements on a 2DEG

At this point, we have the tools to explain the magneto-transport features one can measure in cryogenic temperatures on a 2DEG when applying a perpendicular magnetic field. In the low field regime, the system behaves classically and one observes a linear increase of the Hall resistance, with a constant longitudinal resistance. As the cyclotron radius diminishes with the applied field, at some point it becomes smaller than the phase coherence length and the mean free path. Thus the electronic density of states is affected by the periodic boundary conditions and its physical properties become periodic with the cyclotron radius, thus with $1/B$. This gives rise to an oscillation of the longitudinal resistance, known as Shubnikov-de Haas oscillations.

These oscillations were firstly observed for small fields in Bismuth crystals by Shubnikov and de Haas in 1930 [174]. Results of such a measurement for a GaAs quantum well for constant n_e and changing magnetic fields, taken from T. Ihn [175], are shown in figure 4.8a. For small magnetic fields (0-0.5 T) we observe the classical Hall effect where ρ_{xx} is constant and ρ_{xy} has a linear relation with the magnetic field (constant R_H). For higher magnetic fields (0.5-1 T) the longitudinal resistance oscillates (see figure 4.8a) and the beginning of steps appear for the Hall resistivity. For even higher fields, from approx. 1 T and above, we can see a clear formation of plateaus in the Hall resistivity and a disappearing (zero) longitudinal resistivity with high peaks in between plateaus. For increasing magnetic fields, the cyclotron radius becomes comparable to the Fermi wavelength, thus the very notion a of semi-classical trajectory fails. This regime corresponds to well developed Landau levels, as seen in the precedent section: Thanks to disorder, the chemical potential lies between successive Landau levels for a broad range of magnetic fields. Thus the current is only carried by the edge states, giving rise to vanishing longitudinal resistance, and a Hall resistance equal to the resistance quantum divided by the number of edge states as illustrated in figure 4.8b. In between two magnetic field plateaus, the system percolates changing the number of current carrying edge states. This percolation delocalizes the innermost edge channel within the bulk, giving rise to a finite backscattering and thus a finite longitudinal resistance peak.
This is the integer quantum hall effect that was firstly measured by K. Klitzing [176] in 1980 using a 2DEG created by a silicon MOSFET. He measured the change in longitudinal and Hall resistivity for both changing carrier concentration and different magnetic fields. The Hall resistance plateaus (see figure 4.8) are found at universal values given by the resistance quantum $\frac{h}{e^2}$ divided by the number of current carrying edge channels, namely the filling factor ν: $R_H = \frac{h}{\nu \cdot e^2} = \frac{25.8\,\mathrm{k\Omega}}{N}$.

4.3 Measurement of fractional charge transport in high magnetic fields

Up to know, we just discussed the non-interacting physics of 2D magneto-transport. It turns out that the constraints imposed by the quantized magnetic field ally with Coulomb repulsion giving rise to a class of highly correlated electronic states called fractional quantum Hall states.

4.3.1 Fractional Quantum Hall effect

We already know that the amount of edge channels in the quantum Hall regime is controlled by its dependence on the magnetic field and can be reduced to a single channel for large enough magnetic fields. Then all electrons lie within the lowest energy state, the lowest Landau Level, and, following the arguments provided in the precedent section, the system should not change anymore. However, if we further

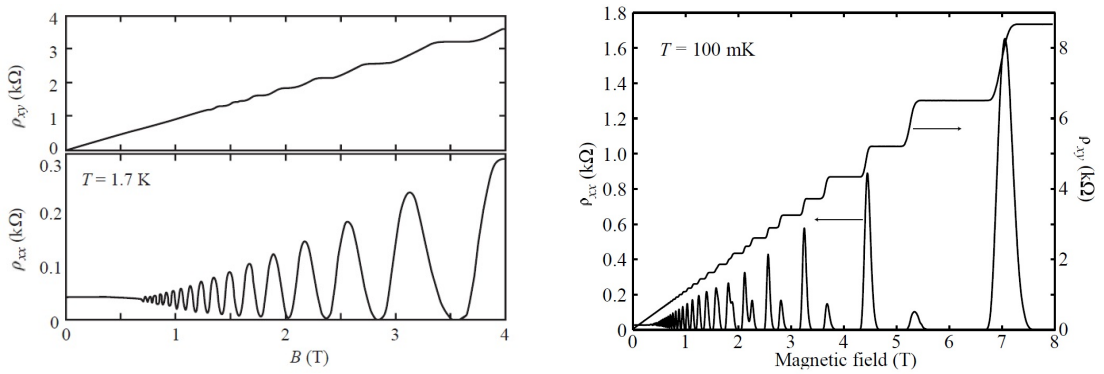

(a) (b)

Figure 4.8: (a) Shubnikov-de Haas oscillation in the longitudinal and Hall resistivity of a 2-DEG in a GaAs quantum well at 1.7 K. Taken from T. Ihn [175]; (b) Measurement of the longitudinal resistivity and the Hall resistivity of a 2-DEG in a GaAs/AlGaAs hetero-structure as a function of the magnetic field, measured at 100 mK. Taken from T. Ihn [175].

increase the magnetic field, the measured resistances also increases exhibiting further plateaus in the Hall resistance, as was measured in 1982 by Tsui, Störmer and Gossard [177]. These new plateaus, shown in figure 4.9a, have resistance values that are multiples of the quantum of resistance and correspond to fractions of the filling factor $v = \frac{1}{3}, \frac{2}{3}$. Later on, in higher mobility samples multiple other plateaus were found for another series of filling factors in the lowest Landau level $v = \frac{1}{5}, \frac{2}{5}, \frac{3}{7}, \frac{4}{9}...$ as well as for lower magnetic fields, corresponding to fractions larger than one $v = \frac{4}{3}, \frac{5}{3}, \frac{7}{5}, \frac{5}{2}...$ [178], with corresponding plateaus and peaks shown in figure 4.9a. While these fractional filling factors can not be explained with the non-interacting electron model of the QHE, the plateaus are accompanied by a vanishing longitudinal resistance and thus the new phenomena show a strong resemblance to the quantum Hall effect.
For the integer quantum Hall effect the bulk electrons in the 2DEG form an incompressible 2D fluid and are thus insulating whenever the Hall conductance is quantized [179], so that the current is only carried by the topologically protected edge channels [28]. The electronic compressibility κ is defined as $\kappa = 1/n_e^2 \cdot \delta\rho/\delta\mu$ with ρ as the electron density and μ the chemical potential. An electronic fluid is thus named incompressible when an energy gap is present in the system in which there are no available states to contribute to the electronic density. $\rho(\mu)$ is hence constant so that the compressibility is zero. This incompressible state in the IQHE is created as electrons are localized by the magnetic field B when the Fermi energy E_F is in between the Landau Levels. In the case of the fractional quantized Hall effect the incompressibility arises from many-body interactions, most dominantly from the Coulomb forces that create an energetic substructure in each Landau Level, resulting in quantized Hall conductance at fractional filling factors [177]:

$$\rho_{xy} = \frac{h}{e^2}\frac{1}{p/q}, \tag{4.9}$$

with the filling factor as $\nu = p/q$. Plateaus are found when p and q are integers. We firstly look at the case of $\nu < 1$ for which all electrons are in the lowest Landau level. Here all electrons have the same kinetic energy so that Coulomb interactions become the dominant force. In 1983 Laughlin [34] proposed a corresponding model for the many body ground state wave functions at $\nu = 1/q$, $(q > 0, odd)$ based on the minimization of the Coulomb potential (The model can also be applied when considering holes, starting from a filled level, so that $\nu = N - 1/q$). In short, any electron has a zero probability to be at another electron's location and for specific values of the filling factor the cyclotron orbits organize so that each of them always cut a fixed amount of other electrons orbits. As a result, while for $\nu = 1$, electrons are densely packed and have no degrees of freedom, they adjust to a macroscopic coordinated motion at high magnetic fields which allows them to "space-out" and to reduce their Coulomb repulsion potential. Thus a dynamic state is established for a specific density and magnetic B field, whose breakage is associated with a huge energetic cost if either the density or the magnetic field is changed.
This coordinated motion is equivalent to the creation of composite particles of electrons and vortices so that an electron that is encircled by a fixed number of other electrons. But when these new composite particle include an integer electronic charge, why is a Hall resistance value observed that corresponds to a fractional effective charge of $q_{eff} = -e/q$ at filling factor $\nu = 1/q$? A simple model description for this was given by Jain in 1989 [180,181]: The magnetic field creates vortices in the conductor, areas that are locally penetrated by the magnetic field and surrounded by a protecting ring current. As the vortex core is void of charge, they are attractive towards electrons and finally trap them. Their combination is energetically beneficial as the vortex screens the Coulomb repulsion, so that the entire system becomes incompressible [34]. In the case of $v = 1/3$ there are three vortices attached per electron that form a composite particle (see figure 4.9b). Changes of the magnetic field will then generate additional vortices that are not attached to any electrons. These electronless vortices are then quasi-holes that carry a third of the electric charge $e/3$ of the composite particles, responsible for the observable current transport of a fractional charges in the FQHE. Interestingly, these excitations do neither follow fermionic nor bosonic statistics but rather anyonic statistics[1] [35,37] which can only be found in 2D systems. The model also applies to higher Landau levels, when the lowest Landau level is completely filled $2 \geq \nu \geq 1$. However, certain fractions are difficult to observe as transport measurements need to be conducted at thermal energies lower than the gap's activation energies $\Delta_{p/q} \sim e^2/(4\pi\epsilon r^2)$ which scales with the Coulomb energy at a distance equal to the magnetic length $r = l_B$ and thus depends on the magnetic field B. In consequence, the higher the fractions to be measured, the smaller is the gap and the more sensitive is the measurement to finite temperature effects.

[1]Exchanging two anyonic particles causes a phase shift of the electronic wave function that is a fraction of 2π.

Other specific filling factors, like the even denominator filling factor 5/2 found in the third Landau level [178], are even more complicated and can not be described with the presented model, based on non-interaction fermionic composite particles, as the 5/2 state instead forms bosonic composite fermion pairs similar to superconducting Cooper pairs [175]. Several theories predict different ground states with different symmetries, which is not described as anyons but mostly as non-abealian anyons [182]. Non-abelian anyons not only have an exchange phase but can also change the state of the system while maintaining the same particle configuration (braiding statistics) which makes it a suitable candidate for quantum computation applications [183].
A first experimental proof of fractional abelian statistics was found in 2020 for a filling factor of $\nu = 1/3$ by Bartolomei et al. who measured the quantum noise in a Hong-Ou-Mandel interferometer of Laughlin quasi-particles [145]. From observed current correlations of anyonic collisions within the interferometer an exchange phase of $\phi = \pi/3$ could be attributed to the anyons. This kind of collision experiment is also a promising candidate for the investigation of non-abelian statistics.

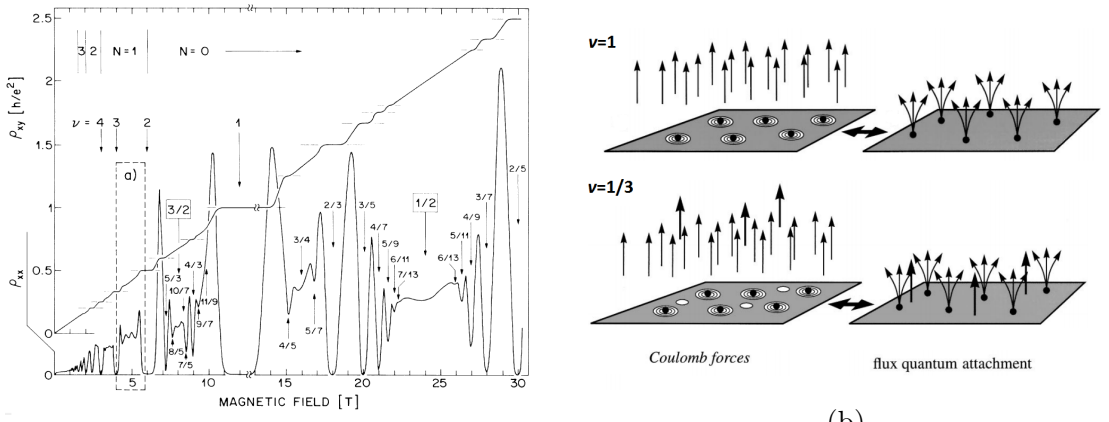

(a) (b)

Figure 4.9: (a) Resistance measurement of the Integer and fractional quantum Hall effect, taken from [178]. The numbers indicate the fractional Landau level filling factors;(b) Creation of bosonic composite particle of electrons and vortices at integer and fractional filling factors, taken from [27].

4.3.2 Probing fractional edge channels

Having excitations carrying only a fraction of the electronic charge is one of the strangest features of fractional Hall physics. Shot noise measurements on QPCs realized in the FQHR, tuned close to perfect transmission, have indeed shown a current spectral density proportional to the backscattered current and a fractional charge [39–41]). While the measurement of low frequency shot noise provided solid proof of the Laughlin picture of "simple" fractions $1/2n + 1$, some controversy arises when measuring more complex fractions such as 2/3 or 2/5 where the value of the charge measured by this procedure is found to unexpectedly change with temperature

[184, 185]. In this case, a method being able not only to detect an average charge (as low frequency noise does) but to distinguish amongst different charges, should they be present simultaneously, would be highly informative.
Recently, a first experiment went into this direction: in 2019, a high frequency measurement was finally realized by Bisognin et al. [62] that provides a measurement of the fractional charge $e/3$ at filling factors 4/3 and 2/3 for a QPC coupled to an RF detection environment. The QPC is driven with a DC bias to emit RF photons when the fractional edge channels are scattered. The result of their experiment is the observation that emitted photons can only have smaller energies than the quasi particle $hf < qV_{DC}$, resulting in a threshold $f_J = qV_{DC}/h$ for the photo-emission. However, the experiment suffered from poor detection efficiency, as the high impedance sample was directly coupled to a $50\,\Omega$ transmission line. Despite long averaging times, this leads to a poor signal to noise ratio even though advanced signal analysis techniques are used. Thus implementing a high detection impedance, with a large detection bandwidth, operating in high magnetic fields would enable faster and more accurate measurements of non-equilibrium dynamics in the fractional quantum Hall regime and thus a systematic investigation of the evolution of the effective charge as a function of sample temperature, and QPC transmission.

4.4 Investigating the Kondo effect

Another mesoscopic effect that can be probed using a single electronic channel tailored in a 2DEG, is the Kondo effect [186]. Originally the Kondo effect describes the observed low temperature divergence of resistivity in metallic materials containing magnetic impurities. For a normal metal the resistivity drops if the temperature is decreased. This is understood as a consequence of the electro-electron and electron-phonon scattering being reduced. For metals that contain a certain amount of magnetic impurities like manganese or iron atoms for example, the resistivity will rise below a critical temperature, later labeled the Kondo temperature T_K due to a scattering caused by the coupling of the Fermi gas to the spins of the impurities. Kondo looked at this problem by studying the electron scattering with a single impurity. His result shows that this scattering of a Fermi gas coupled to a spin $S = 1/2$ has an energy dependence (which is not the case for non-magnetic impurities). For low energies and correspondingly low temperatures, the coupling increases so that the resistivity is increased proportional to $\log T$. Even though this description provides a correct description for lower temperatures it is incorrect in the zero temperature limit as the logarithmic divergence of the resistivity is un-physical, so that the developed model is only valid in a certain temperature range above a critical temperature threshold T_c (The description of the Kondo effect at T close to zero was later solved by the renormalization group theory [187]).
This fundamental coupling has been of interest in quantum transport research since it became possible to create artificial magnetic impurities from the electronic spin trapped in a quantum dot. These can be integrated into electrical circuits and allows to probe Kondo physics as was demonstrated in [30] and [188] for a single electronic

channel coupled to a quantum dot. Quantum dots are essentially electronic islands that are capacitively coupled to the electronic reservoirs by one or several QPCs. In order to probe Kondo physics, the dot is usually attached to two reservoirs via two QPCs, implementing the two channel Kondo effect.
The dot is charged one electron at a time and has different electrical properties for even or odd numbers of electrons. For an even number there is no net spin so that the transport is only governed by simple quantum dot physics, namely an electrostatic blockade of transport due to the finite charging energy as introduced in section 4.1.1. However, a dot with a single spin $S = \pm 1/2$ contains a magnetic moment which hybridises with the spin of the conduction electrons giving rise to an increase in the zero bias conductance known as Kondo ridges [188] as shown in figure 4.10.
There is however one major difference between the Kondo effect arising from dilute magnetic impurities in metals and in semiconducting systems with a quantum dot: For metals, there are many paths for electrons and the impurities introduce additional scattering that increases the overall resistance. In a semiconducting circuit/system there are no free electric paths. All electrical channels go through the impurity so that the scattering promotes the transport across the dot and across the circuit. As a result of this, at low biases strong Coulomb blockade effects should forbid any conductance across the dot but the electronic hybridization modifies the dot's transport properties.

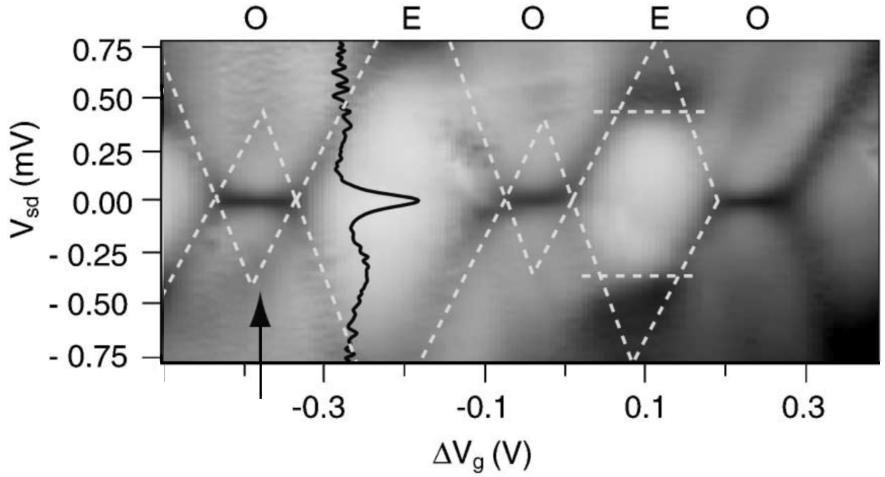

Figure 4.10: Plot of the differential conductance dI/dV in a grey scale (the conductivity increases from bright to dark) as a function of the source drain V_{sd} and the gate voltage V_g of a carbon nanotube quantum dot in the Kondo regime. The standard Coulomb diamonds are indicated as dashed white lines. Dark areas of high conductivity at zero drain bias, the Kondo ridges, appear within diamonds corresponding to odd electrons within quantum dot, marked as O, and is absent in diamonds with even numbers of electrons, labeled with E. A dI/dV cross-section over the drain bias for a Kondo ridge is shown as black curve for the position indicated by the arrow. Figure taken from [189] and modified.

Quantum dots defined in 2DEGs, but also in carbon nanotubes, quickly became model

systems to investigate Kondo physics. Indeed, the electrostatic tunability of crucial parameters such as the tunnel couplings between the impurity and the electrodes offered a control in Kondo physics unparalleled in other physical systems. Notably, the fine tuning of the tunnel coupling symmetry enables to set the system in the unitary regime, where the impurity is equally screened amongst both leads and the conductance at the Kondo ridge reaches the value $2e^2/h$, as if electronic waves where perfectly transmitted by an impurity free wire. To be precise, the combination of spin 1/2 and a single electronic channel gives rise to a non-Fermi liquid regime with a fixed point, well described by the Fermi liquid theory, as discussed in [190] (a more detailed description and review is given in [191]).
Nevertheless, close to unitarity the conductance and noise are finite and exhibit scaling laws demonstrating a critical behaviour [192]. Close to this critical point, the low energy physics can be described by two scattering channels [193]: one transfers the normal charge e, while the other transfers a double charge $2e$. With both channels being equally active, the average transferred charge as measured by low frequency shot noise is $5/3e$ [194]. Consequently it would be expected to observe signatures of both channels as cups at $2eV = hf$, and $eV = hf$ in the low energy (yet quantum) limit with $k_BT \ll hf$,$eV \ll hT_K$. This is realizable for typical Kondo temperatures of about 1 K [195] attainable in 2DEGs, when measuring in the few GHz range.
Recent experiments based on the noise detection of a nanotube quantum dot with an SIS detector [196] successfully measured the high frequency noise $hf \gg k_BT$. A quantum dot, fabricated in a carbon nanotube, was coupled to an SIS quantum noise detector via different SC coupling circuits at 29.5 and 78 GHz. Unfortunately, due to the limits imposed by the design of the sample, the dot could not be tuned to measure the range $hf_{detection} < k_BT_K$, close to unitarity in which effects like co-tunneling processes, 2 electrons emitting one photon, could be expected. So a full test of finite frequency dynamics in the Kondo regime is still missing. Hence we would propose to create a tunable measurement setup with a simple RF power detector measurement as presented in chapter 3 in order to measure the dynamics of the Kondo effect for energies in the GHz range.

4.5 Summary

In this chapter we have introduced several different mesoscopic effects arising from the interplay of Coulomb interaction and quantum coherence: the dynamic Coulomb blockade, the appearance of strongly correlated fluids in the fractional quantum Hall effect and the Kondo effect. Based on the provided review of recent and also ongoing experiments in the respective fields, we have shown that there are several domains that have not yet been able to be measured or fully understood. The common problem relies on the technical difficulty of extracting the high frequency noise signals with an insufficient coupling between the sample and the RF measurement setups. In all three regimes presented, experiments would benefit greatly from the creation of a novel experimental platform that allows to overcome the hurdle of mismatched impedances by creating a new high impedance transformer that is stable under high applied

magnetic fields. Therefore, we present the creation of our experimental platform for RF-measurements in high magnetic fields in the next chapter.

Chapter 5

Building an experimental platform for RF-measurements in high magnetic fields

In this chapter we describe the assembly of an experimental platform enabling the efficient measurement of RF noise emitted by conductors tailored in 2D electron gases and submitted to strong perpendicular magnetic fields. As emphasized in the precedent chapter, such a platform could bring important new information on strongly interacting effects such as dynamical Coulomb blockade, fractional quantum Hall physics or the Kondo effect.
In the first half of this chapter we are going to introduce the necessary clean-room techniques for the fabrication of a mesoscopic conductor and its integration in a cryogenic RF-measurement setup within a dilution refrigerator. In the second half we will be discussing the basic elements of low-noise electronic detection systems and the design and fabrication of a high impedance and large bandwidth RF detection system.

Contents

5.1 Fabrication techniques for 2DEGs

Here we want to briefly present the most important tools that are needed to fabricate mesoscopic conductors, specifically quantum point contacts in AlGaAs/GaAs semiconducting hetero-structures, on a nano- to microscopic scale by common methods like lithography, etching, thin film deposition and doping. While we only give a general description of the common techniques used, a detailed description of our recipes can be found in the Appendix B.

The common top down approach for microscopic semiconductors fabrication is based around optical UV- light lithography, which allows to create resist masks with feature resolution of down to few 100 nm on different substrates. The sample is covered by an optically active resist, which can be shaped after a light exposure and, depending on the resist used, a combination of chemical development and heat treatments to obtain the desired mask shape. The obtainable resolution of advanced vacuum lithography systems is hereby purely dependent on the wavelength of the light, so that smallest features are of the order of 100 nm. After the lithography the semiconducting substrate can be doped, etched or covered with depositions of metallic thin films or oxides. By combining these techniques it is possible to create different microscopic

3D structures of varying shapes and sizes. As the achievable feature sizes of optical lithographies are naturally limited, the break-through for top down nanometric fabrication came with the introduction of the electron beam lithography (EBL). For the EBL, analogous to the light based UV or X-ray lithography, an electron beam is used to expose the sample and pattern an electron-sensitive resist (typically PMMA). The electronic wavelength depends on the acceleration voltage as: $\lambda_e \approx \sqrt{1.5/V}\,\mu$m and is then roughly 0.122 Angstrom for commonly used acceleration voltages of 10 kV, allowing to create nanoscopic features. However, the EBL's resolution is limited by different factors that include for example the used beam spot size, secondary electron scattering and the mechanical stability of the resist [197] so that the achievable resolution is of the order of few nanometers. For this lithography one uses e-beam guns usually found in SEM's or TEM's which are nowadays available in specialized lithography systems equipped with interferometric stages that allow for automated patterning and ultra-precise alignment and stitching of sample areas [1]. However these nano-fabrication techniques are not the only tools required for mesoscopic conductors. The creation of smallest mesoscopic conductors is achieved by controlled growth and doping of semiconducting substrates, summarized as epitaxy and strain engineering, which allow to create confining structures that force electrons into quantum wells or wires. Of importance for us are epitaxially grown hetero-structures (AlGaAs/GaAs) which form a quantum well at their interface which generates a planar confinement potential that leads to a 2D electron gas layer (2DEG). We will use this material to define a quantum point contact within the 2DEG to serve as the main conductor in our experimental setup.

5.1.1 The AlGaAs/GaAs hetero-junction

By combining two semiconducting materials with a different band gap their Fermi levels equilibrate and, following the potential gradient that develops, electrons flow from one material into the other. The resulting depletion layer of positive charge, together with the charge accumulation on the other side, creates an electrical field forcing electrons back, similar to the well-known p-n junction. If however, the difference in the band gap is too big, the developing field is not strong enough for electrons to flow back into the original substrate. They are now trapped in the dip of the electronic potential at the interface, referred to as electron well. For good material combinations a thin 2-dimensional layer of a single electronic mode is thus formed at the interface. In this thesis we will be working with an AlGaAs/GaAs hetero-junction: AlGaAs has a band gap of 2.1 eV and GaAs a gap of 1.4 eV providing a sufficient difference to establish an electron well potential. Furthermore, AlGaAs has almost the same lattice constant as GaAs, due to the Al substitutionally occupying Ga sites, so that the strain from lattice mismatches is negligibly small and does not create any scattering impurities. The most effective method to produce these hetero-structures is via the molecular beam epitaxy (MBE) that was developed by Cho and Arthur [199]. As an advanced vacuum evaporation technique MBE utilizes precise atomic beams of

[1] For further information refer to [198]

different evaporation materials whose deposition compositions can be finely adjusted for layers of less than 1 nm thickness. Using MBE it is possible to finely adjust ratios/gradients of components or to add dopants in layers. This is of importance if one wants to improve the quality of the 2DEG. In order to enhance the charge carrier density and the mobility, defined as the ratio of the electron's average drift velocity divided by the electric field, one has to add electron providing dopants in the AlGaAs layer which is commonly done by implementing Si atoms. Silicon replaces gallium on its lattice sites and provides one more valence electron that is travelling towards the electron well. This n-doped layer is often referred to as delta-layer and is typically 100 nm above the interface. This spacing is necessary because the drawback of the doping in a hetero-structure is an increase of impurities and defects caused by the lattice strain and the introduction of charged impurities (the ionized Si donors). Lattice strain, like any other impurity of the lattice, has a negative impact on the mobility of the 2DEG. To avoid this, one keeps an undoped spacer layer in between the doped regions and the interfacial 2DEG. Finally, one typically adds a protective cap layer of GaAs on top and the full stack, as firstly implemented by Melloch [200], as shown in figure 5.1a. When we look closer at the band diagram of the hetero-structure (see figure 5.1b) starting from the right to the left, we have a flat potential in the GaAs substrate. As we approach the 2DEG interface, the band is bent downwards due to the accumulated charge and jumps at the interface due to the band-gap mismatch of the two materials. The added potential due to the depletion field between the negative electron well and the positive donor ions pulls the electrons towards the junction. The resulting electron well at the interface has a triangular shape with a width of typically 10 nm at the level of the electrons. The electronic levels are quantized in the z-direction with an energy spacing of around 40 meV between the ground state and the first excited level in GaAs [201]. This means that at room-temperature, when the thermal energy of the electrons ($3/2k_BT \approx 38.7\,\text{meV}$) is comparable to the energy spacing, two states may be occupied, while at cryogenic temperatures $k_BT \ll 40\,\text{meV}$ only the lowest state is occupied. At low temperatures, the electrons are completely confined in z-direction but can freely move in x- and y-direction, thus forming a 2DEG. Moving on further through the hetero-structure, the potential drops-off linearly across the charge-free spacer layer until the delta layer. Due to the positive donors in the delta layer, the band is bent upwards here with a different slope, until we have another drop at the interface to the GaAs cap. In the cap-layer the band is either linear or bent, depending on whether it is undoped or doped, up to the surface (for further information see [201]).
The 2DEG used in this thesis are Si-doped AlGaAs/GaAs hetero-structures that were fabricated by U. Gennser from C2N and have carrier densities n_s of the order of $10^{10} - 10^{11}\,\text{cm}^{-2}$ with mobilities of 55-57 m^2/Vs, depending on the aluminium and Si-dopant concentration. The typical carrier density of $2 \cdot 10^{11}\,\text{cm}^{-2}$ corresponds to a Fermi wavelength $\lambda_F = \sqrt{2\pi/n_s}$ of around 50 nm.

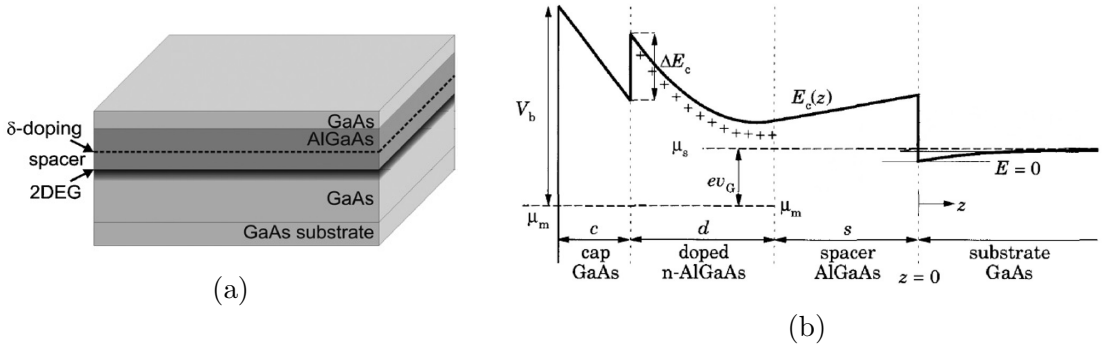

Figure 5.1: (a) Schematic stacking of a AlGaAs-GaAs hetero-structure as done by Melloch [200], taken from [202]; (b) Corresponding band diagram of the AlGaAs-GaAs hetero-structure, taken from [201] for a AlGaAs/GaAs heterostructure with positive gate voltage 0.2 V.

5.1.2 Ohmic contacts

It is within this 2DEG where the quantum point contact is created, however firstly one has to establish contacts from the surface of the substrate to the 2DEG below. As metallic contacts brought onto the semiconductor will form a Shottky barrier of up to few eV, there will be no current flow in the downward direction. As a mean to circumvent this, inter-diffusive ohmic contacts were developed. Traditional material choices for GaAs-AlGaAs substrates are Au, Au-Ge and AuGeNi contacts. These contacts have a solid state reaction with the GaAs at different temperatures, forming a direct contact for gold or create a contact by heavily doping the substrate with Germanium. A more detailed description of the diffusive reaction and the fabrication process can be found in the Appendix D.
The key problem concerning the fabrication of diffusive contacts is to minimize the contact resistance which is increased by any surface residues that prevent or inhibit diffusion. Therefore it is common practice that the ohmic contacts have to be fabricated first on a pristine surface, although it is possible to fabricate them at later stages, if the sample can withstand harsh cleaning conditions to obtain nearly pristine conditions. To be sure though, a lithography process that is residue free needs to be chosen in order to define and deposit the contact material. As UV resist or other optical resist tend to leave nanoscopic residues behind, it is preferable to rely on e-beam lithography with PMMA and related products being developed trace-free.

5.1.2.1 E-beam lithography

For the fabrication of the ohmic contacts and other small features, like the QPC split gates that are added as the final step, we use a resist bi-layer of MAA and PMMA that is spin coated on our AlGaAs/GaAs chips and expose it in an EBL-system "E-line" from Raith. The E-line is equipped with a vacuum system and an interferometric laser stage that allows for precise alignment, with 1 nm tolerance, of the chip and for different patterns on the chip. It is thus possible to define ohmic contacts and the

alignment markers for following fabrication steps, that are spaced out over a distance of several millimeters from one another. The resist is exposed with a 10 kV beam and then developed in an MIBK/IPA solution and rinsed off in IPA to remove any residues of the exposed PMMA. As the MAA's development is trace-free, the sample is immediately ready for the deposition of the ohmic contacts.

5.1.2.2 Physical vapor deposition (PVD) and contact doping

The ohmic contacts are deposited on the chip by physical vapor deposition in a Joule evaporator. Metallic raw materials are placed in tungsten crucibles with the sample mounted above in a vacuum chamber. At minimal pressures of 10^{-8} mbar the crucibles are heated up to melt the metals and the evaporating metal fumes are then deposited onto the sample to form a metallic thin film. The evaporated thickness is measured with an oscillating crystal detector so that a stack of precisely 4 nm Nickel, 60 nm Germanium, 120 nm Gold, 25 nm Germanium and 25 nm Gold is deposited. After the deposition, the resist mask and the excess metal film are removed in a heated acetone bath, leaving the wanted structures behind. The contacts have then to be annealed in order to start the diffusion process. Therefore the sample is heated up in a Jetlight Rapid thermal annealing (RTA) processing and annealing furnace from Jipelec. The chip is heated up in a protective nitrogen-hydrogen atmosphere ($95\% - 5\%$) to 370°C to melt the gold and Germanium. Gold-germanium has an eutectic phase which melts at around 360°C so that the layers start melting at their interfaces and are completely dissolved and mixed after few minutes. The Nickel is stable up to 400°C before it starts to interact with the substrate and the liquid phase. After the liquefaction is complete, the process temperature is increased to 470°C and kept for 80 s. In this time the Nickel breaks the GaAs bonds and a diffusive exchange, predominantly of Ge and Ga, begins. The substrate is heavily doped with Germanium which creates an ohmic contact between the 2DEG and the gold contact on the substrate.

5.1.3 Mesa-Wet etching of GaAs

Up to now we have a 2DEG that is accessible by several contacts but the electronic paths between them are not defined. As we wish to work with edge states in the quantum Hall regime, we need to define the general shape of our sample in the 2DEG, which we will refer to as mesa. The general approach is to remove the 2DEG in areas where it is not needed by wet or dry etching techniques. In most hetero-structures it is already sufficient to remove the dopant layer which will then reduce the mobility of the underlying 2DEG until the regions are no longer conductive, hence 10-100 nm are sufficient (depending on the depth of the dopant layer). The etching can be done in different ways, there are several dry etching techniques that remove GaAs selectively or non-selectively by either plasma etching, reactive ion etching, ion milling or by wet etching techniques which rely on the chemical removal of the material when submerged in a basic or acidic solution. We are using wet etching mainly because it is well established in the semiconductor industry so that formulas exist that provide smooth surface profiles, whereas the atom bombardments of the

dry techniques tend to create rough surfaces and also attack the masking material.

For the wet etching we will be using a $H_3PO_4 : H_2O_2 : H_2O$ solution and protect the mesa with an optical resist mask, that is defined by UV-Lithography. Alternatively it is possible to protect the mesa with a deposition of aluminium, however common Al etchant, based on KOH or TMAH (Tetramethylammoniumhydroxid), that are used for its removal are strongly corrosive towards the ohmic contacts (see our own tests in Appendix D.2) and should be avoided. The orthophosphoric acid is a non-selective etchant for GaAs and its alloys, thus suitable for the etching of the hetero-structure, and also known for the creation of very smooth surface profiles and precisely controllable etch depths of the order of nanometers [203]. However GaAs is not soluble in acids unless its surface is oxidized by H_2O_2 which is thus an essential component of the etching solution. We are using a mixture of 3:1 $H_3PO_4 : H_2O_2$ that is diluted in 80 parts of H_2O in order to slow down the etching rate to an approximate etching rate[2] of 1 nm/s. The sample is then submerged in the etching solution for about 2 minutes to remove 100-120 nm of material and then rinsed in water before the mask is removed in an acetone bath.
It has to be noted, in regard of following process steps, that the resulting etching of GaAs is anisotropic due to its "zinc blende" (fcc) crystal structure that creates an uneven chemical reaction in the different crystallographic directions [203]. Thus typically, in one direction an edge with an angle of 55° is formed while the perpendicular direction creates a "dovetail", an etching pit that may stretch some nanometers underneath the mesa's surface. The latter case needs to be kept in mind in order to deposit enough material to cover the gap between substrate and mesa for the successive deposition of contacts or gates onto the mesa.

5.1.4 Split gates for the QPC

With the mesa and contacts defined one can now fabricate any other needed structure by a combination of the already mentioned lithography, deposition and etching techniques. The last step in any case should be the deposition of the split gates onto the mesa (see figure 5.2a). The gates as are defined by e-beam lithography with a 10 kV beam on a MAA and PMMA bi-layer like for the ohmic contacts. Our split gate design may have widths ranging from 200-1000 nm that taper into symmetrical tips over a length of 500 nm and are deposited as at least 100 nm thick aluminium. To form a QPC, two split gates have to be brought into close contact with a gap of approximately 200 nm in between as shown on the SEM image in figure 5.2b. Aluminium is the metal of choice as it is possible to remove it specifically with KOH or TMAH etchants, in case they were to be damaged and need to be renewed[3].
With this last step the fabrication of the QPC is complete. By simply applying a polarising voltage onto the split gates the underlying mesa is electrically depleted in

[2] this is the effective etch rate for a GaAs/AlGaAs stack where the etching rates for GaAs and AlGaAs are slightly different so that the total etch rate and etching time depends on the cap layer thickness and also the composition of the AlGaAs layer

[3] as mentioned before: this removal process attacks the ohmic contacts and should just be avoided or only be done if the ohmics can be protected

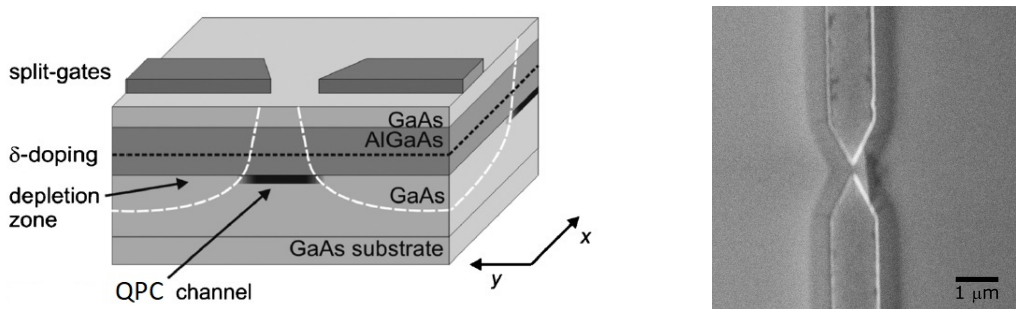

(a) (b)

Figure 5.2: (a) 3D-Schematic of the re-shaping of a 2DEG (dark) into a quantum point contact (QPC) by applying negatively charged metallic gates on top, taken from [204]; (b) SEM image of Al-split gates on GaAs with a 200 nm gap that are used to create a QPC.

a range that is indicated in figure 5.2a, so that the width in the gap is reduced to about 100 nm which allows only a single channel to pass.

5.2 The Cryogenic framework

As for all previous experiments that were concerned with the measurement of mesoscopic quantum conductors, a cryogenic system is the key component in order to enter the quantum regime. In our case a commercialized He_3-He_4 dilution refrigerator from CryoConcept is used that achieves a temperature of 15 mK. This dilution refrigerator is to hoist the sample itself as well as the low noise measurement equipment that requires cooling. While fridges have been commercialized, the wiring and the specifically required measurement components are best to be fitted by hand and tailored to the respective requirements. The challenges here are thus to fit all components in the narrow space of the low temperature stage of the fridge and to connect them to the other measurement equipment (or simple read-out devices), that is commonly placed at room-temperature, without thermally charging the fridge. We will thus firstly introduce the build-up of our dilution refrigerator[4] and then secondly how to mount the sample and other components in order to achieve a minimal electronic temperature within the system.

5.2.1 The fridge

Our system is a "dry" dilution refrigerator from CryoConcept shown in figure 5.3. It is an improved concept of the earlier "wet" dilution refrigerators which needed to be submerged in liquid helium to provide the necessary cooling for the condensation and operation of the fridge. Thus "wet" fridges where designed to be as small as possible

[4]A brief introduction to dilution refrigeration and a detailed description of its working principle is given in Appendix E

in order to reduce the volume and cost of liquid helium used. With the development of the pulse tube, a closed system cryo cooler that uses ^{4}He gas expansion for cooling, it became possible to build "dry" fridges without the need for liquid Helium cooling. Fridges with large cold volumes can be designed, with the constraint of protecting the coldest stages from the room temperature environment by multiple shields. This allows for a more spacious design so that a dry fridge can host a variety of components without limiting their form-factors and allows for easy installations and exchange of additional circuit components.
The fridge is split up in four shielded temperature zones at 50 K, 4 K, 1 K and the dilution unit. Within the 1 K shield an additional intermediate plate at 100 mK is positioned in between the still and mixing chamber plates which is used to thermalize the heat exchangers of the dilution line. When run, all zones are kept at vacuum and the system can be pre-cooled with liquid nitrogen during the cool-down in parallel with the helium pulsed tube, mounted to the 4 K plate. The two-stage pulse tube operates at 60 K in its first stage and at around 4 K on its second stage with varying cooling power for both stages. The entire system is able to produce temperatures of down to 11 mK on its mixing chamber plate which is achievable in the comparably short duration of 24h (48h with full measurement equipment). The mixing chamber plate and an additional table, that is thermally anchored to it, are used to mount all RF-circuit components that need to be kept at low temperatures and the sample.

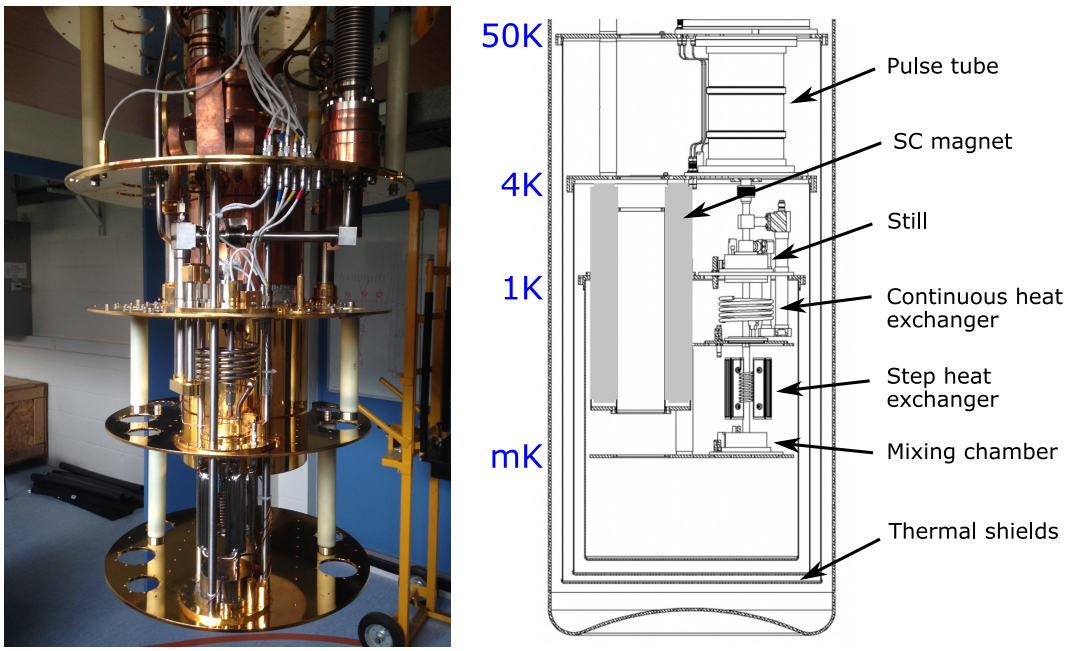

Figure 5.3: (a) Photo of the opened CryoConcept dry fridge, displaying the 4 K, 1 K and mixing chamber stages as well as the dilution unit (front) and the superconducting magnet(background); (b) Sketch of the fridge, rotated by 90 degrees taken from CryoConcept [205]. However, the sketch displays a different thermal anchoring of the pulse tube to the stages which is done using thick copper braids in our case.

Our system is also equipped with a superconducting magnetic coil that can generate

fields of up to 14 T (its 1 K shield is visible in the background) that is mounted on the 4 K stage with its individual thermal shield, reaching downwards. The parallel mounting of the magnet to the dilution unit allows for faster cool-down times of the system, as the magnet is directly anchored to its refrigeration stage, while samples can still be inserted from below into the magnet as they can be mounted on a cold-finger that is cooled from the mixing chamber plate below. This also enables the use of the entire volume around the mixing chamber plate to mount cabling and and voluminous RF circuitry.

5.2.2 Cold-finger and sample mounting

The design of the cold-finger and related parts was created in parallel to the sample design, which we will focus on in section 5.4.1.3, and thus tailored to our specific needs. Its main purpose is to provide a sample holder that is thermally anchored to the mixing chamber plate and extends into the bore of the magnetic coil. Thus the cold-finger is made up from thermally conductive copper with a gold coating to ensure a good thermalization and a massive socket on the plate whose thermal mass acts as a heat sink for any unexpected Joule heating coming from the RF-circuits. The "finger" itself is a thin beam extending into the coil that is completely enveloped in an additional thermal shield made from stainless steel. On the inside of this shield one can fix all required cabling for the mounted sample on top of the cold-finger. To easily mount and remove the sample(s) we have devised a custom made circular printed circuit board (PCB) on which the sample and the connectors to the electrical circuits are fixed.
The PCB is made from a 0.76 mm thick TMMA-10I sheet which provides a dielectric constant of ϵ=10. A 300 μm deep pocket of 8·12 mm^2 is milled into the PCB to place the sample chip[5]. The surface of the PCB is metallized with a 57 μm thick Copper/Zinc/Gold stack to create a metallic ground-plane. Areas that are not metallized are the recessed pocket and its edges, in order to avoid any unwanted short-circuits between the sample and the ground plane, as well as areas where specially designed electrical conductors lead from the center to the mounting places of the RF and DC connectors on the outer circumference. The conductors that are created within this metallization include 4 RF lines and a total of 24 DC lines. The RF line are designed as coplanar wave guides with 50 Ω impedance, thus it is designed as an initially 250 μm wide strip with a 200 μm gaps to the ground plane and tapers down leading up to the RF-plugs, keeping the same width/gap ratio. To connect them, we use straight board plugs with mini-SMP connectors made from gold plated brass and PTFE as dielectric material (Rosenberger 18S101-40ML5) with a base dimension of 4 mm^2. They are soldered onto the PCB with a soldering paste. The DC lines are grouped into 6 lines per side and terminated by each a 6 pin through-plug which are mounted through drillings in the PCB and soldered in place on the PCB backside. The DC conductor line width on the PCB is chosen to match the width of the sample's contact pads of 350 μm with an adequate spacing in between them and to the ground-plane.

[5]To allow the milling of this pocket, four pouches have to be made in the corners

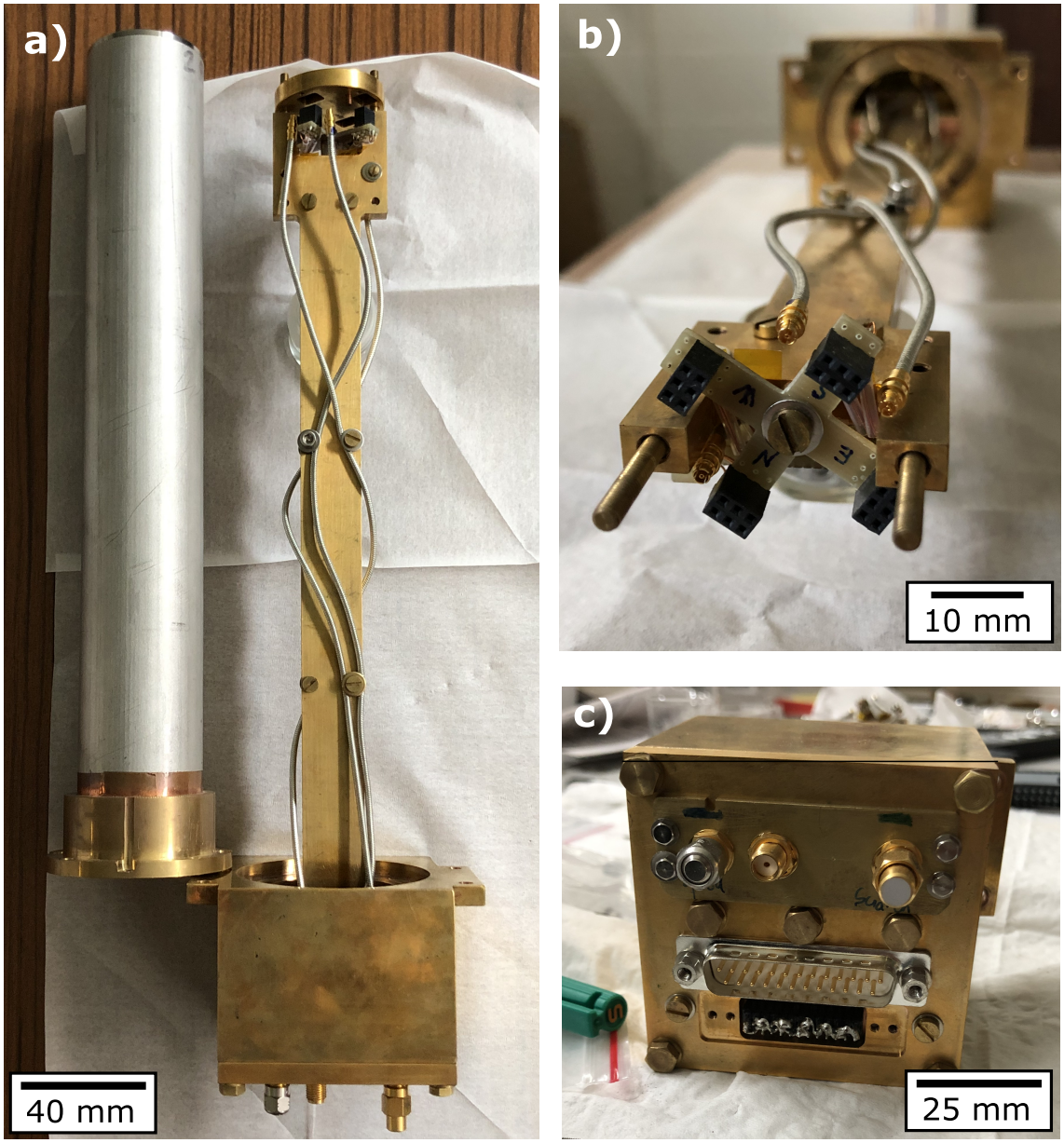

Figure 5.4: Photographs of the dismounted and disassembled coldfinger: (a) Overview of the coldfinger with mounted PCB holder next to its stainless steel shield; (b) Top view of the PCB mount showing the female DC connectors (black) and the mini-SMP connectors, (c) Bottom view of the coldfinger mass and its SMA RF-line connectors (top) and sub-D DC-line connectors (bottom). The mass of the coldfinger is screwed underneath the mixing chamber plate with the finger protruding through it into the magnet. The DC lines inside the coldfinger are split into separate wires, which are glued inside the metallic support bridge with silver epoxy, and connected to female pin contacts in which the PCB is plugged in (see b).

To mount the sample itself, it has to be firstly glued into the pocket using PMMA or similar materials and is then electrically connected to the PCB by wire bonding. The

bonds are either aluminium or gold wires of 25-50 μm diameter. For DC lines single bonds are sufficient whereas three bonds are necessary for the RF-lines to sufficiently emulate the electrical properties of a coplanar wave guide strip. For fewer bonds the local impedance mismatch causes an increase in the impedance of several Ω which needs to be avoided (our tests are presented in appendix F). The ground-plane is bonded all around the chip, but more densely bonded around the RF-lines where RF current densities will be higher.

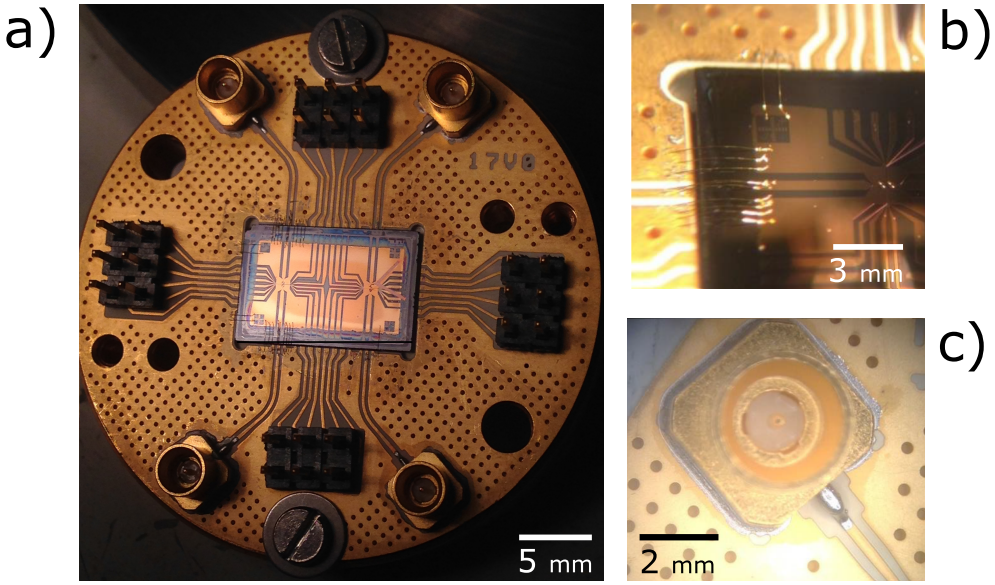

Figure 5.5: (a) Photograph of the test sample A26 glued and wire-bonded onto the custom mounted PCB. Only the RF lines and the ground plane of the left side have been wire bonded. b) and c) are magnified images of the wire-bonds and RF-plug and waveguide respectively.

The fully bonded PCB (shown in figure 5.5) is screwed onto a thicker copper PCB-holder through a set of small holes and provides additional threading to fix an additional (and optional) copper shield over the sample via the second set. The fully prepared PCB can then be mounted upside down on the cold-finger[6]. It is plugged into the female DC pin receivers of the cold-finger and also screwed in place through the larger drillings. The several fixation points ensure a good thermal contact between the PCB/Sample-holder and the cold-finger. While the DC-lines have been glued inside the cold-finger, spaced out and covered in thermally conductive silver-epoxy[7] for better thermalization, the RF cables are mounted to the cold-finger base but are free around the finger's neck. The RF-cables can simply be plugged into the mini-SMP connectors once the PCB is mounted. The connected mini-SMP and DC cables that plug onto the PCB run through the cold-finger and are all together thermalized to the mixing chamber plate temperature thereby assuring that the sample itself is also

[6]During the mounting process it is possible to short the DC pins on the PCB holder backside to prevent electro-statical charging of the sample

[7]EPO-TEK H20E, a silver containing two components epoxy with a low resistivity of $4{\cdot}10^{-6}\,\Omega$m

well thermalized.

5.2.3 Cabling and thermalization

From the base of the cold-finger the sample is connected to the different components and room-temperature equipment via different DC and RF cable lines. The RF components and their arrangement are described in section 5.3.2, instead here we present the thermalization that we installed in the fridge to avoid a thermal charging of the plates via the cables that go in and out of the fridge. Our setup is shown in figure 5.6.
We start with the RF-lines for which we have four separate coaxial lines made from silver plated stainless steel that run from 300 K to the mixing-chamber plate. Due to electronic heat conduction, electrically connecting the sample stage might warm up the mixing chamber plate. To minimize the added thermal load from the lines, the coaxial cables are made from steel with a thin sliver plating, rather than solid copper, because the steel core has a high DC resistivity which decreases the thermal conductivity (and thus the thermal load), while the RF signals propagate only through the highly conductive silver plating due to the skin effect. Two of these coaxial cables are meant to send microwave signals from RT to the sample via the 2 lines (A and B) and the other 2 for the return signals.
To further cool down the electronic temperature in the input lines, attenuators, made up of thin films of highly disordered metals and with an overall attenuation of 80 dB, are placed in the line to thermally anchor the inner conductor of the line to the intermediate thermal plates and thus cool down the electronic temperature step-by-step. The return signals however are transported firstly through NbTi SMA-cables from the MC plate to the cryo amplifier on the 4 K plate and then via silver plated-SS to the detection equipment at 300 K. The lines for the return signals do not have any attenuators to maximize the signal to noise ratio. Thus we forego cooling them and tolerate an increase in the thermal load on the 4 K stage. In addition to this, the superconducting cable provides a low attenuation while it thermally decouples the sample from the cryo-amplification stage as it does not conduct heat.

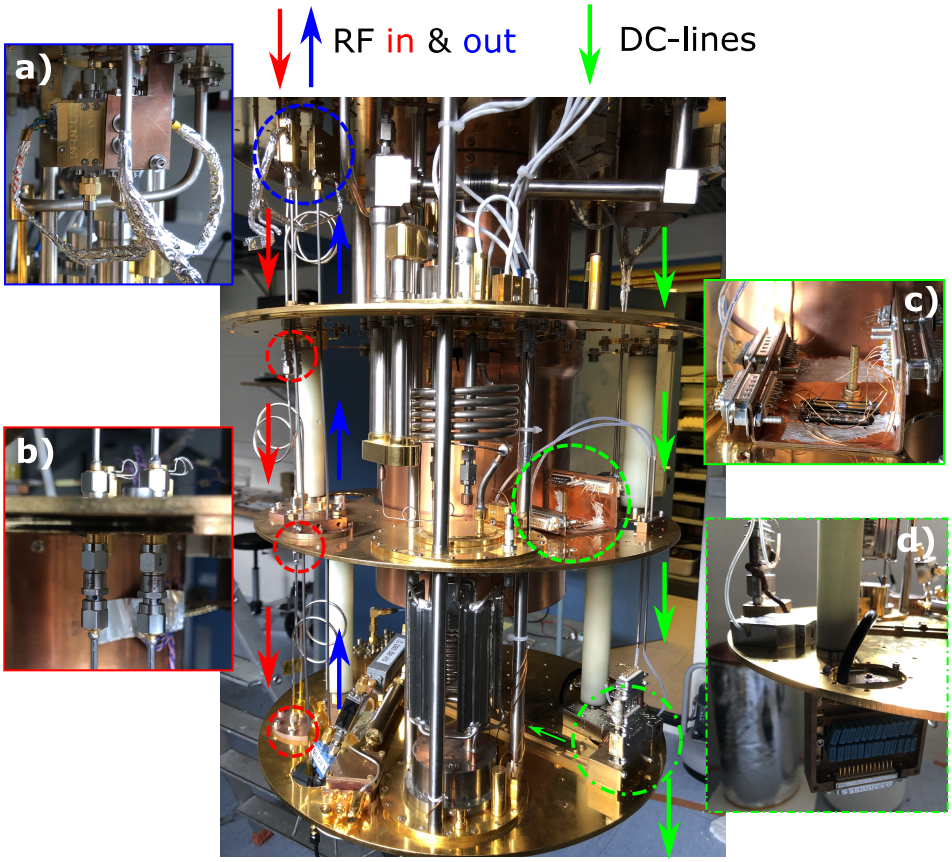

Figure 5.6: Photographs of the dilution refrigerator with implemented wiring including RF and DC cabling as well as other components. The overall layout of the RF lines (red input, blue output) and the DC-lines (green) is indicated by arrows in the central image. The RF-input (red) is guided from 300 K to the MC plate via silver plated stainless-steel coaxial cables from where it can be connected with flexible SMA cables to the coldfinger. Along the line attenuators are placed at every stage in order to thermalize the incoming electrons. A gold plated SMA bulkhead connector is mounted in every stage that connects the line to an attenuator with increasing attenuation for lower temperatures. The RF out-put (blue) prohibits using attenuators as they would diminish the signal to noise ratio and is instead directly connected from the coldfinger to the cryogenic pre-amplifier anchored to the 4K stage (a). The connection to the pre-amplifier is made via NbTi SMA cables and then from the 4 K stage to room temperature by silver plated stainless steel coaxial cables. The DC lines (green) are gathered up in a braided cable which is thermalized at every stage by screwing the connectors on to that stages. The interior individual Manganin wires thermalized at the 100 mK on a copperplate on to which the wires are separately glued with a thermally conducting silver epoxy. On the mixing chamber plate, the lines are diverted into a sub-D connector that will be connected to the coldfinger (d) and another metal-plate thermalizer leading up to SMA plugs from where DC line connections are available to connect to the cold finger when necessary (for example to DC bias the normal tunnel junction used in chapter 4).

The DC lines are made from thin insulated Manganin wires (Magnanin is a copper based alloy with 13 % Manganese and 4 % Nickel) that are kept in a braided cable with stainless steel casing for the most part. Manganin has a residual resistivity ratio of order one, so that its electrical resistance does not change much when cooling down and the addition of Manganese in the alloy reduces the wire's thermal conductance (and also increases the resistivity). The DC cable is thermalized in different ways at several plates. Firstly, the plugs that connect the different cable section that make up the line, are attached to the plate and thus thermalized. However, due to the insulation in between these wires, the inner conductor can not be cooled down efficiently at the lowest stages (lower than 1 K), where the phonon channels become ineffective. To cool down the inner conductor we have built a thermalizer mounted on the 100 mK stage in between the still and mixing chamber plate. The DC braided cables plug into a device where Manganin wires are freed from the braid and glued onto a copper plate with conductive silver epoxy. Thus the inner conductors are well thermalized to 100 mK. Another similar thermalizer, using 30 cm longer more resistive "Isaohm" wires (a Nickel-Chrome alloy) and an electronic shielding, is placed on the MC plate for all DC lines that are not leading into the cold-finger (which is already hosting such a thermalization element). The total DC resistance from RT to the MC plate is about 300 Ω, from whom about 100 Ω come from the last Isaohm thermalization stage, which adds a capacitance of about 100 pF. We thoroughly tested the stability of these elements by measuring their capacitance to ground before, during, and after abruptly dipping a test sample in liquid helium for several days in a row without noticing any significant changes. We have also tested the achievable mixing chamber plate temperature with all RF circuit components and thermalizers equipped. We directly measured the MC temperature, which did not change and remained at 12 mK, and the electronic temperature by fitting the high frequency noise of a voltage biased normal tunnel junction at the coldfinger but also when directly screwed to the MC plate, to be about 30 mK, which provides sufficiently low temperatures for our measurements. Further, with the help of F. Portier's team, we could independently check the rms voltage developing at the input of the sample after the used filtering scheme by measuring the spectral width of the RF power emitted by the AC Josephson effect and determined it to be about 100 nVrms. In consequence $e\delta V$ is about 1 mK and can thus not explain the 30 mK electronic temperature. We thus suspect that the 20 mK difference between the MC plate and measured electronic temperature on the sample arises from inefficient shielding of high energy photons at the level of the MC plate and the 100 mK plate or an inefficient thermal anchoring of the samples. In anyway, the achieved 30 mK temperature is sufficiently low to be well within the quantum limit in the 4-8 GHz band used to equip the fridge (hf/k_BT is about 10 for $f = 6$ GHz and $T = 30$ mK).

5.3 The noise detection setup

In our case we are concerned with the measurement of microwave frequency RF-signals so that, before we cover the components themselves, we want to elaborate on

the general engineering challenges of RF circuits. When working with AC-currents, one has to deal with the phase propagation effects of the EM fields that carry the signal when the signal's wavelength is smaller than the length of the circuit $\lambda \leq L$. Our system has a cabling length of about a meter, so that propagation effects already appear at frequencies of about 100 MHz. We thus need a conductor that guides the developing electromagnetic wave signal without reflecting it. Different designs exists that are generally referred to as transmission lines, with the most common one being the coaxial cable. A coaxial cable provides a fixed impedance for a given frequency range that is standardized to $50\,\Omega$ for commercially available coaxial cables and microwave detection equipment. This proves to be a major problem if we want to connect quantum circuits with an impedance corresponding to the quantum of resistance of a single electronic channel $R_k = 25.8\mathrm{k}\,\Omega$ to a $50\,\Omega$ environment. When impedances are mismatched like this, the result is s substantial loss of signal due to the reflection of the electromagnetic waves at the interface of the measuring equipment and the sample, strongly degrading the detection efficiency. Our solution to overcome this circuit engineering challenge is to use an impedance transformer that converts the standard $50\,\Omega$ impedance into a higher impedance as seen by the sample. Thus we have created a special impedance transformer based on a lumped element resonating coil that is stable at high magnetic fields and can thus function as an on-chip transformer for our sample in experiments with high applied magnetic field.
In this section, we will firstly introduce the basics concerning microwave conductors and the fundamentals of RF-circuit engineering before turning to the essential low noise measurement devices like amplifiers and detectors that we will be using (An in depth description on Microwave engineering can be found in [206]). The design and fabrication of our lumped element impedance transformer will be focused on in more detail in the next section 5.4.

5.3.1 Radio frequency circuit engineering

In order to conduct high frequency electronic signals one cannot rely on common conductors designed as a single metallic conductor. Because high frequency alternating currents propagate as electromagnetic waves on the surface of the conductor, within a finite penetration depth given by the skin effect, they are prone to couple to different sources and could pick up parasitic signals. Thus it is necessary to use a conductor that guides the RF-signals and provides a shielding against any form of losses.
These microwave conductors or transmission lines are build up from an inner conductor that is mantled by an insulating layer and an outer conductor. Thus the inner conductor always has a well-defined ground with a fixed wave impedance. Transmission lines can be designed either in 3D as a coaxial cable (see figure 5.7a) or in 2D as for example a coplanar waveguide (see figure 5.7b). While coaxial cables are the preferred conductors in between RF devices, the coplanar waveguide is a cost-efficient and easy to fabricate solution that will be used pre-dominantly on-chip for our sample fabrication (Further information on coplanar waveguides can be found in [207]).
A transmission line can be simplified into a lumped element circuit network (see figure

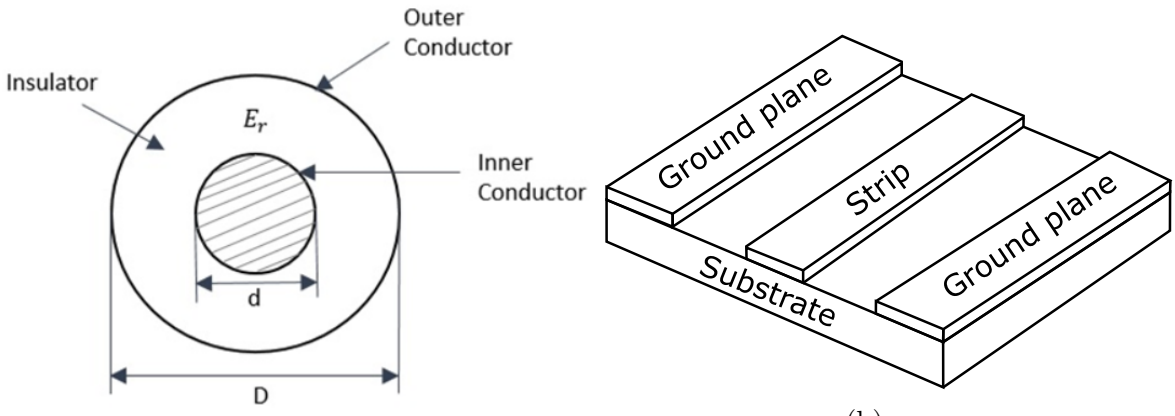

(a) (b)

Figure 5.7: (a) Sketch of the cross-section of a coaxial cable. The current is transported by the inner conductor while the EM waves propagate in the dielectric buffer-layer. The generated opposing current is carried by the outer conductor; (b) Schematic illustration of a coplanar waveguide geometry consisting of three metallic strips on a dielectric substrate [208]). Compared to the coaxial cable, the coplanar waveguide is an open 2D structure with an incomplete shielding. However it is nearly perfect for propagating waves of sizes similar to the gap because the waves are almost completely forced into the substrate due to the narrow spacing of the gaps in between the strips.

5.8), build up from resistors (R), conductors (G), inductors (L) and capacitors (C). The resistance originates from the conducting material, while the inductance accounts for the magnetic field generated by the alternating currents. The conductance and capacitance are found as the leak current and capacity across the insulating material. Based on this we define the characteristic parameters of the transmission line, the transversal admittance $G + j\omega C$ and the longitudinal impedance $R + j\omega L$ per unit length. With these we formulate the characteristic impedance Z_C of the transmission line, which describes the ratio of the voltages $v_{+/-}$ and currents $i_{+/-}$ of a wave propagating in the forward $+$ or backward $-$ direction:

$$Z_C = \frac{v_{+/-}}{i_{+/-}} = \sqrt{\frac{R + j\omega L}{G + j\omega C}} \tag{5.1}$$

Local quantities like the voltage to ground $v(z,t)$ and the current transported through the line $i(z,t)$ result from the superposition of forward and backward waves: $v(z,t) = v_+(z,t) + v_-(z,t)$, and $i(z,t) = i_+(z,t) - i_-(z,t)$. This can often be simplified by assuming an ideal loss-less transmission line so that the ohmic loss of the resistance and the conductance leakage are negligible, giving:

$$Z_C = \sqrt{\frac{L}{C}} \tag{5.2}$$

Other sources of signal loss can be found within a transmission line circuit that

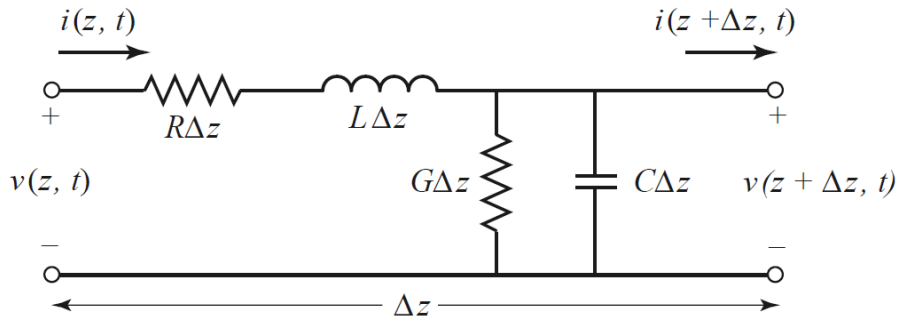

Figure 5.8: Lumped-element representation of a transmission line (or co-axial cable) as a combination of resistance, inductance, conductance and capacitance, taken from [206].

includes different elements. In any real circuit there will be some scattering centers that cause the electromagnetic waves to be reflected, resulting in a loss of transferred power. So firstly, we introduce the general power transfer from a source via the transmission line to a load. In the simplest case of a two-port network, where a signal enters a device or transmission line (see figure 5.9), an applied voltage V_1 generates a current I_1 that is either transmitted or reflected, while likewise this happens from the other side with current I_2 in the opposite direction. So to obtain the total current in one direction, we have to determine the superposition of the two scattered currents. The scattering in this system is described by a scattering matrix $\mathbf{S}$ that relates the incoming and outgoing voltage waves of a two port system referred to as device under test (DUT) as shown in figure 5.9: While S_{11} and S_{22} refer to the reflection of the incoming wave from the according ports, S_{21} and S_{12} are the transmission of the waves across the DUT.

$$S_{11} = \frac{V_1^-}{V_1^+} = \frac{Z_S - Z_L}{Z_S + Z_L} \tag{5.3}$$

$$S_{21} = \frac{V_2^+}{V_1+} \tag{5.4}$$

To maximize the power transmitted, one has to minimize the reflection which is done by matching the impedances of source Z_S and load Z_L, following the maximum power transfer theorem (Moritz von Jacobi 1840). If this is the case, they are referred to as matched, if not, then they are mismatched and part of the incoming wave is reflected as described by the reflection coefficient $|S_{11}|^2$, that takes values from 0 to 1 with 1 being full reflection. In the same fashion we could also use the transmission coefficient, the ratio of the transmitted voltage wave over the incident wave equal to S_{21}, as for an ideal loss-less system $|S_{21}|^2 = 1 - |S_{11}|^2$. However any realistic DUT or just simple transmission lines have intrinsic losses that depend on their geometry and the applied signal frequency.
When designing RF systems it might however be more useful to describe a transmission line in terms of its impedance rather than the scattering of voltage waves.

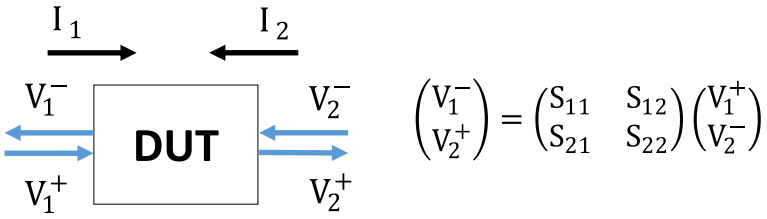

Figure 5.9: Simplified illustration of a 2-port network that links the incoming and outgoing voltage waves via the scattering matrix **S**

Therefore the impedance matrix **Z**, relating the currents to the voltages at every port of the system, can be used:

$$\begin{bmatrix} V_1 \\ V_2 \end{bmatrix} = \begin{bmatrix} Z_{11} & Z_{12} \\ Z_{21} & Z_{22} \end{bmatrix} \begin{bmatrix} I_1 \\ I_2 \end{bmatrix}, \tag{5.5}$$

with $Z_{xy} = V_x/I_y$. The individual Z-parameters describe the conductor under open-circuit conditions: When all ports except one are open, a current is applied to this one port in order to measure the developing voltages at all ports. This is exactly how for example electromagnetic solver programs that we will use in section 5.4.1.1 calculate the propagation of EM waves in the geometric structure of a scattering experiment. In the simple case of a 2-port network, setting port 2 as an open gives Z_{11}, the reverse configuration Z_{22} and with both ports connected one obtains Z_{12} and Z_{21}.
The impedance matrix **Z** can also be obtained by converting the scattering matrix **S** via equation 5.6, with Z_0 being the reference impedance of the system which is commonly $50\,\Omega$.

$$\mathbf{S} = (\mathbf{Z} - Z_0\mathbf{I})(\mathbf{Z} + Z_0\mathbf{I})^{-1} \tag{5.6}$$

5.3.2 Low noise amplification (LNA) and signal detection

Having introduced the basics RF-circuitry, we can now focus on the discussion of the typical RF circuits that we have used to detect the RF power emitted by a DC biased mesoscopic conductor. A full detection system is sketched in figure 5.10: The sample in the cryogenic setup is DC biased with respect to ground, through the low pass branch of a bias tee, and the RF power emitted by the quantum conductor is led to the amplification chain through the capacitive high pass port of the bias tee. The amplification chain consists of a band-pass cavity filter, defining the detection bandwidth, and a pair of RF isolators routing the emitted power to the amplifier, while protecting the sample from the noise emitted by the amplifier operation diverting it to a matched load where it is dissipated and replaced by a blackbody radiation at the temperature of the load. From the cryogenic amplifier, it leads to the RT chain where the signal is further amplified, filtered around the same detection BW and rectified by a fast detection diode. The converted DC voltage signal from the diode is then red-out with a voltmeter.

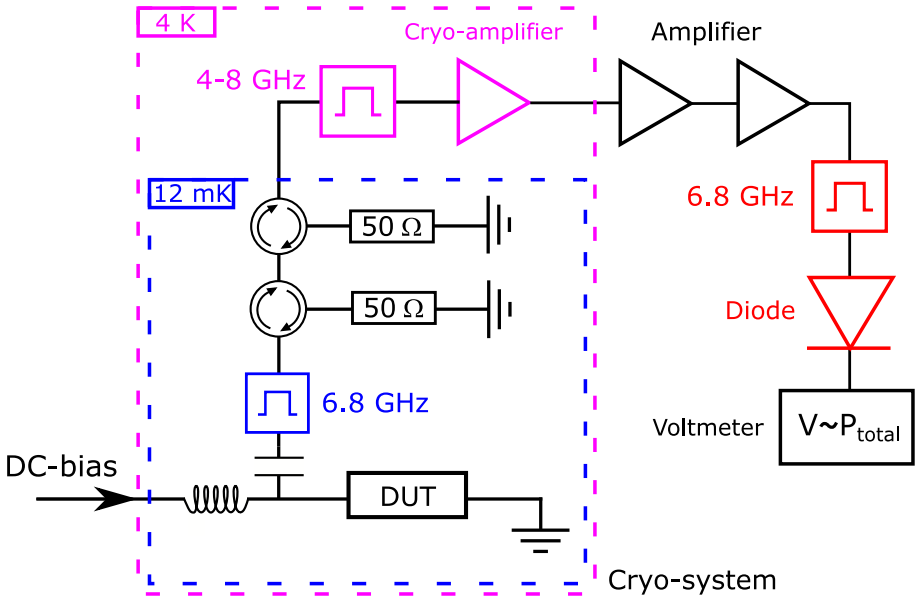

Figure 5.10: Noise measurement with a rectifying diode for a sample in a cryogenic system at temperatures at 15 mK. The RF signal from the sample is coupled to the 50 Ω-matched RF-detection chain via the capacitive port of the bias-tee. In between is a narrow bandwidth cavity filter, setting the detection bandwidth, and two circulators that prevent any reflected signals or incoming signals from the amplifiers from influencing the DUT by redirecting them to ground via a matched 50 Ω resistor that dissipates the incoming power. The transmitted signal is amplified by a cryogenic pre-amplifier with prepended filter at the 4 K temperature stage and by more amplifiers at room temperature. The amplified signal is filtered and converted into a DC voltage signal by the rectifying diode which is then read out via a simple voltmeter.

When setting up such a detection chain, the most important component is the amplifier that allows to enlarge the small signals that we try to measure. An amplifier in general is an electrically active device that increases the amplitude or power of an input signal (voltage, current or both) at its output. The gain G, the ratio of the output to input power greater than 1, is created by a non-linear active device in the circuit of the amplifier. Earliest models used vacuum tubes while modern amplifiers are based on transistors.
Amplifier exist in multiple designs with different applications in mind, such as power amplification or low noise amplification. As we want to measure small noise signals we will be working with low noise amplifiers (LNA). It needs to be able to amplify a low power signal without degrading the signal to noise ratio. Like any active electrical component, an amplifier circuit has an electrical noise floor that is independent of the input power . This noise is added on top of the output signal and decreases the signal to noise ratio, thus LNA's are designed to add as few noise as possible. For a well designed amplifier the noise power and gain do not depend on the frequency in a specified operating bandwidth. It is thus classified as white noise which is often represented as an equivalent noise temperature T_e. The assumption is that a noisy

matched resistor R at temperature T_N emits a Johnson-Nyquist thermal noise having the same power as the noise power added by the operation of the amplifier:

$$P_n = \left(\frac{V_n}{2R}\right)^2 = k_B T_N \tag{5.7}$$

The equivalent noise temperature refers to the noise power P_{noise} added to the amplifier input power, so that the total output is $P_{out} = G \cdot P_{in} + P_{noise}$. Thus the noise temperature is defined as the added noise power measured at the output divided by the amplifier's gain G:

$$T_N = \frac{P_{noise}}{G k_B}, \tag{5.8}$$

which allows to calculate the equivalent temperature and the gain of an amplifier by measuring its output power P when connected to a matched load at two different known temperatures:

$$T_N = \frac{T_1 - \frac{P_1}{P_2} T_2}{\frac{P_1}{P_2} - 1} \tag{5.9}$$

$$G = \frac{P_1 - P_2}{k_B (T_1 - T_2)} \tag{5.10}$$

In our setup we use a cryogenic-HEMT pre-amplifier [8] with a gain of 42 dB at 4 to 8 GHz bandwidth and a noise temperature of about 2 K and a room-temperature amplifier that has a gain of 40 dB at 4 to 8 GHz bandwidth and a noise temperature of 70 K. The application of a cryogenic amplifier allows to obtain higher SNR that would not obtainable with only room-temperature amplifiers as small measurement signals would not be detectable due to the high thermal noise of the room-temperature amplifiers. The cryogenic amplifier not only provides a much lower T_N but can also be placed closer to the sample in the cryogenic system making insertion losses prior to amplification smaller, thus further increasing the signal to noise ratio by few %.
For the measurement of low noise signals in our experiment, it would be sufficient to use just a single cryogenic amplifier but by implementing two addition room-temperature amplifiers, we increase the total gain, which provides more flexibility on the attenuation and mounting of circuit components, e.g. band filters or mixers, for different measurements. On one hand it helps to achieve the right dynamical range for the detection equipment and allows to tune the signal level necessary for different signal detectors, such as VNA's, diodes, acquisition cards and on the other hand the added attenuator, needed to avoid over-saturation of the signal, diminish the standing wave ratio (SWR) that may develop when many RF-devices are placed in a system since they are never perfectly 50 Ω matched.

[8] "LNF-LNC4-8C" from Low noise Factory

5.4 Fabrication of a RF impedance transformer

The last crucial RF component that is missing is the impedance transformer that connects the 50 Ω detection chain and the sample. An impedance transformer is an element transforming a detection impedance over a finite bandwidth, usually realized with the help of electromagnetic resonators.
Transformers can be made from either lumped elements e.g. dense planar coils (see [63,64]) or transmission lines/wave guides like the $\lambda/4$ resonators [65–67], also known as quarter wave transformer. While lumped elements need to be specifically designed as the frequency $f = 1/2\pi\sqrt{LC}$ is dependent on inductance and capacitance, the quarter wave transformer's frequency can be set freely by adjusting its length. The later approach was demonstrated in the context of detecting the RF emission from quantum coherent conductors by E. Zakka-Bajjani et al. [66] for the measurement of shot noise emitted by a QPC with 200 Ω characteristic impedance. Higher impedances were achieved by [68–72] using a chain of superconducting SQUIDs as quarter wave transformer that generate few kΩ of characteristic impedance. The achievable strong coupling was demonstrated between an EM mode and a tunnel junction [72] as well as a quantum dot [73]. Even higher characteristic impedances were achieved for coplanar wave guide resonators with high kinetic inductance of more than 3 kΩ for Niobium-Tungsten hybrid systems [74] and reaching up to 5 kΩ for disordered superconducting aluminium films [75]. Nano-fabricated superconducting coils have even reached Z_c close to 25 kΩ at about 5 GHz by removing the dielectric substrate beneath which diminishes the shunting capacitance [209].
As we will see in brief, a characteristic impedance of about 1 kΩ is already sufficient to provide a detection impedance of about R_k when connected to a 50 Ω line. Even though all mentioned methods provide the required characteristic impedance, the general approach is not suitable for the experiments envisioned in chapter 4. The perpendicular applied magnetic fields, necessary to be working in the quantum Hall regime, would cause any known superconductor to become normal conducting, hence a superconducting material based transformer cannot operate in magnetic fields. Also, we cannot make wires with nano-scale cross-sections (diminishing the coil capacitance and thus enabling higher impedances at a given frequency) since the corresponding intrinsic losses in the normal state would both prohibitively degrade the resonance quality factor, but also give rise to thermalization problems. We found it to be possible to achieve sufficiently high characteristic impedances with lumped resonators made from normal metals with micron-scale cross-section, which can then be used in high perpendicular magnetic fields making it possible to conduct experiments in the fractional Hall regime.

5.4.1 Design of high impedance transformers on-chip

The simplest scheme to increase the finite frequency detection impedance is to place a big inductance in series with a 50 Ω transmission line. The inductance L increases the detection impedance with the frequency, but at some point its shunting capacitance C will provide a lower impedance path to ground. Thus the detection impedance

is only transformed in a finite bandwidth around the self-resonance $f_0 = 1/2\pi\sqrt{LC}$ of the inductance. Achieving large detection impedances at high frequencies is thus challenging as one cannot blindly push the inductive response, but needs to keep the shunting capacitance moderate as well. In this section we introduce the design, fabrication and testing of planar coils made from normal metals fulfilling the demanding constraints of the experiments envisioned in chapter 4.

5.4.1.1 Design of the planar coil resonator

The design of our resonator was based on previous results within our research group, done by C. Rolland, resulting in a spiral inductor that was etched in Niobium on a quartz substrate with a characteristic impedance of 1.97 kΩ at 4.4 GHz resonance frequency [77]. The main challenge of transferring a similar design to our project is to achieve a sufficiently high characteristic impedance and resonant frequency when recreating it on GaAs/AlGaAs substrates. GaAs has a dielectric constant of $\epsilon = 12.9$, which is three times larger than the dielectric constant of quartz ($\epsilon_{SiO_2} = 3.8$), and thus dramatically increases the constraints of the design. Thus, we have optimized the coil design by simulation in the electromagnetic wave solver Sonnet® for the constraints of our experiment.
A first design constraint is to access the quantum regime, $hf \gg k_B T$, which with a dilution fridge temperature of about 15 mK requires to work with frequencies at least in the few GHz range [9]. The fridge has thus been equipped with a detection line where the discrete RF elements (circulators, amplifiers) are specified in the C-Band, so we optimize the design to achieve a resonance frequency centred within the C-Band. Secondly, we need an impedance transformer to match a quantum conductor of about 26 kΩ impedance to a 50 Ω impedance line. The coil itself is used for this as it provides a sizeable inductance in series with the transmission line.
The simplest lumped circuit model describing a planar coil geometry provides a series inductance L with its internal series resistance R and a shunting capacitance C that can be modeled as lumped element RLC circuit shown in figure 5.11b.
Based on this model we define the characteristic properties of the resonator: as the capacitance shunts the inductance, the maximum detection impedance is obtained when their respective impedances are equal: $2\pi L f_0 = 1/(2\pi C f_0)$ so that:

$$f_0 = \frac{1}{2\pi \cdot \sqrt{LC}} \tag{5.11}$$

As illustrated in figure 5.11c, the other parameters controlling the impedance transformation are the characteristic impedance Z_c defined as:

$$Z_c = \sqrt{\frac{L}{C}}, \tag{5.12}$$

and the quality factor Q, which is limited by both the radiative losses Z_{load} and internal losses R,

[9] at $T_{min} = 15$ mK the minimal working frequency is $f_{min} \geq k_B/h \cdot 15 \cdot 10^{-3} K = 312$ MHz

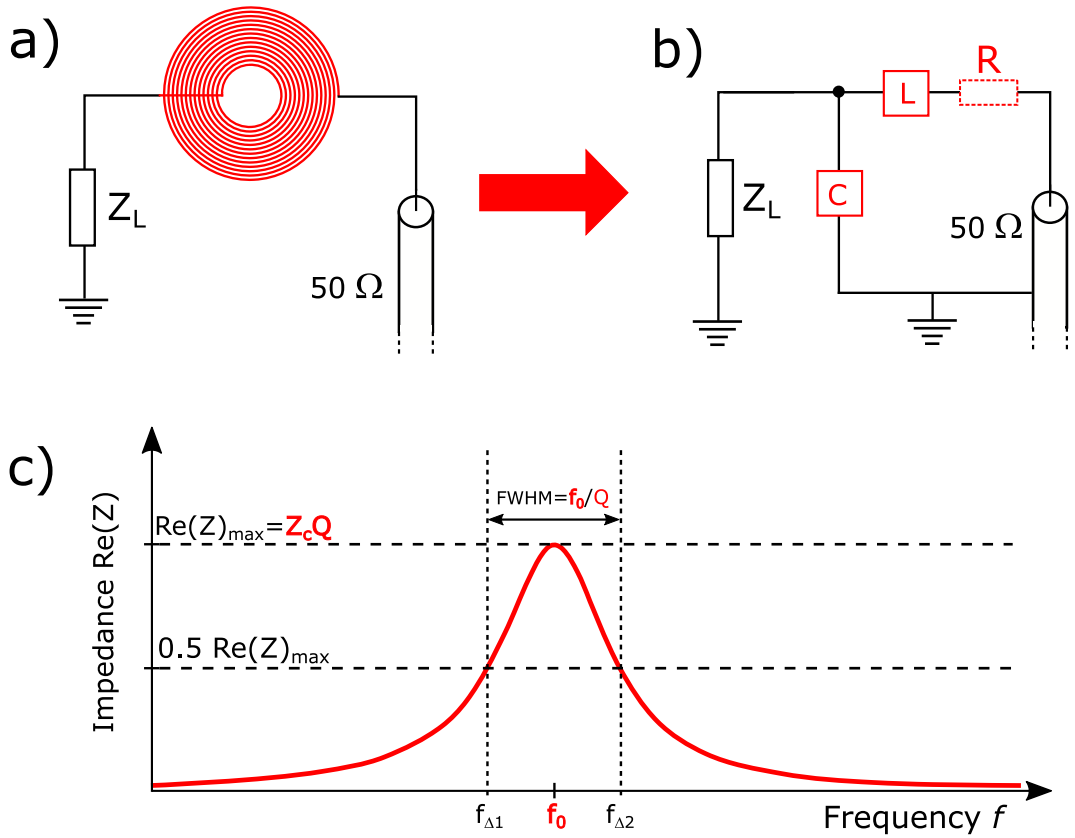

Figure 5.11: Sketch of a planar coil implemented as impedance transformer in between a 50 Ω transmission line and a larger load impedance Z_L (a). The coil is represented as a parallel LC circuit (with inductance L and capacitance C) and a series internal resistance R (b). The output impedance of the coil, with Z_L set as an open, is plotted in (c). The resulting real part of the detection impedance is (in the high Quality factor limit $Q \gg 1$) a Lorentzian with parameters: $f_0 = 1/(2\pi\sqrt{LC})$, $Z_c = \sqrt{L/C}$ and $Q = Z_c/(Z_{load} + R)$.

$$Q = Z_c/(Z_{load} + R), \tag{5.13}$$

from which one can simply estimate the maximum value of the detection impedance:

$$Re[Z_{detection}(f_0)] = Z_c \cdot Q \tag{5.14}$$

and the detection bandwidth:

$$FWHM = f_0/Q \tag{5.15}$$

As a reference, when internal losses are neglected, one can see that a coil with $Z_c = 1\,\mathrm{k}\Omega$ gives about $20\,\mathrm{k}\Omega$ detection impedance with a $Q = 20$. Which would give very comfortable detection BW of about 300 MHz resonating in the middle of the C-band at 6 GHz. In order to reach such figures we need to adjust the coil geometry to increase the inductance that is based on its magnetostatic influence while managing

the coil's internal shunting capacitance. However, using handbook formulas for the calculation of the coils inductance neglects propagation effects as required wire lengths are comparable to the wavelengths within the C-band. Thus, we cannot rely on the lumped element description and need to simulate the EM-waves, accounting for the propagation effects, in the coil design by using the EM-wave solver Sonnet®.

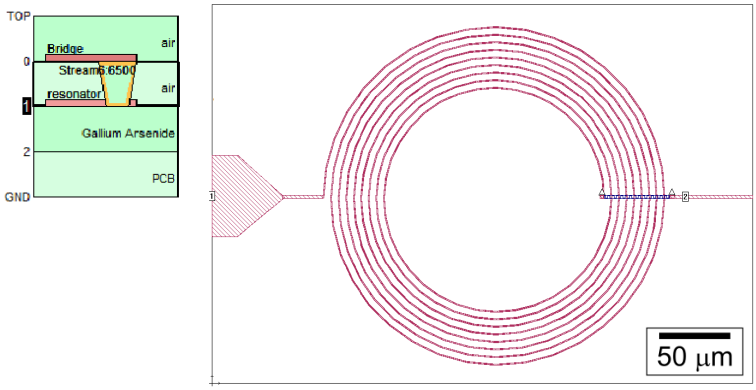

Figure 5.12: Sketch of an inducting coil in the circuit editor of the EM solver software Sonnet®. This coil has 8.5 windings with an inner diameter of 150 μm, both the wire width and the spacing are 1 μm. The layer structure of the model is shown in the top left corner. The port on the left has an intrinsic 50Ω series resistance to emulate an attached detection line.

For the simulation we define a coil in a 2-port network (figure 5.12) with the metallization on top of a GaAs substrate, with dielectric constant $\xi = 12.9$, and air set as surrounding medium with $\xi = 1$. On top of the first metallization layer we add another in which we define a bridge on a dielectric support material in order to connect the inner loop to the second port on the right. For first trials, the material of the coil is assumed to be loss-less. Several simulations were run for varying coil thickness, width, spacing and number of windings to obtain the impedance matrix of the coil from both 50Ω-ports for different frequencies. With the simulated matrix parameters we can calculate the input impedance as seen from Port 1 and the output impedance of the resonator as seen in Port 2 (see equations 5.16 and 5.17). The plotted output impedance Z_{out} then gives access to the resonance frequency, the bandwidth and the characteristic impedance which is Z_c as approximated by equation 5.18.

$$Z_{out} = Z_{22} - \frac{Z_{12} \cdot Z_{21}}{Z_{11} + Z_{source}} \tag{5.16}$$

$$Z_{in} = Z_{11} - \frac{Z_{12} \cdot Z_{21}}{Z_{22} + Z_{load}} \tag{5.17}$$

$$Re(Z_{out})_{max} = \frac{{Z_c}^2}{50\Omega} \tag{5.18}$$

First simulations were done with a flat 2D loss-less material, hence no thickness was attributed to the coil, allowing for fast simulations to determine the ideal amount of

windings for the coil. Even though the coil is not truly a simple lumped element, we could associate an equivalent LC representation using the formulas 5.11, 5.12, 5.13 and 5.14 since the resulting Q-factor is relatively large $Q \gg 1$. We used the calculated inductance L and capacitance C as indicators for the optimization of the design. For planar coils the inductance and capacitance between lines both increase as the number and length of windings increases. For few windings, the increase of the inductance is larger than the capacitance but this changes at a critical length/number of windings when the increase in capacitance outgrows the added inductance. Up to this threshold, the inductance-capacitance ratio is larger than 1 and the characteristic impedance grows. Past the threshold, the ratio drops and the resonators characteristic impedance decreases for further windings added. The maximum of the impedance is thus found at the transition of the ratio for added L/C. In the case of the loss-less coil, we found that the resonance frequency would drop out of the C-Band before reaching this threshold. Suitable impedance and frequency pairs are at around 15.5 windings at the shown geometric parameters (see table 5.1). The results of the simulation are listed in table 5.1 together with the calculated electrical parameters L, C and its resonator parameters.

Table 5.1: Simulation results for planar loss-less coils with different number of windings N, inner diameter D_i, width w and spacing s. Z_c is calculated based on equation 5.18, with f_0 and Q taken from the plot of Z_{out}. The electrical parameters are calculated based on the resonating parameters using equation 5.18 and 5.12, 5.15, 5.11.

N	D_i [μm]	w [μm]	s [μm]	Z_c [Ω]	f_0 [GHz]	Q	L[nH]	C [fF]
13.5	60	1	2	930.483	6.55	28.48	22.6	2.6
14.5	60	1	2	979.365	6	28.57	26.0	2.7
15.5	60	1	2	1030.935	5.52	30.67	29.7	2.8
16.5	60	1	2	1079.446	5.1	31.88	33.7	2.9
17.5	60	1	2	1127.556	4.72	33.71	38.0	3.0
18.5	60	1	2	1175.847	4.39	33.77	42.6	3.1

Based on these first results we refined our simulation by adding a finite resistivity for a selection of suitable materials such as copper, gold and silver. We used silver as reference with a resistivity of the order of 2 nΩm below 4 K. With the introduction of a resistivity, a thickness has to be allocated to it for it to be solved in Sonnet®, which was set to 500 nm. This was firstly done in a 2D-model, where the thickness is only considered numerically, to compare results with the previous loss-less simulation. The 2D simulation showed the same value of characteristic impedance with an expected dampening of the resonance from a quality factor of 30 to 10 due to the intrinsic losses arising from the added coil resistivity. Afterwards the design was simulated with a 3D model. The 3D model is created with multiple layers of meshing throughout the metallization-layer which allow for a more precise simulation of the distribution of the EM-waves and gives a more accurate results. As we have now introduced a resistivity to the coil, the previously assumed simple RLC model, where the Q factor was only limited by external losses in the load resistor R, does not apply anymore because

the non-negligible distributed resistance of the coil complexifies it and the resonance line cannot be obtained from a simple Lorentzian model. Thus the characteristic impedance Z_c is from now on calculated as the integral of the impedance over the frequency as in equation 5.19 as this definition is less model dependent:

$$Z_c = \frac{2}{\pi} \int \frac{Re(Z)}{f} df \tag{5.19}$$

This definition agrees with the real part of a single LC mode in the sense of distributions [210] as $ReZ(\omega) = \frac{\pi}{2C}(\delta(f - \sqrt{(LC)^{-1}} + \delta(f + \sqrt{(LC)^{-1}})$ and thus has a well defined meaning when the Q is high enough, which is the case when the detection BW is the smallest BW in the physical problem.

Table 5.2: Sonnet® simulation results for 3D model coils with varying line width w. The resistivity is 2 nΩm for 500 nm thickness of the metallization. The bridge support height is set to 1.25 μm.

N	D_i [μm]	w [μm]	s [μm]	Z_c [Ω]	f_0 [GHz]	Q	L[nH]	C [fF]
19.5	40	1	1	1152.9	6.16	15.8	29.8	2.2
19.5	40	1.5	1	1082.7	5.73	15.9	30.1	2.6
19.5	40	2	1	1021.1	5.41	15.0	30.0	2.9

Table 5.3: Sonnet® simulation results for 2D model coils with varying spacing s in between the coil's wires. The resistivity is 2 nΩm for a thickness of 100 nm of the metallization. The bridge support height is set to 1.25 μm.

N	D_i [μm]	w [μm]	s [μm]	Z_c [Ω]	f_0 [GHz]	Q	L[nH]	C [fF]
19.5	40	1	1	1273.5	5.94	6.9	34.1	2.1
19.5	40	1	1.5	1251.6	5.53	6.2	36.0	2.3

Using the 3D model the coil was then again optimized by adjusting width, spacing and inner diameter, whose reduction allowed to fit more windings inside the coil with less effective capacitance added and thus an increase in impedance and of the quality factor. The new optimum is at 19.5 windings with an inner diameter of 40 μm for a metal thickness of 500 nm. The variation of the thickness was tested to be non-critical, a doubling of the metallization thickness causes a negligible deviation of 0.1% Z_c, while the change of line width and spacing of the coil noticeably change Z_c and f_0 as shown in table 5.2 and table 5.3. The shown values indicate that we should minimize line width and spacing as far as possible but we decided to work with 1 μm spacing, as it would reduce constraints on the optical lithography fabrication. Even though a wider width diminished Z_c, we decided to keep the width at 2 μm, as it provides a lesser DC series resistance which would also allow to reduce the height of the deposited metallization later on without negative consequences, due the increase of resistance, if need be. With the geometric parameters as is, we have now found our optimal resonator fulfilling our requirements in characteristic impedance, resonant frequency and providing a moderate DC access resistance. We have simulated all its final parameters, with increased bridge support height of 1.5 μm, that are shown in figure 5.13.

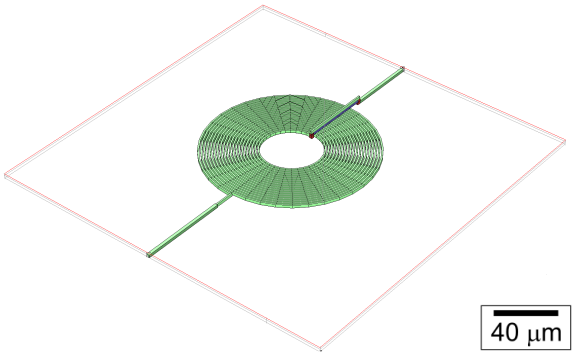

N	D_i [μm]	w [μm]	s [μm]	Z_c [Ω]	f_0 [GHz]	Q	L[nH]	C [fF]
19.5	40	2	1	1021.1	5.41	15.0	30.0	2.9

Figure 5.13: Final Sonnet® simulation of the single coil resonator in the 3D model with finite resistivity of 2 nΩm, 500 nm metal thickness (giving 4 m$\Omega/\square$) and a dielectric bridge support height of 1.5 μm. The geometric parameters and simulated resonant parameters are listed below.

5.4.1.2 Design of the sample on chip

The coils are meant to be deposited on the sample as close as possible to the quantum conductor tailored in a 2D electron gas, in order to diminish any parasitic shunting capacitance which would degrade both the impedance and frequency of the impedance transformer. In order to simulate the integration of the coils onto the sample, we need to define the 2DEG working area, the mesa, which will be accessed through several ohmic contacts. These contacts will then be connected to the coils and the RF-lines and other measurement relevant contacts. We decided to place two coils in series on both sides of the mesa as shown in figure 5.14 and as a result, the environment as seen by the conductor is about the sum of the impedances of both coils, while the resonance frequency should remain in the same order of magnitude. Essentially, we double the impedance so that DCB effects are non-perturbative: $r = \pi Z_c/R_\mathrm{k} = 0.25$ for a total characteristic impedance of 2 kΩ. Also, having two RF lines, and multiple gates that can be used to shape or contact the mesa, we can connect the two coils in different arrangements and use them for different experiments.
A peculiarity of the electromagnetic solver we use, is that in order to access the impedance as seen from the conductor in the geometry shown in figure 5.14, we need to run a new simulation as a 1-Port system where the port is attached to the place where we want to evaluate the impedance, and thus we need to attach 50 Ω to ground in series to the coils. We run several simulations, optimizing the spacing of the layout in order to diminish any cross talk between the coils. As shown by the simulation results shown in figure 5.15, the coils' impedance does essentially add up and it was tested that the resonance peak does not split or alter for distances of down to 25 μm, which we estimated as the minimal space needed to fit-in our mesa. Hence the negligible cross-talk between the coils can be ruled-out for future changes/simulations. For a full simulation we set a comfortable design distance of 30 μm for the coils and

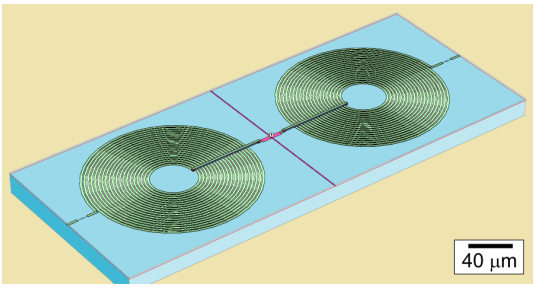

(a) Coupled Coil simulation

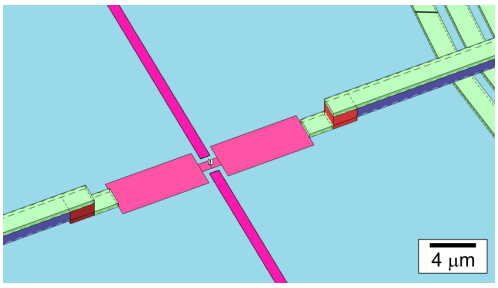

(b) Added mesa

Figure 5.14: (a) 3D visualization of the Sonnet® simulation for two coils connected to a simplified mesa structure (b) with QPC split gates. The simulation has been changed from a 2-port to a 1-port network, by removing the ports on the edge and replacing it with a central port, in order to obtain the impedance as seen by the QPC in the center. The impedance of the transmission lines to ground has thus to be added as ideal 50 Ω resistors at both branches. The coils are modeled as before and placed 30 μm away from the mesa. The mesa is modeled as 2D loss-less material and the QPC gates as 100 nm thick metallic lines.

also added a sizeable mesa with QPC gates, which should add 1-3 fF of capacitance to ground and is thus negligible compared to the mode capacitance, see table 5.15. The resulting impedance as seen from the conductor placed between the coils, see figure 5.15, shows a doubling of the characteristic impedance at a negligible shift of the frequency, as compared to the single resonator, with a quality factor of 13.5 equalling a bandwidth of 400 MHz.

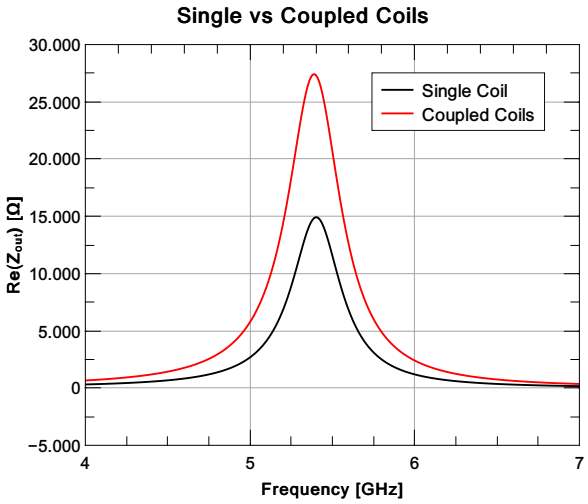

N	D_i [μm]	w [μm]	s [μm]	Z_c [Ω]	f_0 [GHz]	Q	L[nH]	C [fF]
19.5	40	2	1	2010.9	5.40	13.5	59.3	1.5

Figure 5.15: Comparison of the Sonnet® simulation of the real part of the environmental impedance as seen by the conductor (1-Port setup) with just one coil placed in series (black line) or two coils (red line) , one attached to each side of the conductor (a comparable arrangement is shown in figure 5.14a). The conductor is assumed to have infinite impedance and the coils were placed in 30 μm distance between the coil's outer edge and mesa. The obtained output impedance as seen by the QPC is plotted over the frequency and key parameters are listed below.

5.4.1.3 Sample Layout on chip

With the resonator designed the next step is to find a suitable layout to place them on chip together with the 2DEG mesa, all required contacts, gates and RF wires within a ground plane so that any interference of the microwave signals or unwanted charge effects are avoided without influencing our sample area. Step 1 is to define the mesa: it needs to connect both coils, as was already simulated, with the gates for a QPC in the middle. Then on both sides of the QPC we need a contact each for a DC-line contact and a cold ground with split gates that allow to connect/disconnect them. These DC contacts and a number of split gates, in addition to the chirality of charge transport in the QHE regime, enable the definition of many possible paths to be used for characterizing the device in different regimes. So we need to extrude the mesa on both sides to have sufficient space, but the longer the mesa, the more capacitance is added between it and the coils so that Z_c and f_0 drop. We extend by roughly 30 μm so that contacts and a split gate can be fit. The second step is the ground plane which could simply be a rectangular box around our sample area. However, we found that a slightly better quality factor can be obtained by rounding off the corners with little impact on the characteristic impedance. This plane has then to be divided, creating some gaps for the transmission lines that will contact the coils, the DC lines (biasing the sample and different gates) and also other contacts

to larger pads on the edge of the chip. Because gaps in the ground-plane act as a wave-guides, which is the intended purpose for the RF-lines but can be an unwanted source of signal loss or coupling (e.g. between the coils) in the case of the DC-line gap, we block this by creating a bridge across the DC-lines. This ground-cover will be made like the coil bridges as metal being deposited on a BCB support. We have simulated the layout with the newly added elements (see figure 5.16) and found small changes to the resonating parameters, namely a down-shift of the resonance frequency by 400 MHz, presumably caused by the increase in capacitance from the enlargement of the mesa, while the improved screening of ground plane still leads to an higher increase in effective inductance resulting in an increase of about 100 Ω in characteristic impedance.

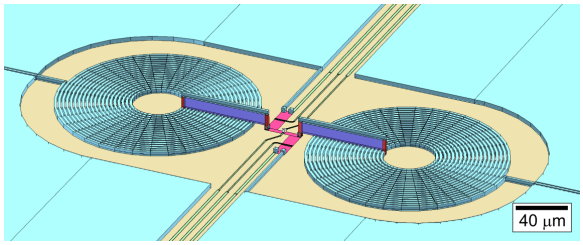

Z_c [Ω]	f_0 [GHz]	Q	L[nH]	C [fF]
2098.2	5.08	14.91	65.7	1.5

(a)

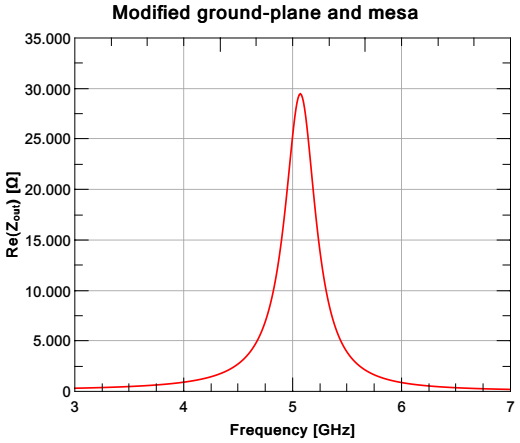

(b)

Figure 5.16: Sample layout and plotted Z_{out} for a 3D Sonnet® simulation including the coil resonators, the enlarged mesa, ground-plane and DC-lines/gates. The DC cover is not shown in the illustration. Coil and mesa settings are kept as before, the ground plane is set to be 500 nm thick with the same resistivity as the coils. The obtained characteristic parameters are shown.

The layout was tweaked further in order to assure a reliable fabrication: The shielding of the DC-lines is extended closer to the mesa, so that the ground is bent around the coils. The DC-lines are reduced in width near the mesa (see figure 5.17), reducing capacitance to the mesa. Markers were added around the sample area to be used for the alignment of the e-beam lithography of the gates. All dimensions were then optimized in sizing and spacing to be created by optical lithography, therefore tolerances of 1-2 μm for wire/pad overlaps were built-in by enlarging the ohmic contacts, the contacts for the bridges within the coils and the dielectric support of the bridge. We then designed the RF lines as 50 Ω co-planar waveguides. The spacing of the line width and the gap was simulated/calculated with a freely available transmission line characteristics calculator Tx-line® for several widths, allowing us to reduce the total size of line and gap as we get closer to the sample bit by bit. The necessary adaptations between segments were shapes as cones with a curvature optimized by Sonnet® (as seen in figure 5.17 on the left and right side for the first adaptation).

The change of conductor width allows us to keep the gap in the ground-plane near the coil minimal while minimizing the DC resistance of the line by using wide segments near the edge of the chip. A full description of the coplanar wave guide design and the testing done is given in appendix F.

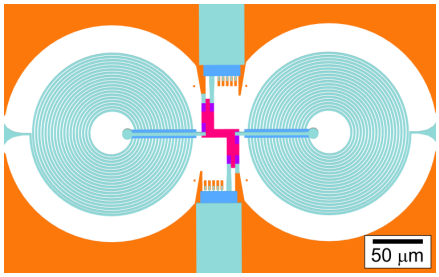

(a) Full layout visualization

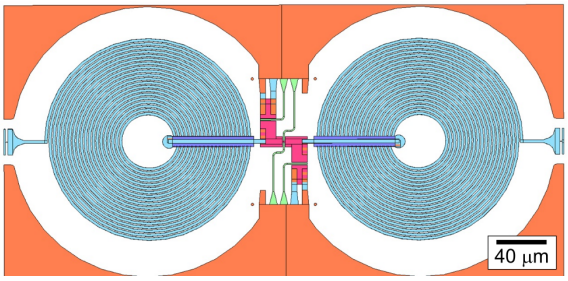

(b) Sonnet simulation

Z_c [Ω]	f_0 [GHz]	Q	L[nH]	C [fF]
2188.8	4.99	13.86	69.8	1.5

Figure 5.17: (a) Graphical illustration of the final sample layout after modifications for optical lithography: Contacts and bridges were enlarged for easier positioning and the ground-plane was extended to decreased capacitance to the DC-lines. (b) 2D view of the final Sonnet® simulation of the sample with adjustments for optical lithography fabrication. The DC-lines are simplified as ground-plane, assuming a perfect cover-layer, to reduce simulation time. The final characteristic parameters are shown below.

The new setup was simulated again with the final parameters shown in figure 5.17. All future changes that were made for the optimization for other elements on the chip were of negligible influence to the sample meaning that these values are our final result for the EM-simulation.
The on-chip design was then continued by firstly placing two samples on one chip in a symmetric arrangement. All lines and the ground plane were extended towards the edge of the chip with cut-outs for alignment markers and test stripes to fit on a $8{\cdot}12\,\mathrm{mm}^2$ substrate, this final design is shown in figure 5.18a. We only show the last version of the layout that will be used in the future, while the fabricated and tested samples in section 5.4.2 were made with older versions. Those layouts were made with different arrangement of the lines, markers and other outer elements but did not change the core sample layout.
The chip layout has also been optimized to be fabricated completely by optical lithography though certain steps can be done by e-beam lithography if necessary. Therefore we leave a free edge of several hundreds of nanometers[10] which in the end enables us to do a high resolution optical lithography and placed four sets of alignment markers in the corners of the ground-plane (see figure 5.18b). They consist out of a coarse alignment cross made-up from several metallic dots with smaller versions in every

[10]For a full explanation see section 5.4.2.3

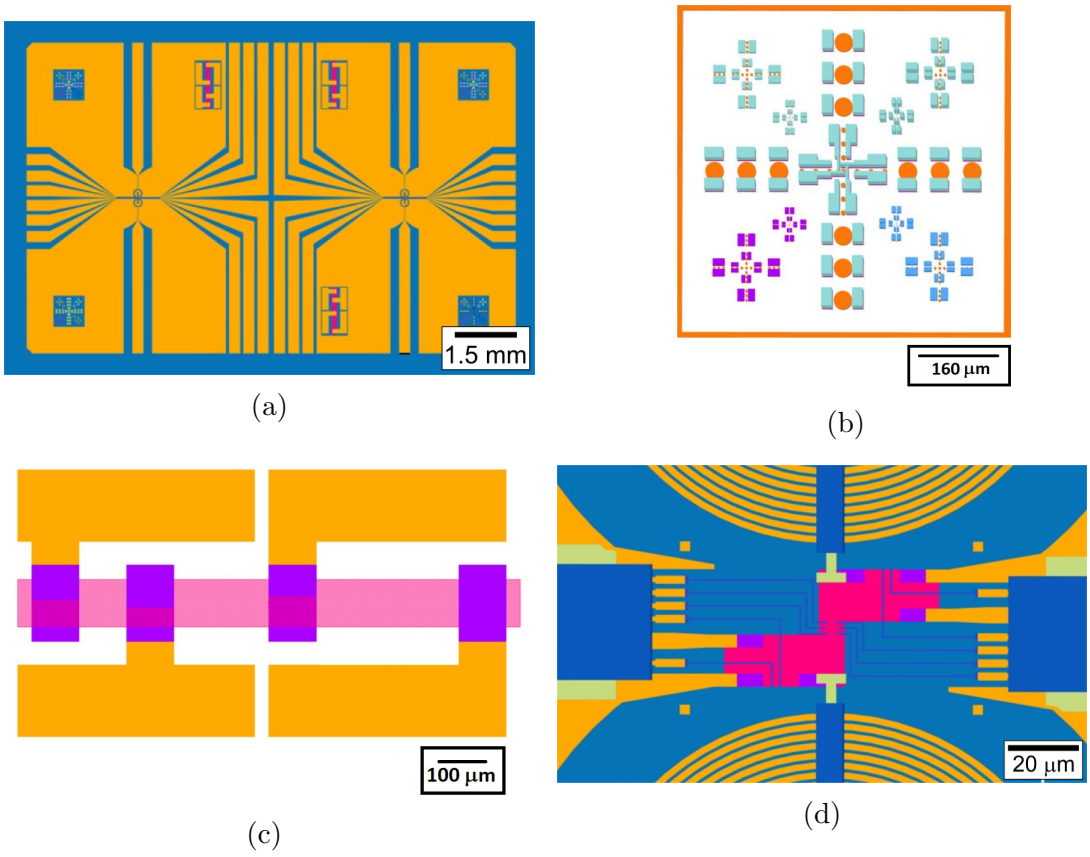

Figure 5.18: (a) Design sketch of the full sample layout on a $8\times12\,\mathrm{mm}^2$ chip drawn in LayoutEditor. (b) Optical alignment markers are positioned in all four corners with a coarse alignment cross and four smaller cross sets. For every lithography step at least one large cross and one small set per corner is used for the alignment. (c) The three test stripes near the center have a mesa bar of $100\,\mu$m width with 100, 200, $300\,\mu$m length in between square ohmic contacts. This is used to test and measure the 2DEG and ohmic contacts after their fabrication as the sample can only be measured after all steps are finished. (d) Magnification of the sample area, all elements are fabricated by optical lithography except for the gates leading onto the mesa.

corner. The processing order is to firstly create the mesa and then the ohmic contacts by e-beam lithography before adding the ground-plane with coils and DC-lines followed by the BCB bridge support and lastly the bridge metallization - a total of 5 lithography steps. The first lithography is supposed to set the marks (dots) that are used for the alignment with the crosses for the following four optical lithography steps. For every lithography step at least one large cross and one small set per corner is used with a corresponding set of alignment bars on the mask to ensure a precise alignment in position and angle.
Furthermore three test sets were added near the central DC-lines, made up from a mesa-stripe with ohmic contacts and metal pads (see figure 5.18c) to allow an easy 2-probe measurement to test the ohmic contacts and the mesa conductivity after

their fabrication. This is necessary because the small sample contacts can only be tested once the entire fabrication is finished as they are too small to be tested with a probe directly. The test stripes allow to detect fabrication errors before needlessly continuing with the fabrication.

5.4.2 Fabrication and Testing

Here we present the experimental fabrication process that we developed to fabricate the planar coil resonator design as described in section 5.4.1.1. We firstly present our test for the choice of suitable materials for the fabrication of the coil by optical lithography as well as simple RF-measurements to verify the simulated properties.

5.4.2.1 Materials for low resistances

With the geometry of the coil and core sample layout fixed, we try to estimate the influence of the material choice and the corresponding resistance of the coils. Therefore we fabricated a series of test samples of Au, Cu and measured their low temperature resistivity at 4.2 K by mounting them on a measurement stick that is submerged in liquid helium. The measurement stick is cabled to allow for 4-probe measurements which we use to measure the resistivity of the metal strips later used in the coils. We created several Cu and Au wires of the same length by physical vapor deposition on SiO_2/Si-substrates that were measured with a 2-point probe at room temperature and when submerged in liquid helium. We calculated the low temperature resistivity and deduced the quality/purity of the thin films based on the residual-resistance-ratio (RRR):

$$RRR = \frac{\rho_{273K}}{\rho_{0K}} \approx \frac{\rho_{273K}}{\rho_{4.2K}} \tag{5.20}$$

Measurements for gold and copper were carried out after their deposition and also a second time after thermal annealing. Best results were obtained for copper samples when annealed in a vacuum furnace at 250°C for 30 min and for gold samples that were annealed in a rapid thermal annealer at 450°C for 30 s. All metal wires had a length of 33.7 mm with a thickness of 500 nm (+2 nm Ti adhesion layer) and a width of around 8-11 μm. The resistivities were calculated from the measured resistance values and a corresponding average of multiple measurements for the wire width:

$$\rho_i = R_i \cdot \frac{500nm \cdot w_{avg}}{33.7mm} \tag{5.21}$$

Table 5.4: Measured resistivity and RRR ratio for gold, and copper wires as fabricated in our laboratory. Measurements were done before and after annealing. The annealing showed an increase in conductivity and purity, making copper and gold viable material choices.

Metal	$\rho_{20°C}$ [$\mu\Omega$cm]	RRR	ρ_{4K} [$\mu\Omega$cm]
Copper	2.32	6.0	0.38
Copper(annealed)	2.00	11.1	0.18
Gold	2.8	5.5	0.57
Gold(annealed)	2.84	15.8	0.18

Based on the results, shown in table 5.4, we can see that both copper and gold need to be annealed, removing vacancies/impurities/grain boundaries left from the deposition, in order to decrease their resistivity to an acceptable level. With the machines and methods used in our lab, we achieve the same resistivity for copper and gold at low temperature. While gold has the advantage of being resistant to oxidation, copper comes at lower material cost and we thus decided to fabricate first (test-) samples using copper as bulk material, with a gold cap-layer to prevent copper oxidization, and then later switch to gold for final samples since we observed a slow oxidation of the cap layered Cu wire.

5.4.2.2 Optical lithography of micron-scale planar coils

Now we describe the fabrication of our test-coils for which we used similar techniques as for the full RF-sample fabrication but focused only on the steps of the coil and the bridges. No mesa or ohmic contacts were fabricated, hence process steps were not adjusted for their fabrication and differ from the full fabrication recipe listed in Appendix B. The recipe for the fabrication of the coil test samples is found in appendix A.
Firstly, we want to give a general introduction to optical lithography which is based on the chemical modification of a polymer resist by interaction with light. These optically-active materials change their structure upon exposure, which allows to specifically dissolve exposed areas with a chemical developer. Patterns and designs can then be created by protecting certain areas from light exposure with a photo mask. Then, after the exposed areas are developed, a resist pattern also called resist mask remains that is then used for metal deposition or etching techniques. The resist mask can afterwards be removed with different chemical removers or solvents. This procedure is commonly referred to as positive lithography, whereas for a negative lithography the exposed areas are made insoluble by cross-linking or other reactions, so that the inverse pattern can be created. In both cases, the maximal resolution of the lithography and thus the minimal size of a features in the mask are in the order of magnitude of the wavelength of the light, the focusing of the beam/microscope used and the resist thickness as well as the lithography technique.
In our laboratory we work with a Suss Microtec photomask aligner at a light wavelength of 365 nm which gives us a critical feature size of 0.6 μm. This critical feature size represents the minimal obtainable size, even though the effective resolution depends on the exposure method. We distinguish here simply between contact and non-contact modes of which there are several types. In the non-contact mode the mask is positioned above the sample with a gap remaining in between. It is a technique that does not require any precaution for the alignment as the mask does not

get degraded by contacting the resist. The downside is however that the interference of the light in the gaps of the mask broadens the lithography. Effectively it is not possible to obtain micron size resolution with non-contact modes of operation (see figure 5.19a and 5.19c). For that reason we have to work in the contact mode where the mask is directly contacting the resist. There is no gap in between so that the light diffraction is reduced, yielding a sharper and correctly sized lithography (see figure 5.19b and 5.19d). The accompanying drawback is that some resist touching that mask may remain so that it is mandatory to clean the mask to avoid damages and deterioration. We will be using the vacuum contact mode which creates a vacuum underneath the mask that pulls the resist into direct contact. The second factor of importance is the resist as commonly positive resists have a rounded-off profile that can enlarge the feature size and leads to further problems with metal deposition or destruction of small features during development. To avoid that, it is advisable to use negative resists, which has the advantage that their edge profile remains sharp and what was a rounding-off for positive resist is turned into an undercut for the negative resist. The surface preserves the lithography while a natural inward slope, the undercut, can also facilitate the lift-off process of the following metal deposition.

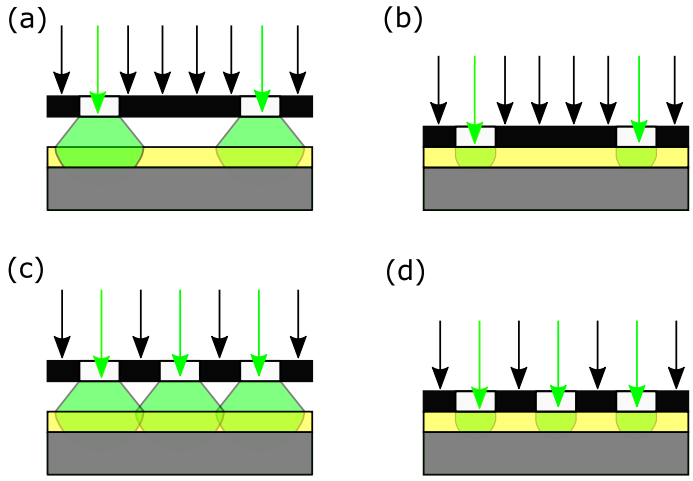

Figure 5.19: Illustrations of optical lithography different resists and contact modes: (a) non-contact mode, (b) contact mode. The diffraction of light causes an enlargement of the feature size which is avoided for the contact mode. (c) For small feature sizes, the diffraction of light overlaps and the features are not resolved in the lithography which is still possible for the contact mode. In all four cases the obtained resist mask for positive resist are yellow and the equivalent for negative resist would be green.

We have thus developed an optical lithography process based on a negative resist achieving micron scale precision in order to fabricate sets of planar coils with smallest features of 1 μm and a thickness of up to 500 nm. The fabrication was done in the exact sizing/spacing as shown in section 5.4.1.1. For that purpose $8{\cdot}12\,\mathrm{mm}^2$ chips of GaAs were cut and cleaned to serve as substrates for the fabrication of the coils. Multiple samples, with different steps of fabrication completed, were obtained and

then characterized for their resonating parameters to compare to the predictions from the simulation of the previous chapter.

5.4.2.3 Spin coating and edge bead removal

The GaAs chip(s) are spin coated with a resist bi-layer consisting of a 200 nm thick LOL2000 undercut layer and a 1.5 μm thick AZ5214-E negative resist layer. We use a thick resist to allow for 500 nm thick metal depositions and an additional undercut layer that shall facilitate the lift-off process in the narrow patterns. A lift-off layer is an optically non-active material that is developed at fixed rates, set by its degree of thermal curing, in the developer to create an undercut beneath the optical resist. Both resists are filtered before usage to get rid of any impurities or dirt in the resist. AZ5214-E is a special resist as it is a positive resist that can be inverted into a negative resist by thermal cross-linking. This is of crucial importance for the process as it will be used in both ways. Because we are using small rectangular chips and not big wafers we have considerable edge bead effects. Edge beads are the agglomeration of resist at the edge of a wafer during spin coating. On a round wafer they are normally flung off, on rectangular substrates however they tend to remain in the corners. These beads are very harmful for our process as they create a gap between the bulk substrate and the photo-mask, even at vacuum contact. Bead heights are of the order of 5-8 μm and thus strongly diminish our resolution. This bead formation is mostly ruled by two factors: the substrate geometry and the Bernoulli effect. Both effects lead to an increased evaporation rate of the resist solvent so that the resist dries up, forming beads near the edges.
The Bernoulli effect describes the increase of the solvent evaporation rate at the moving fronts of the chip, where the air velocity is the highest. If the air is allowed to split up into two streams above and below the sample, we obtain different velocities of the air depending on the path. The velocity of the air flowing over the chip is increased and the pressure proportionally decreased. This vacuum above the resist immensely increases the evaporation rate and causes a large buildup of up to 500% of the nominal resist thickness [211]. The geometrical effect is based on the difference of the radial forces along the different edges of a rectangular chip being spun. The resist will be pushed towards the corners along the edges, following the radial force gradient. The accumulation on the corners is typically observed to have a wave pattern that is caused by the quick drying of resist at the edges, so that following resist is pushed on top by the force gradient and increases the build-up step by step in a wave pattern [211]. Spinning chucks commonly available in our clean-room are designed for circular wafers and need to be of smaller size than the rectangular substrate to fit underneath them, ensuring a good vacuum contact. This means that there will always be some overhang of the chip giving rise to the Bernoulli effect which is superimposed with the chip's geometrical contribution. In this case we obtain a final edge bead distribution as in figure 5.20. In order to avoid this build-up of edge beads, we designed and ordered a recessed chuck, with an inlet pocket of $8.1 \cdot 12.1\,\mathrm{mm}^2$ to fit the chip, from the mechanical workshop of our institute. Brass sheets can be mounted on top in order to adjust the height/depth of the pocket to fit different

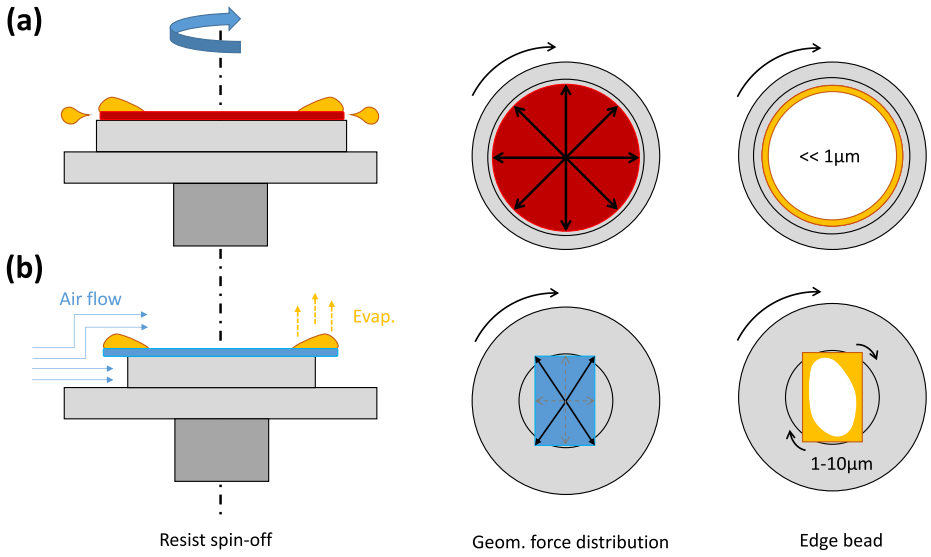

Figure 5.20: Illustrations of spin-coating for round wafers (a) and rectangular chips (b). During the spin-coating, the resist is pushed to the edge of the wafer, where it is typically flung-off due to the high centrifugal force, leaving a minimal edge bead behind. For a rectangular chip the centrifugal forces push the resist towards the corners where it accumulates. In addition to that the typical overhang of a rectangular chip on a circular spinning chuck causes an increased evaporation rate of the resist because of the air flow at the chip front. The division of the air stream and the higher velocity above cause a vacuum that increases the evaporation rate, thus letting the resist in the corners dry quicker. In comparison the edge beads of a rectangular chip can be several times thicker than for round wafers.

substrate thicknesses and resist heights. Spinning with this chuck reduces the build-up greatly but not completely. The remaining beads had to be removed chemically by positive lithography of the AZ resist. Therefore the center of the chip is protected with a photo mask and several hundreds of nano-meters of the edge all around are exposed and developed. The developer does not attack the bulk resist during short exposures so that it can be used for our precise lithography as negative resist without any gap between chip and photo mask.

5.4.2.4 Lithography and metal deposition

The prepared resist with the removed edges is then exposed under the optical mask in the Suss Microtec mask aligner at vacuum contact with an exposure dose of 250 mJ in order to expose the entire thickness of the 1.5 μm AZ layer. After the exposure the sample needs to be thermally cross-linked at 125°C for 2.5 minutes. This step is very sensitive and requires proper calibration of the temperature as too high temperatures will completely harden the resist and too low temperatures will leave parts un-linked. Once the sample has cooled down, it can be exposed again with a flood exposure to

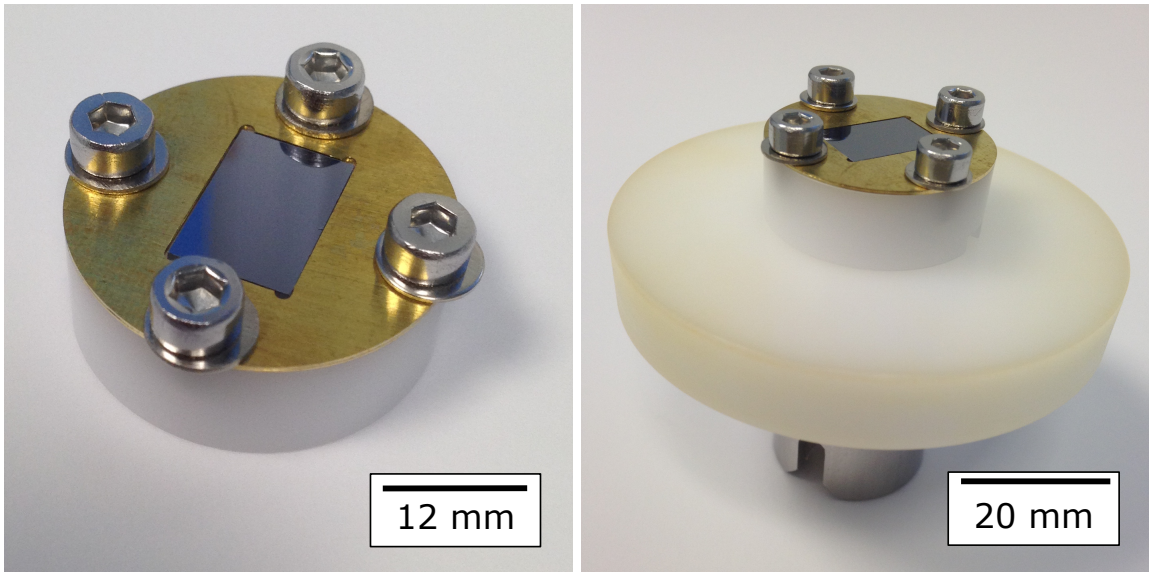

(a) (b)

Figure 5.21: Photographs of the custom made spinning chuck (a) GaAs substrate placed in the recessed cap-adapter made from POM (white) with a 0.2 mm deep pocket of $8.1 \times 12.1\,\mathrm{mm}^2$. The depth of the pocket can be adjusted with a varying number of brass sheets that are screwed in on the cap, thereby creating an even level between the substrate and chuck surface (b) Recessed adapter mounted on the spinning chuck.

expose non cross-linked areas and then developing them in AZ726 (result, see figure 5.22a). The development time for 1.5 μm AZ is around 40 s but it is not critical as the cross-linked resist is insoluble in the developer. The development time, past 40 s, is thus entirely set by the undercut layer development time. Ideally, the undercut should be around 250 nm per side in order to have a stable 0.5 μm base under a 1 μm feature. Hence our LOL2000 layer was soft-baked after spin-coating at 155°C for 5 min to set the according development rate ($r_{dev} > 250nm/40s$). As undercut layers continuously dissolved in the developer, some traces may remain in the resist mask after development. To remove them an oxygen plasma etching is recommended which also improves the adhesion of the metal deposition. We deposited a stack of 15 nm titanium, 500 nm copper and 15 nm gold (figure 5.22b). The titanium serves as adhesion layer between the GaAs substrate and the bulk copper which is covered by the gold cap layer. The gold layer is meant to prevent the copper from oxidizing too quickly. It is important to note that the deposition is done with a physical mask that protects the resist-free edges from the edge-bead removal. If the metal layer were to be deposited on the edge, it could keep the entire metal sheet in place and prevent lift-off.

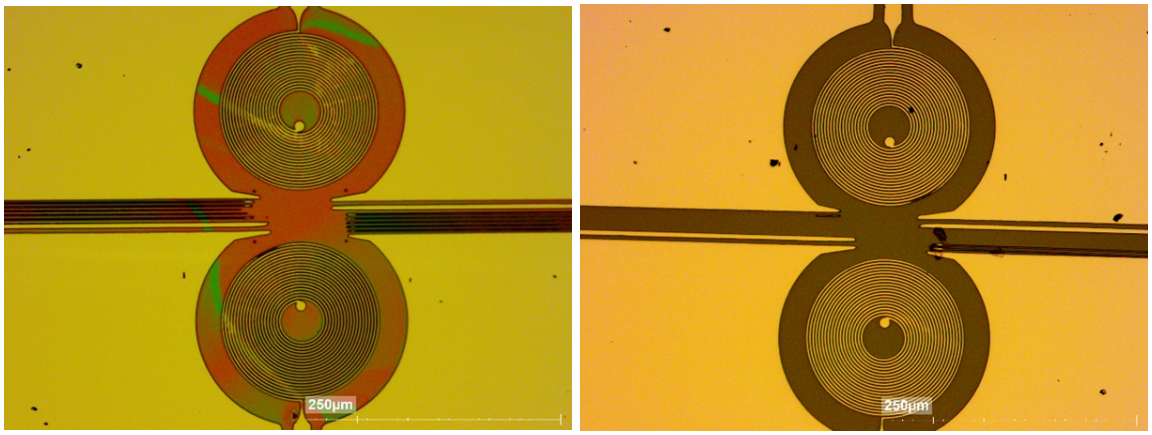

(a) Resist mask A26 (b) Metal deposition A26

Figure 5.22: Micrograph pictures of fabrication steps of sample A26. Shown are the resist mask after development in AZ726 (a) and the lifted-off metal deposition of 15 nm Ti/500 nm Cu/15 nm Au (b). The visibly missing and damaged DC-lines in (b) were not correctly imprinted in (a) due to damages on the mask RFTv2 and are not caused by the fabrication procedure.

5.4.2.5 Metallic bridges across the coil

In order to fabricate a metallic bridge from the center of the coils to where there will be a contact on a real sample, we first need to create a dielectric support structure. The bridge support is made from polymers derived from B-staged bisbenzocyclobutene (BCB), sold as Cyclotene 4000 by Dow Chemicals. The lower viscosity version 4024-40 is chosen, in order to obtain a several micron thick spacer (approximately 5μm after spin coating). BCB is a negative resist that can be shaped simply by optical lithography but its developer also dissolves unexposed areas of the resist, though at much smaller rates, which needs to be taken into account. We use this dark erosion to our advantage as we set the rough shape of the BCB with a non-contact mode lithography, so that our mask can not be contaminated with (hard to remove) BCB residues, and define its shape during the development. We expose the BCB for 15 s with a dose of 150 mJ, after which the BCB is only soft-baked and not cross-linked like other resist because cross-linking the BCB would make it insoluble in any developer. In order to develop the structure, the chip has to be pre-heated to 55°C on a hotplate before submerging it in the developer DS3000 at 35°C for about 3 minutes. To stop the development it is submerged in a second DS3000 bath at room temperature before rinsing it clean. The development rate and the dark erosion of the BCB are highly dependent on the temperature of the DS3000 developer whose temperature needs to be well set and controlled to achieve reproducible results. Ideally, after the development is completed, the thickness has been reduced to 3-4 μm. The developed BCB has then to be cured for 1h at 250°C in an oxygen free environment at finite pressures. BCB, if cured in air, would oxidize by forming SiO_2 on the surface which may cause problems with following fabrication processes. The common alternative of curing in a vacuum furnace is also not suitable because BCB degasses hydrogen at

low pressure so that bubbles might form and destroy the smooth surface of the bridge. As a solution we placed the sample in a vacuum furnace, evacuated to a pressure of 10^{-6} mbar before filling the chamber with nitrogen to a pressure of 10 mbar to create a suitable atmosphere. After the curing any remaining traces (scum) can be removed by reactive ion plasma etching (RIE) with O_2/SF_6 in the ratio 9/1 at 250 μbar. We removed approximately 100-200 nm at 70 V during 15 seconds. As this etching may attack copper, the sample needs to be dipped in acetic acid for 30 s right after the etching to remove any leftover etchant residues. After the shrinkage from the curing and the descum-etching, the final thickness of the BCB support is around 3 μm.
For the metal deposition of the bridges a resist mask of AZ-5214-E is used made from a triple stack amounting to 2.8-2.9 μm thickness in order to thoroughly cover the BCB deposits. The lithography can be done in either contact or non-contact mode with a dose of ca. 500 mJ and the development in AZ726 after the inversion baking process as described in 5.4.2.4. This time, the resist mask can not be plasma cleaned as the BCB would be oxidized. Instead we use a milling with Ar-ions that removes any resist traces and also roughens up the BCB's surface which improves adhesion to metal deposits. The deposited metal stack is a 15 nm Ti adhesion layer before the 300 nm bulk copper with a and 15 nm gold cap layer. The structures are lifted in warm remover 1165 and the result shown in figure 5.23.

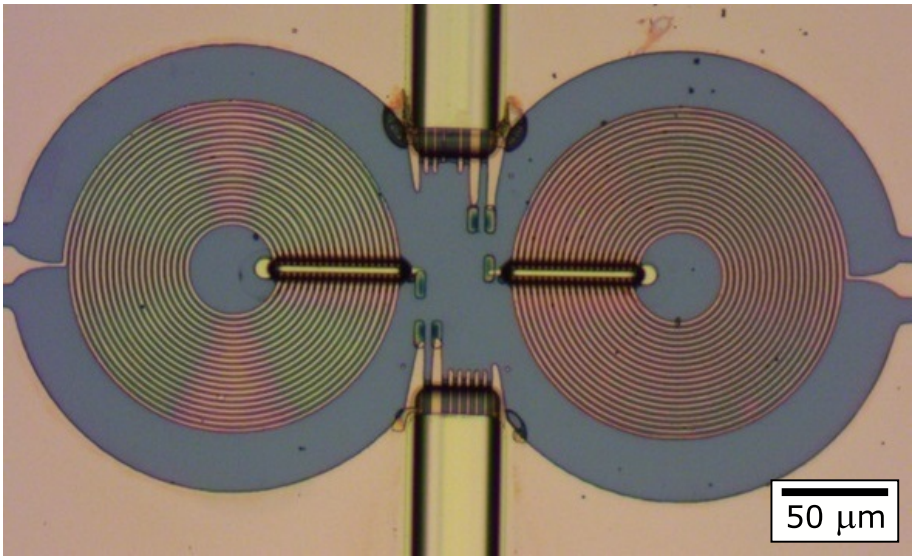

Figure 5.23: Micrograph picture of sample A24 after having completed the fabrication of the resonating coils (15 nm Ti/500 nm Cu/15 nm Au) with bridges across coils and DC-lines. The metallic (15 nm Ti/300 nm Cu/15 nm Au) bridges are deposited on 3 μm thick dielectric BCB supports. A24 was created with dummy-ohmic contacts made from copper and gold to test the alignment of the metallic bridges.

5.4.2.6 RF-measurement of high impedance resonators

The presented samples A24, including coils and bridges and A26 without the bridges as well as another reference sample A28 were glued on PCB's and wire-bonded to the

RF connectors. A28 has the identical layout of the ground-plane and the DC and RF lines as on A24 and A26 but without any coils or bridges. All three samples were measured with a vector network analyzer (VNA) to characterize the reflection signal of the coil.
In the geometry of A28, RF waves travel through the circuit and are reflected by the open circuit at the end of the 50 Ω line on the chip, where otherwise would be the coils that are placed on the other samples A24 and A26. One can see in figure 5.24 that the reflection coefficient approaches 1 in the zero frequency limit, but is getting smaller with increasing frequency. This behaviour comes from the attenuation due to losses in the wires which increases with frequency according to the skin effect. On top of these losses we see small ripples of about 0.2 dB, which come from the finite SWR with a frequency period of about 500 MHz, thus equivalent to $\lambda/4$ standing waves on a length of about 10 cm assuming $c = 2 \cdot 10^8$ m/s. The SWR originates from the used measurement equipment, the SMA to mini-SMP connector used to connect the VNA cable to the PCB, as it can be observed even without a sample or even a PCB connected. Thus for the measurements of samples A24 and A26, we see similar features as on A28, with an additional dip in the reflection coefficient around 5.5 GHz. As the RF waves spend some additional time on the coil due to its resonant behaviour, the dissipation is accentuated around the resonant frequency explaining the dip in the measured reflection coefficients.
In order to better analyse this resonant reflection dip, we thus use the measurement of A28 as a calibration signal for A24 and A26 by subtracting the spurious reflection in the wires as measured in sample A28. The resulting graphs are presented in dB in figure 5.24b. We have obtained the resonant frequency of the coils at approximately 5.5 GHz for both samples, before and after defining the bridge. The only apparent differences are the magnitudes with -4.5 dB for the lone coils and -5 dB for the bridged coils, indicating some additional path that increases dissipation, and a distinct feature at -6.7 GHz for the lone coils. We suspect that the small dip in reflection at 6.7 GHz can be attributed to standing waves developing on the DC-line gap that is not covered by any ground for A26 and might act as a slot-line. Being only present for A26 shows that the ground-bridge across the DC-lines of A24 is successfully inhibiting this spurious resonance. It is also positive to note that the bridge has a negligible influence on the resonance frequency of the coil, meaning that the small bridge does not add any unexpected capacitance to the coil.
The second point is that the resonance frequency is shifted upward by 500 MHz as compared to the simulation. It indicates that the L and C are not as expected, possible reasons are slight fabrication errors that modify the exact shapes of the coil or an increased damping due to the higher DC resistance at room-temperature. As a first approximation, if only one parameter were responsible for the shift the characteristic impedance would change by 10%. As this is normally not the case, L and C change together but at different rates, we would expect a negligible effect of some percent.
To test whether the frequency shift indicates a large or a negligible impact on the EM-properties of the coil it would be necessary to determine the characteristic impedance. Unfortunately, in our case it is not possible to directly obtain this quantity from the

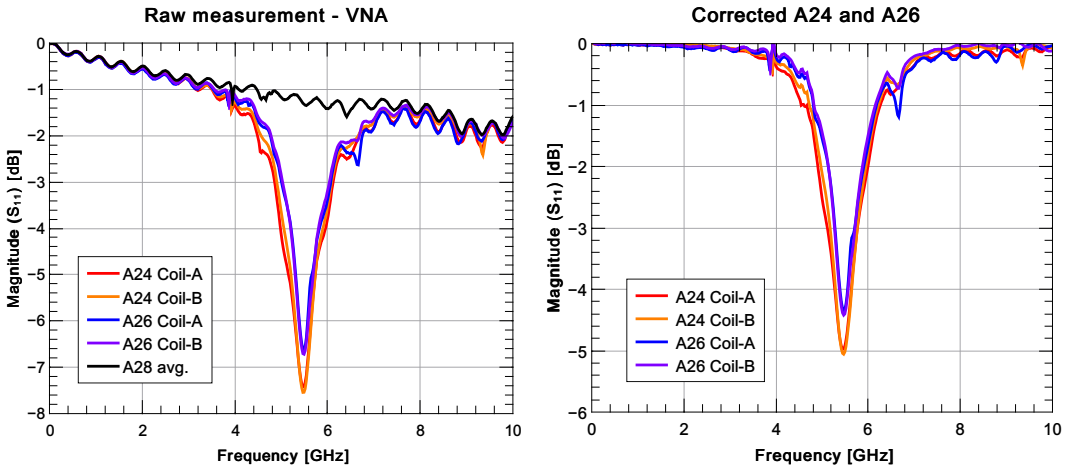

Figure 5.24: Reflection coefficient S_{11} measured for sample sets on both sides (A and B) of samples A28, A24 and A26. (Left) Raw measurement results for the different coils of A24 and A26 denoted as left and right. The different measured RF-lines on A28 were averaged into one single reference curve. (Right) Reflection coefficient for A24 and A26 obtained by removing the insertion losses of the cables, obtained by subtracting the average measured reflection coefficient of the calibration sample A28. The resulting graphs show strong resonances of -4 to -5 dB at a frequency of 5.5 GHz.

amplitudes of a reflection measurement as the quality factor of the resonance is not high enough to distinguish the distributed losses in the coil from the radiative losses in the line. To still get an idea, we can compare our measurement to a simulation of our sample in reflection under the same conditions. So in order to estimate the quality of our fabrication, we use Sonnet® to simulate the samples A24 and A26 as is, thus in reflection and at room-temperature, as shown in figure 5.25. These simulations will be compared to our measurements to check the resonating parameters. For the simulations at room-temperature (and later low temperature) we change the resistivity of the metallization based on our RRR measurements.
The results of the new simulations are shown in figure 5.25: We expect values of approximately 5.3 GHz resonance frequency and -4 dB in signal magnitude for both A24 and A26 at room-temperature in good agreement with the measurements performed at room-temperature.
To obtain a more quantitative agreement, we changed the value of the resistivity. Indeed, the higher the resistivity, the lower is the resulting quality factor of the resonance thus making the dip in the reflection coefficient broader and less peaked. As we see for the simulation in figure 5.25 with a 1.25 $\mu\Omega$cm resistivity (annealed), if we lower the resistivity of our simulation we can obtain the signal strength of our measurements. Hence, the difference in magnitude for A24 and A26 is an indicator for a change in the coils resistivity during its different process steps. While A26 was never heated up and is only the metal as deposited, A24 was effectively annealed when the BCB bridge support was cured and its resistivity is lowered. By adjusting the resistivity of our simulation we match it to the magnitudes of A26 and A24. The according

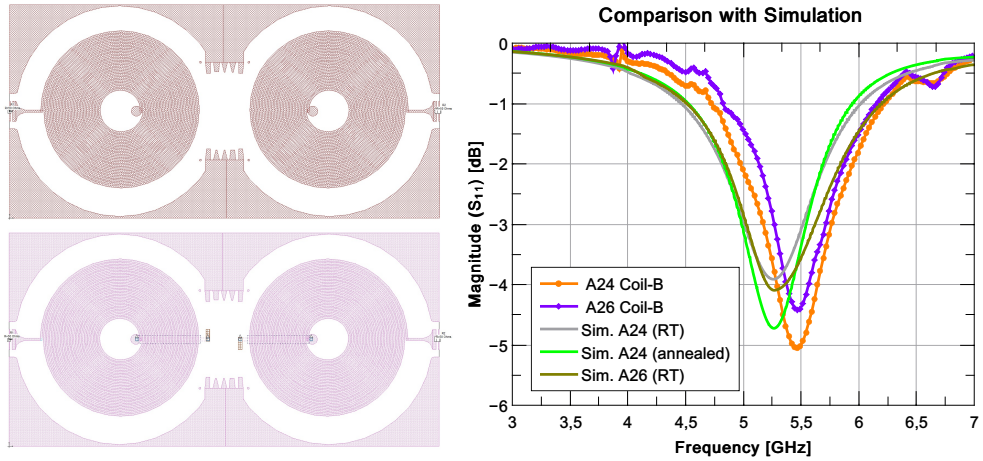

Figure 5.25: Electromagnetic simulations of the reflection coefficient of a 50 Ω line feeding the coil. Left: Layouts used in the electromagnetic solver without bridge (up), and with bridge (down). The Sonnet® simulation were reused from previous 1-port simulations as shown in figure 5.14, with the mesa being removed and the port set to the left edge. Right: Comparison of the simulated reflection curves (grey & brown) to our measurements (orange & purple). We see a shift of the resonance frequency between simulation and measurement of 200 MHz. We are able to adjust the magnitude of our simulation while preserving the resonance shape by adjusting the resistivity, shown with an arbitrary resistivity of 1.25 μΩcm (green), and can match the measured curves.

resistivities are approximately 1.4 μΩcm for A26 and 1.1 μΩcm for A24. These values are not precise, as the simulation can not reproduce the resonant frequency and thus neither the characteristic impedance nor a quantitative value of intrinsic losses in the material, but it should scale with the frequency disagreement of less than 5%. Thus unexpectedly, both resistivities are much lower (around 50%) than the values recorded during our RRR measurement (see table 5.2). This is of course not possible and is an error in our simulation originating from the fixed 50 Ω resistor that was used instead of attributing it to the port as it was done for previous simulations (see for example figure 5.12). The added resistance was needed to represent the impedance of an attached detection line in order to correctly predict the environmental impedances in the 1-port simulation for two coupled coils (see figure 5.14). This same simulation layout has been re-used for the reflection measurement to save time, but incorrectly adds up to the total resistance of the coil as a result. Therefore, to get the correct resistance of the coil from our simulation, we need to include the 50 Ω series resistance into the coil's intrinsic resistance. We verify this firstly for A26: With the dimensions of the coil taken from appendix C.1 we calculate 86 Ω for the resistivity of 1.4 μΩcm set in the simulation, found to be best fitting the data, and add 50 Ω in series to receive 136 Ω. This value matches our estimated 136.9 Ω (see appendix table C.2) of the resistance for the un-annealed coil, with a resistivity of 2.32 μΩcm (see appendix table C.1). Likewise we use the resistivity of 1.1 μΩcm found from fitting the data

measured for A24, which gives us a total resistance (coil + 50 Ω added in simulation) of 118 Ω which matches the DC resistance we expect for the coil using the resistivity of annealed copper (see appendix table C.1). Matching the resistivities and measured reflection amplitudes of A24 and A26 makes us confident in the EM properties of the deposited coils as the change in characteristic impedance should be of the order of 5% like for the shift in their resonant frequency.

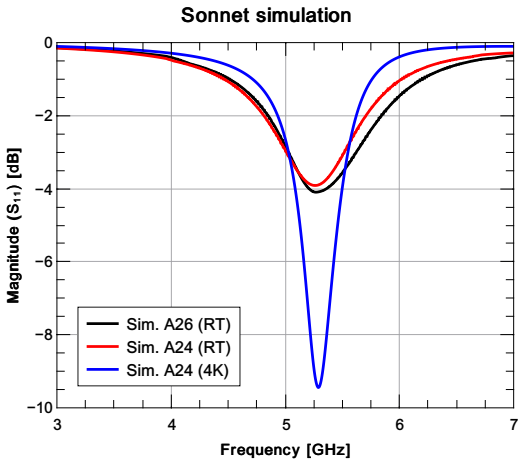

Figure 5.26: Computed reflection coefficient as a function of frequency computed for 3 different scenarios: RT simulations (resistivity used 1.68$\mu\Omega$cm) with and without coil as shown in the layout and a 4 K simulation (resistivity used 195 nΩcm) done for the sample layout of A24.

Based on this we also predict the low temperature properties of the coils from a simulation at 4 K, using the resistivity from our RRR measurements (see figure 5.26). The most notable effect is the change in the quality factor. Indeed, the tenfold decrease in the resistivity makes the DC resistance of the coil drop from about 120 Ω at RT to about 12 Ω at 4 K. In this condition, the quality factor is now mostly limited by radiative losses in the 50 Ω line, and the transformer works as it should: it transfers power to the detection line rather than dissipating it internally. However, because this experimental test is done for an open conductor geometry, it will be different from the bandwidth of a sample incorporating a quantum conductor with an impedance $\simeq R_{\mathrm{K}}$: The coils provide a detection impedances close to R_K so that about when the conductor is coupled to the coil, about half the power is dissipated into the conductor. This will roughly double the final bandwidth to about 500 MHz which is large enough to make the measurements of shot noise fast, yet smaller than the thermal BW of $3k_BT$ of the Fermi distribution so that it should not blur-out any physical features. In conclusion, we have successfully fabricated magnetic field tolerant impedance transformer, implemented as a planar coil made from normal metal with a resonance frequency of 5.5 GHz. By comparison between the samples A24 and A26 we have shown that the bridge across the coil has no unexpected addition of capacitance to the system as the shift in resonance between the two is negligible. We have also shown that any parasitic transmission modes along DC-lines and their channels is effectively prevented by the bridging across the DC-lines. We could also see due to the difference in

resonance strength between the samples that the curing of the BCB bridge support is effectively annealing the metallization, giving us a lower metal resistivity and thus higher Q factor. By comparison to our Sonnet® simulation, of the samples as is, we have shown that we are in good agreement with our measurement. We expect to have successfully fabricated a resonator with high characteristic impedance in the order of 1 kΩ, with changes of few %, at a resonant frequency of 5.5 GHz with an estimated bandwidth of about 300 to 500 MHz, depending on the matching conditions, with detection impedances in the 10 kΩ range at low temperature.

5.5 Full sample fabrication

In this section we put a focus on the challenges and trials concerning the fabrication of the full sample layout that we have designed. We have already introduced the general fabrication of a quantum point contact, based on our design and with the available equipment, in section 5.1 and the fabrication of the resonating coils in section 5.4.2. While one would expect it to be a simple task to combine the two fabrications, it appeared that the marriage of these two multi step process is a complex and difficult endeavour. Indeed, we found several incompatibilities of techniques, chemicals and materials that prevented us from completing our experimental platform within this thesis project. To provide a temporal perspective, the fabrication of full process chips on GaAs/AlGaAs began in August of 2018. Within the next three months the different fabrication were joined together and adjusted to produce the first working samples In November 2018, such a completed sample (without the QPC split gates applied) is shown in figure 5.27.
Unfortunately all fabricated samples showed electrical failures which occurred at different fabrication steps. At first the irregularity of the failure was attributed to problems that occurred for the respective fabrication steps or the general "wear and tear" that can occur, especially when lithography processes may be repeated to adjust the layer alignment. However, even after several more trials, when all process were completed without complications, chips still failed. This led to a time intensive search for the cause of failure during which we decided to launch the absorption noise project presented in chapter 3. It was initially planned to be done with 2DEG samples that were substituted by SIS junctions, based on simpler and more mature nano-fabrication technology in SPEC, in order to secure some results during the thesis. The cause of the fabrication problems for the 2DEG samples was finally identified in May 2019. TMAH based (optical) developers and etchants which are standard materials used in the fabrication of semiconducting devices, such as the GaAs/AlGaAs structures with AuGeNi ohmic contacts that we used, have a corrosive reaction on the ohmics. A small test series on the influence of the exposure duration on the electrical conductance (shown in detail in the appendix D) revealed that a degradation develops for exposure durations of the order of a minute. Conventional fabrications that include mesa etching but no lithography steps should, based on our own experiences, have a total exposure time of far less than a minute. In the case of our multi step process, we have a set exposure time of over a minute, so that any additional exposure will

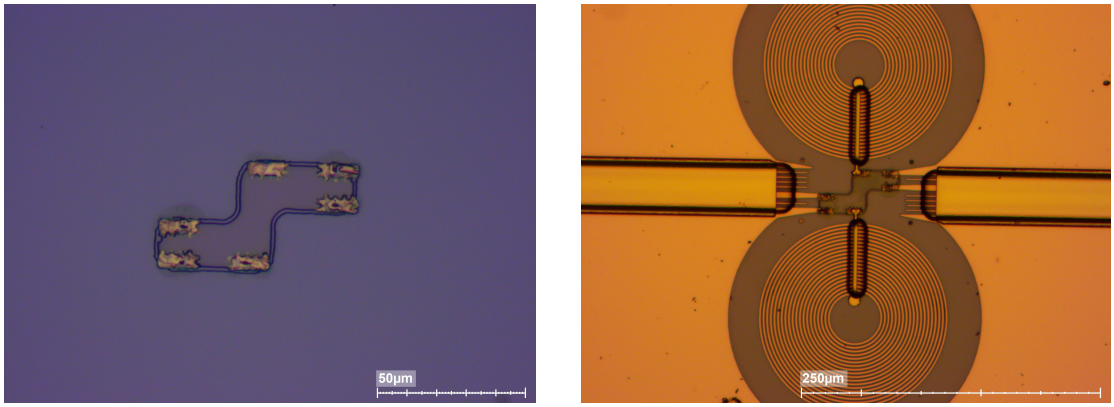

(a) (b)

Figure 5.27: (a) Image of the fabricated mesa with 6 ohmic contacts on GaAs/GaAlAs for sample B4. Due to their small size, these ohmic contacts can not be measured during fabrication, instead test pads at different location on the chip are used. From room-temperature 2-probe measurements the 2DEG resistivity is determined to be 2.8kΩ/□ and a contact resistance of the ohmic contacts of 600 Ω/100 μm which translates to an approximate contact resistance of 4.3 kΩ for the shown contacts; (b) Completed fabrication of the three layer resonating coil design on sample B4. Direct 2-probe measurements of the small ohmic contacts revealed contact resistances of the order 100kΩ which represents a disconnection between the mesa and the ohmic contacts. At first, this occurrence was attributed to an incorrect etching of the BCB bridge but also occurred for later samples, indicating a systematic damaging of the contacts.

likely cause an electrical failure of the chip. Because occasional corrections of optical lithography steps are hard to avoid, we explored the options for protecting the ohmic contacts from the developer/etchant. It is obviously possible to cover the ohmics entirely with a metallic film, but it is not possible to include a full cover in our process without some exposure to the chemical or without risking the functional integrity of the sample. Thus the entire fabrication process was remodelled from the ground up, free of TMAH-based chemicals. The development of this new process has been time consuming as it proved difficult to find compatible chemicals to the already established processes that allow the same fabrication precision and quality. By November 2019 the full fabrication process as shown in appendix B had been completed and partially tested for the mesa and coil fabrication. Due to the end of the project and the redaction of the thesis, a full process sample could not be fabricated in time, so that a final experimental proof of the viability of the recipe is still missing. However we are confident that swift progress on the matter is achievable in the near future.

5.6 Conclusion

In this chapter we have presented the design and construction of an experimental platform for RF-measurements in high magnetic fields. We have presented the fabrication of a mesoscopic conductor, defined by a QPC within the 2DEG of a GaAs/AlGaAs heterostructure, and setup an RF- measurement circuit within a dilution refrigerator that allows for many different detection schemes while providing an effective cooling with electronic temperatures of 30 mK. A sample layout has been designed so that different structures, like a quantum dot, or switches for the different contacts can be used to define many experiments for the same sample design. The most remarkable achievement of this design is fabrication of a lumped element resonator that can be used as a magnetic field tolerant impedance transformer. We have successfully fabricated and tested the characteristic parameters the resonating planar coils, fabricated on GaAs substrates, which provide a characteristic impedance of 1 kΩ (for a single coil) at a resonance frequency of 5.5 GHz with a bandwidth of about 500 MHz.
In the presented sample design, we envision the use of two coils in series leading to an effective characteristic impedance of 2 kΩ with a detection impedance of 27 kΩ. This provides an efficient RF coupling of order 1 to a single channel ($R_K = 25.8\,k\Omega$) and even fractional channels, whose impedance is of the order of $3R_K = 77.4\,k\Omega$, as is needed for the experiments in the different mesoscopic regimes shown in chapter 4. Due to fabrication issues, it was not possible to complete the fabrication of a sample on a 2DEG within the time-frame of the PhD thesis. Nevertheless, we have successfully built-up a methodology which will make it possible to perform a series of various experiments on non-equilibrium dynamics of strongly interacting conductors with unprecedented SNR in the near future.

Part III

Final conclusions

Chapter 6

Conclusions and prospects

Within this thesis project we have developed an experimental platform for the investigation of finite frequency dynamics of a single electronic channel coupled to a single EM mode at high magnetic fields or different mesoscopic conductors and related quantum effects.
Firstly, we have developed a quantum detector of RF voltage fluctuation signals, based on a simple LC-resonator as proposed by Lesovik and Loosen, that allows the measurement of electronic correlations. We chose this novel approach as it allows to measure many different experimental setups without having to abide the constraints that apply to on-chip detectors. In our specific case we are also able to operate the detector when high magnetic fields are applied to the sample which is not possible for the currently state of the art on-chip detectors. Its ability to measure the absorption and emission noise has been demonstrated in chapter 3 for a SIS junction with a tunneling resistance of few kΩ connected to a RF detection circuit via a resonator, build from a 50 Ω cavity filter, showing no back-action effects. We also used it in order to experimentally test the validity of the Kubo formula for out-of-equilibrium systems by equating the admittance measured in a linear response experiment to the difference of absorption and emission noise as extracted from power exchange measurements.
We improved the crucial impedance matching techniques which are necessary for the efficient coupling of high resistance mesoscopic conductors having few electron channels to a RF-detection line and the design and fabrication of a high impedance RF transformer made from planar coils. This impedance transformer provides 1 kΩ of characteristic impedance and can thus generate output impedances of about 10 kΩ. Hence it is possible to couple well to the quantum of resistance $R_k = 25.8\,\mathrm{k}\Omega$ of a single electronic channel. The design, fabrication and testing of our planar coil matching setup is presented in chapter 5.
We have also presented the attempted fabrication of our mesoscopic conductor, defined by a QPC within the 2-DEG of a GaAs/AlGaAs heterostructure, and setup an RF- measurement circuit within a dilution refrigerator that allows for many different detection schemes while providing an effective cooling with electronic temperatures of 30 mK. The sample has been designed so that different structures, like a quantum dot, or switches for the different contacts can be used to define many experiments for the

same sample design. Unfortunately, it was not possible to complete the fabrication of a sample on a 2DEG within the time-frame of the PhD thesis due to fabrication issues.
Nevertheless, we have successfully built up a methodology which will make it possible to perform a series of experiments in the near future. So far we have presented all developments and techniques that are necessary to conduct experiments concerning the coupling of a single channel coupled to a single electromagnetic mode. Even though the actual experiment was not completed within this thesis project, we will give a short outline of the experiments as they will be done in the near future.

Single electronic channel coupled to 1 EM mode
The sample will be similar to the inlay of figure ii.7, a QPC in the mesa defines a single channel that allows electronic transport across the mesa and couples to the series impedance of the resonating planar coils. In a 2-point geometry, this coupling gives rise to dynamical Coulomb blockade effects. The transmission across the QPC can be tuned in-situ in order to investigate how a finite transmission modifies the DCB effects arising from a single mode. We can also characterise this interaction for transmission values close to 0, when a QPC acts as a (well known) tunnel junction, and can exploit this regime to characterize the impedance as seen by the QPC.
With the environmental impedance characterized, it would then be possible to carry out a systematic study on how a finite transmission modifies the DCB coupling for a single conduction channel, or even for two parallel channels, by diminishing the magnetic field so that the spin degeneracy is restored.

Single electronic channel and a single magnetic impurity
With our platform, we have a magnetic field-tolerant quantum detector and a dot defined by QPC's in 2DEG for which we can freely and in-situ tune all transmission parameters and thus the Kondo temperature of the system. It should thus be possible to measure the dynamics of the Kondo effect for energies in the GHz range. We could also probe the change of dynamics for high applied magnetic fields and the expected freezing of screening dynamics that had been probed for DC transport already [212], [213].

Measurement of the electronic channel in the fractional QHE
We propose to measure the interactions of the 1/3 fractional channel in a 6 point geometry, where we use the chirality of the system to remove the influence of DCB effects by shorting the system to ground on-chip. The detection scheme is illustrated in figure 6.1: We DC bias the system on both sides with V_{bias} or an AC bias with RF synthesizer to probe finite frequency dynamics. The channels interact at the QPC whose transmission can be varied by the gates before the signals are picked up by our impedance transformers, the planar coils. The detection efficiency in this case is also independent of the QPC transmission value as it only depends on the fractional resistance quantum, that is established between the detection coil and the cold ground. Thus different regimes like tunneling $T \ll 1$ or weak and intermediate back-scattering $T \approx 1$ can be probed with the same detection impedance. The detection back action that originates from the transformers can then be removed from the measurement system by contacts to ground. The high SNR offered by this

scheme, should allow a systematic investigation of the full crossover between the tunneling limit and the weak backscattering limit.

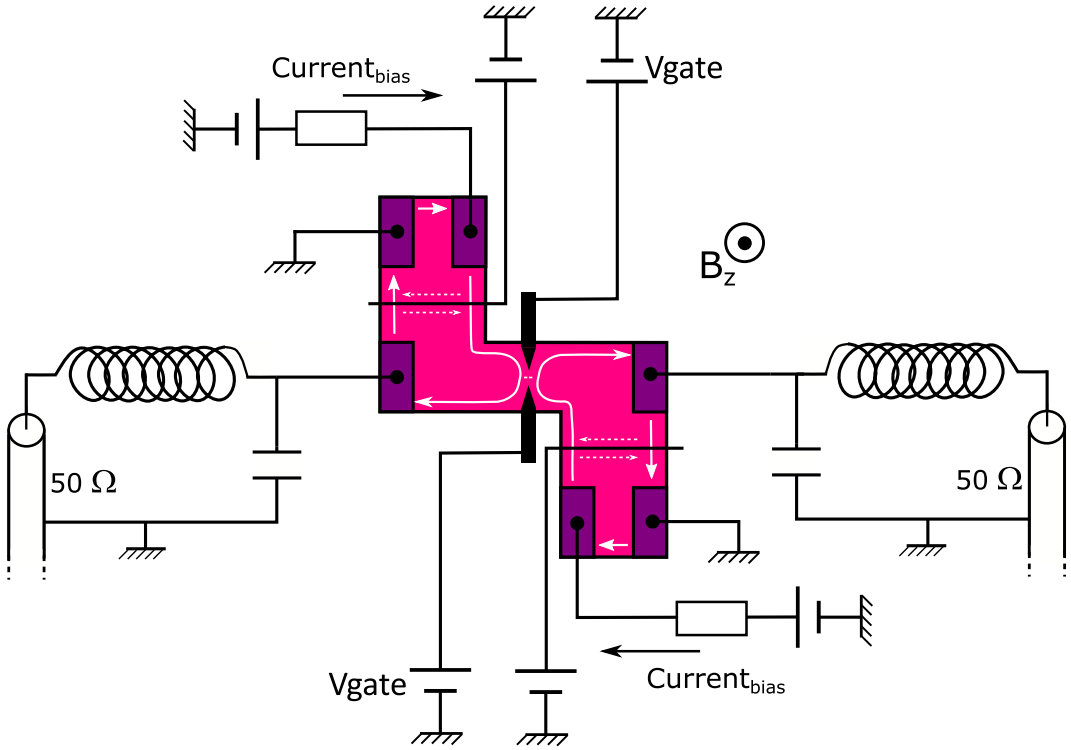

Figure 6.1: Schematic illustration of the 6-point geometry measurement to be used to probe the Fractional quantum Hall effect dynamics. Edge-channels are shown in white and propagate clockwise for the given field direction but can be reversed by reversing the field. The 6-point geometry can be switched into a 2-point geometry by using split-gates.

Appendices

Appendix A

Micron-scale optical lithography

This is the fabrication recipe as used to fabricate the high impedance planar coil resonators, described in section 5.4 of the main text, on Gallium arsenide substrates. The recipe uses a resist bi-layer for easier lift-off of the metal deposited and the invertible AZ5214-E resist in its negative state in order to obtain a high precision lithography. This recipe was used for sample A24 and A26 (see section 5.4.2.6) and later replaced by the recipe B.4 as it had to be optimized to be compatible with the fabrication of ohmic contacts.

A.1 Sample preparation

The GaAs substrate used is available as 3 inch wafers that are cut into sizeable chips with a diamond-tip scriber and cleaved by hand. The cleaning of the chips to remove dust and dirt from the cleaving is done in the clean-room.

Sample preparation:

Scribe:	Partition GaAs wafer into $8{\cdot}12\,\mathrm{mm}^2$ chips
Cleave:	Break with tape covered glass substrates
Clean:	Submerge in Acetone with ultra-sound for more than 30 s
Rinse:	IPA and de-ionized water
Dry:	2 min at 120°C on hotplate

A.2 Spin-coating

In order to prevent minimize edge-bead build-up, the spin-coating is done with recessed chucks. Any remaining edge beads are removed in the following edge bead removal step. To ensure better adhesion of the undercut layer (LOL2000) we use a primer here.

Ti primer:

Dispense:	30 s static
Spin:	30 s at 3000 rpm/3000 acc
Soft-bake:	2 min at 120°C (optional)

LOL2000 (100-200 nm, filtered):

Dispense:	static
Pre-spin:	7 s at 400 rpm/400 acc
Spin:	45 s at 6000 rpm/4000 acc
Dry-spin:	8 s at 2000 rpm/4000 acc
Soft-bake:	5 min at 155°C on hotplate

AZ 5214-E (1.4-1.5 μm, filtered):

Dispense:	static
Spin:	60 s at 4000 rpm/4000 acc
Soft-bake:	45 s at 100°C on hotplate

A.3 Edge bead removal

We remove the edge beads by repeating a positive lithography of the edges by using our edge bead removal mask (see figure A.1a) that only exposes several hundred of nano-meters of the edge. The optical lithography is done with the MJB4 Suss Microtec mask aligner which operates at 10 mW/cm^2 with a light wavelength of 365 nm.

EBR of AZ

Exposure:	30 s MJB4 (Align & Flood)
Development:	40 s in AZ 726
Exposure II:	30 s MJB4 (Align & Flood)
Development II:	40 s in AZ 726
Exposure III:	30 s MJB4 (Align & Flood)
Development III:	40 s in AZ 726

A.4 Optical lithography

The optical lithography of the coils is done using the mask shown in figure A.1b. For the maximum of resolution, the initial exposure has to be done at vacuum contact. The following inversion baking, to cross-link the exposed resist, is the most critical step and requires precise calibration. The shown parameters are calibrated for the right hotplate in Lithography bench 2 of our clean-room. After the inversion bake, the sample is flushed with light so that prior protected regions are made solvable and then removed with the developer. The developed resist mask should be plasma etched before the metal evaporation to remove resist traces.

Exposure AZ

Inversion:	2.5 s on MJB4 in vacuum contact(5 s pump/5 s wait)
Post-bake:	2.5 min at 125°C on hotplate
Exposure:	30 s Flood exposure
Development	40 s in AZ726, rinse for 15 s in de-ionized water

RIE plasma etching – if necessary

Etching:	O_2 20 cc at 6 μbar and 140 V for 40 s

A.5 Metallization

The metallization as used for A24 and A26 is copper in majority which, despite the gold cap layer, will oxidize over time. An oxygen-poor storage environment is recommended for this samples.

Metal deposition (MEB 450 PLASSYS) - P110:
The sample is mounted in a brass mask, covering the edges, and screwed on the sample holder before pumping to ca. $5*10^{-7}$ mbar (2-3 h – The Ti reduces the pressure further). Metal deposition as seen below:

Table A.1: Metal thicknesses as deposited by the MEB450 for coil & Ground.

Layer	Thickness [nm]	Current [mA]	Rate [nm/s]
Ti	15	190	0.1
Cu	500	343	1.0
Au	15	303	0.1

Lift-off

Bath 1:	40-45 min M1165 (NMP) 50°C with agitation after 10 min
Bath 2:	5 min M1165 (NMP) at room-temperature
Rinse:	de-ionized water

(a) (b)

Figure A.1: Micrograph pictures of the photo masks (RFTv2) used for the optical lithography of the micron-scale planar coils (A-series). Shown are (a) the edge-bead removal (EBR) mask and (b) the mask for the coil. Yellow coloured areas correspond to the chromium/chromium oxide on the transparent quartz substrate.

Appendix B

RF-Sample fabrication process

This appendix contains the full fabrication procedure to create our RF sample: the ensemble of our planar high impedance coils fabricated on top of AlGaAs/GaAs substrate, connected by AuGeNi contacts to the underlying 2DEG which we shape by chemical wet-etching and later on by the application of split gates. The step by step fabrication is shown in figure B.2 (and the corresponding optical masks in figure B.3) at the end. This procedure has been revised several times and puts its main focus on the preservation of the quality of the ohmic contacts throughout the process. Critical process steps will be marked and explained in detail, if necessary.

B.1 Substrate preparation

The used substrates for the fabrication are AlGaAs/GaAs hetero-structures, produced by U. Gennser at C2N. The precise fabrication method and resulting wafer may have different electrical properties or impurities on the surface. Impurities may be indium or gallium which can be found on back and front sides of the wafer. Generally wafers with gallium impurities are to be preferred over indium traces because gallium can simply be removed by a wet-etching process. For the electrical parameters as determined by C2N see table B.1. The wafers as obtained from C2N are scribed and cleaved into 8×12 mm^2 chips that are then cleaned before further processing:

Table B.1: Provided AlGaAs test samples by U. Gennser with their characteristic 2DEG properties and Al concentration ($Al_xGa_{1-x}As$). The chips have a total thickness of roughly $650\,\mu$m with indium traces on 13MS05, 08JN16 and 08JN10 and gallium traces for 18AV01.

Lot number	Carrier density n_s [cm^{-2}]	Mobility m [cm^2/Vs]	Depth [nm]	Al content
13MS05	3.3E11	550 000	110	28%
08JN16	2.0E11	570 000	93	33%
08JN10	1.6E10	560 000	78	33%
18AV01	1.7E11	-	120	-

Sample preparation:

Bath 1:	Acetone with low Ultrasound for 30 s
Bath 2:	IPA with low Ultrasound for 30 s
Rinse:	Deionized water
Dry/Dehydration:	On hotplate for 2 min at 100-120°C
Ga etching *(optional)*:	Few minutes in MF319 (control in intervals)

B.2 AuGeNi Ohmic contacts

The ohmic contacts will be fabricated by e-beam lithography as the used PMMA/MAA bi-layer allows a residue-free development for optimal thermal inter-diffusion. The ohmic contacts are deposited (figure B.2a) and annealed (figure B.2b) in order to diffuse the Ge into the AlGaAs layer, contacting the 2DEG.

E-beam lithography (E-line) - Grey room:
For the spin coating the chip has to be placed on blue tape (no recessed chuck) to avoid any backside residues. The filtration of MAA is difficult and unnecessary.

Resist:	450 nm MAA EL-10 (Spin 60 s 2000/2000); Soft-bake 150°C 90 s
Resist:	120 nm filtered PMMA 950 A3 (Spin 62 s 3000/1500); Bake 170°C 15 min
Exposure*:	E-line, 30 μm aperture at 10 kV with dose 100 μCb/cm^2
Development:	MIBK:IPA (1:4) for 50-60 s; Rinse in deionized water 60 s

*Run Wraith/ElphyQuantum as "rft" and use the position list with all element entries. The complete exposure time for the lithography is roughly 55 min.

RIE Plasma etching (Plassys MG200) - Clean room:

Etch:	O_2 6 μbar/20 cc/50 V (set to 1.0*)/30 s - removes 15 nm PMMA
Cool:	The sample is left to cool before taking it out

* !Attention! The set voltage is too low to be preset (Source does not start), the process needs to be started at 0.0 and gradually increased to 1.0.

Metal deposition (ZIVY Joule evaporator) - Grey room:
Typical pumping time: 2 hrs for P=1·10^{-6} mbar, 5-6 hrs P_{min}=1-2·10^{-7} mbar. The sample is fixed with a brass mask (1 inter-layer, see figure B.1), protecting the edges from any deposition.

Mount:	High position with brass mask
Pump:	P<10^{-8} mbar (ca. 5 h)
Deposition:	Manual deposition, thicknesses and rates below
Cool:	Let the sample cool down for 10 min
Dismount:	Take out sample and remove brass mask
Bath 1:	Acetone at 80°C for 10 min
Bath 2:	Acetone at RT for 5 min
Bath 3:	IPA at RT
Rinse:	Deionized water

Table B.2: Thicknesses and deposition rates for AuGeNi ohmic contacts as deposited with the ZIVY Joule evaporator.

Layer *	Thickness [nm]	Current [A] **	Rate [nm/s]
Ni (8)	4	ca. 90	0.2
Ge (5)	60	ca. 225	0.3
Au (3)	120	ca. 225	0.4
Ge (5)	25	ca. 210	0.2
Au (3)	25	ca. 210	0.2

* The numbers refer to the number setting for the metal on the oscillator crystal detector. ** The current values may vary depending on filling level and position of the crucibles (± 10 A).

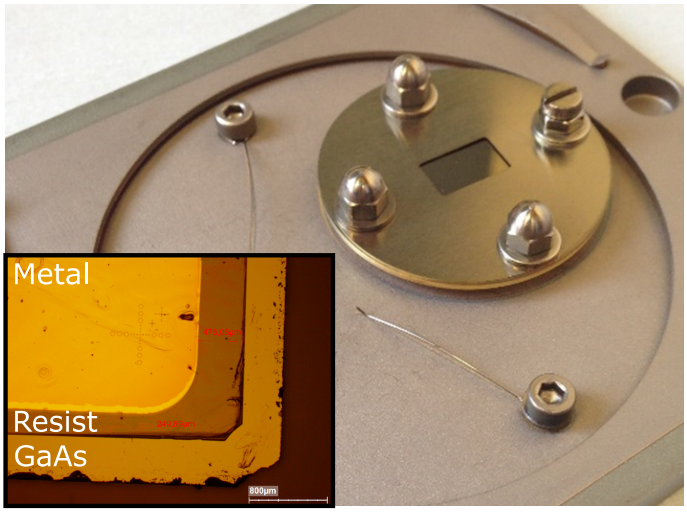

Figure B.1: Photo of a GaAs substrate mounted in the brass mask used for all metal evaporations (shown as inset) after the optical lithography. The $6 \times 10\text{mm}^2$ cut-out of the top mask prevents any metal deposition on the unprotected chip edges that result from the EBR.

Rapid thermal annealing (Jetlight 50) - Characterization room:

Mount: The sample is placed on the SiO_2 wafer used as sample holder
Anneal: Heat profile "1JMAuGeNi" in N_2/H_2 atmosphere (5% H_2)

Table B.3: Temperature settings for the ohmic contact diffusion anneal for the RTA Jetlight 50 ("1JMAuGeNi").

Step	Pre heat	Mixing	Diffuse	Cool
Temperature	120°C	370°C	470°C	120°C
Duration	2 min	2 min	80 s	20 s

Ohmic contacts and the mesa can be tested with the test-pads using a probe station. Expected values for the resistance should be in the order of $<1\,\mathrm{k}\Omega$ for $100\,\mu$m distance between pads.

B.3 Mesa definition

In order to create a mesa pattern in a GaAs/AlGaAs hetero-structures the surface has to be etched until the dopant layer is reached (shown in figure B.2c). In our case with a thin cap-layer of GaAs and an approx. 100 nm AlGaAs layer we need to etch roughly 80-110 nm to remove the dopants. In order to have a non-selective etching of both GaAs and AlGaAs we use a mixture of phosphoric acid and hydrogen peroxide. Due to compatibility issues with using Al-masks and corresponding etchants (the optical developer MF-319 and other TMAH containing products etch Al, Ga and probably Ni), we are using a resist mask to protect the 2-DEG where we want to define the mesa. The resist mask is created by optical lithography with the MJB4 Suss Microtec Mask aligner. We firstly remove the edge bead of the resist by using an EBR-mask (see figure B.3a) that exposes only the edge, before using our final mesa mask shown in figure B.3b.

Optical lithography - Clean room:
Spin-coating on the recessed spinning chuck with 2-brass sheets to adjust for the thickness.

Primer:	Microposit Primer (Spin 5 s 1000 rpm/200 acc; 30 s 6000/4000)
Resist:	1.4 μm S1813 (Spin 60 s 4000 rpm/4000 acc); Soft-bake 110°C 60 s
EBR:	Exp. Gap 30 s & dev. in MF 319 for 30 s
	Repeat 2-3 times if necessary
Exposure:	L. Vac. (5 s/5 s) for 30 s
Development:	MF319 for 30 s; Rinse in deionized water

Mesa etching - Cleanroom:

Etch solution:	3 H_3PO_4 - 1 H_2O_2 - 80 H_2O
Etch:	120 nm during 2 min* (for 18AV01)
Removal:	Acetone at 60°C for 5-15 min

*Etching rate for GaAs-AlGaAs-GaAs is roughly 1.0 nm/s but may vary depending on the cap-layer thickness and Al-concentration. Adjust the etching time to the Depth of the used substrate (see table B.1).

B.4 Ground plane and Coils

The Ground and all RF/DC lines are fabricated together with the planar coil resonators by optical lithography (see figure B.2d). The used optical mask (version RFTv4) is shown in figure B.3c.

Optical lithography (MJB4) - Clean room:
Spin-coating on the carrier chuck for the undercut-layer (SF-8) and on the recessed chuck with 2 brass sheets for the resist layer (AZ).

Resist:	500 nm filtered SF-8 (60 s 4000 rpm/4000 acc); Soft-bake 160°C 5 min**
Resist:	1.4 μm filtered AZ5214-E (60 s 4000 rpm/4000 acc); Soft-bake 100°C 45 s
EBR:	Exp. Gap 30 s & dev. in AZ developer (dil. 1:1) for 30s Repeat 2-3 times if necessary
Exposure:	L. Vac. (5 s/5 s) for 2.5 s, Inv.-bake* at 125°C for 2.5 min Flood exposure for 30 s
Development:	AZ developer (dil. 1:1) for 60 s; Rinse deionized water

* We use the right hotplate in Lithography booth 2, set to 125°C (if another hotplate has to be used, the process temperature needs to be re-calibrated). ** used left hotplate in Lithography booth 2

RIE Plasma etching (Plassys MG200) - Clean room:

Etch:	O_2 6 μbar/20 cc/150 V/40 s - 20 nm AZ removed (0.5 nm/s)

Metal deposition (MEB 550 PLASSYS) - Grey room:

Mount:	Place sample in the brass mask and screw on sample holder (see figure
Pump:	$5{\cdot}10^{-7}$ mbar for about 2 h
Deposition:	Automatic metal deposition see below:
Dismount:	Unscrew and remove brass mask
Bath 1:	Remover PG at 60°C for 20 min.
Bath 2:	IPA at RT for 2-5 min
Rinse:	Deionized water

Table B.4: Metal thicknesses as deposited by the MEB550 for coil & Ground.

Layer	Thickness [nm]	Current [mA]	Rate [nm/s]
Ti	15	67	0.1
Au	300	370	1.0

Ohmic contacts and the mesa can be tested again with the test-pads using a probe station (<1 kΩ for 10 μm distance between pads). We can also measure the DC lines accessing the mesa: DC lines on same side: 10-12 kΩ; DC lines across mesa: 60-70 kΩ.

B.5 Dielectric supported Bridges

Build-up of the BCB support structure for the metallic bridge that will connect the coils to the ohmic contacts/Mesa. BCB is a thick, viscous and negative resist which we shape by optical lithography as shown in figure B.2e (corresponding mask shown

in figure B.3d). The height can be modified by changing the developer temperature due to different dark erosion rates. After the development the BCB needs to be cured to be stable after which it can not be removed by any chemical. Any kind of reworking needs to be done before the curing.

Optical lithography (MJB4) - Clean-room:
Spun on tape and carrier chuck for the Primer and on the recessed chuck with 2 brass sheets for BCB (Use of special chuck set dedicated to BCB). The BCB layer has an initial thickness of 5 μm and will be reduced to 3.5 μm during the post-processing.

Dry:	2 min at 100°C
Primer:	AP3000 (10 s 1000 rpm/200 acc // 35 s 6000 rpm/1000 acc // 20 s 3000 rpm/1000 acc); Soft-bake 100°C 60 s
Resist:	5 μm BCB 4024-40 (8 s 1000 rpm/200 acc // 32 s 5000 rpm/2000 acc); Soft-bake 65°C 3 min
Exposure:	Exp. gap for ca. 15 s (150 mJ Dose) (25 mJ/μm $\rightarrow$ 13.3-14.3 s for 5.3-5.7 μm)
Development*:	Preheat sample on hotplate 55°C 5 min; DS3000 (35°C) few min*, DS3000(RT) 2 min 20 s
Rinse:	2 baths of deionized water
Fix-Soft-bake**:	Hotplate 100°C 60 s

* All development baths need to be at temperature before starting and the chip has to move from the hotplate into the bath without delay. The important development time is the warm DS3000, if the bridge should be smaller, the process can be repeated or that time extended. ** The fix-soft-bake stabilizes the BCB and ends the development process. If the bridges are well aligned they are fixed by soft-baking for 1 min at 100°C.

Optional: Scrapping/Reworking - Clean-room:
If the bridges are misaligned (shifts are possible as the resist at exposure is very thick), the bridges shall not be fixed but can be removed with primary stripper A. Stripper A needs to be at temperature before the sample is put in to prevent any corrosion damages.

Mount:	Place the sample in the handling-cage
Removal:	Lower in Primary Stripper A (opaque) at 80°C and 5 min soak*
Rinse:	IPA and DI water

* Heating prevents water absorption, which would make it corrosive to metals.

Curing (Vacuum oven) - Characterization room:

Mount:	Place sample in the oven, under the heater in central position
Pump:	Evacuated the chamber to ca. 10^{-6} mbar
Pressurize:	Stop the vacuum pump, seal the chamber, Inject N_2 to 10 mbar
Cure:	1 h at 250°C*, ramp rate 500°C/h
Cool:	Around 1h in the oven
Clean:	IPA and DI water

* The highest temperature, due to overshoot after 30 min, was 258°C at a pressure of 12 mbar in the chamber.
Attention: the PID controller was reset and parts were changed, the old config is no longer valid.

Descum (Plassys MG200) - Cleanroom):
Reactive Ion Etcher Plassys MG200 is used to remove approximately 100-200 nm BCB, which removes all scum and dirt on the chip, finely shapes the bridges edges and smooths the surface profile.

Etch:	45 cc O_2 & 5 cc SF_6 250 μbar/80 V* /20 s**
Cool:	15-20 min ***
Bath (optional)***:	Dip in 10% acetic acid for 10 s

* The controller on the machine can be pre-set to 2.0. ** With 70 V(=20 W) for 25 s measured a 7 nm/s etching rate. *** Leave sample at rest for 15-20 min to cool down and let left-over chemicals evaporate, they may otherwise spoil the surfaces. *** If copper is used, the sample has to be dipped in 10% acetic acid right after the etching. Otherwise the copper will corrode and copper crystals may form on the sample.

B.6 Metallic bridge

To deposit the metallic bridges onto the BCB as shown in figure B.2f, we conduct a lithography with triple stacked AZ resist (mask shown in figure B.3e). Unlike previous steps, the resist can cannot be etched with standard plasma techniques due to the exposed BCB being oxidized (which would create SiO_2 layers). In order to clean the lithography and to enhance the surface roughness of the BCB for better adhesion to the deposited metal, we use an Ar-ion milling right before the metal evaporation. The milling and deposition are both done together in one process using the MEB 550 PLASSYS e-gun.

Optical lithography (MJB4) - Clean-room:
Spin-coating on the recessed chuck with 2 brass sheets for the resist layer (AZ).

Resist:	2.7 μm triple stack filtered AZ5214-E 2x (Spin 60 s 4000 rpm/4000 acc); Soft-bake 100°C 60s 1x (Spin 60 s 4000 rpm/4000 acc); Soft-bake 100°C 45s
EBR:	Exp. Gap 30 s & dev in AZ developer (dil 1:1) for 30s Repeat 5-6 times if necessary
Exposure:	L. Vac. (5 s pump/5 s wait) for 4.8 s, Inv.-bake 125°C for 2.5 min Flood exposure for 60 s
Development:	AZ developer (dil 1:1) for 60 s; Rinse deionized water

Ion-milling & Deposition (MEB 550 PLASSYS) - Grey room:
Predicted/measured etch rate for the chip center is ca. 11 nm/min. the inhomogenity of the milling across the chip is ±1 nm.

Mount:	Place sample in the brass mask and screw on sample holder
Pump:	$5{\cdot}10^{-7}$ mbar (crucible) for about 2h
Milling:	Automatic milling of 1 nm BCB with 3 cc Ar (settings below)
Deposition:	Automatic deposition (thickness and rates below)
Dismount:	Unscrew sample and remove brass mask
Bath 1:	R1165 at 60°C for 20 min.
Bath 2:	R1165 at RT for 5 min
Rinse:	IPA and deionized water

Table B.5: Controller settings for the ion source during the Ar-ion milling of MEB-550.

Time [s]	Beam current [mA]	Beam voltage [V]	Acceleration voltage [V]
60	12-13	500	75

Table B.6: Metal thicknesses as deposited by the MEB-550 for the bridge metallization.

Layer	Thickness [nm]	Current [mA]	Rate [nm/s]
Ti	15	67	0.5
Au	300	430	1.0

At this stage we can check all the connections to the mesa via ohmic contacts by measuring on the larger contacting pads on the edge of the chip using a probe station. We can measure the 2-point resistance of the DC line and ground contacts (clearly visible in figure B.2d) as well as the RF-line/coil contacts (see figure B.2f). Expected values for neighbouring DC line to ground contacts are 10-12 kΩ while any pairing of DC line and ground contact across the mesa should give 60-70 kΩ. Measuring both RF lines across the mesa yields a resistance of the order of 25 kΩ while any pairing to a non-RF contact is about 40-50 kΩ.

B.7 QPC and other Gates

In this last step the gates used for the quantum point contact and other split gates are added. The gates are done by e-beam lithography in the E-line with aluminum deposited, which could be chemically removed if necessary.

E-Beam Lithography (E-line) - Grey room:

Resist:	450 nm filtered MAA EL-10 (Spin 60 s 2000 rpm/2000 acc); Soft-bake 150°C 90 s
Resist:	120nm filtered PMMA 950 A3: (Spin 62 s 3000 rpm/1500 acc); Bake 170°C 15 min
Exposure*:	10 kV, 10 μm apert. 0.02 nA at WD10, Dose 170 $\mu C/cm^2$
Development:	MIBK:IPA (1:4) for 50 s; Rinse deionized water 60 s

* Run Wraith/ElphyQuantum as rft and use the corresponding position list with all element entries. The complete exposure time for the lithography is roughly 3-10 min.

Evaporation (MEB 450 PLASSYS) - P110:

Pump:	ca. $< 5{\cdot}10^{-7}$ mbar for about 2-3 h
Deposition:	Automatic deposition see below:
Bath 1:	Acetone at 80°C for 10 min
Bath 2:	Acetone at RT for 5 min
Bath 3:	IPA at RT
Rinse:	Deionized water

Table B.7: Metal thicknesses as deposited by the MEB450 for the gates and patches.

Layer	Thickness [nm]	Current [mA]	Rate [nm/s]
Al	100	365	1.0

B.8 Wirebonding

The completed chip is glued onto the PCB with PMMA as adhesive that needs to be hardened at 150°C for several minutes. The sample can then be wire-bonded from the pads of the chip to the corresponding lines on the chip. For the wire bonding we use the automatic wedge bonder "tpt10" with 25 μm Al wire. The bonding is done at the following settings:

Temperature:	ca. 150°C, heated sample holder
Bond1 settings (chip):	280/500/500 (Force/US-power/time)
Bond2 settings (PCB):	390/390/390 (Force/US-power/time)

For the connection of DC-lines a single wire is sufficient while at least three are needed to to conserve the aspect ratio of the co-planar line and achieve a better impedance matching. Likewise at least three bonds are required for the ground connections directly adjacent to the the RF-lines to create a continuous connection for the ground currents, but it is recommendable to add more.

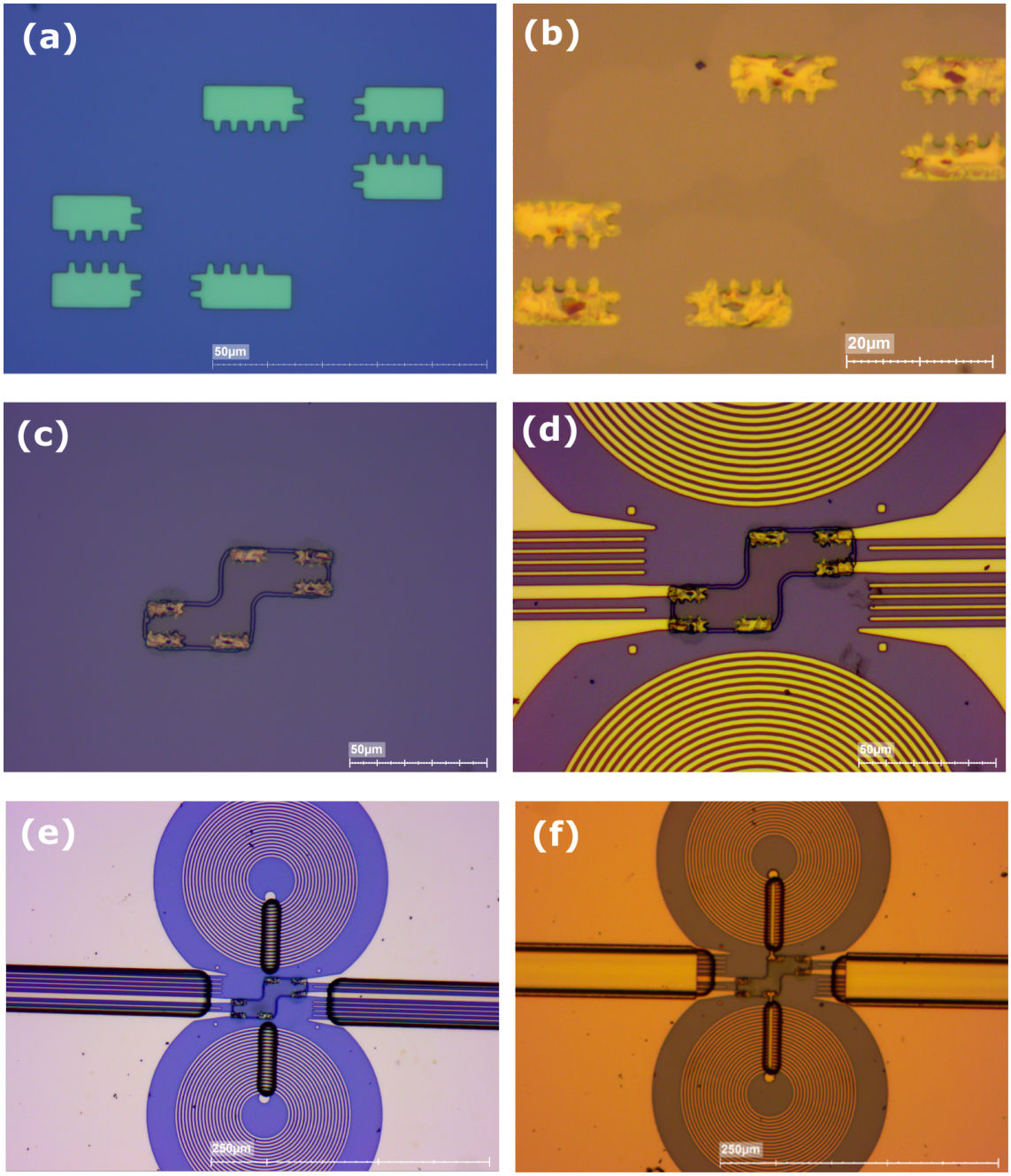

Figure B.2: Micrographical images of the RF- sample after different fabrication steps. The AuGeNi ohmic contacts are deposited after the e-beam lithography (a) and then annealed to diffuse into the underlying 2DEG (b). The substrate and the contacts are masked and the wet etched to create the mesa. After this the coils, ground-plane and DC-lines are deposited following an optical lithography (d). Onto the metallization of the coils and DC lines, dielectric (BCB) bridges are created (e) which serve as a support for the successive lithography and metallization (f) of the bridges that connect the coils to the mesa and the covers for the DC-lines.

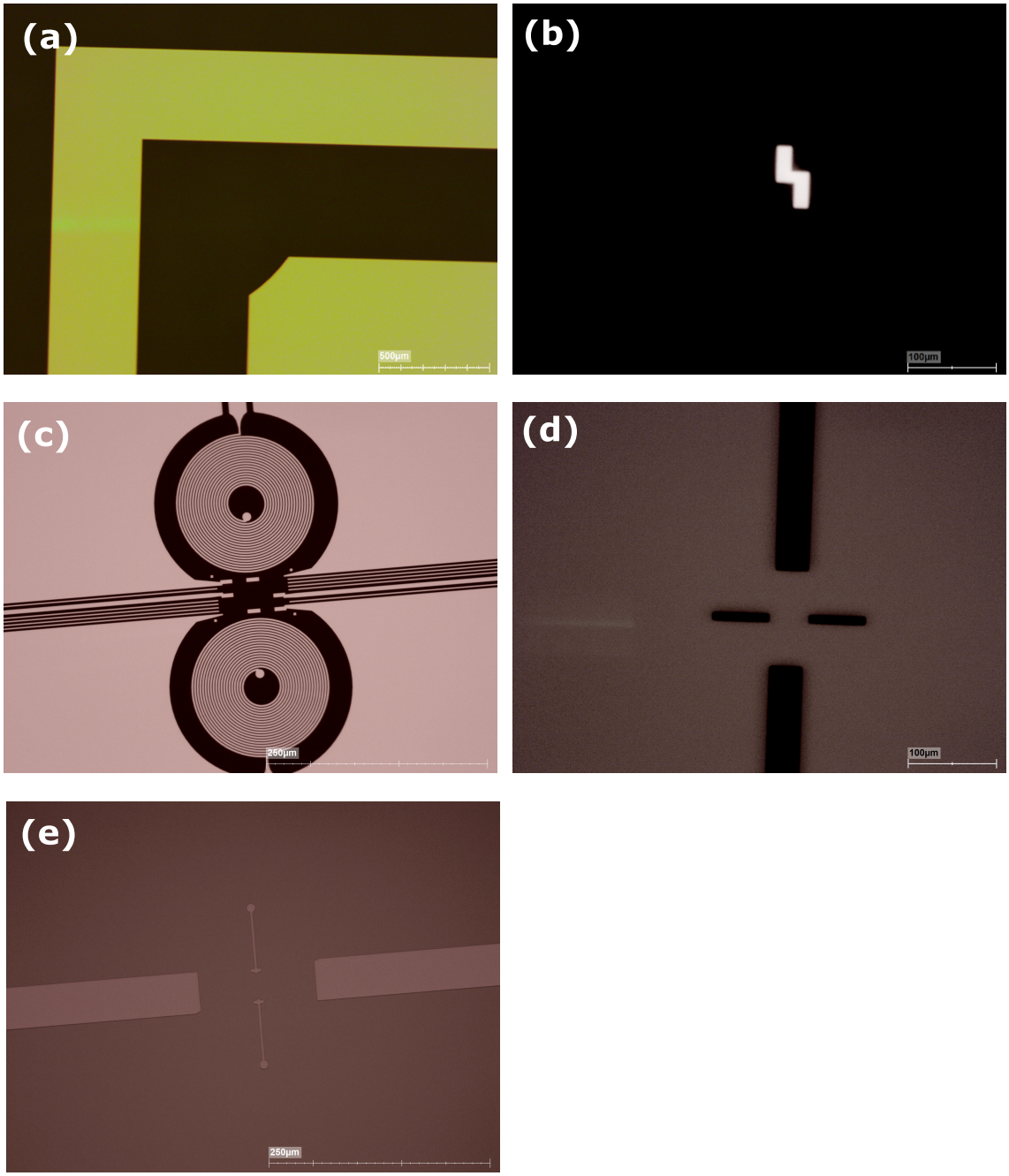

Figure B.3: Micrograph pictures of the photo masks (RFTv4) used for the different optical lithographies of the full sample fabrication on AlGaAs/GaAs (B-series): (a) EBR mask; (b) Step 2 - Mesa area; (c) Step 3 - Sample area including coils, DC-lines and newly added protective pads for the ohmic contacts; (d) Step 4 - Cut-outs for the inverse exposure of the BCB bridge support; (e) Step 5 - Metallic bridges (center) to connect coils and mesa and metallic covers for the DC-lines (left, right).

Appendix C

DC resistivity of materials and resistance of tested coils

C.1 DC resistivity of deposited metals

Here we list the calculated DC resistances for the DC and RF-lines as well as the coils of our sample design as calculated for the listed and measured resistivities of different metallizations in table C.1:

Table C.1: Measured resistivities for different used materials at RT and below 4 K, with calculated sheet resistances for 500 nm thickness.

Material	ρ_{RT} [$\mu\Omega$cm]	ρ_{4K} [$\mu\Omega$cm]	sheet [Ω/squ]
Cu deposited	2.32	0.38	0.046 / 0.0076
Au deposited	2.80	0.57	0.056 / 0.0114
Cu annealed	2.00	0.18	0.040 / 0.0036
Au annealed	2.84	0.18	0.057 / 0.0036

C.2 Calculation of the DC resistance of tested coils

The layout of the chip with its full DC and RF line, as used for samples A 24 and A26 as described in section 5.4.2, is shown in figure C.1.
The lengths and widths of elements are taken from our design or are estimated, as for the coil by equation C.1 where N is the number of turns , h is the width (wire + gap) and D_0 the inner diameter. The results are shown in table C.2.

$$L_{coil} = \pi N(D_0 + h(N-1)) \tag{C.1}$$

$$L_{coil} = \pi * 19.5(38\mu m + 3\mu m * 18.5) = 5.9mm \tag{C.2}$$

Table C.2: Element DC-resistance at RT and 4 K. The DC and RF lines are split into their larger and narrower segments.

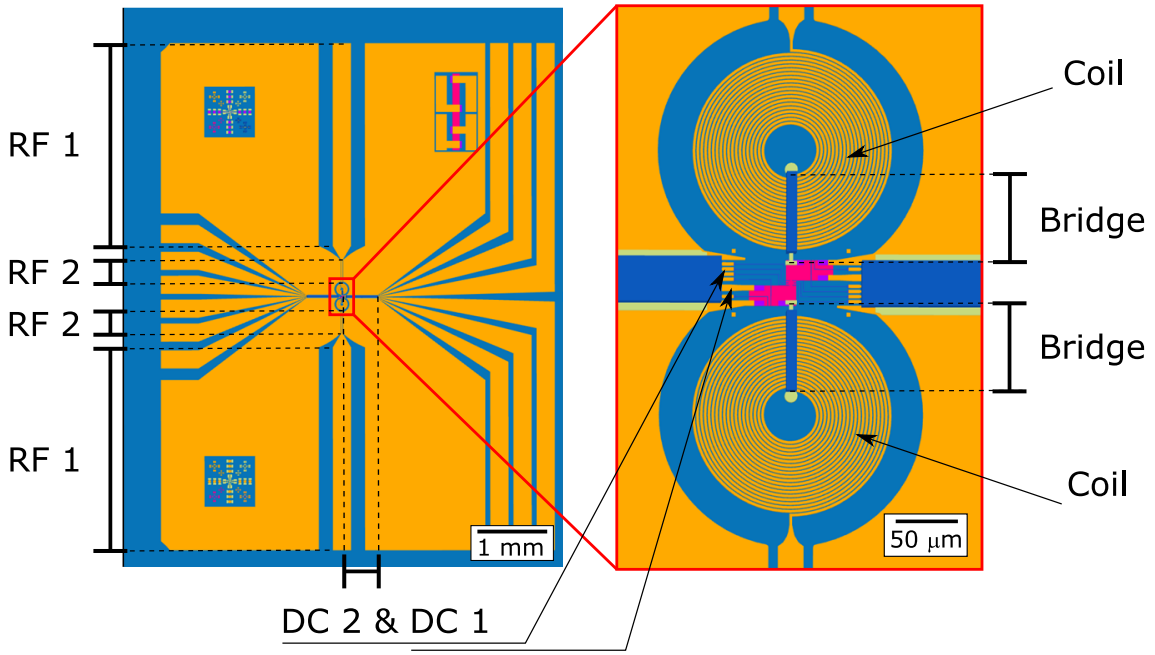

Figure C.1: Sample layout with marked lengths of the different RF and DC line segments: (left) half side of a chip and (right) zoom of the sample area. The RF line's segment 1 has a width of 250 μm and transitions into RF segment 2 with 20 μm and is further connected to the coil with 2 μm and the bridge with 3 μm width. The DC lines have the same length but different widths, DC line 1 used to connect ohmic contacts has a width of 5 μm and the remaining lines are 1.5 μm.

Element	L [μm]	w [μm]	t [μm]	R_{RT} [Ω]	R_{4K} [Ω]
RF-line 1 (Cu)	3000	250	500	0.48	0.045
RF-line 2 (Cu)	300	20	500	0.70	0.063
Coil (Cu)	5900	2	500	136.9	12.322
DC-line 1 (Cu)	458	5	500	3.66	0.330
DC-line 2 (Cu)	442	1.5	500	11.79	1.061
Bridge (Cu)	70	3	300	0.93	0.084

Appendix D

On the fabrication of AuGeNi contacts

D.1 Summary of diffusive AuGeNi reactions

To establish good electrical contact to semiconducting materials has been a technical challenge that saw much progress over the past decades. Generally, when traditional metal conductors are brought into contacts with a semiconducting material, a Schottky potential barrier is formed that prevents the electronic flow. Many material combinations for ohmic contacts to a variety of semiconducting substrate were discovered since then that form highly conducting ohmic contacts. A good review for different ohmic contacts to GaAs and other semiconductors is given by Baca [214] and general reading about semiconductors, their fabrication and ohmic contacts can be found in the books of Pearton [215] and Sze [216]. Here we want to focus on the ohmic contact fabrication on GaAs substrates which was firstly realized with pure gold contacts. The Shottky barrier of gold contacts is of the order of 0.9eV but can be reduced to almost 0 after heat treatment causing a solid-state reaction of gold with GaAs. Au-Ga forms at the interface with a low solubility of As so that it sublimates and is either lost or reforms as precipitates on the surface:

$$Au + GaAs \longrightarrow Au - Ga + As_g \tag{D.1}$$

This reaction depends purely on the solid-state reactions of the metals or, if heated to the melting point of the compound (500°C), a liquid phase reaction. The interaction suffers from different complexes that can be formed and the inhomogeneous reaction between GaAs and gold in general. This can be caused by a native oxide layer of the substrate or other surface layers that inhibit a strong reaction. In addition to that, the solid-state reaction has a directionality that also leads to a bad surface morphology, typically pyramidal pits will form along the 100 and 111 axis of GaAs. Attempts were made to create smoother ohmic contacts by diffusing Ge into the substrate, as done by Braslau et al. [217] in 1967. They used the liquid Au-Ge eutectic to dissolve the GaAs and diffusively exchange Ga and Ge. The Ga is dissolved into the liquid gold and the germanium, as a counter flow, is implemented into the substrate.

The incorporated Ge creates a n^+ doping under the surface, diminishing the Schottky barrier and thus creating an ohmic contact. The materials are evaporated as Au/Ge with a Ni layer for better surface wetting. However the Ni has a far more important role as it breaks down the GaAs and also binds the Ge to diffuse it into the substrate. The reactivity of the Ni is thereby independent of its position of the stack as it will always accumulate at the interface of GaAs. The general reaction is:

$$Au + Ni + GaAs \longrightarrow Au - Ga + Ni - As \tag{D.2}$$

The interaction of the Ni with As creates a very homogeneous surface as opposed to the parallel occurring gold solid state reaction. The Ni breaks the GaAs and bonds to the As atoms, allowing the gallium to out-diffuse into the gold and move towards the surface [218]. While the Ni promotes homogeneous reactivity it does not create the ohmic contact, the presence of Ni even increases the Schottky barrier. But it enables the diffusion of Ge in order to create a n^+ doped layer along the Ga vacancies, by a slightly more complex reaction (see figure D.1a): Ni starts forming NiGaAs at the interface at temperatures of around 300°C which break down to NiGa and NiAs at higher temperatures and may contain small amounts of Ge. At the same time the germanium mixes with the gold forming the eutectic at 370°C, starting the reaction of Ni and Ge to form NiGe. For even higher temperatures above 400°C all secondary and ternary phases decompose except for NiGe. The Ga and As are thus released and they diffuse into the gold or may regrow on the interface as GaAs. Hence the Ge is incorporated in the substrate as NiGe under re-grown GaAs and creates the ohmic contact Ni-Ga-As-Ge. Because of this reaction, it is important to find the optimum ratio of Ni to Ge and the according thermal treatment for the diffusion. Generally, several nanometers in thickness are required for the diffusion to be efficient enough to penetrate down to the 2-DEG while a thicker layer increases the contact resistivity and may also prevent the exchange of Ga and Ge. Regarding the heat treatment one has to take care that the Ni particles do not grow into coarse particles. The contact resistance is low if Ni particles are small and well distributed but if Oswald ripening occurs, the resistance will increase as shown by Tahamatan (see figure D.1b). For his deposition of alloyed AuGeNi on GaAs depending on the particle size, contact resistances of 10^{-1} to 10^{-7} Ωcm^2 were observed.

D.2 Ohmic contact degradation

During the fabrication of the RFT-sample several ohmic contacts that were fabricated before the mesa is defined, but following the same recipe as described in appendix B.2, were observed to lose connectivity during further processing of the sample. The cause for this was identified as an etching of the contacts by the used optical developers AZ726 and MF319 which both contain the chemical base TMAH (Tetramethylammonium hydroxide). To test the failing mechanism, a test array of 16 (4×4) ohmic contacts was fabricated on AlGaAs/GaAs and etched minute by minute while measuring the contacts with a 2-probe station. The results of the measurement or the first pair of every column and the total average resistance are shown in figure D.2. We

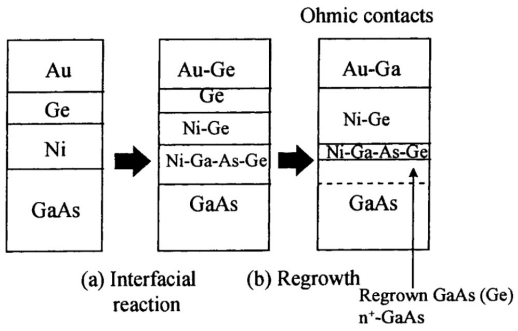

(a) AuGeNi solid-state reaction

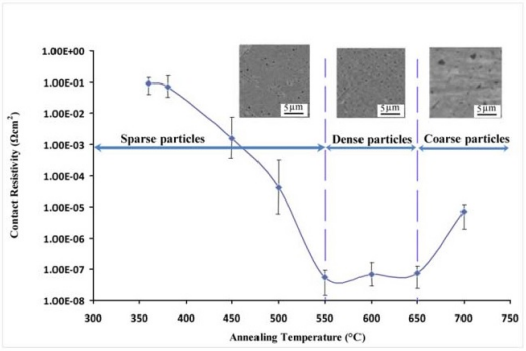

(b) Ni-particle growth

Figure D.1: (a) Idealized schematic of the evolution of phases during formation of an ohmic contact to n-GaAs using Au/Ge/Ni metallization [215]. The real interfaces are highly non-planar and occur pre-dominantly in Ni-pillars. (b) Measured contact resistances of AuGeNi contacts after rapid-thermal annealing for 1 min at different temperatures (20 s pre-heat at 240°C) [219]. Depending on the temperature a ripening of the diffusing Ni causes an increase in contact resistance.

can clearly see that the resistance measured increases after 2-3 min exposure to the base and strongly increases after 5 minutes. With the measured contact resistances of the order of 1 kΩ or above, the contacts can not be used for experiments anymore. Visually the pads did not show any drastic changes, except for a slight change of contrast between different grains or phases. We have no visual indicators of any specific etching reaction.

But due to the common use of TMAH as silicon etchant for different applications in the industry, it is known that the following metals are TMAH resistant: Cr, Pt, Ge [220], Au[1]. Likewise it is known to attack aluminum and also Ti [221]. While the Al etching capabilities are common knowledge in the industry, titanium is assumed to be stable if developer temperatures are below 80°C [221] but it may have a slow but finite etch rate even at room-temperature. From our own fabrication we also know that gallium is etched and we believe that a slow etching of Ni may take place, even though it may not be the reason for the electrical failures that we experience after several minutes. Nickel is quite similar to titanium in structure and often times the same etchants are attacking both metals. Hence we think it is reasonable that a slow etching reaction may take place. We have tested this by submerging an ohmic contact test chip in MF319 over night for several hours. After several hours (14 h) the contacts had peeled off, revealing a clean substrate underneath (figure D.3). As no Nickle, which normally gives a red hue under the microscope, is visible, neither on the substrate nor on the backside of the peeled contact, we know that nickel is indeed etched. We can also see that the mesa stripe may be subjected to some pitting, possibly by attacking the Al within the AlGaAs, if exposed through impurities or defects.

[1]Microchemicals Gold etching manual 2013

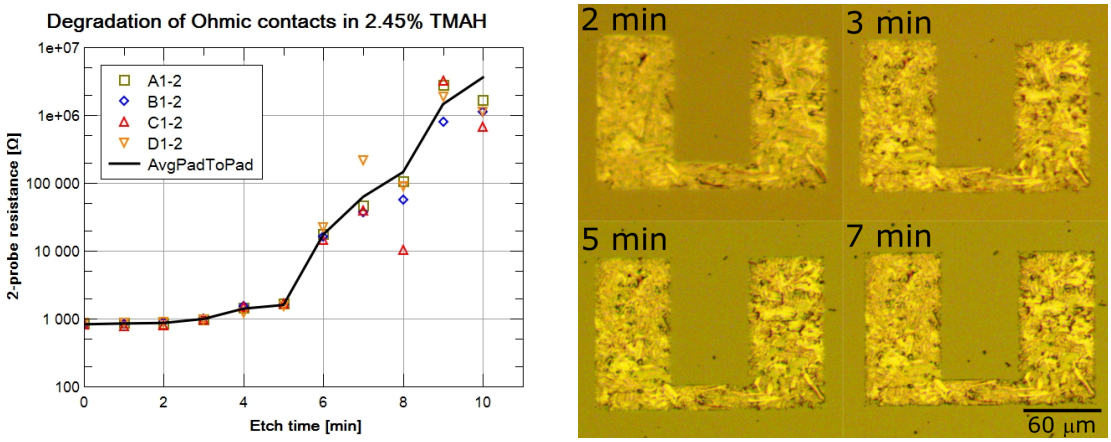

(a) 2-Probe measurement

(b) Contact B2

Figure D.2: (a) Plot of measured 2-probe resistances of our test sample array for selected pads ($100{\cdot}200\,\mu m^2$). The average is calculated with all 12 measurements. The etching starts at around 2-3 min increasing the resistance and starts to fully destroy the pads after 5 min with a manifold increase in resistance. (b) Optical images of AuGeNi contact B2 after 2, 3, 5 and 7 min of etching in MF319. Over time the contrast between Au-rich and Ga/Ge-rich phases becomes stronger as gallium is etched away. But there is no clear visual indicator regarding the decrease in the conductivity of the contact.

So we know that the materials that are likely to be etched are the nickel wetting-layer and the gallium that diffuses from the substrate into the contact. We formulate two hypotheses for the short-term failure of the contacts: Firstly, there may be a complex phase of Ni-Ga-Ge-Au at the interface that is weak to TMAH due to high contents of Ga and Ni. Secondly, as the Ni diffusion, which starts the Ge-Ga exchange, occurs in pillars, we assume that the diffusion of Ga is locally limited. This means that as the eutectic solidifies and forms pure lamellas, there might be Ga pillars (tubes, disk, needles etc.) in these contact zones that may be etched away completely, disconnecting the pad from the mesa. As countermeasures one has to either replace the chemical products in question or use a protective layer. We have tested that a fully enclosing gold cap layer protects the ohmic contact, but it is not compatible with the sample design. The cover layer acts as a masking layer for the following etching of the mesa, thus a finite width of 2DEG, equal to the cover layer overhang, surrounds the ohmic contact. When working in the quantum Hall regime, this could cause the ohmic contacts to be disconnected when the edge channels are not in contact with the ohmics. This can be prevented with a partial capping layer, covering the top without fully protecting the edges of the contact, but when tested it showed not to be effective. The chosen solution has thus been to adjust the fabrication recipe by replacing all corrosive chemicals as described in section 5.1.3 of the main text and the recipe in appendix B.3.

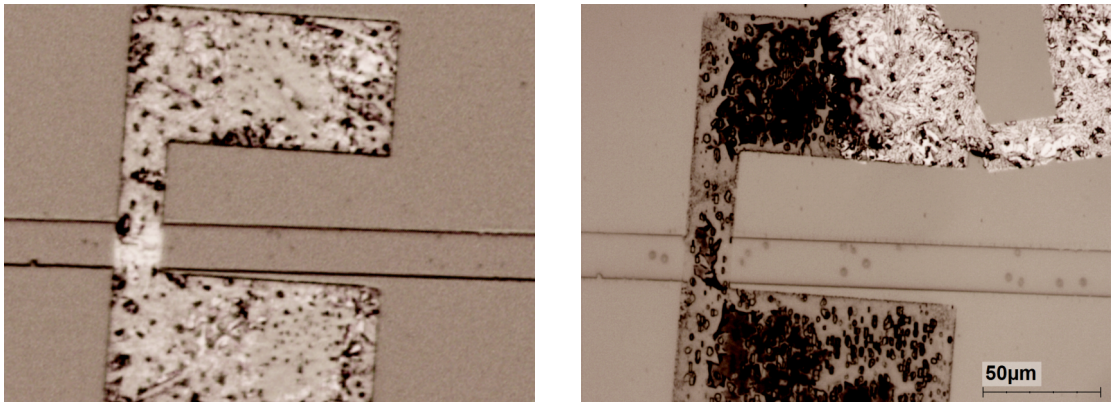

(a) Etched 60s (b) Etched 14h

Figure D.3: Optical images of ohmic contact test chip C5Q4 contact A3 after 60 s (a) and 14 h (b) of etching in MF319. The long term exposure to TMAH causes the pads to lift off the substrate. We can see that the area underneath the lifted-off pad shows the same color contrast as the surrounding substrate, indicating that the Ni-layer is gone, which would have provided a red hue. There is also no trace or hue on the underside of the peeled-off and folded metal sheet.

D.3 Test of AuGeNi contacts at RT and low T

D.3.1 RT fabrication tests

We have tested several ohmic contacts fabricated on AlGaAs/GaAs substrates at room temperature and determined optimal achievable contact resistances to the 2DEG by using our laboratory's equipment. The crucial steps, influencing the quality of the contact, are the lithography, the contact size/composition and the annealing, all while avoiding any destructive chemical reactions during and after their fabrication.

Table D.1: Rapid thermal annealing (Jipelec jetlight 50) of AuGeNi contacts, fabricated by e-beam lithography on $5\times5\text{mm}^2$ chips of AlGaAs/GaAs (08JN16). Chip 5 and chip 6 were cut into quarters which were individually annealed. The sizes of ohmic contacts vary slightly but are of the order of $100\times200\mu$m. The resulting average contact resistance are illustrated in figure D.4

Chip	Pre-heat	Mixing	Diffusion	Cool	Note
1-full	120°C, 2 min	370°C, 4 min	470°C, 4.5 min	0°C, 4.5 min	Oven no gas flow
2-full	120°C, 2 min	370°C, 4 min	470°C, 4.5 min	0°C, 4.5 min	Oven no gas flow
3-full	120°C, 2 min	370°C, 4 min	470°C, 5 min	0°C, 4.5 min	-
4-full	120°C, 2 min	370°C, 4 min	470°C, 4 min	0°C, 4.5 min	-
5-1	120°C, 2 min	370°C, 2 min	470°C, 80 s	120°C, 20 s	-
5-2	120°C, 2 min	370°C, 2 min	470°C, 20 s	120°C, 20 s	-
5-3	200°C, 2 min	-	550°C, 3 min	120°C, 30 s	-
5-4	120°C, 2 min	370°C, 2 min	470°C, 50 s	-	inhom. anneal
6-1	120°C, 2 min	370°C, 2 min	470°C, 80 s	120°C, 20 s	Oxidized

We have started by creating our ohmic contact with metal stacks of 4 nm nickel, 60 nm germanium, 120 nm gold and a cap layer of 25 nm germanium and 25 nm gold, the common recipe of the group, which are done by e-beam lithography and Joule evaporation. The stacks were deposited on $5\times5\,\mathrm{mm}^2$ AlGaAs/GaAs chips (08JN16) and then annealed in the rapid thermal annealer Jipelec jetlight 50 on Si-wafers as substrate holder to diffuse the contacts into the 2-DEG. The process parameters for the samples are listed in table D.1, the averaged results of the contact resistance measurement are listed in figure D.4b. Based on the results, we found the optimal annealing condition for chip5Q1 with a diffusion step duration of 80 s. Even though chip5Q4 showed a better quality of annealing for most pads after only 50 s, we concluded that the time for the diffusion was too short as some pads showed resistances of up to 1.5 kΩ.

During the elaboration of the fabrication processes of the RFT-samples, ohmic contacts were made first with optical lithography before switching back to e-beam lithography. The reason for this is that the used negative resist AZ 5214-E leaves a nanoscopic thin film of cross-linked polymers behind. This residue has a thickness of around 14-20 nm and prohibits the diffusion of the ohmic contacts (This was found later during sample fabrications on AlGaAs of samples B1 and B2). Harsh cleaning of the resist mask by O_2 plasma ashing at 200 W for several minutes can remove most traces, allowing the afterwards deposited contacts to diffuse but results in a lower quality compared to samples done by e-beam lithography (see table D.2). The fabrication was tested again with the best results obtained by e-beam lithography so that the fabrication process was changed accordingly. But it had to be adapted further to prevent the etching of the mesa by TMAH as described in section D.2. TMAH free developers are now used but an exposure to acid/basic reactions can not be avoided if the mesa is etched after the ohmics are fabricated. We have hence tested the contact resistance of ohmic contacts with the mesa being fabricated first. We compared the traditional Al-mask, that is removed with TMAH, and an optical resist (S1813) mask that is removed with acetone. Both tests were done with small ohmic contact $6\times14\,\mu\mathrm{m}^2$ with fingers that will be used in the final sample. The Al-masked sample showed resistances of around 10-50 kΩ or more for different distances. The resist

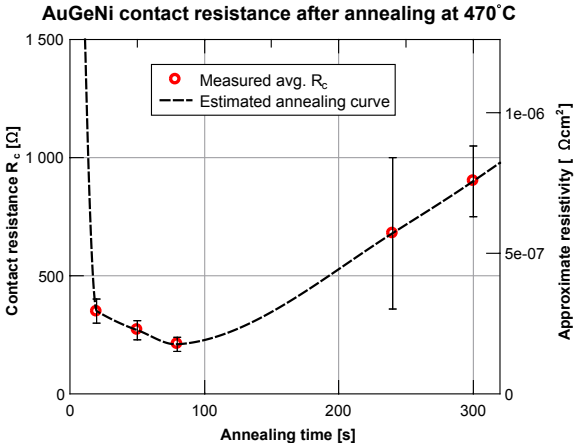

(a) Resistance-annealing curve

t_{anneal} [s]	R_c [kΩ]	Δ R_c	Chip
20	0.35	0.05	5-2
50	0.21	0.04	5-4
80	0.21	0.03	5-1
80	0.40	0.23	6-1
240	0.68*	0.32	4-full
300	0.90	0.15	3-full

(b) Averaged pad contact resistance

Figure D.4: Estimated annealing time curve (a) for the contact resistance of AuGeNi obtained from rapid thermal annealing(Jipelec jetlight 50) of our test samples (b) at 470°C. The contacts, without a defined mesa, were measured with a 2-point probe. From measurements with varying mesa distance the sheet resistivity of the 2DEG was determined to subtract from the 2-probe resistances to obtain individual contact resistance of the pads (*defect contacts were not included).

mask shows a much better result with 4-20 kΩ, which matched our expectations for a pristine substrate surface.

Table D.2: Listed average ohmic contact resistance R_c for different samples fabricated by optical and e-beam lithography. Pads are $160\times100\,\mu m^2$ with the 160 μm edge facing one another. The pads were measured with unconfined mesa and a 100 μm mesa stripe defined in between. For chips B1 and B2 the ohmics did not diffuse into the substrate. As a result no contact resistance could be measured and the pads easily detached from the substrate.

Chip (Batch)	Lithography	Unconfined R_c [kΩ]	Confined R_c [kΩ]	Note
B1 (08JN16)	Optical	n.c.	n.c.	Not diffused
B2 (08JN16)	Optical	n.c.	n.c.	Not diffused
B4 (13MS05)	Optical	0.49	0.35	Plasma cleaned
B7 (18AV01)	E-beam	0.38	0.25	Long pre-mixing
B9 (18AV01)	E-beam	0.35	0.26	Overheated

D.3.2 Tested AuGeNi contacts at 30mK

We have tested the contact resistance of ohmic contacts ($10\times20\,\mu m^2$, including fingers) fabricated on AlGaAs/GaAs (Batch 13MS05). The ohmics were fabricated after the definition of the mesa by Al-masked TMAH etching. Hence the measured resistances will be worse than for a TMAH-free sample but the high and low temperature relation can be used as a reference for other samples. For the room temperature

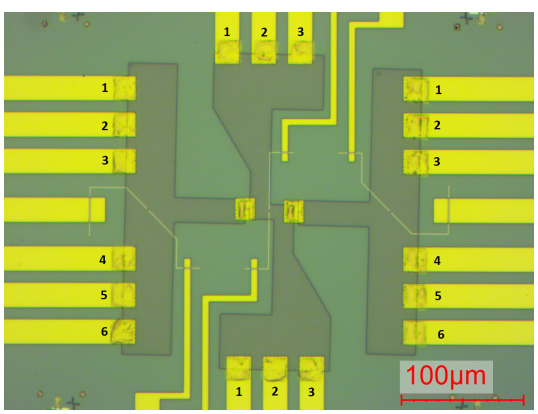

(a) Sample area

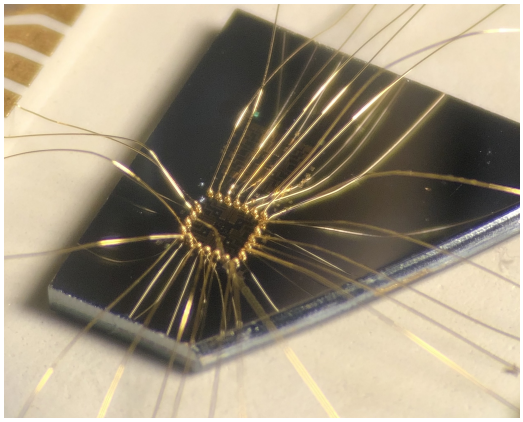

(b) Bonded on PCB

Figure D.5: Sample QG2's ohmic contacts were measured at room temperature and at temperatures of 30 mK in the dilution refrigerator. The contacts are connected to larger gold pads that can be measured with a probe station at room temperature and were wire-bonded on a PCB for the fridge measurement.

measurement the 2-point resistance of the different pads were measured with a fixed starting point for each side. Based on the design, we calculated the mesa resistance in between and deduced an estimation of the average contact resistance from these measurements. For the mesa sheet resistance we used 3.5 kΩ/□ which we determined from test stripes around the sample. We obtain the contact resistances listed in table D.3 with an average of 0.522 kΩ for right side and 2.623 kΩ for the left side (see figure D.5a). While the right side gives a reasonable result, the left side appears to have a consistent increase, which was also found in other samples and might be related to a fabrication issue. We then determined the individual values in relation to set values for P1 and P2, based on the measurement P1-P2, and compared them to the low temperature values that were measured directly through the our dilution refrigerator's measurement setup. The measurements were done in the quantum Hall regime with two electronic channels so that $R_k/2$ was subtracted from all measurement values. The final results are compared in table D.4. We see that as expected the contact resistance for most ohmic contacts diminishes. On average we find a reduction by 2.5 times from the room temperature value with certain contacts going down to even a sixth of their original resistance. However, contacts that were distinctively worse than others at room temperature have gotten worse when cooled down. We are unable to find a clear rule of thumb but assume that several kΩ of added contact resistance at room-temperature indicate a failure at low temperatures. So a simple room-temperature measurement can be used as a simple way to find faulty contacts that would fail at low temperature.

Table D.3: Measured 2-point resistances R_{2p} of different ohmic contacts of sample QG2, labeled as P1-7 for the left, top, right and bottom contacts as shown in figure D.5a, and estimated contact resistances $2R_c$ after subtracting the mesa resistance. The listed mesa resistance is obtained from the square distance of the sample design and previously determined 2-DEG resistivity of 3.5 kΩ/□. The top contacts have too low 2-probe resistances, indicating that the contacts are shorted (possibly by the wire bonding), hence the contact resistance can not be obtained (N.A.).

-	P1-2	P1-3	P1-5	P1-6	P1-7
Mesa [□]	1	1.83	3.19	4.1	5.01
Mesa r [kΩ]	3.50	6.41	11.17	14.35	17.535
$R_{2p,left}$	7.30	10.52	15.45	18.41	24.62
$R_{2p,right}$	3.62	6.84	12.53	14.89	18.45
$R_{2p,top}$	2.99	5.20	-	-	-
$R_{2p,bott}$	10.91	12.87	-	-	-
$2R_{c,left}$	3.80	4.11	4.28	4.06	7.09
$2R_{c,right}$	0.12	0.43	1.36	0.54	0.92
$2R_{c,top}$	N.A.	N.A.	-	-	-
$2R_{c,bott}$	7.41	6.47	-	-	-

Table D.4: Comparison of the individual contact resistance R_c for different ohmic contacts of sample QG2, labeled as P1-7 for the left, top, right and bottom contacts as shown in figure D.5a, measured at room temperature and at 30 mK in the dilution refrigerator.

-	P1	P2	P3	P5	P6	P7
$R_{c,left}$ (RT) [kΩ]	1.90	1.90	2.21	2.38	2.16	5.19
$R_{c,right}$ (RT) [kΩ]	0.06	0.06	0.37	1.3	0.48	0.86
$R_{c,top}$ (RT) [kΩ]	short	short	short	-	-	-
$R_{c,bott}$ (RT) [kΩ]	3.75	3.75	2.72	-	-	-
$R_{c,left}$ (30mK) [kΩ]	0.47	-	1.23	0.43	-	77.90
$R_{c,right}$ (30mK) [kΩ]	0.30	-	0.36	0.30	-	0.29
$R_{c,top}$ (30mK) [kΩ]	short	-	0.28	-	-	-
$R_{c,bott}$ (30mK) [kΩ]	1.1	-	1.85	-	-	-

Appendix E

The ^{3}He-^{4}He dilution refrigerator

The fabricated sample can then be introduced into our cryogenic system, a ^{3}He-^{4}He dilution refrigerator. Dilution refrigerators are able to achieve temperatures far below 1 K that can not be reached with common cooling techniques. The traditional evaporation cooling is only able to achieve temperatures of down to 0.3 K by using liquid ^{3}He, which has been possible since the development of the ^{3}He liquefaction by Kamerlingh Onnes in the early 20th century [222]. A fridge based on the liquid helium works like any normal house-hold refrigerator, where the latent heat for the evaporation of the liquid medium in the fridges closed loop is taken from the environment. The dilution refrigerator however, uses the heat of mixing of two components (dilution enthalpy) that was found to be feasible for mixtures of ^{4}He and its isotope ^{3}He. First experiments were done using simple mixing tanks where both liquids were added and temperatures below 0.3 K were measured. From this one-shot mixing approach researchers would soon create first designs of a continuously operating ^{3}He-^{4}He dilution refrigerator that allowed to separate and recycle the mixture components. The first design was made in Leiden by Das et al in 1965 and successfully reached 0.22 K [223]. The ^{3}He-^{4}He dilution fridge has seen tremendous improvement over the decades so that modern commercially available fridges are able to achieve temperatures of 8-10 mK. Some experimentally used refrigerators in Leiden University by Frossati [224] and in Lancaster by Pickett [225] are even achieving temperatures down to 2 mK.

E.1 The ^{3}He-^{4}He phase diagram

To understand how these fridges operate, it is firstly important to understand the phase diagram of the ^{3}He-^{4}He solution (see figure E.1). For temperature above 1 K the two liquids are in perfect solution, but for temperatures below 1 K the solubility of ^{3}He in ^{4}He changes, causing the mixture to separate into two phases. Depending on the concentration of ^{3}He (and the temperature) we recover a ^{3}He-rich phase and a ^{4}He rich solution that contains a finite amount of ^{3}He. We call these phases the concentrated and the dilute phase (referring to ^{3}He concentration). The dilute phase always has a finite solubility of ^{3}He, even near zero temperature where the soluble concentration is still 6.6%. The heavier diluted phase will sink to the bottom, so that

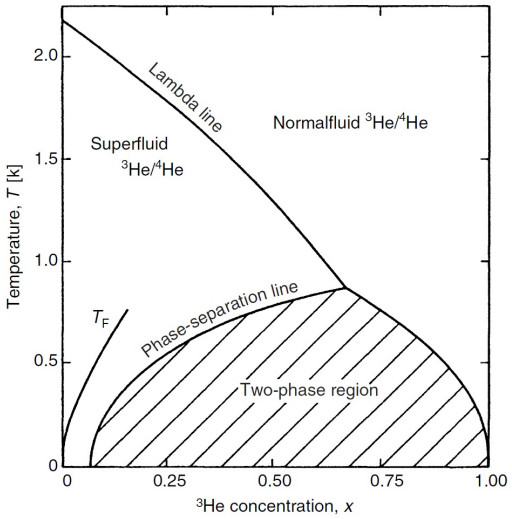

Figure E.1: Phase diagram of liquid ^{3}He-^{4}He mixtures at saturated vapor pressures, taken from [226], [227]. The mixture can be in either normal- or super-fluid state, separated by the lambda line, but will in both cases de-mix, into a concentrated ^{3}He phase and ^{4}He with a finite solubility of more than 6.6% ^{3}He, below the phase-separation line.

the lighter ^{3}He has to passed from the concentrated phase into the dilute phase in order to create the dilution cooling. The taken heat from the environment is used to increase the internal energy of the diluted ^{3}He. It corresponds to the mixing enthalpy which depends on the temperature and the different entropy of ^{3}He in the dilute and concentrate phase (equ. E.1) which we can obtain from experimentally measured specific heat following equ. E.2).

$$\Delta H = H_D - H_C = TS_D - TS_C \tag{E.1}$$

$$S_i = \int_0^T \frac{C(T')}{T'} dT' = C \cdot T \tag{E.2}$$

The specific heat for the dilute phase (106 T [J/mol/K]) and the concentrated phase (22 T [J/mol/K]) are known for temperatures below 40mK, so that we obtain a positive mixing enthalpy, indicating an endothermic reaction proportional to T^2:

$$\Delta H = T(S_D - S_C) = T^2(C_D - C_C) = 84T^2[\frac{J}{mol}] \tag{E.3}$$

Because the cooling is created by the mixing of ^{3}He atoms in the dilute phase, it can be seen that cooling power depends not only on the enthalpy of ^{3}He but also on the molar flow of ^{3}He between the phases. The finite solubility of the dilute phase ensures a high molar flow rate which increases the total cooling capacity of the refrigerator (see equation E.4). The solubility of ^{3}He in ^{4}He can even be increased at higher pressures of up to 9.5% at 10 bar which further raises the cooling capacity.

$$\Delta Q = \Delta H \cdot \Delta n_{^3He} = 84 \cdot \Delta n_{^3He} \cdot T^2[W] \tag{E.4}$$

E.2 The dilution unit

The dilution cooling for the Helium isotope mixture is possible due to the positive mixing enthalpy of ^{3}He going into the dilute phase but in order to keep this mixing reaction continuously running, one needs to be able to remove the ^{3}He from the solution and to recycle it. For standard evaporation cooling refrigerators this would be done by simply pumping on the evaporated liquid. For a dilution refrigerator this is problematic because the mixing direction is downwards from concentrate to diluted phase, so that one needs an arrangement as shown in figure E.2, where we can pump directly on the dilute phase. This setup is the dilution unit that is the core of any dilution refrigerator: Firstly, the incoming ^{3}He gas needs to be condensed by a pre-cooling unit before it is led into a mixing chamber were the two phases are formed at low enough temperatures. The osmotic pressure difference of ^{3}He between both phases creates the necessary pressure to force the helium atoms into the dilute phase which generates the cooling power. The dilute phase itself is forced into another chamber above the mixing chamber, called the "still", by the liquid pressure where it can then be pumped on. The still is operated to heat up to 0.7 K so that the ^{3}He, which has a lower vapor pressure than ^{4}He, is evaporating and removed by the vacuum pumps. Thereby the dilute phase's ^{3}He concentration is lowered, causing ^{3}He to move from the mixing chamber into the still and we obtain an effective pumping of the ^{3}He through the dilute phase. The evacuated helium is then condensed and recycled, thus re-injected into the mixing chamber, to obtain a closed refrigeration loop.
The condensing of the ^{3}He can be done in different ways, traditionally divided into two categories of either wet or dry fridges. In a wet fridge the dilution unit is fully submerged in liquid ^{4}He at 4.2 K with an operated ^{4}He pot that cools the recycling ^{3}He down to 1.5 K. The more modern dry fridge uses a pulse tube instead of a ^{4}He pot. A pulse tube is simply a multi-stage cryo cooler that uses ^{4}He gas at high pressures to generate cooling by gas expansion. Doing so the gas is cooled down to 4 K and then condensed by passing through an impedance. The liquid is then further cooled down through heat exchanges with the outgoing mixture. These cooling systems are designed as closed loops so that it is not necessary to submerge the fridge in liquid helium anymore, hence the differentiation dry/wet.
In both cases the ^{3}He is liquefied and further cooled down. This cool-down is also aided by heat-exchangers between the ^{3}He gas and the still which further cools the recycled gas (in return the gas warms the still) and some heat exchangers to the evacuated dilute phase. These heat exchangers are crucially important as they allow to remove the thermal energy of the incoming helium liquid which would diminish the effective cooling power of the mixing chamber. The effective cooling power of the mixing chamber depends on the balance of the heat consumed by the mixing reaction and the incoming heat of the environment. By minimizing the incoming heat we

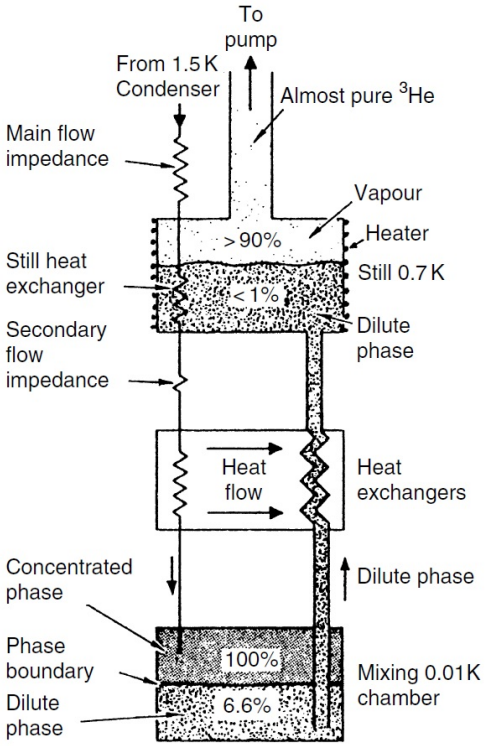

Figure E.2: Schematic drawing of a ^{3}He-^{4}He dilution unit taken from [228]. At the beginning of the process ^{3}He is condensed at 1.5 K and further cooled by the heat exchangers of the still before being led into the mixing chamber. In the mixing chamber it is injected into the ^{3}He-rich concentrate phase from where single ^{3}He atoms are driven down into the ^{4}He-rich dilute phase due to the osmotic pressure. The dilute phase is led into the still where the ^{3}He is evaporated due to its lower vapor pressure as compared to ^{4}He. The evaporated gas is pumped on and recycled in the loop.

hence increase the available cooling power at a given temperature.

Appendix F

RF-Design of coplanar waveguides (CPW)

Here we present the design of the planar RF-conductors which connect the sample across its chip and the PCB it is mounted on to the commercial coaxial cables of the described RF-circuitry.

F.1 RF-Design and simulation of CPW's

The coplanar waveguide (CPW) shall generally have a large cross-section to minimize dissipation and an impedance of 50 Ω, matching the source impedance. We have thus selected a width of 250 μm for the central conductor of the waveguide on the PCB and chip. On the chip however this requires an adaptation to connect to the 2 μm width of the coil's conductor. In order to design the CPW with a 50 Ω impedance, the corresponding gap spacing has to be determined. Several tools can be used to either simulate or calculate a CPW's impedance: The first option is the statical calculation software "Tx line 2003" ® that provides the impedance for given geometrical parameters by numerical calculations. However this calculation assumes a 2D conductor so that it is only valid for a thickness of few nm. In our case, the deposited conductor thickness range up to 500 nm which makes Tx-line's result unreliable so that they have to be verified by a full simulation of the conductor in the electromagnetic wave solver Sonnet®.
Using Tx-line® we have calculated the optimal gap dimensions of the conductor and used this to create the Sonnet® simulation model (see figure F.1a). In this 3D model, the surrounding planes and the center strip have a thickness of 500 nm and a resistivity of either gold or copper as listed in appendix C.1. The center strip is connected via two ports at both ends that are connected to a 50 Ω load. To correctly model the charge distribution at the edges of the metal planes, negative ports were added to them as well. This is the recommended procedure following the Sonnet® manual to model a coplanar waveguide. The obtained simulations yield a characteristic impedance that unexpectedly varies with the frequency. This decrease of the characteristic impedance is caused by an increased capacitance due a point defect of the charge distribution

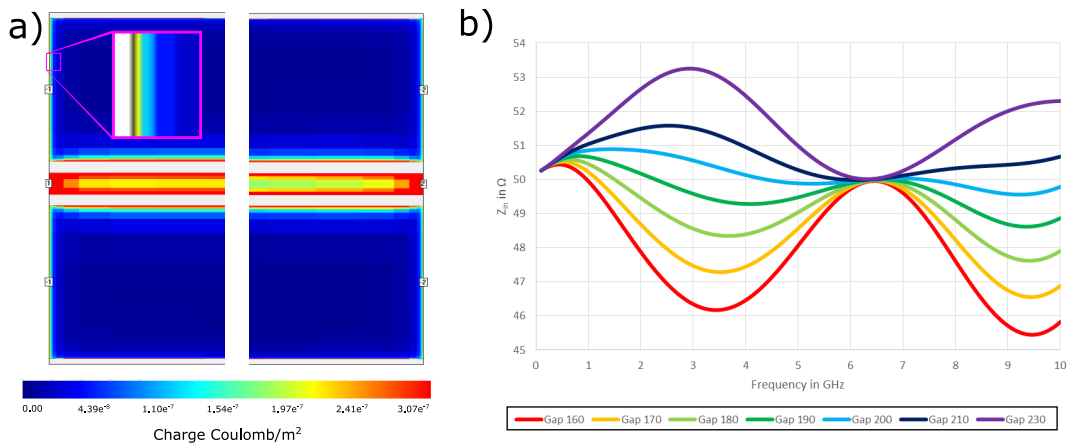

Figure F.1: (a) Illustration of the Sonnet® transmission line model with 2 ports at the central strip and each 2 ports at the surrounding metal planes. The colourization represents the simulated charge distribution across the transmission line which shows a point defect along the termination of the metal planes, causing an erroneous simulation results. A magnification of the charge distribution at the edge is shown in the magenta frame. By extending the length of the simulated transmission line this effect becomes negligible and the correct sinusoidal behaviour of the input impedance of the CPW is recovered as plotted in b).

in the surrounding metal planes upon reaching the edges. As the edge conditions effectively equalize the charge along the edge of the defined port, it erroneously reproduces the increased charge level near the CPW along the edge of the metal planes. It is not known how to remove or prevent this simulation error but its effect can be minimized by extending the length of the simulated transmission line section.
The RF line is extended to a length in the order of cm to weaken the influence of the defect (We used 0.9 cm) and we are able to determine a characteristic impedance. The obtained data is now a sinusoidal curve of a CPW that can be interpreted in several ways. Firstly, the characteristic impedance can be determined from the transmission line equation:

$$Z_{in} = Z_c \frac{Z_{Load} + iZ_c \tan(\beta l)}{Z_c + iZ_{Load} \tan(\beta l)} \tag{F.1}$$

To obtain Z_c from the simulated input impedance as described by the Z parameters ($Z_{in} = Z_{11} - Z_{12}Z_{21}/(Z_{22} + Z_{Load})$ and the known load impedance Z_{Load} and length l of the CPW, we split-up Z_{in} into its real and imaginary parts:

$$Z_c = \sqrt{Re(Z_{in})Z_{Load} + \frac{Im(Z_{in})Z_{Load}}{Re(Z_{in}) - Z_L}} \tag{F.2}$$

From the obtained values an average value of Z_c is approximated by linear fitting.
The second possibility here is the observation of Z_{in} directly. The transmission lines functions as a quarter wave transformer which shows a minimum at $\lambda/2$, if $Z_c < Z_{Load}$,

or a maximum if $Z_c > Z_L$. In that case the characteristic impedance is given by the input impedance red-out at $\lambda/4$:

$$Z\left(\frac{\lambda}{4}\right) = \frac{Z_c^2}{Z_{Load}} \tag{F.3}$$

Thirdly, we can use the same transmission line equation (equation F.1) in order to fit the CPW graphs for arbitrarily set characteristic impedance values, trying to match the simulation. The final results of these calculations and simulations are shown in figure F.2, indicating the optimal gap width to be at 195 μm.

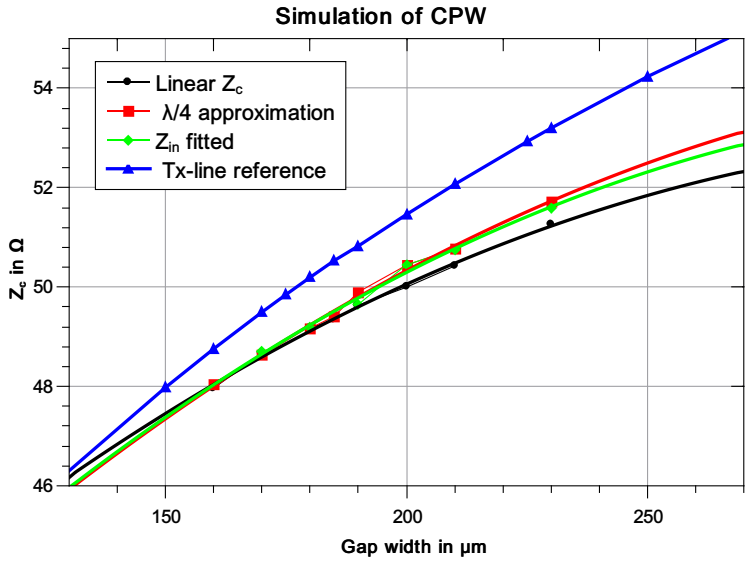

Figure F.2: (a) Plot of the characteristic impedance of a CPW with 250 μ center strip for different gap widths. The characteristic impedances was calculated numerical with Tx-line® and simulated with Sonnet®. The obtained Input impedance was used to calculate the linearised characteristic impedance or determined by the quarter wavelength transformer approximation.

The same procedure was used to create the adaptations in between the lines of different widths. Suitable width/gap pairs were calculated by Tx-line® and then tested in Sonnet® to determine the ideal aspect ratio of the transition. We decided to use two adaptations instead of one, a first reducing from 250 to 20 μm and a second for the transition from 20 to 2 μm. The new CPW with a width of 20 μm and a gap of 8 μm was tested as the 250 μm line before. This new arrangement allows to have smaller gaps near the coils and thus decreases the chance of signal loss or cross talk between the coils and the surrounding.
At first simple linear transition between the known gap ratios of 250 and 20 μm was tested but does not result in a 50 Ω impedance. In order to determine the correct profile of the adaptation we iterated the optimal gap distance by simulation for widths of 40, 80 and 160 μm in addition to the known values for 20 and 250 μm. The result shown in figure F.3a shows that the ideal gap width has a parabolic behaviour, which is equivalent to a linear relation between the gap width/strip width aspect ratio

and the strip width but remains constant for small widths (see figure F.3b). The found aspect ratios were translated into a Sonnet® simulation and simulation results showed a nearly 50 Ω impedance. The first adaptation is realized by narrowing done the strip and gap with different slopes, while the second adaptation changes only the central strip width following the shown profile.

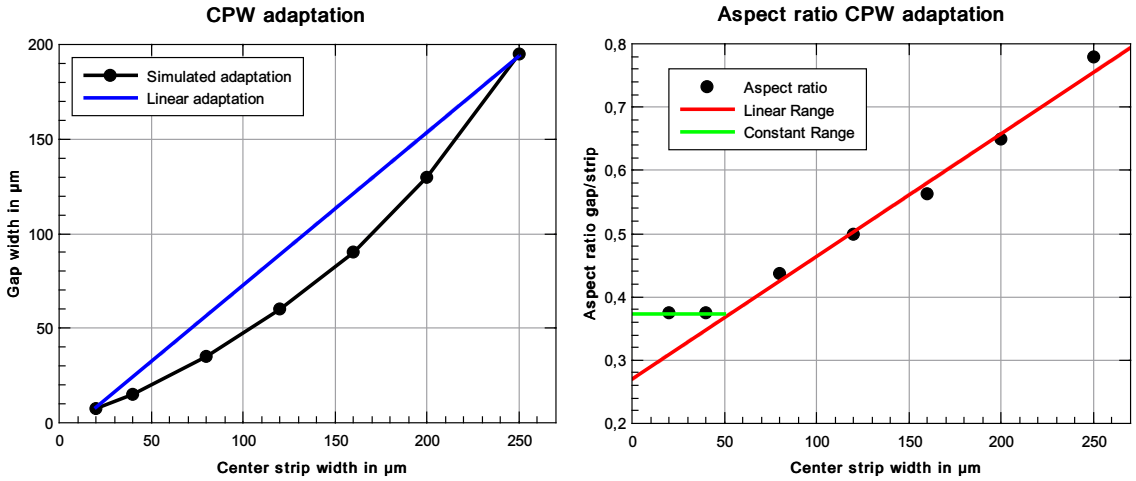

(a) (b)

Figure F.3: Simulation results for the gap width for several CPW sizes for a 50 Ω impedance (a). The aspect ratio of the CPW (b) for the different sizes is given by gap width divided by the central strip width. The Gap values for widths of 20 and 250 were taken from previous results, others were iterated by simulation.

F.2 Test measurement of a fabricated CPW

The final design of the CPW for PCB and the larger section on-chip was tested with a metallized sample on GaAs. The sample is made from 500 nm thick copper and has a conductor line width of 250 μm, a gap of 195 μm and a total length of length 7 mm. The sample is glued on the PCB and the CPWs wire bonded. The lines can be connected to test equipment via the min-SMP plugs on the PCB (see figure F.4). In order to test the impedance of the coplanar wave guides on the PCB and the chip, as well as the quality of the wire-bonding and RF-plug soldering we rely on a time-domain reflectometry (TDR) measurement using an oscilloscope. A time domain reflectometer consists of a pulse generator and a sampler. The generator sends a short pulse along the transmission line to be tested while the sampler, an oscilloscope, displays the waveforms on the line. If the far end is terminated in the required impedance and if there are no defects in the line, then all the energy of the pulse will travel along the line without any reflection occurring. But if there is a defect or a general discontinuity in the line, energy will be reflected back to the reflectometer where it is detected. As it takes a finite time for the pulse to travel

along the line, defects can be localized based on the time delay. Furthermore the sampler also allows to calculate the mismatch from the detected signals.

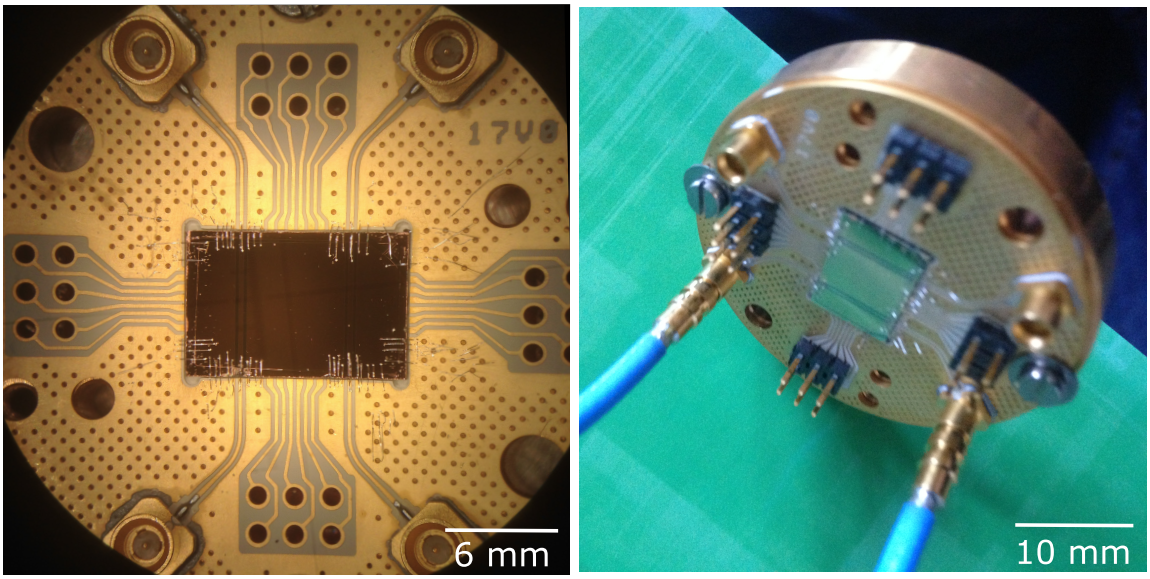

(a) (b)

Figure F.4: (a) Microscopic image of the wire bonded sample A0. The central conductors are connected with two bonds and the ground-planes with 3 or more per section. The RF ports are clock-wise numbered from 1-4 starting on the top right. (b) Photo of sample A18 that is mounted and connected to via gold mini-SMP cables, as A0 before, but has a higher density of wire bonds: three for the central conductor and many close bonds right next to those bonds. The higher bonding density reduces the discontinuity observed for A0.

The initial test sample A0 was glued on the PCB with PMMA and wire-bonded as shown in figure F.4a with 2 Al-wire bonds between the central conductors of chip and PCB, while a second sample A18 has been tested with three bonds. Also, for A18 additional wires were added to the surrounding bondings ca. 1 per side of each ground.
When bonded, the samples are mounted with the PCB on the sample holder and connected to the reflectometer with golden min-SMP cables. To calibrate the measurement, the connecting RF cables were measured separately. Based on the measured reflection signal can be connected to the known length of the cable which, under the assumption of the similar signal propagation speeds in gold and copper, allows to translate the later measured signal response times to the distances on the PCB and chip. The 10 cm gold cable has a response time of 9600 ps. Thus a time difference 0.1 ps corresponds to a distance of approximately 1.1 mm.
The ports were measured individually with the opposing port as an open. Shown data has been corrected for intrinsic losses and the signal of the gold cables was cut. The results for A0 are shown in figure F.5 left: Ports 1 and 2 are short circuited and thus left-out, so only the results for port 3 and 4 are shown.

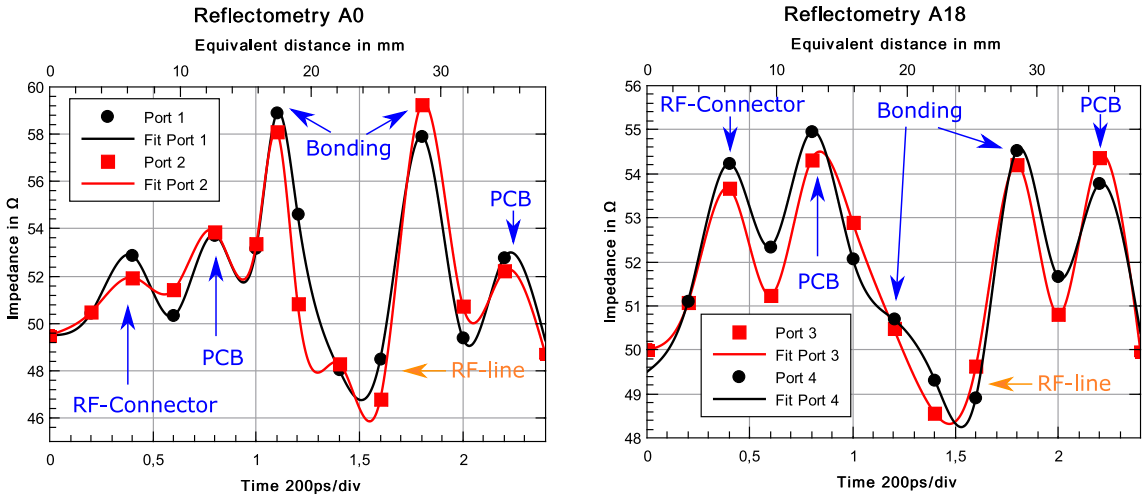

Figure F.5: Reflectometry measurement of the RF test samples A0 (a) and A18 (b) mounted on a PCB via an RF connector. The measurement data has already been corrected for the signal loss and the time divisions have been converted to a length scale based on the calibration measurement. A0 and A18 have the same design but are connected with 2 (a) and 3(b) wire bonds between the PCB line and the RF-line on chip. Adding a third bond greatly decreases the signal loss, thus deceasing the impedance.

The measured time signal can be converted into lengths of the conductor in order to allocate the specific impedance spikes to their corresponding sections of the sample. It thus provides a measurement of the entire line on the PCB and clearly shows both wire bonding connections as well as the CPW on the PCB and the RF connector as peaks. The line is mirror symmetric at the center of the RF-line at 1.5 division (or 24 mm) which has an average impedance of 48 Ω. Starting from the left, the measured RF connector shows a value of 53 Ω which likely caused by the soldering connection on the PCB. The PCB lines themselves should be 50 Ω but are found to be at 53 and 54 Ω which was traced back to a fabrication error of the PCB manufacturer. For the wire bonds however, the measured impedance of 58 to 59 Ω are a clear indicator that the two bonds in place are not sufficient to create a continuous connection and cause a loss of the RF-signal. As a result of this increase in dissipation, the obtainable quality factor of our resonators may be reduced by about 20%. This can be prevented by adding a third wire (or more) to the bonding as was done for sample A18 whose measurement is shown in figure F.5 right. Port 1 and 2's measurements are again neglected as the bonding was not very good, the bonds did not adhere, resulting in the same impedance spikes as for A0, but correctly established for port 3 and 4. For A18 we find the approximate line impedance at 49.3 Ω which is in good agreement with our design. RF-connector and PCB line are close to the expected values as seen from A0 but the bonding connections have been greatly improved, decreasing their impedances to 51 and 55 Ω. The difference of the values in both measurements indicates a directionality that corresponds well with the positioning of the bonds on the chip: two bonds were placed at the beginning of the line, whereas the third bond

was added later and stretches over the pre-existing ones. As a result, it appears that from the PCB to the chip the three bonds function as a nearly perfect guide, while in the reverse direction some loss occurs due to the specific placement of the third bond.
In conclusion, we have designed and tested our CPW's on the PCB and fabricated on a GaAs chip. We have shown by a reflectometry measurement that our design is indeed a nearly $50\,\Omega$ transmission line and can thus be used in our experimental setup. Furthermore we found that we are able to establish a good quality connection between the CPWs on PCB and on chip when at least three wire bonds are established.

Bibliography

[1] R. Landauer. Electrical resistance of disordered one-dimensional lattices. *The Philosophical Magazine*, 21(172):863–867, 1970.

[2] P. W. Anderson, D. J. Thouless, E. Abrahams, and D. S. Fisher. New method for a scaling theory of localization. *Physical Review B*, 22(8):3519–3526, October 1980.

[3] F. D. Parmentier, A. Anthore, S. Jezouin, H. le Sueur, U. Gennser, A. Cavanna, D. Mailly, and F. Pierre. Strong back-action of a linear circuit on a single electronic quantum channel. *Nature Physics*, 7:935–938, September 2011.

[4] Y. Gefen, Y. Imry, and M. Ya. Azbel. Quantum oscillations and the Aharonov-Bohm effect for parallel resistors. *Physical Review Letters*, 52(2):129–132, January 1984.

[5] Y. Gefen, Y. Imry, and M. Ya. Azbel. Quantum oscillations in small rings at low temperatures. *Surface Science*, 142(1-3):203–207, July 1984.

[6] R. A. Webb, S. Washburn, C. P. Umbach, and R. B. Laibowitz. Observation of the Aharonov-Bohm oscillations in normal-metal rings. *Physical Review Letters*, 54(25):2696–2699, June 1985.

[7] V. Chandrasekhar, M. J. Rooks, S. Wind, and D. E. Prober. Observation of Aharonov-Bohm electron interference effects with periods h/e and h/2e in individual micron-size, normal-metal rings. *Physical Review Letters*, 55(15):1610, October 1985.

[8] S. Datta, M. R. Melloch, S. Bandyopadhyay, R. Noren, M. Vaziri, M. Miller, and R. Reifenberger. Novel interference effects between parallel quantum wells. *Physical Review Letters*, 55(21):2344, November 1985.

[9] M. H. Devoret, D. Esteve, H. Grabert, G.-L. Ingold, H. Pothier, and C. Urbina. Effect of the electromagnetic environment on the Coulomb blockade in ultrasmall tunnel junctions. *Physical Review Letters*, 64(15):1824–1827, April 1990.

[10] L. J. Geerligs, V. F. Anderegg, P. A. Holweg, J. E. Mooij, H. Pothier, D. Esteve, C. Urbina, and M. H. Devoret. Frequency-locked turnstile device for single electrons. *Physical Review Letters*, 64(22):2691–2694, May 1990.

[11] R. Cron, M. F. Goffman, D. Esteve, and C. Urbina. Multiple-charge-quanta shot noise in superconducting atomic contacts. *Physical Review Letters*, 86(18), April 2001.

[12] C. Altimiras, U. Gennser, A. Cavanna, D. Mailly, and F. Pierre. Experimental test of the dynamical Coulomb blockade theory for short coherent conductors. *Physical Review Letters*, 99(25):256805, December 2007.

[13] S. Jezouin, M. Albert, F. D. Parmentier, A. Anthore, U. Gennser, A. Cavanna, I. Safi, , and F. Pierre. Tomonaga-Luttinger physics in electronic quantum circuits. *Nature Communications*, 4:1802, April 2013.

[14] A. A. Clerk, M. H. Devoret, S. M. Girvin, F. Marquardt, and R. J. Schoelkopf. Introduction to quantum noise, measurement, and amplification. *Reviews of Modern Physics*, 82:1155–1208, April 2010.

[15] H. B. Callen and T. A. Welton. Irreversibility and generalized noise. *Physical Review*, 83(1):34–40, July 1951.

[16] N. Wiener. Generalized harmonic analysis. *Acta Mathematica*, 55(1):117–258, 1930.

[17] A. Khintchine. Korrelationstheorie der stationären stochastischen Prozesse. *Mathematische Annalen*, 109:604–615, December 1934.

[18] N. Wiener. *Extrapolation, Interpolation, and Smoothing of Stationary Time Series. With Engineering Applications*. MIT Press, Cambridge, 1949.

[19] R. Kubo. Statistical-mechanical theory of irreversible processes. *Journal of the Physical Society of Japan*, 12(6):507–586, June 1957.

[20] A. O. Caldeira and A. J. Leggett. Quantum tunnelling in a dissipative system. *Annals of Physics*, 149(2):374–456, September 1983.

[21] B. Yurke and J. S. Denker. Quantum network theory. *Physical Review A*, 29(3):1419, March 1984.

[22] C. W. Gardiner and M. J. Collett. Input and output in damped quantum systems: Quantum stochastic differential equations and the master equation. *Physical Review A*, 31(6):3761, June 1985.

[23] G. B. Lesovik and R. Loosen. On the detection of finite-frequency current fluctuations. *Journal of Experimental and Theoretical Physics Letters*, 65:295–299, February 1997.

[24] Y. M. Blanter and M. Büttiker. Shot noise in mesoscopic conductors. *Physics Reports*, 336(1-2):1–166, September 2000.

[25] Th. Martin. Noise in mesoscopic physics. *Les Houches Session LXXXI*, 2005.

[26] K. von Klitzing. The quantized Hall effect. *Reviews of Modern Physics*, 58(519), July 1986.

[27] H. L. Stormer. Nobel lecture: The fractional quantum Hall effect. *Reviews of Modern Physics*, 71(4):875, July 1999.

[28] S. Das Sarma and A. Pinczuk. *Perspectives in Quantum Hall Effects: Novel Quantum Liquids in Low-Dimensional Semiconductor Structures*. Wiley, 1996.

[29] Z. F. Ezawa. *Quantum Hall Effects. Recent Theoretical and Experimental Developments*. World Scientific, 3rd edition, 2013.

[30] D. Goldhaber-Gordon, H. Shtrikman, D. Mahalu, D. Abusch-Magder, U. Meirav, and M. A. Kastner. Kondo effect in a single-electron transistor. *Nature*, 391:156–159, January 1998.

[31] L. P. Kouwenhoven and C. M. Marcus. Quantum dots. *Physics World*, 11(6):35–39, June 1998.

[32] H. Steinberg, G. Barak, A. Yacoby, L. N. Pfeiffer, K.W. West, B. I. Halperin, and K. Le Hur. Charge fractionalization in quantum wires. *Nature Physics*, 4:116–119, December 2008.

[33] L. A. Landau, E. Cornfeld, and E. Sela. Charge fractionalization in the two-channel Kondo effect. *Physical Review Letters*, 120(18):186801, May 2018.

[34] R. B. Laughlin. Anomalous quantum Hall effect: An incompressible quantum fluid with fractionally charged excitations. *Physical Review Letters*, 50(50):1395–1398, May 1983.

[35] D. Arovas, J. R. Schrieffer, and F. Wilczek. Fractional statistics and the quantum Hall effect. *Physical Review Letters*, 53(7):722, August 1984.

[36] B. I. Halperin. Statistics of quasiparticles and the hierarchy of fractional quantized Hall states. *Physical Review Letters*, 52(18):1583, April 1984.

[37] A. Stern. Anyons and the quantum Hall effect - a pedagogical review. *Annals of Physics*, 1:204–209, January 2008.

[38] V. J. Goldman and B. Su. Resonant tunneling in the quantum Hall regime: Measurement of fractional charge. *Science*, 267(5200):1010–1012, February 1995.

[39] R. de Picciotto, M. Reznikov, M. Heiblum, V. Umansky, G. Bunin, and D. Mahalu. Direct observation of a fractional charge. *Nature*, 389:162–164, 1997.

[40] L. Saminadayar, D. C. Glattli, Y. Jin, and B. Etienne. Observation of the e/3 fractionally charged Laughlin quasiparticles. *Physical Review Letters*, 79(13):2526, September 1997.

[41] M. Reznikov, R. de Picciotto, T. G. Griffiths, M. Heiblum, and V. Umansky. Observation of quasiparticles with one-fifth of an electron's charge. *Nature*, 399:238–241, May 1999.

[42] Th. Giamarchi. *Quantum Physics in One Dimension*. Calrendon Press, 2004.

[43] M. Ferrier, T. Arakawa, T. Hata, R. Fujiwara, R. Delagrange, R. Deblock, Y. Teratani, R. Sakano, A. Oguri, and K. Kobayashi. Quantum fluctuations along symmetry crossover in a Kondo-correlated quantum dot. *Physical Review Letters*, 118(19):196803, May 2017.

[44] G.-L. Ingold, Yu. V. Nazarov, H. Grabert, and M. H. Devoret. *Single Charge Tunneling*, volume 294 of *NATO ASI Series B*, chapter Charge Tunneling Rates in Ultrasmall Junctions, pages 21–207. Plenum Press, 1992.

[45] O. Parlavecchio, C. Altimiras, J.-R. Souquet, P. Simon, I. Safi, P. Joyez, D. Vion, P. Roche, D. Esteve, and F. Portier. Fluctuation-dissipation relations of a tunnel junction driven by a quantum circuit. *Physical Review Letters*, 114(12):126801, March 2018.

[46] I. Safi and H. Saleur. One-channel conductor in an ohmic environment: Mapping to a Tomonaga-Luttinger liquid and full counting statistics. *Physical Review Letters*, 93(12):126602, September 2004.

[47] P. K. Tien and J. P. Gordon. Multiphoton process observed in the interaction of microwave fields with the tunneling between superconductor films. *Physical Review*, 129(2):647–651, January 1963.

[48] R. Aguado and L. P. Kouwenhoven. Double quantum dots as detectors of high-frequency quantum noise in mesoscopic conductors. *Physical Review Letters*, 84(9):1986–9, February 2000.

[49] R. Deblock, E. Onac, L. Gurevich, and L. P. Kouwenhoven. Detection of quantum noise from an electrically-driven two-level system. *Science*, 301(5630):203–206, July 2003.

[50] E. Onac, F. Balestro, B. Trauzettel, C. F. J. Lodewijk, and L. P. Kouwenhoven. Shot noise detection on a carbon nanotube quantum dot. *Physical Review Letters*, 96(2):026803, January 2006.

[51] P.-M. Billangeon, F. Pierre, H. Bouchiat, and R. Deblock. Emission and absorption asymmetry in the quantum noise of a Josephson junction. *Physical Review Letters*, 96(13):136804, April 2006.

[52] P.-M. Billangeon, F. Pierre, H. Bouchiat, and R. Deblock. AC josephson effect and resonant cooper pair tunneling emission of a single cooper pair transistor. *Physical Review Letters*, 98(21):216802, May 2007.

[53] G. Granger, D. Taubert, C. E. Young, L. Gaudreau, A. Kam, S. A. Studenikin, P. Zawadzki, D. Harbusch, D. Schuh, W. Wegscheider, Z. R. Wasilewski, A. A. Clerk, S. Ludwig, and A. S. Sachrajda. Quantum interference and phonon-mediated back-action in lateral quantum-dot circuits. *Nature Physics*, 8:522–527, June 2012.

[54] J. Basset, H. Bouchiat, and R. Deblock. High-frequency quantum admittance and noise measurement with an on-chip resonant circuit. *Physical Review B*, 85(8):085435, February 2012.

[55] J. Basset, H. Bouchiat, and R. Deblock. Emission and absorption quantum noise measurement with an on-chip resonant circuit. *Physical Review Letters*, 105(16):166801, October 2010.

[56] C. Mora, C. Altimiras, P. Joyez, and F. Portier. Quantum properties of the radiation emitted by a conductor in the Coulomb blockade regime. *Physical Review B*, 95(12):125311, March 2017.

[57] T. J. Thornton, M. Pepper, H. Ahmed, D. Andrews, and G. J. Davies. One-dimensional conduction in the 2D electron gas of a GaAs-AlGaAs heterojunction. *Physical Review Letters*, 56(11):1198–1201, January 1986.

[58] H. Z. Zheng, H. P. Wei, D. C. Tsui, and G. Weimann. Gate-controlled transport in narrow GaAs/AlGaAs heterostructures. *Physical Review B*, 34(8):5635–5638, October 1986.

[59] B. J. van Wees, C. W. J. Beenakker H. van Houten, J. G. Williamson, and C.T. Foxon. Quantized conductance of point and contacts in a two-dimensional electron gas. *Physical Review Letters*, 60(9):848, February 1988.

[60] D. A. Wharam, T. J. Thornton, R. Newbury, M. Pepper, H. Ahmed, J. E. F. Frost, D. G. Hasko, D. C. Peacock, D. A. Ritchie, and G. A. C. Jones. One-dimensional transport and the quantisation of the ballistic resistance. *Journal of Physics C: Solid State Physics*, 21(8):L209–L214, January 1988.

[61] B. J. van Wees, L. P. Kouwenhoven, H. van Houten, C. W. J. Beenakker, J. E. Mooij, C. T. Foxon, and J. J. Harris. Quantized conductance of magnetoelectric subbands in ballistic point contacts. *Physical Review B*, 38(5):3625–3627, August 1988.

[62] R. Bisognin, H. Bartolomei, M. Kumar, I. Safi, J.-M. Berroir, E. Bocquillon, B. Placais, A. Cavanna, U. Gennser, Y. Jin, and G. Fève. Microwave photons emitted by fractionally charged quasiparticles. *Nature Communications*, 10(1708):1–7, April 2019.

[63] W. W. Xue, B. Davis, F. Pan, J. Stettenheim, T. J. Gilheart, and A. J. Rimberg. On-chip matching networks for radio-frequency single-electron transistors. *Applied Physics Letters*, 91(9):093511, August 2007.

[64] W. W. Xue, Z. Ji, F. Pan, J. Stettenheim, M. P. Blencowe, and A. J. Rimberg. Measurement of quantum noise in a single-electron transistor near the quantum limit. *Nature Physics*, 5:660–664, July 2009.

[65] T. Holst, D. Esteve, C. Urbina, and M. H. Devoret. Effect of a transmission line resonator on a small capacitance tunnel junction. *Physical Review Letters*, 73(25):3455–3458, December 1994.

[66] E. Zakka-Bajjani, J. Ségala, F. Portier, P. Roche, D. C. Glattli, A. Cavanna, and Y. Jin. Experimental test of the high-frequency quantum shot noise theory in a quantum point contact. *Physical Review Letters*, 99(23):236803, December 2007.

[67] M. Hofheinz, F. Portier, Q. Baudouin, P. Joyez, D. Vion, P. Bertet, P. Roche, and D. Esteve. Bright side of the Coulomb blockade. *Physical Review Letters*, 106(21):217005, May 2011.

[68] M. A. Castellanos-Beltran and K. W. Lehnert. Widely tunable parametric amplifier based on a superconducting quantum interference device array resonator. *Applied Physics Letters*, 91(8):083509, July 2007.

[69] V. E. Manucharyan, J. Koch, L. I. Glazman, and M. H. Devoret. Fluxonium: single cooper pair circuit free of charge offsets. *Science*, 326(5949):113–116, October 2009.

[70] M. T. Bell, I. A. Sadovskyy, L. B. Ioffe, A. Yu. Kitaev, and M. E. Gershenson. Quantum superinductor with tunable non-linearity. *Physical Review Letters*, 109(13):137003, September 2012.

[71] Yu. Krupko, V. D. Nguyen, T. Weißl, É. Dumur, J. Puertas, R. Dassonneville, C. Naud, F. W. J. Hekking, D. M. Basko, O. Buisson, N. Roch, and W. Hasch-Guichard. Kerr nonlinearity in a superconducting Josephson metamaterial. *Physical Review B*, 98(9):094516, September 2018.

[72] C. Altimiras, O. Parlavecchio, P. Joyez, D. Vion, P. Roche, D. Esteve, and F. Portier. Dynamical Coulomb blockade of shot noise. *Physical Review Letters*, 112(23):236803, jun 2014.

[73] A. Stockklauser, P. Scarlino, J. V. Koski, S. Gasparinetti, C. K. Anderson, C. Reichl, W. Wegscheider, T. Ihn, K. Ensslin, and A. Walraff. Strong coupling cavity QED with gate-defined double quantum dots enabled by a high impedance resonator. *Physical Review X*, 7(1):011030, March 2017.

[74] J. Basset, D. Watfa, G. Aiello, M. Fechant, A. Morvan, J. Estève, J. Gabelli, M. Aprili, R. Weil, A. Kasumov, H. Bouchiat, and R. Deblock. High kinetic inductance microwave resonatorsmade by He-beam assisted deposition of tungsten nanowires. *Applied Physics Letters*, 114(10):102601, March 2019.

[75] W. Zhang, K. Kalashnikov, W.-S. Lu, P. Kamenov, T. DiNapoli, and M. E. Gershenson. Microresonators fabricated from high-kinetic-inductance aluminum films. *Physical Review Applied*, 11(1):011003, January 2019.

[76] C. Kaiser, A. F. Panchula, and S. S. P. Parkin. Finite tunneling spin polarization at the compensation point of rare-earth-metal–transition-metal alloys. *Physical Review Letters*, 95(4):047202, July 2005.

[77] C. Rolland, A. Peugeot, S. Dambach, M. Westig, B. Kubala, Y. Mukharsky, C. Altimiras, H. le Sueur, P. Joyez, D. Vion, P. Roche, D. Esteve, J. Ankerhold, and F. Portier. Antibunched photons emitted by a DC-biased Josephson junction. *Physical Review Letters*, 122(18):186804, May 2019.

[78] A. Kumar, L. Saminadayar, D. C. Glattli, Y. Jin, and B. Etienne. Experimental test of the quantum shot noise reduction theory. *Physical Review Letters*, 76(15):2778, April 1996.

[79] M. Reznikov, M. Heiblum, H. Shtrikman, and D. Mahalu. Temporal correlation of electrons: Suppression of shot noise in a ballistic quantum point contact. *Physical Review Letters*, 75(18):3340–3343, October 1995.

[80] A. H. Steinbach, J. M. Martinis, and M. H. Devoret. Observation of hot-electron shot noise in a metallic resistor. *Physical Review Letters*, 76(20):3806, May 1996.

[81] N. W. Ashcroft and N. D. Mermin. *Solid State Physics*. Saunders College Publishing, 1976.

[82] J. J. Lin and J. P. Bird. Recent experimental studies of electron dephasing inmetal and semiconductor mesoscopic structures. *Journal of Physics: COndensed Matter*, 14(18):501–596, April 2002.

[83] C. W. J. Beenakker and H. Van Houten. Quantum transport in semiconductor nanostructures. *Solid State Physics*, 44:1–228, 1991.

[84] H. Duprez, E. Sivre, A. Anthore, A. Aassime, A. Cavanna, A. Ouerghi, U. Gennser, and F. Pierre. Macroscopic electron quantum coherence in a solid-state circuit. *Physical Review X*, 9(2):021030, May 2019.

[85] C. Jiang and D. C. Tsui. Threshold transport of high-mobility two-dimensional electron gas in GaAs/AlGaAs heterostructures. *Applied Physics Letters*, 53(16):1533–1535, October 1988.

[86] I. Giaever. *Nobel Lectures, Physics 1971-1980*, chapter Electron Tunneling and Superconductivity, pages 137–153. World Scientific Publishing Co., December 1973.

[87] I. Giaever. Energy gap in superconductors measured by electron tunneling. *Physical Review Letters*, 5(4):147–148, August 1960.

[88] P. W. Anderson and J. M. Rowell. Probable observation of the josephson superconducting tunneling effect. *Physical Review Letters*, 10(230), March 1963.

[89] B. D. Josephson. Possible new effects in superconductive tunnelling. *Physics Letters*, 1(7):251–253, July 1962.

[90] L. Esaki. New phenomenon in narrow germanium p-n junctions. *Physical Review Journals Archive*, 109(2):603, January 1958.

[91] R. C. Jaklevic, J. Lambe, A. H. Silver, and J. E. Mercereau. Quantum interference effects in Josephson tunneling. *Physical Review Letters*, 12(7):159–160, February 1964.

[92] R. C. Jaklevic, J. Lambe, J. E. Mercereau, and A. H. Silver. Macroscopic quantum interference in superconductors. *Physical Review Journals Archive*, 140(5A):A1628, November 1965.

[93] J. Tucker. Quantum limited detection in tunnel junction mixers. *IEEE Journal of Quantum Electronics*, 15(11):1234–1258, November 1979.

[94] M. Kjaergaard, M. E. Schwartz, J. Braumüller, P. Krantz, J. I.-J. Wang, S. Gustavsson, and W. D. Oliver. Superconducting qubits: Current state of play. *Annual Reviews*, 11:369–395, March 2020.

[95] L. Esaki and Y. Miyahara. A new device using the tunneling process in narrow p-n junctions. *Solid-State Electronics*, 1(1):13–14, March 1960.

[96] J. Faist, F. Capasso, D. L. Sivco, C. Sirtori, A. L. Hutchinson, and A. Y. Cho. Quantum cascade laser. *Science*, 264(5158):553–556, 1994.

[97] L. Mihály and M. C. Martin. *Solid State Physics: Problems and Solutions*. Wiley, 2nd edition, February 2009.

[98] R. Landauer. Spatial variation of currents and fields due to localized scatterers in metallic conduction. *IBM Journal of Research and Development*, 1(3):223–231, July 1957.

[99] R. Landauer and M. Büttiker. Resistance of small metallic loops. *Physical Review Letters*, 54(18):2049, May 1985.

[100] M. Büttiker. Scattering theory of thermal and excess noise in open conductors. *Physical Review Letters*, 65(23):2901–2904, December 1990.

[101] M. Büttiker. Scattering theory of current and intensity noise correlations in conductors and wave guides. *Physical Review B*, 46(19):12485–12507, November 1992.

[102] G. B. Lesovik. Excess quantum noise in 2D ballistic point contacts. *Pis'ma Zh. Eksp. Teor. Fiz.*, 49(9):513–515, May 1989.

[103] Th. Martin and R. Landauer. Wave-packet approach to noise in multichannel mesoscopic systems. *Physical Review B*, 45(4):1472, January 1992.

[104] L. S. Levitov and H. Lee. Electron counting statistics and coherent states of electric current. *Journal of Mathematical Physics*, 37(10):4845, 1996.

[105] Y. Imry, H. G. Craighead, P. Jena, P. A. Lee, A. H. Macdonald, S. Mukamel, M. A. Reed, and J. C. Spence. *Introduction to mesoscopic physics*. Oxford University Press, 1997.

[106] M. H. Pedersen, S. A. van Langen, and M. Büttiker. Charge fluctuations in quantum point contacts and chaotic cavities in the presence of transport. *Physical Review B*, 57(3):1838, January 1998.

[107] M. Büttiker. Absence of backscattering in the quantum Hall effect in multiprobe conductors. *Physical Review B*, 38(14):9375, November 1988.

[108] J. B. Johnson. Thermal agitation of electricity in conductors. *Physical Review*, 32(1):97–109, July 1928.

[109] H. Nyquist. Thermal agitation of electric charge in conductors. *Physical Review*, 32(1):110–113, July 1928.

[110] W. Schottky. Über spontane Stromschwankungen in verschiedenen Elektrizitätsleitern. *Annalen der Physik*, 362(23):541–567, 1918.

[111] D. C. Glattli. Quantum shot noise of conductors and general noise measurement methods. *The European Physics Journal Special Topics*, 172:163–179, 2009.

[112] V. A. Khlus. Current and voltage fluctuations in microjunctions between normal metals and superconductors. *Zh. Eksp. Teor. Fiz*, 93(6):2179–2190, December 1987.

[113] S.-R. E. Yang. Quantum shot noise spectrum of a point contact. *Solid State Communications*, 81(5):375–378, 1992.

[114] A. Einstein. Zur Elektrodynamik bewegter Körper. *Annalen der Physik*, 332(10):891–921, June 1905.

[115] I. Safi and P. Joyez. Time-dependent theory of nonlinear response and current fluctuations. *Physical Review B*, 84(20):205129, November 2011.

[116] I. Safi. Driven quantum circuits and conductors: A unifying perturbative approach. *Physical Review B*, 99(4):045101, January 2019.

[117] I. Safi. Fluctuation-dissipation relations for strongly correlated out-of-equilibrium circuits. *Physical Review B*, 102(4):041113, July 2020.

[118] D. Rogovin and D. J. Scalapino. Fluctuation phenomena in tunnel junctions. *Annals of Physics*, 86(1):1–90, July 1974.

[119] P. Février and J. Gabelli. Tunneling time probed by quantum shot noise. *nature communications*, 9(4940), November 2018.

[120] U. Gavish, Y. Imry, Y. Levinson, B. Yurke, and Y. V. Nazarov. *Quantum Noise in Mesoscopic Physics*, chapter What Quantity is Measured in an Excess Noise Experiment?, pages 297–311. Kluwer Academic Publishers, 2003.

[121] A. Clerk, Michel Devoret, Benjamin Huard, Robert Schoelkopf, and Leticia F. Cugliandolo. *Quantum Machines: Measurement and Control of Engineered Quantum System*, volume 96 of *Les Houches 2011*, chapter Quantum noise and quantum measurement. Oxford Scholarship Online, 2014.

[122] R. H. Koch, D. J. Van Harlingen, and J. Clarke. Observation of zero-point fluctuations in a resistively shunted Josephson tunnel junction. *Physical Review Letters*, 47(17):1216, October 1981.

[123] C. Eichler, D. Bozyigit, and A. Wallraff. Characterizing quantum microwave radiation and its entanglement with superconducting qubits using linear detectors. *Physical Review A*, 86(3):2106, September 2012.

[124] C. Eichler, C. Lang, J. M. Fink, J. Govenius, S. Filipp, and A. Wallraff. Observation of entanglement between itinerant microwave photons and a superconducting qubit. *Physical Review Letters*, 109(24):240501, December 2012.

[125] A. Grimm, F. Blanchet, R. Albert, J. Leppäkangas, S. Jebari, D. Hazra, F. Gustavo, J.-L. Thomassin, E. Dupont-Ferrier, F. Portier, and M. Hofheinz. Bright on-demand source of antibunched microwave photons based on inelastic cooper pair tunneling. *Physical Review X*, 9(2):021016, April 2019.

[126] M. Kindermann, Yu. V. Nazarov, and C. W. J. Beenakker. Feedback of the electromagnetic environment on current and voltage fluctuations out of equilibrium. *Physical Review B*, 69(3):035336, June 2004.

[127] A. L. Grimsmo, F. Qassemi, B. Reulet, and A. Blais. Quantum optics theory of electronic noise in coherent conductors. *Physical Review Letters*, 116(04):3602, January 2016.

[128] R. J. Schoelkopf, P. J. Burke, A. A. Kozhevnikov, D. E. Prober, and M. J. Rooks. Frequency dependence of shot noise in a diffusive mesoscopic conductor. *Physical Review Letters*, 78(17):3370, April 1997.

[129] J. Basset. *High frequency quantum noise of mesoscopic systems and current-phase relation of hybrid junctions*. Phd thesis, University Paris South, October 2011.

[130] E. Onac, F. Balestro, L. H. Willems van Beveren, U. Hartmann, Y. V. Nazarov, and L. P. Kouwenhoven. Using a quantum dot as a high-frequency shot noise detector. *Physical Review Letters*, 96(17):1776601, May 2006.

[131] M. A. Reed. Quantum dots. *Scientific American*, 268(1):118–123, January 1993.

[132] L. P. Kouwenhoven, C. M. Marcus, P. L. McEuen, S. Tarucha, R. M. Westervelt, and N. S. Wingreen. *Mesoscopic Electron Transport*, volume 345 of *E: Applied Sciences*, chapter Electron Transport in Quantum Dots, pages 105–214. NATO ASI Series, 1997.

[133] S. Gustavsson, R. Leturcq, B. Simovič, R. Schleser, T. Ihn, P. Studerus, K. Ensslin, D. C. Driscoll, and A. C. Gossard. Counting statistics of single electron transport in a quantum dot. *Physical Review Letters*, 96(7):076605, February 2006.

[134] S. Gustavsson, I. Shorubalko, R. Leturcq, T. Ihn, K. Ensslin, and S. Schön. Detecting terahertz current fluctuations in a quantum point contact using a nanowire quantum dot. *Physical Review B*, 78(3):035324, July 2008.

[135] B. D. Josephson. Supercurrents through barriers. *Advances in Physics*, 14(56):419–451, October 1965.

[136] R. Delagrange, J. Basset, H. Bouchiat, and R. Deblock. Emission noise and high frequency cut-off of the kondo effect in a quantum dot. *Physical Review B*, 97(4):041412, January 2018.

[137] D. Watfa, R. Delagrange, A. Kadlecov, M. Ferrier, A. Kasumov, H. Bouchiat, and R. Deblock. Collapse of the josephson emission in a carbon nanotube junction in the kondoregime. *arXiv cond-mat.mes-hall*, September 2020. 2009.09740.

[138] A. Barone and G. Paterno. *Physics and Applications of the Josephson Effect*. John Wiley and Sons Inc., July 1982.

[139] E. V. Sukhorukov, G. Burkard, and D. Loss. Noise of a quantum dot system in the cotunneling regime. *Physical Review B*, 63(12), March 2001.

[140] Benjamin Roussel, Pascal Degiovanni, and Inès Safi. Perturbative fluctuation dissipation relation for nonequilibrium finite-frequency noise in quantum circuits. *Physical Review B*, 93(4):5102, January 2016.

[141] A. Anthore, Z. Iftikhar, E. Boulat, F. D. Parmentier, A. Cavanna, A. Ouerghi, U. Gennser, and F. Pierre. Circuit quantum simulation of a Tomonaga-Luttinger liquid with an impurity. *Physical Review X*, 8(3):031075, September 2018.

[142] X. G. Wen. Chiral Luttinger liquid and the edge excitations in the fractional quantum Hall states. *Physical Review B*, 41(18):12838, June 1990.

[143] X. G. Wen. Non-abelian statistics in the fractional quantum Hall states. *Physical Review Letters*, 66(6):802, February 1991.

[144] G. Moore and N. Read. Nonabelions in the fractional quantum hall effect. *Nuclear Physics B*, 360(2-3):362–396, August 1991.

[145] H. Bartolomei, M. Kumar, R. Bisognin, A. Marguerite, J.-M. Berroir, E. Bocquillon, B. Plaçais, A. Cavanna, Q. Dong, U. Gennser, Y. Jin, and G. Fève. Fractional statistics in anyon collisions. *Science*, 368(6487):173–177, April 2020.

[146] Ph. Nozières and A. Blandin. Kondo effect in real metals. *Journal de Physique France*, 41(3):193–211, March 1980.

[147] Ian Affleck. Non-fermi liquid behavior in kondo models. *Journal of the Physical Society Japan*, 74:59–66, August 2005.

[148] R. Lambeir, A. Vanitterbeek, and G. J. Vandenberg. Measurements on the electrical resistivity of thin iron films at liquid helium temperatures. *Physica*, 16(11-12):907–914, 1950.

[149] N. Mostovetch and B. Vodar. Variations, en fonction du potentiel applique, de la resistance electrique des depots metalliques tres minces aux basses temperatures. *Comptes rendus hebdomadaires des séances de l'Académie des sciences*, 230(934), 1950.

[150] C. J. Gorter. A possible explanation of the increase of the electrical resistance of thin metal films at low temperatures and small field strengths. *Physica*, 17(8):777–780, May 1951.

[151] T. A. Fulton and G. J. Dolan. Observation of single-electron charging effects in small tunnel junctions. *Physical Review Letters*, 59(1):109, March 1987.

[152] P. Joyez and D. Esteve. Single-electron tunneling at high temperature. *Physical Review B*, 56(4):1848, July 1997.

[153] David Pines and Phillippe Nozières. *The Theory Of Quantum Liquids Volume I: Normal Fermi Liquids*, volume 1. Basic Books, January 1989.

[154] R. E. Peierls. *Quantum Theory of Solids*. Oxford University Press, 1955.

[155] S. Tomonaga. Remarks on Bloch's method of sound waves applied to many-Fermion problems. *Progress of Theoretical Physics*, 5(4):544–569, July 1950.

[156] J. M. Luttinger. An exactly soluble model of a many-Fermion system. *Journal of Mathematical Physics*, 4(9):1154–1162, September 1963.

[157] D. C. Mattis and E. H. Lieb. Exact solution of a many-Fermion system and its associated Boson field. *Journal of Mathematical Physics*, 6(2):304–312, February 1965.

[158] F. D. M. Haldane. 'Luttinger liquid theory' of one-dimensional quantum fluids. I. Properties of the Luttinger model and their extension to the general 1d interacting spinless Fermi gas. *Journal of Physics C: Solid State Physics*, 14(19):2585–2609, July 1981.

[159] J. von Delft and H. Schoeller. Bosonization for beginners — refermionization for experts. *Annalen der Physik*, 7(4), December 1998.

[160] O. M. Auslaender, A. Yacoby, R. de Picciotto, K. W. Baldwin, L. N. Pfeiffer, and K. W. West. Tunneling spectroscopy of the elementary excitations in a one-dimensional wire. *Science*, 295(8255556):825–828, February 2002.

[161] E. Levy, A. Tsukernik, M. Karpovski, A. Palevski, B. Dwir, E. Pelucchi, A. Rudra, E. Kapon, and Y. Oreg. Luttinger-liquid behavior in weakly disordered quantum wires. *Physical Review Letters*, 97(19):196802, November 2006.

[162] Y. Jompol, C. J. B. Ford, J. P. Griffiths, I. Farrer, G. A. C. Jones, D. Anderson, D. A. Ritchie, T. W. Silk, and A. J. Schofield. Probing spin-charge separation in a tomonaga-luttinger liquid. *Science*, 325(5940):597–601, July 2009.

[163] Y. Jin, O. Tsyplyatyev, M. Moreno, A. Anthore, W. K. Tan, J. P. Griffiths, I. Farrer, D. A. Ritchie, L. I. Glazman, A. J. Schofield, and C. J. B. Ford. Momentum-dependent power law measured in an interacting quantum wire beyond the luttinger limit. *Nature Communications*, 10(2821), June 2019.

[164] C. L. Kane and M. P. A. Fisher. Transport in a one-channel Luttinger liquid. *Physical Review Letters*, 68(8):1220, February 1992.

[165] D. S. Golubev and A. D. Zaikin. Coulomb interaction and quantum transport through a coherent scatterer. *Physical Review Letters*, 86(21):4887, May 2001.

[166] A. Levy Yeyati, A. Martin-Rodero, D. Esteve, and C. Urbina. Direct link between Coulomb blockade and shot noise in a quantum-coherent structure. *Physical Review Letters*, 87(4):046802, July 2001.

[167] M. Kindermann and Yu.V. Nazarov. Interaction effects on counting statistics and the transmission distribution. *Physical Review Letters*, 91(13):136802, September 2003.

[168] Edouard Boulat. Full exact solution of the out-of-equilibrium boundary sine gordon model. *arXiv*, December 2019. 1912.03872.

[169] O. Parlavecchio. *Quantum Microwave Photons Emitted in Dynamical Coulomb Blockade*. Phd thesis, Sorbonne University, December 2014.

[170] E. H. Hall. On a new action of the magnet on electric currents. *American Journal of Mathematics*, 2(3):287–292, September 1879.

[171] R. B. Dingle. Some magnetic properties of metals II. The influence of collisions on the magnetic behaviour of large systems. *Proceedings of the Royal Society A*, 211(1107):517–525, 1952.

[172] R. R. Gerhardts. Cumulant approach to the two-dimensional magneto-conductivity problem. *Surface Science*, 58(1):227–234, August 1976.

[173] L. Wang and R. F. O' Connell. Landau-level width: Magnetic-field and temperature dependences. *Physical Review B*, 37(6):3502–3057, February 1988.

[174] L. Schubnikov and W. J. de Haas. A new phenomenon in the change of resistance in a magnetic field of single crystals of bismuth. *Nature*, 126:500, October 1930.

[175] T. Ihn. *Semiconductor Nanostructures: Quantum states and electronic transport*. Oxford UniversityPress, February 2010.

[176] K. v. Klitzing, G. Dorda, and M. Pepper. New method for high-accuracy determination of the fine-structure constant based on quantized hall resistance. *Physical Review Letters*, 45(6):494, August 1980.

[177] D. C. Tsui, H. L. Stormer, and A. C. Gossard. Two-dimensional magnetotransport in the extreme quantum limit. *Physical Review Letters*, 48(22):1559, May 1982.

[178] R. Willett, J. P. Eisenstein, H. L. Stormer, D. C. Tsui, A. C. Gossard, and J. H. English. Observation of an even-denominator quantum number in the fractional quantum Hall effect. *Physical Review Letters*, 59(15):1776–1779, October 1987.

[179] R. E. Prange and S. M. Girvin. *The Quantum Hall Effect*. Springer-Verlag New York, 1 edition, 1987.

[180] J. K. Jain. Composite-Fermion approach for the fractional quantum Hall effect. *Physical Review Letters*, 63(2):199, July 1989.

[181] J. K. Jain. The composite Fermion: A quantum particle and its quantum fluids. *Physics Today*, 53(4):39–45, April 2000.

[182] R. L. Willett, C. Nayak, K. Shtengel, L. N. Pfeiffer, and K. W. West. Magnetic field-tuned aharonov-bohm oscillations and evidence for non-abelian anyons at v=5/2. *Physical Review Letters*, 111(18):6401, October 2013.

[183] C. Nayak, S. H. Simon, A. Stern, M. Freedman, and S. D. Sarma. Non-abelian anyons and topological quantum computation. *Reviews of Modern Physics*, 80(3):1083, September 2008.

[184] Y. C. Chung, M. Heiblum, and V. Umansky. Scattering of bunched fractionally charged quasiparticles. *Physical Review Letters*, 91(21):216804, November 2003.

[185] A. Bid, N. Ofek, M. Heiblum, V. Umansky, and D. Mahalu. Shot noise and charge at the 2/3 composite fractional quantum Hall state. *Physical Review Letters*, 103(23):236802, December 2009.

[186] J. Kondo. Resistance minimum in dilute magnetic alloys. *Progress of Theoretical Physics*, 32(1):37–49, July 1964.

[187] K. G. Wilson. The renormalization group: Critical phenomena and the Kondo problem. *Reviews of Modern Physics*, 47(4):773, October 1975.

[188] S. M. Cronenwett, T. H. Oosterkamp, and L. P. Kouwenhoven. A tunable Kondo effect in quantum dots. *Science*, 281(5376):540–544, July 1998.

[189] M. R. Buitelaar, T. Nussbaumer, and C. Schönenberger. Quantum dot in the kondo regime coupled to superconductors. *Physical Review Letters*, 89(25), December 2002.

[190] I. Affleck and A. W. W. Ludwig. Critical theory of overscreened kondo fixed points. *Nuclear Physics B*, 360(2-3):641–696, August 1991.

[191] I. Affleck. Quantum impurity problems in condensed matter physics. *arXiv*, 2008. arXiv:0809.3474, Lecture Notes, Les Houches.

[192] T. Delattre, C. Feuillet-Palma, L. G. Herrmann, P. Morfin, J.-M. Berroir, G. Fève, B. Plaçais, D. C. Glattli, M.-S. Choi, C. Mora, and T. Kontos. Noisy kondo impurities. *Nature physics*, 5:208–212, January 2009.

[193] E. Sela, Y. Oreg, F. von Oppen, and J. Koch. Fractional shot noise in the Kondo regime. *Physical Review Letters*, 97(8):086601, August 2006.

[194] M. Ferrier, R. Delagrange, J. Basset, H. Bouchiat, T. Arakawa, T. Hata, R. Fujiwara, Y. Teratani, R. Sakano, A. Oguri, K. Kobayashi, and R. Deblock. Quantum noise in carbon nanotubes as a probe of correlationsin the Kondo regime. *Journal of Low Temperature Physics*, September 2019.

[195] W. G. van der Wiel, S. De Franceschi, T. Fujisawa, J. M. Elzerman, S. Tarucha, and L. P. Kouwenhoven. The kondo effect in the unitary limit. *Science*, 289(5487):2105–2108, September 2000.

[196] J. Basset, A. Yu. Kasumov, C. P. Moca, G. Zaránd, P. Simon, H. Bouchiat, and R. Deblock. Measurement of quantum noise in a carbon nanotube quantum dot in the Kondo regime. *Physical Review Letters*, 108(4):046802, January 2012.

[197] A. N. Broers, A. C. F. Hoole, and J. M. Ryan. Electron beam lithography—resolution limits. *Microelectronic Engineering*, 32(1-4):131–142, September 1996.

[198] G. Rius, A. Baldi, B. Ziaie, M. Z. Atashbar, and B. Bushan. *Handbook of Nanotechnology*, chapter Introduction to Micro-/Nanofabrication, page 51. Springer, 4 edition, 2017.

[199] A. Y. Cho and J. R. Arthur. Molecular beam epitaxy. *Progress in Solid-State Chemistry*, 10(Part 3):157–191, 1975.

[200] M. R. Melloch. Molecular beam epitaxy for high electron mobility modulation-doped two-dimensional electron gases. *Thin Solid Films*, 231(1-2):74–85, August 1993.

[201] J. H. Davies. *The Physics of Low-dimensional Semiconductors*. Cambridge University Press, 1997.

[202] T. Schäpers and R. Waser. *Nanotechnology Volume 3: Information Technology*, chapter Phase Coherent States. Wiley-CH, June 2008.

[203] A. G. Baca and C. I. H. Ashby. *Fabrication of GaAs Devices*. Number 6 in EMIS processing. The Institution of Electrical Engineers, September 2005.

[204] H. van Houten, C. W. J. Beenakker, B. J. van Wees, and M. Reed. *Semiconductors and Semimetals*, volume 35, chapter Quantum Point Contacts, pages 9–112. Academic Press Inc., 1992.

[205] Cryo-Concept. http://cryoconcept.com/expertise/super-conducting-cryogen-magnets. Figure taken from Website, January 2020.

[206] D. M. Pozar. *Microwave Engineering*. JohnWiley & Sons, Inc., 4 edition, 2012.

[207] R. N. Simons. *Coplanar Waveguide Circuits, Components, and Systems*. John Wiley & Sons, Inc., March 2001.

[208] C. P. Wen. Coplanar waveguide: A surface strip transmission line suitable for nonreciprocal gyromagnetic device applications. *IEEE Transactions on Microwave Theory and Techniques*, 17(12):1087–1090, December 1969.

[209] M. Peruzzo, A. Trioni, F. Hassani, M. Zemlicka, and J. M. Fink. Surpassing the resistance quantum with a geometric superinductor. *arXiv*, July 2020. 2007.01644.

[210] H. Pothier. *Blocage de Coulomb et Transfert de Un par Un*. PhD thesis, Universite Paris 6, September 1991.

[211] G. A. Luurtsema. Spin coating for rectangular substrates. Master thesis, The department of electrical engineering and computer scineces, University of California, Berkely, July 1997.

[212] S. De Franceschi, R. Hanson, W. G. van der Wiel, J. M. Elzerman, J. J. Wijpkema, T. Fujisawa, S. Tarucha, and L. P. Kouwenhoven. Out-of-equilibrium Kondo effect in a mesoscopic device. *Physical Review Letters*, 89(15):156801, September 2002.

[213] R. Leturcq, L. Schmid, K. Ensslin, Y. Meir, D. C. Driscoll, and A. C. Gossard. Probing the Kondo density of states in a three-terminal quantum ring. *Physical Review Letters*, 95(12):126603, September 2005.

[214] A. G. Baca, F. Ren, J. C. Zolper, R. D. Briggs, and S. J. Pearton. A survey of ohmic contacts to III-V compound semiconductors. *Thin Solid Films*, 308-309:599–606, October 1997.

[215] S. J. Pearton. *Processing of Wide Band Gap Semiconductors*. William Andrew Inc., 1 edition, 2000.

[216] S. M. Sze and K. K. Ng. *Physics of Semiconductor Devices*. JohnWiley & Sons, Inc., 3 edition, April 2006.

[217] N. Braslau, J. B. Gunn, and J. L. Staples. Metal-semiconductor contacts for GaAs bulk effect devices. *Solid-State Electronics*, 10(5):381–383, May 1967.

[218] A. Iliadis and K. E. Singer. Metallurgical behaviour of Ni/Au-Ge ohmic contacts to GaAs. *Solid State Communications*, 49(1):99–101, January 1984.

[219] S. Tahamtan, S. P. Abbasi, A. Hodaei, M. S. Zabihi, and J. Sabbaghzadeh. A study on AuGeNi ohmic contact to n-GaAs using microstructural characteristics. In *2011 Symposium on Photonics and Optoelectronics (SOPO)*, pages 1–4, Wuhan, China, May 2011. IEEE.

[220] V. Loup, L. Gabette, MC. Roure, R. Kachtouli, M. Jourdan, P. Besson, and S. Petitdidier. Silicon and SiGe alloys wet etching using TMAH chemistry. *ECS Transactions*, 58(6):47–55, 2013.

[221] O. Powell, D. Sweatman, and H. B. Harrison. The use of titanium and titanium dioxide as masks for deep silicon etching. *Smart Materials and Structures*, 15:81–86, December 2005.

[222] H. Kamerlingh Onnes. The liquefaction of helium. *KNAW Proceedings*, 11:168–185, 1908.

[223] P. Das, R. Debruyn Ouboter, K. W. Taconis, J. G. Daunt, D. O. Edwards, F. J. Milford, and M. Yaqub. *Low Temperature Physics LT9*, chapter A Realization of a London-Clarke-Mendoza Type Refrigerator, pages 1253–1255. Springer Science, 1965.

[224] G. Frossati. Obtaining ultralow temperatures by dilution of ^{3}He into ^{4}He. *Journal de Physique Colloques*, 39(C6):C6–1578–C6–1589, 1978.

[225] D. I. Bradley, T. W. Bradshaw, A. M. Guenault, V. Keith, B. G. Locke-Scobie, I. E. Miller, G. R. Pickett, and Jr W. P. Pratt. A dilution refrigerator combining low base temperature, high cooling power and low heat leak for use with nuclear cooling. *Cryogenics*, 22(6):296–304, June 1982.

[226] J. Wilks and D. S. Betts. *An introduction to liquid helium.* Oxford University Press, 2nd edition, 1987.

[227] D. S. Betts. *An introduction to millikelvin technology*, volume VIII of *Cambridge Studies in Low Temperature Physics.* Cambridge University Press, 1989.

[228] F. Pobell. *Matter and Methods at Low Temperatures.* Springer-Verlag Berlin Heidelberg, 3rd edition, 2007.

université PARIS-SACLAY
ÉCOLE DOCTORALE
Physique en l'Île-de-France (PIF)

Titre : Dynamique à fréquence finie de conducteurs quantiques corrélés

Mots clés : Physique mésoscopique, blocage de Coulomb dynamique (DCB), 2DEG, bruit quantique

Résumé : Dans ce travail, nous présentons les nouvelles méthodes expérimentales que nous avons développées afin d'étudier la physique fondamentale du transport électronique à travers des conducteurs mésoscopiques, en se basant sur la mesure des fluctuations électriques.
Dans la première partie de la thèse, nous présentons une nouvelle conception d'un détecteur quantique sans rétroaction pour mesurer séparément la densité spectrale de puissance des fluctuations de courant pour les fréquences positives (bruit d'absorption) et négatives (bruit d'émission). Nous extrayons le bruit d'absorption et d'émission d'une mesure de la puissance échangée entre un conducteur quantique et un résonateur linéaire à fréquence finie, testé pour une jonction SIS couplée à un filtre à cavité. Nos résultats soulignent la signification physique de la formule de Kubo qui, couplée à une description quantique du dispositif de mesure, fournit une version quantique du théorème de Joule.
Dans la deuxième partie de la thèse, nous présentons la conception et la construction d'une plate-forme expérimentale pour les mesures RF dépendantes du temps dans les champs magnétiques élevés. L'objectif est de mesurer efficacement un conducteur quantique sur une large gamme de fréquence, ce qui donne lieu à une contre-action de détection sur ses propriétés de transport, connue sous le nom de Blocage de Coulomb Dynamique (DCB). Nous souhaitons étudier de tels effets dans le cas élémentaire d'un canal de conduction unique, avec une transmission arbitraire, interagissant avec un mode électromagnétique unique. Le principal défi consiste à concevoir des résonateurs RF à haute impédance utilisés comme transformateur d'impédance pour coupler efficacement le canal unique à haute impédance (25,8 kΩ) à l'équipement de détection RF désadapté de 50Ω. Pour notre installation, nous avons d'abord conçu et testé un résonateur tolérant aux champs magnétiques, une bobine métallique plane, qui fournit une impédance caractéristique de 1 kΩ à une fréquence de résonance de 5,4 GHz. En utilisant deux résonateurs en série, il est possible d'obtenir une impédance de détection efficace de 27 kΩ qui assure un couplage suffisant à un seul canal. Avec toutes les méthodologies développées dans cette thèse, il est maintenant possible de réaliser une série remarquable d'expériences diverses dans un futur proche.

Title : Finite frequency dynamics in correlated quantum conductors

Keywords : Mesoscopic Physics, Dynamic Coulomb blockade (DCB), 2DEG, Quantum noise

Abstract : In this work, we present the new experimental methods that we have developed in order to investigate the fundamental physics of electronic transport across mesoscopic conductors based on the measurement of electrical fluctuations.
In the first part of the thesis we present a novel design of a back-action free quantum detector to separately measure the power spectral density of current fluctuations for positive (absorption noise) and negative (emission noise) frequencies. We extract the absorption and emission noise from a measurement of the power exchanged between a quantum conductor and a finite frequency linear resonator, tested for a SIS junction coupled to a cavity filter. Our results stress the physical meaning of the Kubo formula which, coupled to a quantum description of the measurement setup, provides a quantum version of Joule's theorem.
In the second part of the thesis, we present the design and construction of an experimental platform for time dependant RF-measurements in high magnetic fields. The goal is to efficiently measure a quantum conductor over a large frequency span, which gives rise to a detection back-action on its transport properties, known as Dynamical Coulomb Blockade (DCB). We wish to investigate such effects in the elementary case of a single conduction channel, with arbitrary transmission, interacting with a single electromagnetic mode. The main challenge is the engineering of high impedance RF resonators used as impedance transformer to efficiently couple the high impedance single channel (25.8 kΩ) to the mismatched 50Ω RF-detection equipment. For our setup we have firstly designed and tested a magnetic field tolerant resonator, a planar metallic coil, that provides a characteristic impedance of 1 kΩ at a resonance frequency of 5.4 GHz. Using two resonators in series, an effective detection impedance of 27 kΩ is achievable that provides sufficient coupling to a single channel. With all the methodologies developed in this thesis, it is now possible to perform an amazing series of various experiments in the near future.

Université Paris-Saclay
Espace Technologique / Immeuble Discovery
Route de l'Orme aux Merisiers RD 128 / 91190 Saint-Aubin, France